Development of High-performance Electrocatalysts for Hydrogen Production from Fresh and Seawater Splitting

by

Chen Meng

Graduate School of Science and Technology

Hirosaki University

2023

ABSTRACT

Direct electrolytic splitting of water for the production of pure hydrogen (H_2) is a promising technology that can help achieve carbon neutrality. Especially, recently, seawater electrolysis to replace freshwater electrolysis for the H_2 production becomes more and more attractive since the seawater occupies about 97% of water resource on the earth and a large amount of sustainable energy including ocean energy could be produced in the future. However, owing to the high concentration of chlorine ions (Cl^-) in seawater, the chlorine evolution reaction and/or hypochlorite generation reaction always compete with the oxygen evolution reaction (OER) at the anode, and simultaneously chloride corrosion occurs on both the anode and cathode. Thus, effective electrocatalysts with high selectivity toward the OER and excellent resistance to chloride corrosion should be developed. In this dissertation, I focus on the development of state-of-the-art electrocatalysts for water and seawater splitting, especially at a high current density even in the natural seawater-based electrolytes.

Firstly, non-noble metal-based electrocatalysts for hydrogen evolution reaction (HER) was developed. Herein, to achieve effective interface construction on the HER electrocatalysts, epitaxial growth of NiS on the surface of one-dimensional (1D) Ni_3S_2 nanowire on nickel foam (NF) was performed, in which a Ni_3S_2/NiS electrocatalyst with a heterojunction structure via a solid-state phase transformation was synthesized. Benefiting from the strong charge transfer at the Ni_3S_2/NiS heterojunction interface, it is found that the d-band center was downshifted compared to the single component (Ni_3S_2 or NiS), which effectively optimized the valence state and the H adsorption of Ni, thus improved the HER activity. The obtained Ni_3S_2@NiS-250/NF showed the robust HER catalytic performance with a low overpotential of 129 mV to deliver the

current density of 10 mA cm^{-2} with a small Tafel slope (75.5 mV dec^{-1}) in 1 M KOH media. Moreover, it exhibited superior durability for at least 50 h. This work provides a novel strategy for designing nickel sulfide-based catalysts for HER with high performance.

Secondly, since the designing of cost-effective catalysts with high-activity and ultra-stability for HER is important in the scaling-up of water electrolysis process, a Zn-VO_x-Co two-dimensional (2D) nanosheet with well-integrated heterostructure was successfully synthesized on carbon fiber paper (CFP) by a facile electrodeposition approach. Interestingly, the obtained nanosheets composed of amorphous VO_x-Co and Zn-Co crystalline phases with a heterostructure. Density functional theory (DFT) calculations reveled that the dual-doping of Zn and VO_x optimized the d-band center of Co and balanced the adsorption and desorption of H, which enhanced intrinsic electrocatalytic HER activity. As a result, by using the optimum catalyst, a current density of 10 mA cm^{-2} at an overpotential as low as 46 mV and long-term electrochemical stability over 36 h in 1 M KOH solution was achieved. This work opens a new avenue for designing electrocatalysts with unique crystalline-amorphous heterostructure by dual-doping to achieve tunable surface properties as well as d-band structure.

Lastly, since seawater splitting requires highly active and stable electrocatalysts to sustain electrolysis without chloride corrosion, especially for the anode, a novel boron (B) doped $MnFe_2O_4$ spinel-type electrocatalyst with a heterostructure was derived from MnFe-MOF-74 precursor and applied for seawater electrolysis. It is found that the introduction of B species can effectively optimize the electronic configuration of $MnFe_2O_4$, with the promoted electron transfer ability between neighboring O to Fe_{Oh}, thereby significantly reducing the energy barrier of the electron transfer and boosting

the reaction process. As expected, in the real seawater environment, it required a low overpotential of 330 mV for OER to drive a current density of 100 mA cm^{-2} at 60 ℃, and high stability for over 200-h continuing test without producing hypochlorite and corrosion. This work provides a new strategy for enhancing the intrinsic activity of spinel-type oxides in seawater splitting.

In conclusion, three state-of-the-art electrocatalysts have been successfully obtained for the freshwater and seawater electrolysis. The catalytic mechanisms have been explored in details. It is expected to provide promising low-cost electrocatalysts for the hydrogen production from water especially seawater electrolysis, and give the guidance for the design of effective electrocatalysts.

ACKNOWLEDGEMENTS

First of all, I would like to give my heartfelt appreciate to all the people who had ever helped me during my PhD course!

My sincere and heartly thanks and appreciation to my supervisor professor Dr. Guoqing Guan, whose suggestions, encouragements, guidance, patience and supports for my research and daily life during my PhD program. It is my honor to benefit from his personality and diligence, which I will treasure in my whole life. I feel so lucky to be one of your students.

I am also thankful to Professor Abuliti Abudula for his advices on my research during my staying in Hirosaki University.

I am extremely grateful to Dr. Yufei Ma for recommending me to work towards PhD in Hirosaki University, and his advices and guidance for my manuscript writing. Also, I would like to acknowledge to Dr. Kai Yan at Sun Yat-sen University and Dr. Xiumin Li at Zhengzhou University for their suggestions on my research.

I am thankful to all professors and staffs at Institute of Regional Innovation (IRI) and Graduated School of Science and Technology, Hirosaki University, for all kind supports.

I would like to extend my sincere thanks to all members in our lab for all their kind suggestions and supports, especially the water-splitting group member, who is waiting me to return home and providing emotional helps.

Thanks to all of my friends from China, for their concern and emotional supports.

I would like to acknowledge to China Scholarship Council (CSC) for the financial support during the Covid-19 period in Japan.

Lastly, I sincerely thank my parents and brother for their kind supports and believes. They are my motivation to be a better person, as well as my everything.

Thank you all very much!

Chen Meng

TABLE OF CONTENTS

ABSTRACT i

ACKNOWLEDGEMENTS iv

TABLE OF CONTENTS v

LIST OF TABLES x

LIST OF FIGURES xii

CHAPTER 1 Introduction 1

1.1 REACTION MECHANISM OF WATER ELECTROCATALYSIS 2

1.1.1 Theoretical of hydrogen evolution reaction (HER) 2

1.1.2 General mechanism of the OER in water electrolysis 4

1.1.3 Fundamentals of seawater electrolysis 5

1.1.4 Key Parameters for HER and OER 13

1.2 METHODS FOR ELECTRODE FABRICATION 16

1.2.1 Precipitation method 17

1.2.2 Sol-gel method 18

1.2.3 Hydrothermal/solvothermal method 18

1.2.4 Microwave-assisted method 19

1.2.5 Electrodeposition method 19

1.3 CATHODE MATERIAL DESIGN FOR HER 20

1.3.1 Transition metal alloy (TMAs) 20

1.3.2 Transition metal sulfides (TMS) 22

1.3.3 Transition metal carbides (TMCs) 23

1.4 ANODE MATERIAL DESIGN FOR OER 24

1.4.1 Noble metal oxide-based oxides 24

1.4.2 Non-noble metal oxides 26

1.4.3 Spinel- type oxides 27

1.4.4 Perovskite-type oxides 30

1.4.5 Transition metal layered double hydroxide (TM-LDH) 31

1.5 MATERIAL DESIGN FOR SEAWATER SPLITTING 33

1.5.1 Transition metal oxide compounds 33

1.5.2 Performances of electrocatalyst based electrocatalysts at high current density 36

1.5.3 Perspectives of the seawater splitting 38

1.6 OBJECTIVE OF THIS STUDY 40

1.7 SCOPE OF THIS DESSERTATION 41

CHAPTER 2 Heterojunction engineering of Ni_3S_2/NiS nanowire for electrochemical hydrogen evolution 57

2.1. Introduction 57

2.2 Experimental section 59

2.2.1 Chemicals and Materials 59

2.2.2 Material Characterizations 60

2.2.3 Electrochemical performance tests 61

2.2.4 Computational method 61

2.3. Results and discission 62

2.3.1 Synthesis and characterization of Ni_3S_2@NiS-250/NF electrode 62

2.3.2 HER performance 70

2.3.3 DFT calculations 77

2.4 Conclusions 80

References 81

CHAPTER 3 Zn-VO_x-Co nanosheets with amorphous/ crystalline heterostructure for highly efficient hydrogen evolution reaction 88

3.1 Introduction 88

3.2 Experimental section 91

3.2.1 Chemical and Materials 91

3.2.2 Preparation of Zn-VO_x-Co Nanosheet Based Electrode 91

3.2.3 Material Characterizations 92

3.2.4 Electrochemical measurements 92

3.2.5 DFT calculation 93

3.3 Results and discussion 94

3.3.1 Characteristics of Zn-VO_x-Co 2D ultrathin nanosheets 94

3.3.2 Electrocatalytic property 108

3.3.3 DFT calculations 118

3.4 Conclusions 124

References 125

CHAPTER 4 Tuning octahedron sites in $MnFe_2O_4$ spinel by boron doping for highly efficient seawater splitting 133

4.1 Introduction 133

4.2 Experimental section 135

4.2.1 Chemical and materials 135

4.2.2 Synthesis of Samples 136

4.2.3 Catalyt characterization 137

4.2.4 Electrochemical measurements 138

4.2.5 Computational Method 140

4.3 Results and discussion 140

4.3.1 Characterization of B-$MnFe_2O_4$@MFOC electrocatalyst 140

4.3.2 Electrochemical performance for OER 158

4.3.3 DFT Calculations 163

4.3.4 Electrochemical performance for OER in seawater solution 168

4.4 Conclusions 175

References 175

CHAPTER 5 Conclusions and Prospects 183

5.1 Conclusions 183

5.2 Prospects 185

CURRICULUM VITAE 186

List of Publications and Presentations 188

List of Patents 191

LIST OF TABLES

Table 1.1 Features of various electrocatalyst fabrication methods.....20

Table 2.1 Ni $2p_{3/2}$ binding energies of Ni_3S_2/NF, Ni_3S_2@NiS-200/NF, Ni_3S_2@NiS-250/NF and Ni_3S_2@NiS-300/NF 70

Table 2.2 Summary of the HER performances of Ni_3S_2/NF, Ni_3S_2@NiS-200/NF, Ni_3S_2@NiS-250/NF and Ni_3S_2@NiS-300/NF 71

Table 2.3 Comparison of HER catalytic activities with the reported HER catalysts from Ni-based materials in 1M KOH. 72

Table 3.1 Co $2p_{3/2}$ and V $2p_{3/2}$ binding energies of pure Co, Zn-Co, VO_x-Co and Zn-VO_x-Co electrocatalysts. 106

Table 3.2 Comparison of HER catalytic activities with the reported HER catalysts from Co-based materials after iR-correction in 1M KOH. 111

Table 3.3 Summary of the HER performances of Zn-VO_x, pure Co, Zn-Co, VO_x-Co and Zn-VO_x-Co in 1 M KOH solution. 111

Table 3.4 Summary of the distance and angles between Co atoms in pure Co and VO_x-Co samples.....124

Table 4.1 Summary of Raman peak positions and areas of B-$MnFe_2O_4$@MFOC and MFOC. 144

Table 4.2 Summary information details of elements on B-$MnFe_2O_4$@FMOC measured from XPS. 156

Table 4.3 Summary of the OER performances of B-Mn_3O_4@MOC, B-Fe_3O_4@FOC, MFOC and B-$MnFe_2O_4$@FMOC. 160

Table 4.4 Comparison of OER catalytic activities with reported OER catalysts from oxides materials in 1M KOH. 160

Table 4.5 Summary of the distance and angles between Fe-O and Mn-O atoms in

$MnFe_2O_4$ and B-$MnFe_2O_4$.....165

Table 4.6 Comparison of OER catalytic activities with reported OER catalysts171

LIST OF FIGURES

Figure 1.1 (a) the classic four-steps OER mechanism of proton-coupled electron transfer (AEM) and (b) the idenlized OER mechanism based on the direct pairing of two lattice oxygens (LOM) in the anionic redex process [21]. 5

Figure 1.2 Pourbaix diagram of an artificial model solution (0.5 M NaCl solution with electrolytes to control the pH and no other chlorine species) depicting the thermodynamic equilibrium of H_2O/O_2 (green line), Cl^-/Cl_2-HOCl-OCl^- (red line) [20]..... 7

Figure 1.3 Surface structure of the fully-oxygen-covered RuO_2 (110) phase, denoted as $RuO_2(110)$-O_{ot}, in which all one-fold coordinatively unsaturated ruthenium atoms, Rucus (red balls), are capped by on-top oxygen (green balls). Blue balls indicate Ru_{2f} atoms, which are bridged by one-fold coordinatively unsaturated oxygen atoms (O_{br}). Adsorbates on Ru_{CUS} or Ru_{2f} are indicated with the subscript “ot” (on-top) or “br” (bridge), respectively [24]. 8

Figure 1. 4 Volcano plot for the ClER (gray) and OER (black) over RuO_2 (110). The size of the line (dotted lines) reflects the standard deviations as a result of the standard deviations in the linear scaling reactions [29]. 10

Figure 1.5 the stability window of the TMOs electrode [24]. 11

Figure 1.6 Snapshots of classical molecular dynamics simulations of electrolyte systems above the electrode surface [30]..... 12

Figure 1.7 (a) Precipitation [36]. (b) Sol-gel [43]. (c) Hydrothermal [46]. (d) Microwave-assisted [50]. (e) Electrodeposition [6]..... 17

Figure 1.8 Redistribution of the electron densities after the CoNi clusters have covered by one to three layers of graphene. The differential charge density ($\Delta\rho$) is defined as the difference in the electron density with and without the

CoNi cluster. The red and blue regions are regions of increased and decreased electron density, respectively [56]. 22

Figure 1.9 (a) Schematic illustration of the preparation of IrO_2/V_2O_5 oxides electrocatalysts. (b) SEM image of $IrO_2/V2O_5$. (c) and (d) HR-TEM images of IrO_2/V_2O_5. Calculated free energy diagrams of OER on the (e) Ir_4O_8/V_2O_5 and (f) IrO_2 under pH = 0 and 14, respectively. (g) -pCOHIP curves for O* intermediate adsorption on Ir active sites for Ir_4O_8/V_2O_5 and IrO_2 [67].....26

Figure 1.10 (a) Spinel crystal structure; (b) Schematic illustration for the preparation process of $NiCo_2O_4$@CC; (c) the schematic diagram for the synthetic procedure of the $Ir_1Ni_{1.6}Mn_{1.4}O_4$; (d) HR-TEM image of $Ni_{1.6}Mn_{1.4}O_4$, the inset reveals the corresponding FFT image. (e) HAADF-STEM image of 0.459% $IrNi_{1.6}Mn_{1.4}O_4$, indicative of the Ir-SAs; (f) the HAADF-STEM energy dispersive X-ray mapping, the bars represent 10 nm. (g) the wavelet transforms for the K^3-weighted Ir L^3-edge EXAFS signals of $Ir_1Ni_{1.6}Mn_{1.4}O_4$ compared to Ir foam and IrO. 29

Figure 1.11 (a) Sketch of the fabrication procedure for MnO_2 and Mn_2O_3 electrodes, functionalized with Fe_2O_3 or Co_3O_4 for seawater splitting [95]. (b-d), TEM images of NiFe-PBA-gel-cal after OER test. (e) SAED pattern of d. (f) Ni *2p* edge and (g) O*1s* edge of NiFe-PBA-gel-cal before and after OER test. (h) OER mechanism with concerted and nonconcerted proton-electron transfer. Procedure a: H_218O was used to active the catalyst and $H_2{}^{16}O$ served as electrolyte for the O_2 evolution; Procedure b: $H_2{}^{16}O$ was used to active the catalyst and $H_2{}^{18}O$ served as electrolyte for the O_2 evolution. (i) Schematic illustration of the water-splitting electrolyzer and (j) overall water-splitting performance of NiFe-PBA-gel-cal//NiFe-PBA-gel-cal electrode couple in

alkaline freshwater and simulated seawater (inset: hypochlorite detection result of the electrolyte after seawater splitting stability test) [100].....34

Figure 2.1 Schematic depiction of the fabrication of Ni_3S_2/NF and Ni_3S_2@NiS/NF electrodes 62

Figure 2.2 XRD patterns of Ni_3S_2/NF, Ni_3S_2@NiS-200/NF, Ni_3S_2@NiS-250/NF and Ni_3S_2@NiS-300/NF electrodes 64

Figure 2.3 XRD pattern of (a) pure nickel foam substrate and (b) $Ni(OH)_2$ 64

Figure 2.4 (a-b) SEM images of Ni_3S_2@NiS-250/NF and (c-f) corresponding elemental mappings of Ni and S on the Ni_3S_2@NiS-250/NF surface 65

Figure 2.5 SEM images of (a) pure nickel foam, (b) Ni_3S_2@NiS-250/NF in a large scale, (c) $Ni_3S_{2'}$/NF and (d) Ni_3S_2@NiS-200/NF and (e) Ni_3S_2@NiS-300/NF.....65

Figure 2.6 (a-b) TEM and (c) HR-TEM images of Ni_3S_2@NiS-250/NF electrocatalyst; (d-g) TEM-EDS mappings of Ni_3S_2@NiS-250/NF electrocatalyst; (h) Image intensity line profiles taken alone the yellow line in Figure 2.6c; (i) the EDS spectrum of Ni_3S_2@NiS-250/NF electrocatalyst...67

Figure 2.7 (a) Full XPS profiles of Ni_3S_2/NF, Ni_3S_2@NiS-200/NF, Ni_3S_2@NiS-250/NF and Ni_3S_2@NiS-300/NF electrocatalysts; (b) High resolution XPS spectra of Ni *2p* of (b_1) Ni_3S_2/NF, (b_2) Ni_3S_2@NiS-200/NF, (b_3) Ni_3S_2@NiS-250/NF and (b_4) Ni_3S_2@NiS-300/NF electrocatalyst 68

Figure 2.8 High resolution XPS spectra of S *2p* of (a) Ni_3S_2; (b) Ni_3S_2@NiS-200; (c) Ni_3S_2@NiS-250 and (d) Ni_3S_2@NiS-300. 69

Figure 2.9 (a) Polarization curves of the samples; (b) relationship between overpotentials of NF (I), Ni_3S_2/NF (II), Ni_3S_2@NiS-200/NF (III), Ni_3S_2@NiS-250/NF (IV) Ni_3S_2@NiS-300/NF (V) and Pt-C (VI); (c)

Estimation of C_{dl}, data obtained from **Figure 2.10**; (d) the Nyquist plots of electrodes with an applied potential of 200 mV; (e) Tafel plots derived from overpotential and log (R_{ct}), data obtained from **Figure 2.11** (f) durability of the Ni_3S_2@NiS-250/NF modified electrode with an initial polarization curve and after 3000 cycles and (g) Operation stability of the Ni_3S_2@NiS-250/NF electrode running at -250 mV in 1 M KOH solution for 50 h. 71

Figure 2.10 Cyclic voltammograms of (a) Ni_3S_2; (b) Ni_3S_2-NiS-200/NF; (c) Ni_3S_2-NiS-250/NF and (d) Ni_3S_2-NiS-300/NF based electrodes with various scan rates in 1 M KOH solution 73

Figure 2.11 (a) Nyquist plots of the Ni_3S_2@NiS-250/NF measured at various overpotential (100, 125, 150, 175 and 200 mV); (b) Dependence of the charge transfer resistance (R_{ct}) on the overpotential. 74

Figure 2.12 Tafel slope of as-prepared samples and Pt/C. 74

Figure 2.13 Operation stability of the Ni_3S_2/NF running in 1M KOH solution for 12h 75

Figure 2.14 the XRD pattern of Ni_3S_2@NiS-250/NF after the stability test in 1 M KOH solution for 50 h 75

Figure 2.15 (a) SEM; (b) TEM; (c) HR-TEM; (d)-(f) the EDS spectrum of Ni_3S_2@NiS-250/NF after the stability test in 1 M KOH solution for 50 h... 75

Figure 2.16 Top and side views of the optimized structures of Ni_3S_2 (101), NiS (021) and Ni_3S_2/NiS 77

Figure 2.17 Density of states (DOS) of Ni_3S_2, NiS and Ni_3S_2/NiS 78

Figure 2.18 (a) Optimized structure of adsorbed H; (b-c) *p*DOS of d-states and (e) free energies of adsorption on the Ni_3S_2, NiS and Ni_3S_2/NiS heterostructures 79

Figure 2.19 Top views of the optimized structures of adsorbed H on Ni_3S_2 (101), NiS (021) and Ni_3S_2/NiS.....80

Figure 3.1 Schematic illustration of the preparation of Zn-VOx-Co 2D nanosheets. 94

Figure 3.2 Optical images of the prepared electrodes.....95

Figure 3.3 XRD patterns of pure Co, Zn-Co, VOx-Co and Zn-VO_x-Co electrodes. (a) Full spectrum; (b) Corresponding zoom-in regions between 2θ of 40° and 50°. 96

Figure 3.4 XRD pattern of (a) pristine CFB substrate; (b) VO_x-Co and Zn-VO_x-Co powders and (c) pure Zn and Zn-VO_x.....96

Figure 3.5 SEM images of Zn-VOx on CFP; (b-e) Corresponding EDX elemental mappings of Zn, V and O in Zn-VOx based electrode. 97

Figure 3.6 SEM images of a pristine carbon fiber paper substrate. 98

Figure 3.7 (a)-(d) SEM images of pure Co based electrode. 98

Figure 3.8 (a)-(c) SEM images of Zn-Co based electrode; (d)-(f) Corresponding EDX elemental mappings of Co and Zn in Zn-Co based electrode.....99

Figure 3.9 (a)-(d) SEM images of VO_x-Co based electrode; (e)-(h) Corresponding EDX elemental mappings of Co, V and O in VO_x-Co based electrode. 99

Figure 3.10 (a), (b) and (c) Representative SEM images of Zn-VO_x-Co on CFP; (d) EDS spectrum of Zn-VO_x-Co; (e)-(i) Corresponding EDX elemental mappings of Co, Zn, V and O on Zn-VO_x-Co surface.....100

Figure 3.11 (a) TEM image of Zn-VO_x-Co; (b) HRTEM image of Zn-VO_x-Co. 102

Figure 3.12 (a) TEM image of VO_x-Co; (b) HRTEM image and FFT pattern (inset) of VO_x-Co. 102

Figure 3.13 (a) TEM image of Zn-VO_x-Co 2D ultrathin nanosheets; (b) HR-TEM image showing the hetero-phase structure, in which the crystalline domains are marked by the dashed white curves. (b_1), (b_2) Corresponding FFT patterns of the selected regions marked by pink and blue squares, respectively; (c) HETEM image enlarged in (b) image; (d)-(g) TEM-EDS mappings of Zn-VO_x-Co; (h) Image intensity line profiles taken alone the yellow line in Figure c; (i) EDS line scanning spectra of Zn-VO_x-Co 2D ultrathin nanosheets in Figure d. 103

Figure 3.14 (a) High resolution XPS spectrum of O *1s* in Zn-VO_x-Co electrocatalyst and (b) Valence-band spectra of pure Co, Zn-Co, VO_x-Co and Zn-VO_x-Co. 105

Figure 3.15 (a) Full XPS profiles of pure Co, Zn-Co, VO_x-Co and Zn-VO_x-Co electrocatalysts; (b) High resolution XPS spectra of Co *2p* of pure Co (b_1), Zn-Co (b_2), VO_x-Co (b_3) and Zn-VO_x-Co (b_4); (c) High resolution XPS spectra of V *2p* of VO_x-Co and Zn-VO_x-Co; and the charge distributions in (d) Zn-Co, (e) VO_x-Co and (f) Zn-VO_x-Co, respectively. 106

Figure 3.16 Water contact angles on (a) pure Co; (b)Zn-Co; (c) VO_x-Co and (d) Zn-V O_x-Co surfaces. 107

Figure 3.17 LSV curves of (a) Zn-VO_x-Co based electrodes prepared by using different amounts of Zn precursor (molar amount) during the electrodeposition. And (b) Zn-VO_x-Co based electrodes prepared by using different amounts of NH_4VO_3 precursor (molar amount) during the electrodeposition. 109

Figure 3.18 (a) Polarization curves of Zn-VO_x (I), pure Co (II), Zn-Co (III), VO_x-Co (IV), Zn-VO_x-Co (V) , 20% Pt-C (VI), and Zn-VOx-Co based electrodes

after iR compensation; (b) Relationship between overpotential; (c) Comparison of Zn-VO_x-Co with other works; (d) Tafel plots for HER; (e) Estimation of C_{dl} by plotting the current density variation, data obtained from **Figure 3.19**; (f) Nyquist plots of as-prepared electrodes; (g) Durability of the Zn-VO_x-Co with an initial polarization curve and after 3000 cycles in 1 M KOH solution; (h) Multi-current step test of Zn-VO_x-Co based electrode at current densities of 10, 50, 100, 150, 200, 250 and 300 mA cm^{-2}; (i) the stable operation of the Zn-VO_x-Co based electrode running at -100 mV for 36 h. 110

Figure 3.19 Cyclic voltammograms of (a) Zn-VO_x; (b) pure Co; (c)Zn-Co; (d) VO_x-Co and (e) Zn-VO_x-Co based electrodes with various scan rates in 1M KOH solution. 113

Figure 3.20 HER ECSA-normalized LSV curves of Zn-VO_x, pure Co, Zn-Co, VO_x-Co and Zn-VO_x-Co. 115

Figure 3.21 Time dependence of H_2 production over Zn-VO_x-Co catalyst 115

Figure 3.22 (a) and (b) TEM images; (c)-(f) TEM-EDS mapping images of Co, Zn, V and (g) Corresponding EDS line scanning spectra of Zn-VO_x-Co after stability test. 116

Figure 3.23 (a) Full XPS profiles and high resolution XPS spectra of (b) Co *2p* in Zn-VO_x-Co electrocatalysts after the stability test. 116

Figure 3.24 Valence-band spectra of Zn-VO_x-Co and Zn-VO_x-Co electrocatalysts after the stability test. 117

Figure 3.25 (a) Polarization curves, (b) Tafel plots, (c) Nyquist plots of pure Co, Zn-Co, Zn-VO_x and Zn-VO_x-Co based electrodes; (d) multi-current step test of Zn-VO_x-Co based electrode at current densities of 10, 50, 100, 150, 200,

250 and 300 mA cm^{-2}; (e) stable operation of Zn-VO_x-Co running at -200 mV in 1 M PBS solution for 24 h. 117

Figure 3.26 Density of states (DOS) of pure Co and Zn-Co..... 121

Figure 3.27 Top (upper) and side (lower) views of the optimized structures of pure Co, Zn-Co, VO_x-Co and Zn-VO_x-Co. 121

Figure 3.28 (a) Pure Co and (b) VO_x-Co models with serial numbers 121

Figure 3.29 (a-d) *p*DOS of d-states of model structures of pure Co, Zn-Co, VO_x-Co and Co-VO_x-Co, respectively; (e) optimized structure of adsorbed H on the four models; (f) relationship between the HER overpotential versus d-band center; (g) free energies of H adsorptions on the pure Co, Zn-Co, VO_x-Co and Co-VO_x-Co. 122

Figure 3.30 Side views of charge density distributions in Zn-Co and Zn-VO_x-Co. 123

Figure 3.31 Top views of the optimized structures of adsorbed H on (a) pure Co, (b) Zn-Co, (c) VO_x-Co and (d) Zn-VO_x-Co. 123

Figure 4.1 Optical images of the as-prepared electrodes 141

Figure 4.2 (a) Schematic illustration of the preparation of B-$MnFe_2O_4$@MFOC coated NF electrode; (b) XRD pattern of MFOC; (c) XRD pattern of B-$MnFe_2O_4$@MFOC and (d) Raman spectra of MFOC and B-$MnFe_2O_4$@MFOC. 143

Figure 4.3 XRD patterns of Mn-MOF, Fe-MOF and MnFe-MOF precursors... 143

Figure 4.4 XRD patterns of (a) FOC, B-Fe_3O_4@FOC and (b) MOC, B-Mn_3O_4@MOC..... 144

Figure 4.5 TGA patterns of MFOC and B-$MnFe_2O_4$@MFOC 144

Figure 4.6 SEM images of (a) pure nickel foam; (b) Mn-MOF-74; (c)Fe-MOF-74

and (d) MnFe-MOF-74 precursors.....145

Figure 4.7 Water contact angles on (a) MFOC and (b) B-$MnFe_2O_4$@MFOC...146

Figure 4.8 (a-f) EDS elemental mappings of C, O, Fe, Mn and B on B-$MnFe_2O_4$@MFOC; (g) corresponding EDS spectrum.....146

Figure 4.9 SEM images of B-$MnFe_2O_4$@MFOC with (a-b) $NaBH_4$ treating time for 10 min; (c-d) $NaBH_4$ treating time for 40 min. 147

Figure 4.10 SEM images of (a-b) FOC, (c-d) B-Fe_3O_4@FOC formed on NF and high magnification of nanowire of the B-Fe_3O_4@FOC.....148

Figure 4.11 SEM images of (a-b) MOC, (c-d) B-Mn_3O_4@FOC formed on NF and high magnification of nanowire of the B-Mn_3O_4@MOC.....148

Figure 4.12 SEM images of (a) MnFe-MOF precursor; (b) MFOC and (c-d) B-$MnFe_2O_4$@MFOC; (e) TEM images of B-$MnFe_2O_4$@MFOC; (f) HR-TEM image showing nanosheet@ nanowire heterostructure, in which the nanosheets are marked by white dashed curves; (g) HRTEM image enlarged the pink dashed square in (f) image; (h) corresponding FFT pattern of the (g) image; (i-j) HRTEM images enlarged the yellow dashed square in (f) image; (k-p) TEM-EDS mappings of B-$MnFe_2O_4$@MFOC. 150

Figure 4.13 (a) TEM image of MFOC; (b) HR-TEM of MFOC (insert: FFT pattern) 150

Figure 4.14 (a)TEM image; (b)HR-TEM image; (c)EDS spectrum and (d-f) TEM-EDS mappings of B-Fe_3O_4@FOC 151

Figure 4.15 (a)TEM image; (b)HR-TEM image; (c)EDS spectrum and (d-f) TEM-EDS mappings of B-Mn_3O_4@MOC 151

Figure 4.16 EDS spectrum of B-$MnFe_2O_4$@MFOC.....152

Figure 4.17 TEM-EDS mapping of MFOC 152

Figure 4.18 (a) Full XPS profiles of B-Fe_3O_4@FOC, B-Mn_3O_4@MOC, MFOC and B-$MnFe_2O_4$@MFOC; High-resolution XPS spectra of (b) Fe *2p*; (c) Mn *2p*; (e) B *1s* and (f) O*1s* of B-$MnFe_2O_4$@MFOC; (d) EPR spectra of $MnFe_2O_4$ and B-$MnFe_2O_4$@MFOC. 153

Figure 4.19 High resolution XPS spectra of Fe *2p* in (a) MFOC and (b) B-Fe_3O_4@FOC; Mn *2p* in (c) MFOC and (d) B-Mn_3O_4@MOC 155

Figure 4.20 Mn *3s* XPS spectra of the B-$MnFe_2O_4$@MFOC 156

Figure 4.21 XRD pattern of standard $MnFe_2O_4$ 156

Figure 4.22 High resolution XPS spectra of (a) Fe *2p* and (b) Mn *2p* in B-$MnFe_2O_4$ @FMOC and standard $MnFe_2O_4$. 157

Figure 4.23 XPS spectra of B 1s in (a) B-Fe_3O_4@FOC and (b) B-Mn_3O_4@MOC 157

Figure 4.24 High resolution of O *1s* in as-prepared samples 158

Figure 4.25 LSV curves of B-$MnFe_2O_4$@FMOC based electrodes prepared by (a) using different amounts of $FeSO_4 \cdot 7H_2O$ and $MnSO_4 \cdot H_2O$ precursors (molar amount) (b) using different temperatures and (c) by using different $NaBH_4$ treating time. 159

Figure 4.26 OER polarization curves of B-Mn_3O_4@MOC (I), B-Fe_3O_4@FOC (II), MFOC (III) and B-$MnFe_2O_4$@MFOC (IV) in 1 M KOH; (b) related overpotentials; (c)Tafel plots; (d) current density as a function of scan rate derived from the CV curves at; (e) Nyquist plots and equivalent circuit model (inset); (f) polarization curves of the B-$MnFe_2O_4$@MFOC electrode before and after 3000 CV cycles; (g) multi-current step test and (h) the chronoamperometry curves of the B-$MnFe_2O_4$@MFOC electrode at the constant potential corresponding to the current density of 100 mA cm-2 for 7

days. 159

Figure 4.27 Cyclic voltammograms of (a) B-Mn_3O_4@MOC; (b) B-Fe_3O_4@FOC; (c) FMOC and (d) B-$MnFe_2O_4$@FMOC based electrodes with various scan rates in 1 M KOH solution. 161

Figure 4.28 OER ECSA-normalized LSV curves of B-Mn_3O_4@MOC; (b) B-Fe_3O_4@FOC; (c) FMOC and (d) B-$MnFe_2O_4$@FMOC 161

Figure 4.29 Density of states (DOS) of pure carbon and Mn, Fe oxides doped into carbon species 164

Figure 4.30 Top (upper) and side (lower) views of the optimized structures of $MnFe_2O_4$ and B-$MnFe_2O_4$ 164

Figure 4.31 (a), (b) $MnFe_2O_4$ and (c), (b) B-$MnFe_2O_4$ models with serial numbers 165

Figure 4.32 Total DOSs of (a) $MnFe_2O_4$ and (b) B-$MnFe_2O_4$; pDOSs of (c) $MnFe_2O_4$ and (d) B-$MnFe_2O_4$; charge distributions in (e-f) $MnFe_2O_4$ and (g-h) B-$MnFe_2O_4$; (i) band structures of $MnFe_2O_4$ and B-$MnFe_2O_4$; (j) elementary steps; Gibbs free energy diagrams of $MnFe_2O_4$ and B-$MnFe_2O_4$ for OER process at (k) U=0 V and (l) U=1.23 V. 166

Figure 4.33 (a) Fe density states of $MnFe_2O_4$ and (b) Fe density states of B-$MnFe_2O_4$; (c) Mn density states of $MnFe_2O_4$ and (d) Mn density states of B-$MnFe_2O_4$. 167

Figure 4.34 Photograph of (a) seawater collected from Aomori Bay near Aomori, Japan; (b) 1 M KOH, seawater and 1 M KOH+ seawater electrolysis 169

Figure 4.35 OER polarization curves of as-prepared sample in (a) simulated seawater (0.5 M NaCl+1M KOH solution) and (b) 1M KOH+ natural seawater solution under different temperatures; (c) Comparison of the overpotentials

for B-$MnFe_2O_4$@MFOC electrode; (d) measured and theoretical gaseous products over B-$MnFe_2O_4$@MFOC electrocatalyst; (e) Corrosion potentials (green) and corrosion current densities (red) of B-$MnFe_2O_4$@MFOC electrode in natural seawater; Chrono potentiometric curves of B-$MnFe_2O_4$@MFOC electrode for 200 h in (f) 1M KOH+0.5M NaCl and (g) 1M KOH+ seawater; (h) Schematic illustration of a seawater-splitting electrolyzer using B-$MnFe_2O_4$@MFOC for both electrodes; (i) Overall seawater splitting performance of MFOC‖MFOC and B-$MnFe_2O_4$@MFOC‖B-$MnFe_2O_4$@MFOC couples in 1M KOH+ natural seawater; (j) Chrono-potentiometric curves at 100 mA cm^{-2} for 24 h. 170

Figure 4.36 Corrosion polarization curves of (a) FMOC and (b) B-$MnFe_2O_4$@FMOC. 170

Figure 4.37 (a) TEM and (b)HR-TEM images; (c)-(h) TEM-EDS mapping images of C, O, B, Fe and Mn of B-$MnFe_2O_4$@FMOC after the stability test..... 173

Figure 4.38 High-resolution XPS spectra of (a) Fe *2p*; (b) Mn *2p* and (c) B *1s* in B-$MnFe_2O_4$@MFOC after the stability test..... 173

Figure 4.39 Polarization curves of MFOC and B-$MnFe_2O_4$@MFOC; (b) Tafel plots of MFOC and B-$MnFe_2O_4$@MFOC in 1M KOH+ natural seawater solution..... 174

Figure 4.40 Side (a) and top (b) views of the digital photographs of the OER solutions for the iodometric titration, showing the absence of ClO^- production in this case. 174

CHAPTER 1 Introduction

The growing energy demand and exhaustive exploitation of fossil fuels are driving energy crises and environmental pollution issues, necessitating the development of alternatives such as hydrogen, wind, tide, and solar energy [1, 2]. Hydrogen is recognized as an ideal clean energy source for a sustainable society because it has the highest weight energy density (approximately 120 MJ kg^{-1}) with no pollution by-products [3-5]. Electrolytic water splitting is one of the current technologies used for hydrogen production. Water splitting involves two crucial reactions, i.e., hydrogen evolution reaction (HER) at the cathode and oxygen evolution reaction (OER) at the anode, and the thermodynamic equilibrium potentials of 0 V and 1.23 V for the HER and OER, respectively [6-8]. Many water splitting processes with acidic, alkaline and neutral freshwater-based electrolytes have been reported. Recently, using seawater, which covers 71% of our planet's surface and represents 97% of the water resources in the world, to replace the freshwater for generating hydrogen draw more and more attentions. Meanwhile, the theoretical potential of ocean energy including offshore wind, waves, tides, and floating solar energy is several times the total global energy demand; however, ocean energy is always unstable, and transportation costs are high. Yet if hydrogen can be efficiently produced on-site from seawater electrolysis using ocean energy, the energy can be efficiently stored in the form of stable hydrogen. Moreover, this use of hydrogen could generate pure fresh water for daily life. Therefore, seawater should be considered an ideal feedstock for electrocatalytic hydrogen production in the future.

Currently, research on seawater electrolysis is still in the initial stage, and the critical challenge in direct seawater electrolysis is to solve the issues resulting from the high content of chloride anions (Cl^-), specifically the competition between the OER and

chlorine oxidation reaction (ClOR). Generally, different chloride species for example, Cl_2 (pH < 3.0), HClO (3.0 < pH < 7.5), and ClO^- (pH > 7.5), can be generated at different pH ranges, which reduces the efficiency of the OER [12]. While, the aggressive Cl^- ions in natural seawater could affect or even terminate both the HER and OER by corroding both catalysts and substrates [13]. It was found that Cl^- could react directly with electron-deficient transition metals to re-construct the composition of the catalyst, leading to severe corrosion, especially in the case of electrolysis at a high current density [14, 15]. To avoid the generation of Cl_2 and other chloride species during electrolysis, it is necessary to improve the selectivity of the OER by enlarging the potential window between the OER and ClOR in an alkaline environment. It was found that the potential window could reach up to approximately 490 mV in a pH range from 7.5 to 14 owing to the large equilibrium potential, which can potentially provide the best way to achieve 100% Faradaic efficiency of O_2 generation [16,17]. Here, it is difficult to overcome chlorine crossover and corrosion, and the process always suffers from electricity consumption and a high cell voltage (＞1.7 -2.4 V) [18, 19]. Thus, the development of a low-cost, energy-saving electrolysis technology and electrocatalysts with Cl^- resistance, high activity, widespread availability, and desirable stability remains a significant challenge for cost-effective and sustainable hydrogen production.

1.1 REACTION MECHANISM OF WATER ELECTROCATALYSIS

1.1.1 Theoretical of hydrogen evolution reaction (HER)

Water electrolysis includes two half-cell reactions: the anodic OER and cathodic HER [20]. Herein, HER is a two-electron transfer reaction, and the HER in acidic solution mainly includes three possible elementary reactions (Eq1.1-1.3):

$$Volmer\ step:\ H^+ + e^- \rightarrow H_{ad} \qquad \text{(Eq. 1.1)}$$

$$Heyrovsky:\ H^+ + e^- + H_{ad} \rightarrow H_2 \qquad \text{(Eq. 1.2)}$$

$$Tafel\ step:\ 2H_{ad} \rightarrow H_2 \qquad \text{(Eq. 1.3)}$$

In alkaline media, the Volmer step (Eq. 1.4) is the reduction of a water molecule adsorbed on the surface of the electrode into an adsorbed hydrogen atom and negatively charged hydroxide anion. Subsequently, the adsorbed hydrogen atom either combining with another adsorbed hydrogen atom to generate a hydrogen molecule that leaves the surface (Eq. 1.5) or attacked by another water molecule to produce a hydroxide anion and a hydrogen molecule (Eq. 1.6). The reaction proceeds electrocatalytic hydrogen evolution via Volmer-Heyrovsky or Volmer-Tafel mechanism depending on the catalytic surface state [10, 11]. Though the HER in alkaline solution involves simple reactants and only two electrons for each hydrogen molecule, the multiple elemental reactions induce an accumulation of energy barriers with slow kinetics.

$$Volmer\ step:\ H_2O + e^- \rightarrow H_{ad} + OH^- \qquad \text{(Eq. 1.4)}$$

$$Tafel\ step:\ 2H_{ad} \rightarrow H_2 \qquad \text{(Eq. 1.5)}$$

$$Heyrovsky:\ H_2O + H_{ad} + e^- \rightarrow H_2 + OH^- \qquad \text{(Eq. 1.6)}$$

In the HER process, the Volmer reaction always first occurs no matter the HER via the Heyrovsky reaction, the Tafel reaction route or both. For HER, it is essential to identify the rate-determining step. If the Volmer reaction is the rate-determining step, it is only necessary to increase the edge active sites on the electrode surface to make the transfer of electrons more easily, thereby providing more electrolytic active centers for hydrogen adsorption. If hydrogen desorption is a speed-determining step, it is only necessary to increase the physical parameters of the electrode (such as surface roughness) to increase the electron transfer rate by increasing the electrode reaction

area and inhibiting the growth of bubbles, thereby increasing the electrolysis rate.

1.1.2 General mechanism of the OER in water electrolysis

Owing to the positive Gibbs free energy value (ΔG), water splitting does not spontaneously occur. In the water electrolysis process, external energy is necessary to decrease ΔG for water splitting, in which the electrical energy is converted into chemical energy with the generation of oxygen and hydrogen. The Gibbs free energy value can be calculated using (Eq. 1.7):

$$\Delta G=-n\times E\times F \qquad \text{(Eq. 1.7)}$$

where F is Faraday's constant, E the theoretical water decomposition voltage, and n the number of electrons exchanged during the electrode reaction. As such, for water electrolysis, E should exceed 1.23 V. OER is a four-electron transfer reaction, which means that the crucial step for water splitting should be controlled by the OER process. It has two different possible mechanisms for OER process, i.e., adsorbate evolution mechanism (AEM) and lattice oxygen mediated (LOM) mechanism (shown in **Figure 1.1**).

In the AEM system, the H_2O molecule is adsorbed on the surface of electrocatalyst and then the OH* is generated on the active site. Then, *OH subsequently undergoes proton coupling and electrons removal to produce O* species. The generated O* reacts with another water molecule to form *OOH. Finally, the *OOH specie is oxidized with the released O_2 (Eq. 1.8-1.11):

$$H_2O + * \rightarrow {}^*OH + H^+ + e^- \qquad \text{(Eq. 1.8)}$$

$$OH^* \rightarrow O^* + H^+ + e^- \qquad \text{(Eq. 1.9)}$$

$$O^* + H_2O \rightarrow OOH^* + H^+ + e^- \qquad \text{(Eq. 1.10)}$$

$$OOH^* \rightarrow {}^*O_2 + H^+ + e^- \qquad \text{(Eq. 1.11)}$$

Another OER mechanism is called lattice oxygen mechanism (LOM), which

proceeds on two neighbouring active sites. There are four steps in LOM: (1) two HO* on the active sites undergo deprotonation and generate the -O* species; (2) the O-O bond is formed by two oxo species directly coupling; (3) O_2 is released and two oxygen vacancies are generated and (4) reoccupation of their vacancies with OH^-. Because the *OOH species do not appear in LOM cycle, the limitation of the scaling relationship between *OOH and *OH could be broken.

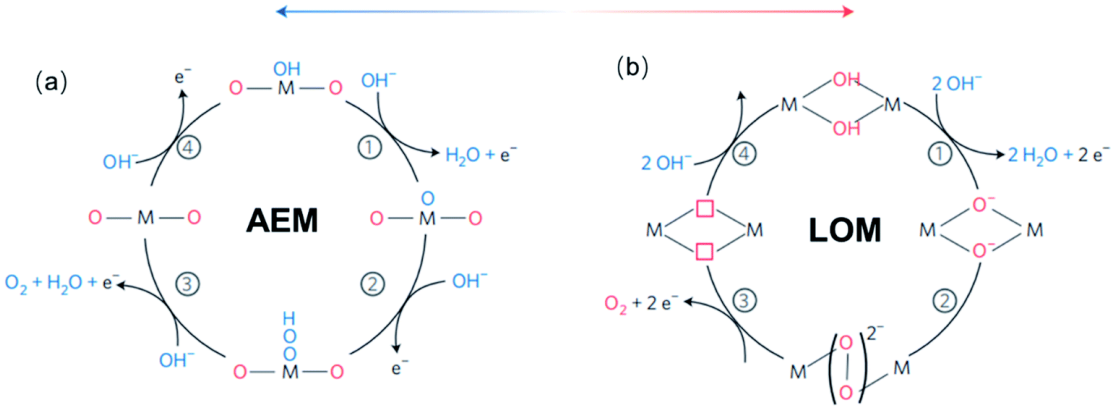

Figure 1.1 (a) The classic four-steps OER mechanism of proton-coupled electron transfer (AEM) and (b) the idealized OER mechanism based on the direct pairing of two lattice oxygens (LOM) in the anionic redox process [21].

1.1.3 Fundamentals of seawater electrolysis

The redox reaction during seawater electrolysis should be similar to that during freshwater electrolysis. However, the composition of natural seawater is very complex, comprising various dissolved ions (e.g., Na^+, Ca^{2+}, Mg^{2+}, Br-, Na^+, Br^-, and I^- in addition to Cl^-), bacteria/microbes, and small particulates. [22]. Bacteria/microbes and small particulates in seawater may poison and corrode the electrodes. For the HER on the cathode, as the electrolysis current increases, the local pH near the cathode surface can dramatically increase, resulting in the precipitation of Ca $(OH)_2$ and Mg $(OH)_2$, which block the active sites on the electrocatalyst. For the OER on the anode, the major challenge is the effect of Cl^- in seawater, which always leads to complicated side reactions, inducing the ClER, which competes with the OER. In general, Cl^- ions in

seawater can severely erode the active sites and convert the active metal sites to the corresponding hydroxide via a metal chloride-hydroxide formation process. Corrosion in the presence of Cl^- involves three steps: polarization, dissolution, and hydroxide formation. At a high anodic potential, Cl^- ions can be easily adsorbed on the positively polarized active surface. These anions coordinate with the adsorbed ions, which could cause dissolution (soluble chlorides) owing to the adsorption and permeability of Cl^-. The formation of OH^- ions accelerates hydroxide formation from the metal and chloride ions. In summary, the corrosion mechanism follows three reactions (**Eqs. 1.12-1.14**), which are as follows:

Adsorption: $M + Cl^- \rightarrow MCl_{ads} + e^-$ (Eq. 1.12)

Dissolution: $MCl_{ads} + xCl^- \rightarrow MCl_x^-$ (Eq. 1.13)

Hydroxide formation: $MCl_x^- + xOH^- \rightarrow M(OH)_x + xCl^-$ (Eq. 1.14)

It is already known that the equilibrium potential (U^o) of the OER is 1.23V, which is preferred over that of the ClER (U^o=1.36V) from a thermodynamic point of view. However, OER comprises a four-electron transfer process, but only two electrons are involved in both ClER and hypochlorite formations. As such, the latter may possess faster kinetics than the OER process, especially at a high current density. In addition, at the industrial level, the chemical reactions related to Cl^- can be affected by the electrolysis temperature, applied potential, and pH value of the solution. Dionigi *et al.* constructed a Pourbaix diagram (**Figure 1.2**) to explain chloride chemistry in seawater [23].

In an acidic solution,

$$2Cl^- \rightarrow Cl_2 + 2e^-; \quad E^0 \approx 1.36\ V_{SHE} \qquad \text{(Eq. 1.15)}$$

One can see that CIER is a two-electron reaction and requires only a single intermediate. Therefore, ClER is the major reaction in acidic seawater solutions over many

electrocatalysts on the anode [14]:

In an alkaline solution,

$Cl^-(aq)+2OH^-(aq)\rightarrow ClO^-(aq)+H_2O(l)+2e^-$; $E^0=1.72V-0.059\ pH$ (Eq. 1.16)

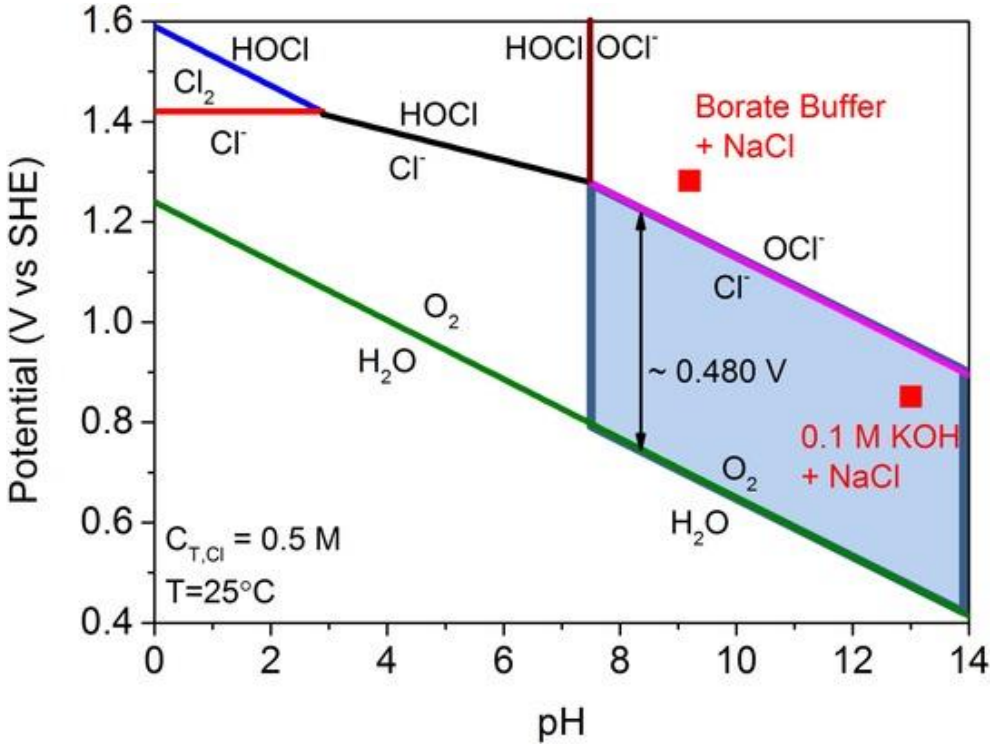

Figure 1.2 Pourbaix diagram of an artificial model solution (0.5 M NaCl solution with electrolytes to control the pH and no other chlorine species) depicting the thermodynamic equilibrium of H_2O/O_2 (green line), Cl^-/Cl_2-HOCl-OCl^- (red line) [20].

It is evident that the hypochlorite formation reaction is also a two-electron transfer reaction. Moreover, the standard electrode potential for hypochlorite formation gradually increases with increasing pH, especially when the pH is higher than 7.5. According to the Pourbaix diagram, the electron potential difference between the hypochlorite and oxygen evolution is fixed at approximately 480 mV, indicating that a maximum overpotential of 480 mV is necessary to avoid interference from any chlorine-based chemistry in alkaline media. As such, alkaline conditions are more suitable for seawater splitting.

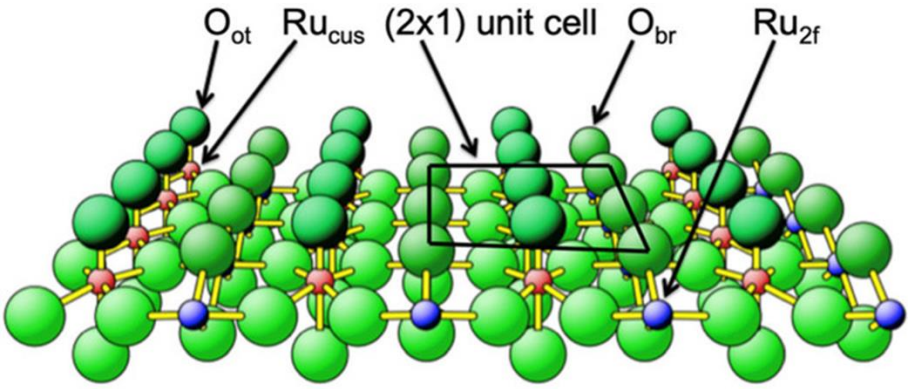

Figure 1.3 Surface structure of the fully-oxygen-covered RuO_2 (110) phase, denoted as $RuO_2(110)$-O_{ot}, in which all one-fold coordinatively unsaturated ruthenium atoms, Ru_{cus} (red balls), are capped by on-top oxygen (green balls). Blue balls indicate Ru_{2f} atoms, which are bridged by one-fold coordinatively unsaturated oxygen atoms (O_{br}). Adsorbates on Ru_{CUS} or Ru_{2f} are indicated with the subscript "ot" (on-top) or "br" (bridge), respectively [24].

To explore the competition between the ClER and OER in seawater electrolysis, Exner *et al.* [24] investigated the selectivity and stability range of the benchmark RuO_2 (110) electrocatalyst combined with the linear scaling relationship of the surface Pourbaix diagram and kinetic descriptions. The authors used the free energy difference between ClO^- from the ClER and OOH^- from the OER adsorbate as a measure of selectivity and stability. They performed density functional theory (DFT) calculations with the corresponding surface structure model of single crystalline RuO_2 (110) shown in **Figure 1.3**, in which on-top oxygen (O_{ot}) capped all one-fold coordinatively unsaturated Ru surface atoms (Ru_{cus}) and, at the same time, the undercoordinated surface oxygen (O_{br}) bridged the neighboring Ru_{2f} atoms, where the RuO_2 (110)-O_{ot} was identified as the active surface in the OER and ClER. Consequently, the reaction mechanism of ClER could be explained by three pathways: the Volmer-Tafel, Volmer-Heyrovsky, and Krishtalik. In that study, on the RuO_2 (110)-O_{ot} surface, the ClER was ascribed to the Volmer-Heyrovsky mechanismm [25], which included the adsorption

and discharge of a Cl^- anion (the Volmer step) on the active Ru_{cus}-O_{ot} site to form Ru_{cus}-OCl_{ot} as the reaction intermediate (**Eq. 1.17**), and then directly recombined with the adsorbed Cl intermediate species in the Ru_{cus}-OCl_{ot} with another free Cl^- anion from the electrolyte (the Heyrovsky step) to release the Cl_2 molecule (**Eq. 1.18**).

$$Ru_{cus}\text{-}O_{ot}+Cl^- \rightarrow Ru_{cus}\text{-}OCl_{ot}+e^- \quad \text{(Volmer step)} \quad \text{(Eq. 1.17)}$$

$$Ru_{cus}\text{-}OCl_{ot}+Cl^- \rightarrow Ru_{cus}\text{-}O_{ot}+Cl_2+e^- \quad \text{(Heyrovsky step)} \quad \text{(Eq. 1.18)}$$

It should be noted that the ClER over RuO_2 requires the construction of the O_{ct} and OCl_{ot} adsorbates, in which either the Volmer step or the Heyrovsky mechanism constitutes the rate-determining reaction step (RDS), which in turn depends on the overpotential. For a small overpotential, the RDS is the Heyrovsky step, whereas the Volmer step dominates the kinetics if the overpotential is increased ($\eta_{ClER}=U-U^0_{ClER}$ > 0.1 V; U indicates the potential, and U^0 is the equilibrium potential) [26, 27].

Compared with the ClER, the underlying reaction kinetics are much more complex on the RuO_2 surface in the OER process because the four-electron transfer involves several intermediates. Rossmeisl *et al.* assumed that a coupled electron–proton transfer takes place on the RuO_2 (110) surface [28]. It was suggested that the OH_{ot}, O_{ot}, and OOH_{ot} intermediate adsorbates are formed on the undercoordinated Ru_{cus} sites during the electrocatalytic cycle process (Eq. 1.19-1.22).

$$Ru_{cus}\text{-}O_{ot} + H_2O \rightarrow Ru_{cus}\text{-}OOH + H^+(aq) + e^- \quad \text{(Eq. 1.19)}$$

$$Ru_{cus}\text{-}OOH_{ot} \rightarrow Ru_{cus} + O_2 + H^+(aq) + e^- \quad \text{(Eq. 1.20)}$$

$$Ru_{cus} + H_2O(aq) \rightarrow Ru_{cus}\text{-}OH_{ot} + H^+(aq) + e^- \quad \text{(Eq. 1.21)}$$

$$Ru_{cus}\text{-}OH_{ot} \rightarrow Ru_{cus}\text{-}O_{ot} + H^+(aq) + e^- \quad \text{(Eq. 1.22)}$$

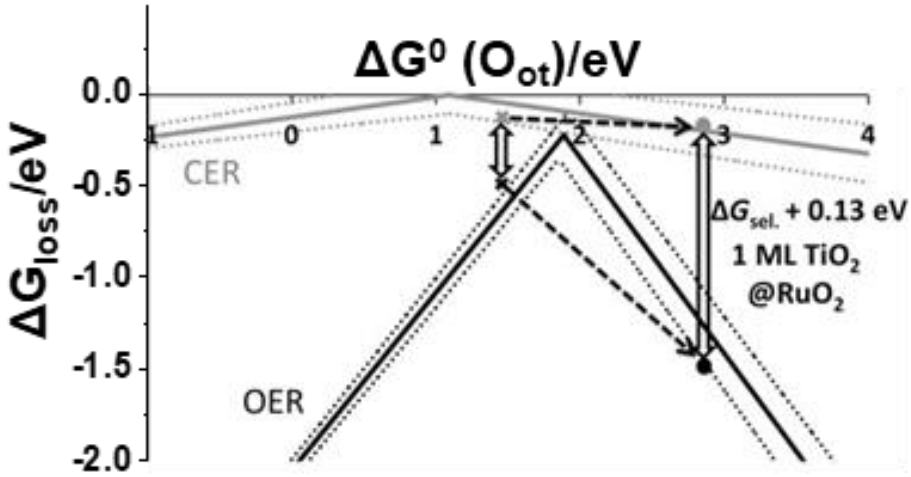

Figure 1. 4 Volcano plot for the ClER (gray) and OER (black) over RuO_2 (110). The size of the line (dotted lines) reflects the standard deviations as a result of the standard deviations in the linear scaling reactions [29].

Typically, the Gibbs free energy can describe a single electron process using the formula $\Delta G = \Delta G^0 - eU^o$, where U^o indicates the equilibrium potential for the OER or ClER, and ΔG^0 the Gibbs free energy at an electric potential $U = 0$ V. The loss in Gibbs energy (ΔG_{loss}) is defined as the step with the most unfavorable ΔG at the equilibrium potential, which can be used to evaluate the thermodynamic barrier during the competition between the ClER and OER processes. **Figure 1.4** shows the ΔG_{loss} volcano diagram describing the OER and ClER activities. Compared with that of the OER, the volcano plot of the ClER is quite flat. This difference also indicates a variation in the number of reaction intermediates. Clearly, both the ClER and OER possess maximum activity at the middle value of $\Delta G^0 (O_{ot})$. The Gibbs free energy required for the ClER selectivity (ΔG_{sel}) is determined by the difference between $\Delta G_{loss}{}^{ClER}$ and $\Delta G_{loss}{}^{OER}$ when referenced to the same potential ($U^o = 1.36$ V) for both losses, which expresses the selectivity for the OER. A strategy for improving the selectivity while maintaining the activity of the OER is to replace the topmost Ru atoms with Ti atoms [29]. In this way, the OER selectivity can be enhanced by several orders of magnitude

while the high activity for the reaction is maintained. Another factor that dominates thermodynamics directly affecting selectivity and stability is the surface energy disparity of OOH and OCl adsorption. The increase in the surface energy disparity between OOH_{ot} and the OCl_{ot} adsorbate could weaken the OOH_{ot} adsorption to the underlying metal atoms. Hence, the stability window of the electrocatalysts could shift to higher potentials and pH values by increasing the surface energy of OOH_{ot} adsorption, as shown in **Figure 1.5**.

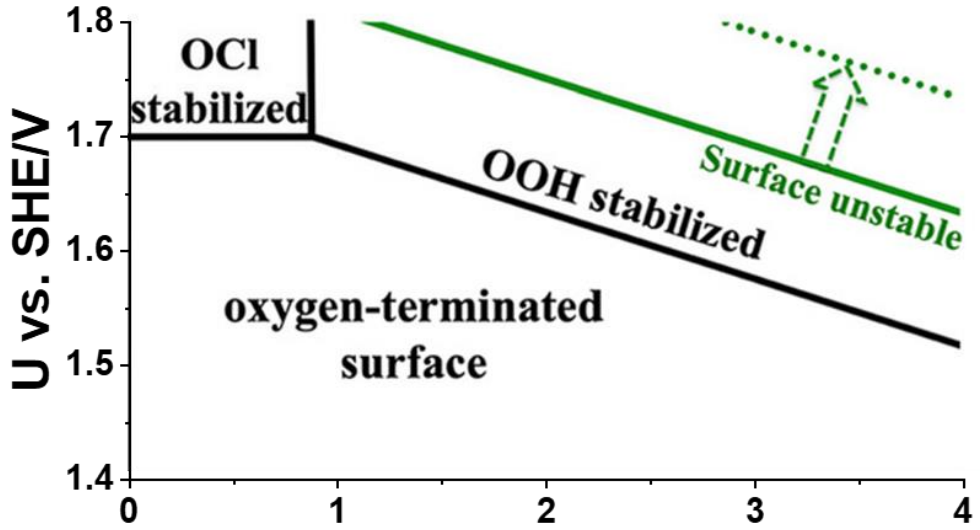

Figure 1.5 the stability window of the TMOs electrode [24].

Regulating the electrolyte composition to achieve anti-corrosion during seawater electrolysis is another crucial factor for improving stability. Ma *et al.* found that sulfate (SO_4^{2-}) as the addition agent in the alkaline seawater electrolyte could alleviate chloride corrosion at the anode, resulting in a significant improvement in the operational stability of the anode [30]. **Figure 1.6** shows the results of classical molecular dynamics simulations of the electrolyte system over the electrode surface to explore the role of sulfate in improving anode stability. Here, Cl^- anions tend to be enriched on the electrode surface in the absence of sulfate anions. However, with the introduction of

sodium sulfate, divalent sulfate is preferentially absorbed on the electrode surface and pushes Cl^- away from the electrode surface by electrostatic repulsion. This phenomenon was also observed for a nickel-iron layered double hydroxide (NiFe-LDH) electrocatalyst. The NiFe-LDH remained stable at 400 mA cm^{-2} for 500-1000 hours in simulated and real seawater in the presence of SO_4^{2-}, which was 3 to 5 times higher than that of the electrolyte without SO_4^{2-}. Such a pulsing effect with the electrolyte additive could be generally applicable to other OER electrodes, which should be favorable for the scaling up of alkaline seawater electrolysis [31, 32].

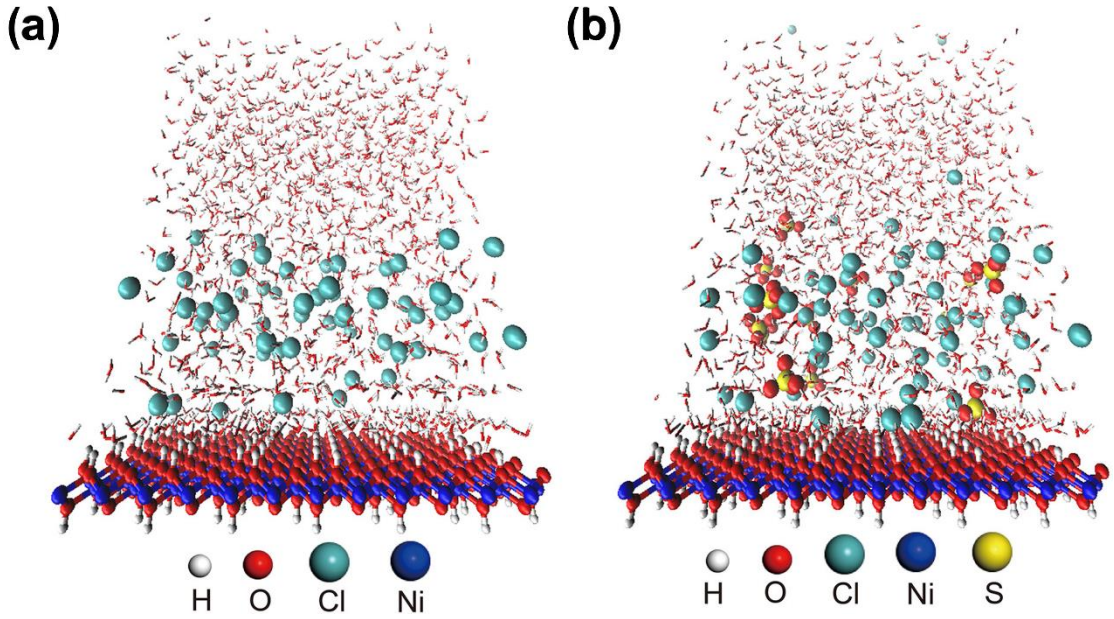

Figure 1.6 Snapshots of classical molecular dynamics simulations of electrolyte systems above the electrode surface [30].

In addition to the development of highly efficient catalysts with long-term stability, it is essential to design an appropriate high-performance and low-cost electrolyzer for the application of seawater electrolysis. Currently, in the laboratory, the main electrolyzer types include single cells, “H”-type cells, and flow-type cells. For future industrial applications, four leading configurations-anion exchange membrane water electrolyzer (AEMWE), proton exchange membrane water electrolyzer (PEMWE),

alkaline water electrolyzer (AWE), and high-temperature water electrolyzer (HTWE) could be considered. Because of the complicated situation in seawater, in test conditions at the laboratory level, different pH levels are always used in simulated seawater or alkaline seawater.

1.1.4 Key Parameters for HER and OER

To accurately evaluate the HER and OER electrocatalytic performance, there are many parameters were listed below.

Electrode

The electrocatalyst performance depends on the work electrode in the three-electrode system. Due to the effect of conductivity and wettability of surface, the work electrode was classified into the stereo electrode and flat surface electrode. As one kind of flat work electrons, the glassy carbon electrodes (GCE) are normally used to evaluate the performance of electrocatalyst. The electrocatalyst powder could test on the GCE but the loading was limited because the electrodes are allowed only follow the single way of penetration. Moreover, the electrocatalyst stable on the GCE require the binder, such as Nafion solution. However, it should be noticed that the excessive binder hinders the active sites on the surface of electrocatalyst and increase the resistance during the evaluation. Compared with the flat electrode, the stereo electrode, such as nickel foam, cupper form, and carbon-based substrate possess the large surface area and multi-layer pore structure. Especially, grown the electrocatalysts on the 3D substrate directly could increase the conductivity and active sites due to the abundant pathway for diffusion between the electrolytes and electrocatalyst from all sides.

Overpotential

The overpotential is one of the most vital parameters to evaluate the electrocatalysts performance, which indicated that the difference of potential between

the electrodes when one electrode deviates from the equilibrium and in equilibrium potential of the other electrode reaction. In brief, the polarization of the electrode is caused overpotential. In ideal, the applied potential should be equal to the equilibrium potential and the theoretical potentials for the HER and OER are 0 and 1.23 V, respectively. However, the sluggish reaction kinetics and the intrinsic electrolyte resistance cause the additional potential. To evaluate the activity of electrocatalysts, the overpotential yield a current density of 10 or 100 mA cm^{-2} is selected and the electrocatalysts with the lower overpotential indicated the high active performance. Moreover, the overpotential normalized to the active surface area of electrocatalyst could be more standard way to evaluated the performance of electrocatalyst due to the loading amount is hard to unify.

Tafel slope (b) and exchange current density (j_0)

To reflect the reaction mechanism and evaluate the reaction kinetics, the Tafel slope was developed for a significant indicator. Tafel slope depicts the relationship between the applied η and the current density, which get from the polarization curve. Tafel slope could be calculated via the Tafel equation (Eq. 1.23) and it could be observed that a smaller Tafel slope indicated that the electrocatalyst required lower overpotential to achieve the higher current, thus suggested that the faster reaction kinetics and higher activity.

$$\eta = a + b \log (j / j_0) \quad \text{(Eq. 1.23)}$$

Where η is the overpotential, bis the Tafel slope, j denotes the current density and j_0 means the exchange density.

In addition, the exchange current density is obtained by extrapolating the Tafel curve to zero overpotential, and it indicated that the intrinsic current density when η is zero. The higher j_0 means a higher intrinsic electron transfer rate between the electrolyte

and electrode.

Faradic efficiency

Faradaic efficiency (current efficiency, faradaic yield or coulombic efficiency) could describe the efficiency with electrons in an electrochemical system participate in a desired reaction. For HER, assuming that the current density has a Faradaic yield of 100%, the Faradaic efficiency can be obtained by calculating the ratio of the hydrogen production detected by the experiment to the theoretical hydrogen production. For the OER, the theoretically produced O_2 amount can be calculated with assuming four electrons are consumed and one O_2 is generated. The Faradaic efficiency can be described as follow:

$$\text{Faradaic efficiency}=4Fn_{O_2}/(It) \quad \text{(Eq. 1.24)}$$

Where I mean the constant oxidation current, t is the certain time.

Turn over frequency

The turnover frequency (TOF) can be defined as the number of catalytic active sites per second that the catalyst converts reactants into target products. The conversion frequency could reflect the intrinsic activity of each catalytic site. The TOF value can be calculated to the follow equation:

$$TOF=jA/4Fn \quad \text{(Eq. 1.25)}$$

Where j is the current density, A is the area of work electrode, and n means the number of the active sites. However, it is difficult to accurately calculate the conversion frequency of solid-state (polycrystalline) catalytic materials. Some hydrogen evolution nanocatalyst exist both available surface atoms/catalytic groups and unavailable internal atoms/catalytic species. Thus, only the number of surface atoms or available catalytic sites of catalytic materials was calculated to obtain the conversion frequency number. Another calculation method is to obtain the conversion frequency by counting all catalytic species in the catalytic material.

Stability

Considering the electrocatalyst for HER and OER was operated under extreme conditions (e.g., a strong acid at Ph 0 or a strong base at Ph 14). Therefore, it is crucial for catalytic possess the good structure and stability. Currently, three methods are generally used to evaluate the stability of electrocatalysts: the first one is the current-time (I-t) curve, which is fix the voltage (the current corresponding to the voltage generally greater than 10 $Ma \cdot cm^{-2}$), and the record time is more than 10 h. The other one is current pressure-time (V-t) curve, observed by changing trend of the recorded voltage with time; the third method is to determine the stability of the material by performing continuous multiple (generally greater than 500) CV or LSV scans.

1.2 METHODS FOR ELECTRODE FABRICATION

Electrocatalysts are always supported on substrates to fabricate the electrodes for water electrolysis. Electrodes can be classified either as stereo or flat surface electrodes. Substrates with a large three-dimensional (3D) surface area and/or multi-layer pore structures such as nickel foam (NF), copper (CF), and carbon-based substrates are generally used for stereo electrodes [33]. The direct growth of electrocatalysts on these 3D substrates could increase their conductivity, provide more active sites with abundant pathways for the diffusion of the electrolyte and generated gases, and enhance their mechanical stability even at high current density conditions. The methods for the fabrication of such electrodes comprise three broad categories: vapor, solid, and solution phases. A combination of two or three electrodes is used for the preparation of the electrode. Vapor-phase methods include chemical vapor deposition, spray pyrolysis, magnetron sputtering, atomic layer deposition, and plasma methods. Solid-phase methods include high-temperature combustion, nitrate decomposition, flux growth, pulsed laser, and metal-organic framework-derived methods. The solution-phase method is the most commonly used approach, and includes precipitation, sol-gel,

hydrothermal/solvothermal, microwave-assisted, and electrochemical methods, as illustrated in **Figure 1.7.** The most significant advantage of the solution-phase method is its simple fabrication process and high yield. In addition, the particle size and morphology of electrocatalysts can be easily adjusted using common reagents at relatively low temperatures. To date, various electrode fabrication approaches have been designed the compositions, structures, defects, and morphologies of electrocatalysts for seawater splitting. **Table 1.1** summarizes the benefits and drawbacks of various electrocatalyst fabrication methods. In the following sections, the fabrication methods of electrocatalysts are discussed in detail.

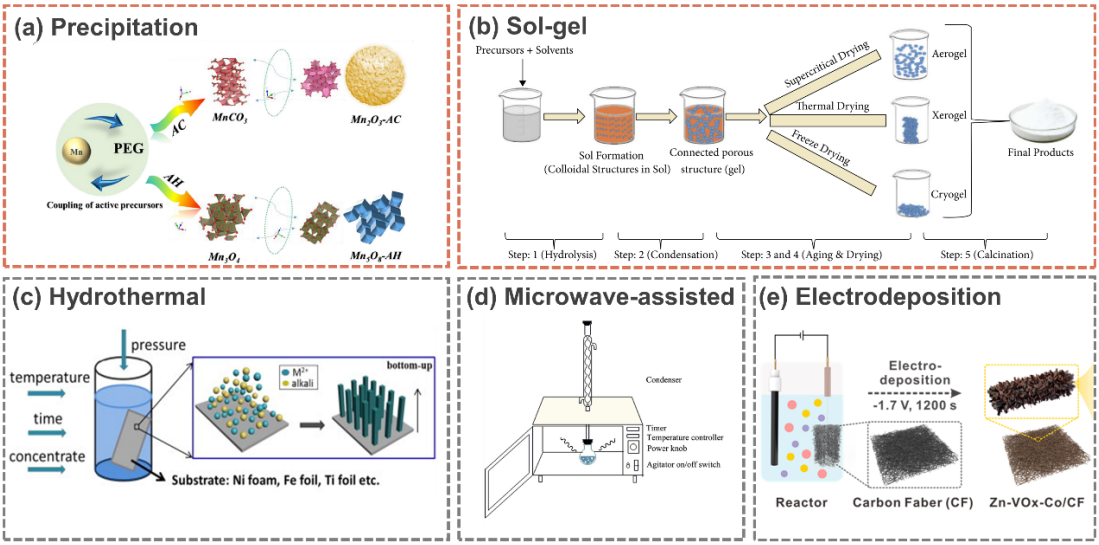

Figure 1.7 (a) Precipitation [36]. (b) Sol-gel [43]. (c) Hydrothermal [46]. (d) Microwave-assisted [50]. (e) Electrodeposition [6].

1.2.1 Precipitation method

The precipitation methods usually used to add a precipitant into a solution with mixed contents, then the precipitates are collected by filtering or centrifugation. Occasionally, the final product is obtained by calcination at a high temperature to decompose the precursor. Common precipitants are NaOH [34], KOH [35], $(NH_4)_2CO_3$ [36], and urea [37, 38]. For example, $Co_xFe_{3-x}O_4$ nanoparticles can be synthesized using

$FeCl_3$ and $CoCl_3$ as the mixed contents and NaOH as the precipitant with a Ph between 11 and 12 [39].

1.2.2 Sol-gel method

The sol-gel method is a facile method for the preparation of metal oxide-based electrocatalysts with special nanostructures. Typically, a metal salt is used as the precursor with chelating agents such as citric acid, propionic acid, or ethylene glycol [40-43]. The sol is generally obtained by uniformly mixing the reactants, followed by an aging process, and the final electrocatalyst is obtained after calcination. For example, Wen *et al.* [44] used nitrate as the metal precursor and citric acid as the chelating agent, and heated the dry gel at 800 °C for 4 h to obtain $Ni_xMn_{3-x}O_4$ nanosized electrocatalysts. The sol-gel method always possesses some advantages, such as low synthesis temperature, formation of a homogenous multi-component system, and easy control of the stoichiometric ratio of the product.

1.2.3 Hydrothermal/solvothermal method

The hydrothermal/solvothermal high-pressure solution method is another common technique for preparing various metal oxides, including nanosized spinel and perovskite electrocatalysts [45]. Using this method, the morphology of the catalysts can be adjusted by tuning the reaction temperature and pressure. Typically, the metal salt precursors in aqueous or non-aqueous solutions (e.g., ethanol, isopropanol, and dimethylformamide) are mixed uniformly by continuous stirring, and then the obtained solution is transferred into a Teflon-lined stainless-steel autoclave, which is sealed and heated for several hours. A high-temperature and high-pressure environment is generated automatically, promoting the recrystallization of metal ions. Various electrocatalysts with nanoarray structures such as 1D nanorods, 2D nanosheets, and hierarchical structures have been successfully obtained. Moreover, besides single-phase metal oxide electrocatalysts (e.g., NiO [46] and Co_3O_4 [47]), various composite

electrocatalysts with multiple metal ions (e.g., Co_3O_4@Ni-Co-O [48] and $Co_{3-x}Fe_xO_4$ [49]) have also been prepared using this method. This solution-based synthetic strategy has many advantages: it is energy efficient and conveniently manipulated, offering excellent control of the nanosized and morphology, and greater capability and flexibility for the preparation of electrocatalysts or direct growth of electrocatalysts on the substrate. In addition, it can provide a stable high-pressure reaction environment at a relatively low temperature and make the preparation process safer and more economical.

1.2.4 Microwave-assisted method

Microwave-assisted chemical reactions are one of the most effective methods for preparing electrocatalysts with nanostructures and highly specific surface areas. In particular, because of the high-energy irradiation effect of microwaves, this method can greatly shorten the reaction time, simplify the medium, and lower the reaction temperature (sometimes lower than 100 °C) [50].

1.2.5 Electrodeposition method

Electrodeposition is a low-cost and rapid method for preparing electrocatalysts directly on a substrate. A typical three-electrode system, including one working electrode, one stable reference electrode, and one counter electrode, is always used for electrodeposition under various modes, such as the potentiostat and galvanostatic modes. For example, Feng *et al*. [51] used 10 Mm Zn $(NO_3)_2$ as a Zn source and 50 Mm NH_4NO_3 solution as the electrolyte to successfully electrodeposit ZnO nanorod arrays (NRA) on the nickel foam (NF). Then the CeO_2 layer was further coated on the surface of the ZnO NRAs to form a ZnO@CeO_2 NRAs-NF electrode by electrodeposition in a solution containing 2 Mm Ce $(NO_3)_2$ and 10 Mm NaCl. In addition, another electrodeposition method, electro-polymerization, was used to coat the conductive polymer on the metal oxide-based electrocatalyst, and abundant vacancies were generated on the final composite using the plasma engraving method,

resulting in an excellent electrocatalyst [52].

Table 1.1 Features of various electrocatalyst fabrication methods

Fabrication method	Fabrication parameter	Advantage	Disadvantage
Precipitation	• Ph value • Calcination temperature • Calcination time	• Relatively simple • Short calcination time • Good product performance	• High temperature • Agglomeration is not uniform
Sol-gel	• Precursor concentration • Ph value • Reaction temperature • Reaction time	• Unnecessity of high temperature for sintering • Homogeneously mixing at a molecular level • Easily proceeding of	• More production steps leading to the specimen broken • Relatively expensive raw materials
Hydro-thermal/ solvothermal	• Reaction temperature • Reaction concentration • Equipment filling degree	• Saving energy • Convenient manipulation • Excellent controlling of the nano-size and morphology	• Equipment requires high temperature and pressure resistant steel • Technically difficult temperature and pressure controlling
Microwave-assisted	• Power of output energy • Reaction time • Heating cycle • Intermittent time	• Greatly shorten the reaction time • Simplify the medium • Lower the reaction temperature (may lower than 100 ^{o}C)	• Poor dispersion • Large mass transfer resistance • Few accessible active sites
Electro-deposition	• Solution concentration • Reaction temperature • Stirring speed • Current density	• Flexible production method • Highly efficiency • Suitable industrial production	• Low performance of the final product • Difficult to prepare ideal and complex thin film materials

1.3 CATHODE MATERIAL DESIGN FOR HER

1.3.1 Transition metal alloy (TMAs)

Alloying transition metal already to be an effective method for improving the HER

activity in alkaline solution. In 1980s, Brown and co-worker studied the activity of Ni-based binary and ternary alloy electrocatalysts for the HER, where the NiMo alloy outperformed the other congeners in alkaline solution. And the performance of Mo-based alloy is NiMo > CoMo > FeMo [53]. Recently, Fang *et al.* prepared a porous NiMo nanowire-like arrays on the nickel foam for HER [54]. The unique structure possesses a large specific surface area and exposed more active sites. The as-prepared electrocatalyst showed an outstanding HER performance, which could comparable to the commercial Pt/C. Thereafter, a $MoNi_4$ alloy supported by MoO_2 on nickel foam was prepared via regulating the outward diffusion process of Ni atoms in $NiMoO_4$ during calcination. DFT results revealed the $MoNi_4$ could decrease the energy barrier of H_2O dissociation and accelerate the sluggish kinetics of Volmer step in alkaline media. Thus, the $MoNi_4$ exhibited low overpotential of 15 mV at a current density is 10 mA cm^{-2} and small Tafel slope of 30 mV dec^{-1}.

However, due to the alloy electrocatalyst always dissolute under harsh condition, the application of alloys is limited by the poor stability. Constructing heterostructure with alloy and other chemical species is vital to the practical application of water splitting. Deng and co-workers [55] encapsulated FeCo alloy into N-doped CNTs (NCNTs). The prepared FeCo@ NCNTs-NH heterostructure showed high HER activity with an overpotential as low as 280 mV at 10 mA cm^{-2}. Besides, the FeCo@ NCNTs-NH electrocatalyst acquired outstanding stability, which can react in acidic solution over 10000 CV cycles due to the protection of the carbon wall to the alloy nanoparticles. Few-layer graphene encapsulated alloys is the other method to improve the stability of alloy based electrocatalyst. The CoNi alloy nanoparticles were encapsulated in few layered graphene-spheres (CoNi@ NC), which improved the long-term stability in acidic solution [56]. DFT calculations indicates the electron of a CoNi nanocluster

could penetrate through three graphene layers (**Figure 1.8**). And the electron density on the graphene surface synergistically increased by the electron density redistribution and N dopants, resulting in higher proton affinity and superior HER activity of the graphene shells.

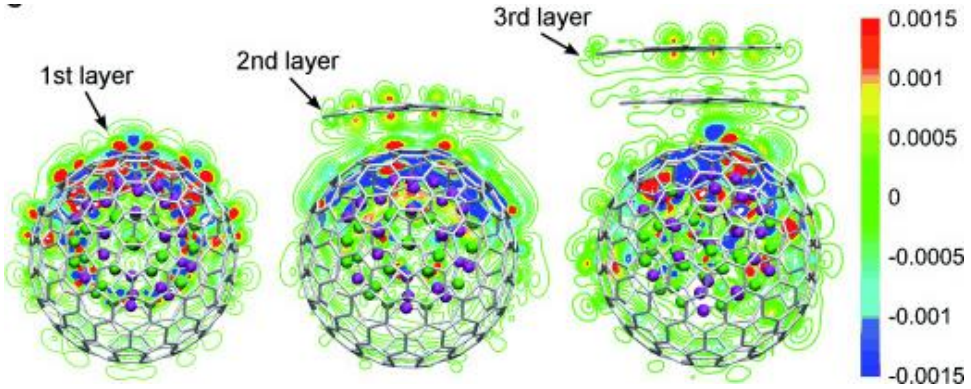

Figure 1.8 Redistribution of the electron densities after the CoNi clusters have covered by one to three layers of graphene. The differential charge density ($\Delta\rho$) is defined as the difference in the electron density with and without the CoNi cluster. The red and blue regions are regions of increased and decreased electron density, respectively [56].

1.3.2 Transition metal sulfides (TMS)

Typically, the structure of the transition metal sulfide could be divided into two distinct classes: nanolayered M_xS_y (M=Co, Fe, Ni, Cu, Zn., etc.) and layered MS_2 (M-Mo, W). A layer MS_2 always exhibit sandwich structure in which one layer is bonded with two layers of sulfur. According to the configurations and bonding, it can be classified to several kinds of phase, concerning 1T, 2H and 3R (where the digit stands for the layer number and the T, H and R means tetragonal, hexagonal and trigonal lattice, respectively). The H and T phases are most common in MS_2, where the transition metal atoms are centered at octahedral configurations and trigonal prismatic [57]. The 2D layered structures of WS_2 and MoS_2 facilitated H adsorption due to exposing numerous active sites in HER. Based on the DFT results, the ΔG_{H^*} value on the (1010) edge of MoS_2 is 0.08 eV, which is close to that of Pt (0 eV). Moreover, most of MS_2 type catalysts are semiconductors, some layered MS_2 materials even indicate the metallic

properties. However, the HER activity of MoS_2 and WS_2 are still lower than commercial noble metal-based catalysts due to the limited density of active sites and high kinetic barriers of H_2 generation. Thus, it is an effective method to boost the HER activity by increasing the number of exposed active sites and enhancing the intrinsic activity of the edge sites.

The nonlayered M_xS_y share the marcasite or pyrite structure, in which the transitional metal atoms are octahedrally bonded to adjacent sulfur atoms. The surface energies and electronic structure of pyrite-type M_xS_y are related to the intrinsic surface-state [58]. Similar to the layered MS_2, the HER performance of the M_xS_y could also be improved by morphology control, phase control and optimizing the electronic structure by doping heteroatoms. Jiang et al. synthesized three different nickel sulfides: NiS, NiS_2 and Ni_3S_2 via the microwave-assisted method [59]. The experiment results indicate the Ni_3S_2 exhibit the highest HER performance due to the large electrochemical active area, unique surface chemistry and high electrical conductivity. Non-metal atom N doped Ni3S2 on the nickel foam substrate was also prepared via one-step ammonia treatment. The obtained electrocatalysts exhibited the highly efficient HER activity, with an overpotential as low as 155 mV to achieve the current density of 10 mA cm^{-2} in alkaline solution. According to the DFT results, the NH_3 treatment introduced the heteroatom N dopants as the additional active sites (such as in (100) face), also created new active face (such as (-111) face) with lower ΔG_{H^*} on Ni and S sites. Moreover, other method to improve the HER activity was also reported, such as V-incorporated Ni_xS_y nanowire [60] and Mn doped Ni_3S_2 nanosheets [61].

1.3.3 Transition metal carbides (TMCs)

Transition metal carbides (TMCs) are highlighted by some advantages, such as high electronic conductivity, noble-metal-like electronic configuration and wide pH applicability. Among that, the property of noble-metal-like electronic configuration

renders TMCs to adsorb and activate hydrogen, thus exhibiting the similar HER activity with Pt. Since the HER activity on Mo_2C was discovered by Hu and co-workers in 2012, the study on TMCs electrocatalysts has been developed rapidly [62]. Great efforts have been devoted to design transitional metal carbides nanostructure (Mo, W, V, Ta, Fe, Co, etc.) with numerous active sites, large surface area, good conductivity, and significantly reducing the overpotential for HER.

One of the key approaches is to achieve high HER performance by exposing highly active surface via nano crystallization. In a model of Mo_2C, the DFT results identified the high activity of Mo terminated (001) than that of C, indicating that the surface Mo atoms is the active sites in Mo_2C. However, the active sites of Mo surface always covered by inert carbon layers due to the high temperature synthesize process. Reduction in nanoparticle size could improve the abundance of active sites and activity of TMCs. Giordance and co-workers employed the urea as carbon and nitrogen sources to convert the products from metal carbides to prepare the carbonitrides and nitrides [63]. The as prepared sample exhibit ultrafine nanoparticle due to the homogenous nucleation in metal-metal gels. The small MoC particle needs 198 and 176 mV to get the current density of 10 mA cm^{-2} in acidic and alkaline solution, respectively.

1.4 ANODE MATERIAL DESIGN FOR OER

1.4.1 Noble metal oxide-based oxides

Currently, the benchmark noble metal oxide-based OER electrocatalysts are RuO_2- and IrO_2-based, as these possess a special rutile structure with noble metal atoms located in the center of octahedral sites connected with corner oxygen atoms by sharing the corners. It has already been confirmed that RuO_2 and IrO_2 exhibit facet-dependent performance, such that different OER activities are observed at different crystallographic planes. It is reported that OER kinetics over the (110), (100), (101), and (111) lattice faces of RuO_2 and found that the (100) face is the most active in an

alkaline solution [64, 65]. It has been reported that OER performance using 2% Cu-doped RuO_2 is better than that of pure RuO_2 because the Cu species can reduce the binding energy of OER-related intermediates (e.g., HO^-, O^-, and HOO^-) in neighboring Ru active sites [66]. In addition, the Cu dopant could decrease the surface oxygen vacancy formation energy and promote an additional lattice oxygen vacancy-aided water dissociation pathway.

In general, the construction of strong oxide-support interactions (SOSI) is a convincing method for adjusting the electronic structure and atomic configurations of supported catalysts. Zheng *et al.* anchored ultrafine IrO_2 nanoclusters (~1 nm) on vanadium oxide (V_2O_5) using SOSI, as shown in **Figure 1.9a** [67]. The SEM and HR-TEM (**Figure 1.9b-d**) indicate that disordered IrO_2 nanoclusters (NCs) with a small size of ≈ 1 nm can be uniformly embedded on the porous skeleton of V_2O_5. The calculated free-energy diagrams and crystal orbital Hamilton population (**Figure 1.9e-g**) demonstrate that the disordered IrO_2 active sites with flexible redox states in IrO_2/V_2O_5 can serve as electrophilic centers and balance the adsorption of intermediates and effectively facilitate the process of O-O coupling, thereby propelling the fast turnover of water decomposition.

In addition to use of noble metal oxides with a rutile structure, noble metals are usually optimized by mixing them with non-noble metal oxides to lower the noble metal content and improve catalytic activity and/or stability. A continuous cobalt-cobalt oxide (Co-CoO) lateral hetero-structure implanted with well-dispersed rhodium (Rh) atoms shelled on the conductivity porous 1D Cu foam was prepared for the HER and OER under alkaline media [68]. The synergistic effect between the uniform Ru atoms and the Co-CoO heterostructure resulted in rich multi-integrated activity and robust stability in seawater. The properties of individual components with their synergistic effects could

result in enriched active sites and improved conductivity, thereby enabling catalytic reactions via specific pathways for electrolysis in freshwater-based electrolytes.

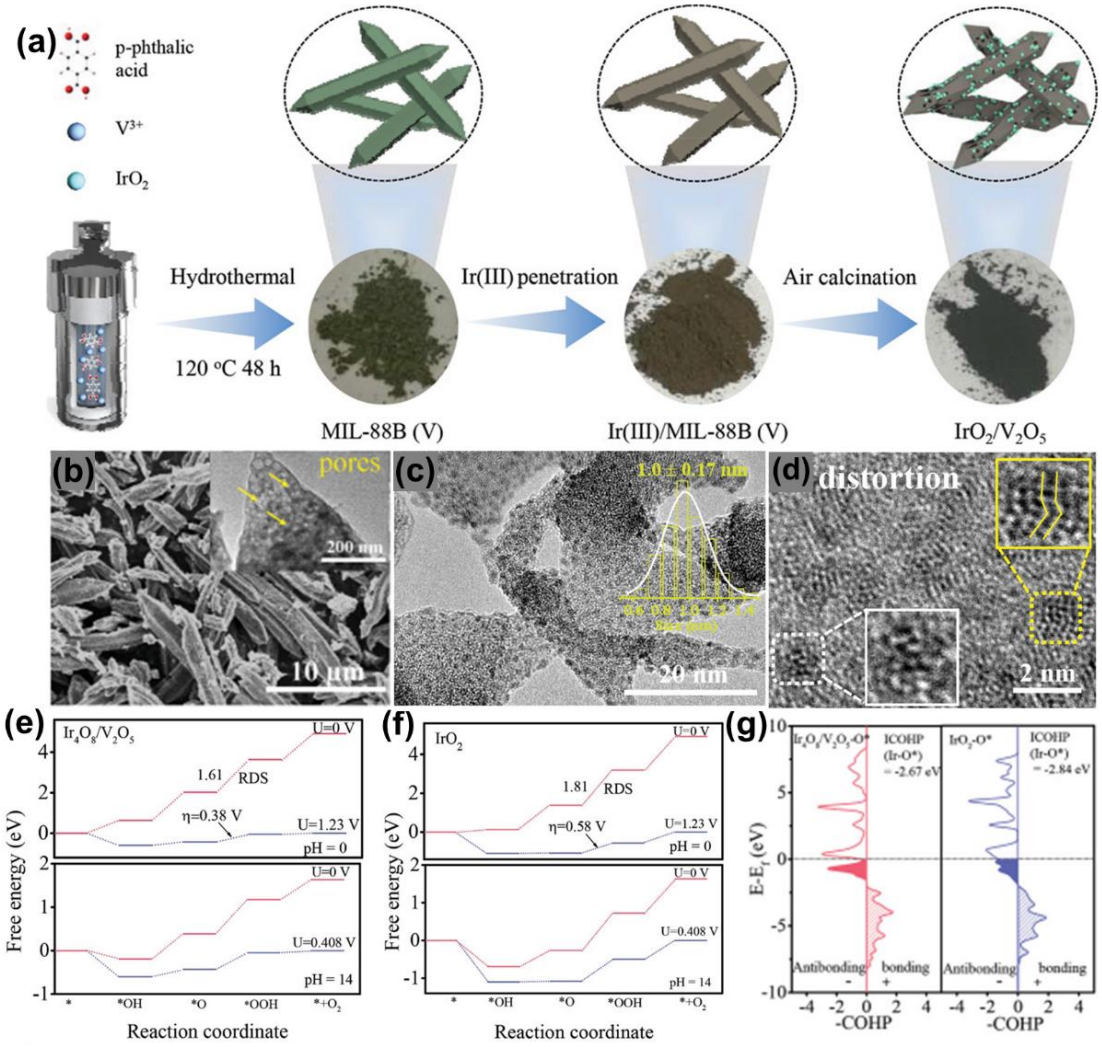

Figure 1.9 (a) Schematic illustration of the preparation of IrO_2/V_2O_5 oxides electrocatalysts. (b) SEM image of $IrO_2/V2O_5$. (c) and (d) HR-TEM images of IrO_2/V_2O_5. Calculated free energy diagrams of OER on the (e) Ir_4O_8/V_2O_5 and (f) IrO_2 under pH = 0 and 14, respectively. (g) -pCOHIP curves for O* intermediate adsorption on Ir active sites for Ir_4O_8/V_2O_5 and IrO_2 [67].

1.4.2 Non-noble metal oxides

Non-noble-based oxides with tunable structures and good cycling stability have been developed as low-cost electrocatalysts for electrolytic water [69]. The activity of a single transition metal-based oxide always depends on the metal type, supported

substrate material, and metal oxidation state. For example, Mn oxides (Mn_xO_y) can be divided into four types with different oxidation states: MnO (+2, NaCl structure type), Mn_3O_4 (+2/+3, tetragonally distorted or cubic spinel-type), Mn_2O_3 (+3, polymorphs), and MnO_2 (+4, several polymorphous). Supported nanostructured MoO_x [70] and MnO_x-nanorods [71] have been used as OER electrocatalysts. Metta *et al.* [72] pprepared MnO_x/CNTs by a deposition-precipitation and impregnation process, and it was found that the high dispersion of the active component MnO_x on the substrate could further improve the intrinsic catalytic activity, and unique deposition methods resulted in the oxidation states of Mn cations changing during the synproportionation reaction process. Two composite materials with different initial oxidation states of Mn: Mn^{2+} were observed under impregnation, whereas Mn^{4+} species were generated from deposition-precipitation. As such, the obtained 5 wt. % MnO_x/CNT electrocatalysts exhibited high performance in the electrolysis of fresh water. As one of the most abundant and low-cost transition metals, Cu-based electrocatalysts have been widely used in the HER/OER. For example, highly dispersed CuO_2 octahedrons with uniform sizes inlaid on 3D nickel foam (oct-CuO_2-NF) have been fabricated [73]. Owing to the high dispersion of the uniform octahedral structure and strong interaction with NF, oct-CuO_2-NF exhibited superior activity and stability in alkaline media. Because the OER activities of non-noble oxides depend heavily on the metal type, metal oxidation state, and supported substrate, OER activity and selectivity can be improved by doping elements, optimizing the oxide structure, and combining it with other compounds.

1.4.3 Spinel- type oxides

Spinel-type oxides are typically described as AB_2O_4 (A = Mn, Zn, Co, Cu, Ni, Fe, etc., and B = Cr, Mn, Co, Ni, Mo, etc.), which form one of three structures, normal, inverse, or complex, depending on the metal cations occupying the octahedral or tetrahedral sites [74, 75]. For the normal spinel (**Figure 1.10a**), metal A charged as +2

occupies the center of the tetrahedrally coordinated position, while cation B charged as +3 occupies the octahedral position, and the O^{2-} positions as the polyhedral vertexes. Wei et al. [76] reported that the metal cations occupying the octahedral sites play an efficient role in the OER process because of the large overlap of the lying eg-3d orbital in the octahedrally coordinated metal cations with an orbital of O *2p*. In general, the catalytic performance of such catalysts for the OER is ascribed to their structure, valence, morphology, and controllable composition.

Spinel-type oxides have recently been used for OER. It was found that the performance of Ni- and Co-containing spinel-type oxides for the OER is superior to that of Co_3O_4 and Ni- and Co-containing oxides [77]. Yang *et al.* [78] adopted a facile quenching approach (shown in **Figure 1.10b**) to realize the simultaneous doping of metal and generation of vacancies for the reconfiguration of the desired surface of spinel $NiCo_2O_4$, improving the OER activity in alkaline freshwater media. In addition, DFT calculations showed that the high activity should result from the strong electronic synergies among the metal cations, where the electronic structures were well regulated by the metal doping, thereby achieving near-optimal adsorption energies for the OER intermediates. Cobalt-based spinel-type oxides always possess appreciable charge-transfer propensity and stability. A spinel oxide $CoFe_2O_4$ with a partially inverse structure was also explored as a HER and OER bifunctional catalyst using a coprecipitation and inert calcination method [79]. It was found that the generation of O vacancies can be altered by the nanoparticle size, and the electron structure can be tuned by the generated oxygen vacancies created by altering the adsorption/desorption kinetics of the reaction intermediates, thereby resulting in high selectivity. The obtained catalysts, named AP-$CoFe_2O_4$ NPs with diameters of 20 nm (CoF-2) and 55 nm (CoF-3), showed the ability to accelerate the adsorption of intermediates at neighboring metal

centers. As a result, the calculated turnover frequency (TOF) of CoF-3 reached 3.43 and 5.12 O_2 s^{-1} at overpotentials of 398 and 416 mV, respectively.

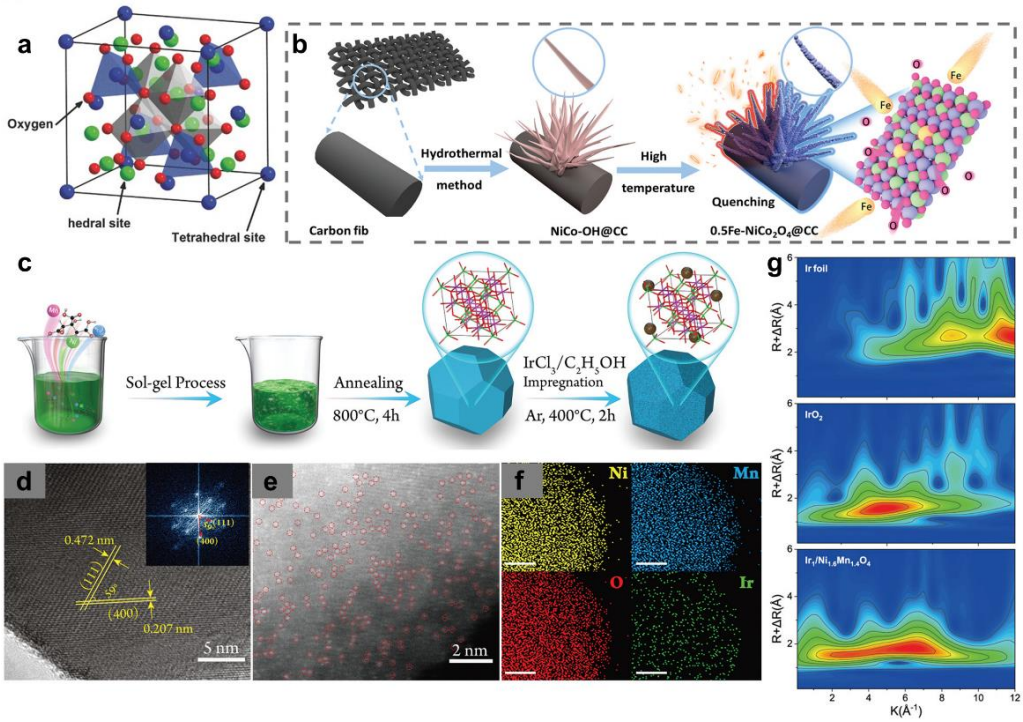

Figure 1.10 (a) Spinel crystal structure; (b) Schematic illustration for the preparation process of $NiCo_2O_4$@CC; (c) the schematic diagram for the synthetic procedure of the $Ir_1Ni_{1.6}Mn_{1.4}O_4$; (d) HR-TEM image of $Ni_{1.6}Mn_{1.4}O_4$, the inset reveals the corresponding FFT image. (e) HAADF-STEM image of 0.459% $IrNi_{1.6}Mn_{1.4}O_4$, indicative of the Ir-SAs; (f) the HAADF-STEM energy dispersive X-ray mapping, the bars represent 10 nm. (g) the wavelet transforms for the K^3-weighted Ir L^3-edge EXAFS signals of $Ir_1Ni_{1.6}Mn_{1.4}O_4$ compared to Ir foam and IrO_2.

MMn_2O_4 (M is a metal) is another spinel-type metal oxide. Manganese possesses advantages such as low cost, low toxicity, high abundance, multiple valences, and a prominent Jahn-Teller effect. The physicochemical properties of MMn_2O_4 are greatly dependent on the preparation conditions, which significantly affect its composition, structural parameters, oxidation states, and cation distributions. Considering that the cubic spinel $NiMn_2O_4$ and Ni_2MnO_4 exhibit similar structures, Wen *et al.* [44] tuned the OER activity of NiMn-based oxides by preparing a $NiMn_{3-x}O_4$ solid solution (shown in

Figure 1.10c), which exhibited excellent Cl oxidation resistance in seawater electrolysis. Iridium single atoms (Ir-SAs) were introduced into $NiMn_{3-x}O_4$ to further improve the intrinsic OER activity by increasing the number of active sites and thus alleviating the effect of insoluble precipitates. As shown in the HR-TEM image (**Figure 1.10d**), the dominant (011) crystal plane was confirmed. The HAADF-STEM and corresponding mapping of 0.459% Ir-$Ni_{1.6}Mn_{1.4}O_4$ (**Figure 1.10e** and **f**) indicate that the Ir atoms were discretely anchored on the $Ni_{1.6}Mn_{1.4}O_4$ nanocrystal. In addition, by comparing the corresponding wavelet transforms for the k^3-weighted Ir L3-edge EXAFS signals of $Ir_1/Ni_{1.6}Mn_{1.4}O_4$ with those of Ir foil and IrO_2 (**Figure 1.10g**), it can be seen that IrO_2 was the center of $Ir_1/Ni_{1.6}Mn_{1.4}O_4$, which is crucial for Ir-SAs to enhance the intrinsic OER activity with improved interfacial charge transfer.

1.4.4 Perovskite-type oxides

Perovskite-type oxides, as semiconductors with flexible compositions and structures and precisely controllable bandgaps, have also been considered as promising OER catalysts for seawater electrolysis [80, 81]. The general formula of perovskites is typically described as ABO_3, where the A site is occupied by rare-earth or alkaline metal atoms with a 12-fold oxygen coordination and the B-site atom is a transition metal cation with a 3*d*, 4*d*, or 5*d* configuration with a 6-fold oxygen coordination. Shao-Horn et al. [82] reported that the intrinsic activity of perovskite oxides with $e_g = 1$ is even higher than that of noble metals in the OER because the e_g orbital directly toward an O_2 molecule overlaps the O-2p_δ orbital more than the t_{2g} and O-2p_π orbitals overlap. Owing to the highly flexible crystal structure and composition, the e_g number of perovskite can be tuned through doping in the A or B sites.

Recently, $A_{n+1}B_nO_{3n+1}$-type Ruddlesden–Popper (RP) Co-based perovskites, such as $La_{0.5}Sr_{1.5}Ni_{1-x}O_{4+\delta}$ RP and $LaSr_3(Co_{0.5}Fe_{0.5})_3O_{10-\delta}$), have been found to be excellent OER catalysts [83, 84]. Moreover, hybridizing RP-type cobalt-based and ABO_3-type

perovskites can exert a synergistic effect to improve the OER performance of a single component. For example, Wang *et al.* [85] prepared a perovskite hybrid with RP-type $LaSr_3Co_{1.5}Fe_{1.5}O_{3-\delta}$ and ABO_3-type $La_{0.25}Sr_{0.75}Co_{0.5}Fe_{0.5}O_{3-\delta}$ through a self-assembly process, which greatly accelerated the oxygen redox kinetics during the OER process and enhanced the activity. Shao *et al.* [86] synthesized a perovskite hybrid containing RP-type $La_xSr_{2-x}CoFe_{1-y}O_{4-\delta}$ and AB_3-type $La_xSr_{1-x}CoFe_{1-y}O_{3-\delta}$ with an electrochemically induced amorphous crystalline phase, which also exhibited superior OER activity. Liu *et al*. [87] proposed a new top-down evolution method to prepare a Co-based perovskite hybrid (P/RP-SNCF) by converting part of the ABO_3 type $SrNb_{0.1}Co_{0.7}Fe_{0.2}O_{3-\delta}$ (P-SNCF) to RP-type $Sr_3NbCoO_{7-\delta}$ (RP-SNCF) via an annealing treatment. From the TEM and HR-TEM, it was found that RP-SNCF can be directly grown on the surface of P-SNCF, which could cause a strong interaction between the two phases, and the active surface of P/RP-SNCF could be reconstructed.

1.4.5 Transition metal layered double hydroxide (TM-LDH)

As one sort of two-dimensional (2D) layered clays, the general formula of LDHs is $[M^{2+}_{1-x}M^{3+}x(OH)_2]^{x+}[A^{n-}_{x/n}]^{x-}\cdot mH_2O$, which could be simplified as ($M^{2+}_{1-x/x}$-M^{3+}-A-LDH). One of the important properties of LDHs could tune of the chemical composition, including the M^{3+} and M^{2+} in the main sheet, the tunable charge density (M^{3+}/M^{2+} ratio) and interchangeable interlayer anions (A^{n-}). The structure of LDHs could be stabilized by electrostatic interactions between the anions and brucite-like layers, and hydrogen bonds between anions, interlayer H_2O and hydroxyl plates. The LDHs have been extensively used in OER areas due to their wide adaptability of different types and ratios of metals in the interlayer space and large interlayer distance.

Bulk nickel hydroxide can be divided into two hydrotalcite-like phase (α-phase) and brucite-like phase (β-phase) nickel hydroxide. And the interlayered distance of α and β-phase Ni $(OH)_2$ are about 8.0 and 4.6 Å, respectively. Due to the different

ion/electron transfer characteristics, the OER activity and stability of α and β-phase Ni $(OH)_2$ are widely divergent. Luan et al. systematically explored the structure effects of α- Ni $(OH)_2$ on OER performance [88]. The different bud-like, petal-like, flower-like and sheet-like structure was synthesized via a simple lamellar reverse micelle method. The as-prepared samples exhibit the high OER performance due to the favorable substance adsorption/diffusion properties, high reactivity of active sites and large accessible surface area.

Typically, incorporation of other metals may improve the number of LDHs active sites and regulate the electronic structure of pristine metal hydroxide. Chen and co-workers Cu, Mn doping into Co $(OH)_2$ could modulate the electronic structure thus enhanced positive charging of the matrix metal ions (I.e., $Co^{(2+\delta)+}$, $0<\delta<1$) toward boost the OER performance [89]. As a result, the Cu-Co $(OH)_2$ exhibit better OER performance because the high valences $Co^{(2+\delta)+}$ in the Cu-Co $(OH)_2$ generated more than those in Co $(OH)_2$ and Mn-Co $(OH)_2$. Heteroatoms Fe doping into nickel based (oxy)hydroxide was seemed as a promising method to improve the OER performance. Boettcher et al. found the incorporation of Fe improved the activity of Ni(O)OH significantly [90]. And they demonstrated the Fe affects the NiOOH electronic structure, and then exerts some partial-charge transfer activation on the Ni. Later, Bell and co-worker explored deeply. They identified the octahedral sites were occupied by active Fe^{3+} species with the short Fe-O bonds in (Ni, Fe) OOH, which shared one edge with surrounding $[NiO_6]$ octahedra [91]. Notably, Boettcher and co-workers further explored the role of Fe in Ni-based OER electrocatalyst, which is dependent on the local structure. They calculated the Fe-NiO_xH_y was 100-fold more active than individual NiO_xH_y [92]. And the finding indicated that the FeO_xH_y was initially incorporated into NiO_xH_y from solution at surface/defect/edge sites, and influenced the Ni redox behavior. Furthermore,

Shen's group reported 2D Mo- and Fe- modified Ni $(OH)_2$/NiOOH nanosheets with a 280 mV overpotential at the current density of 100 mA cm^{-2} and the outstanding stability for 50h in alkaline solution. DFT and experiment results demonstrated that Mo- and Fe- modified Ni $(OH)_2$/NiOOH donated to the best adsorption energy for OER intermediates, thus increased the OER performance. Meanwhile, the dual-modified Ni $(OH)_2$/NiOOH by Mo- and Fe- was more stable than Mo- or Fe- modified Ni $(OH)_2$/NiOOH.

1.5 MATERIAL DESIGN FOR SEAWATER SPLITTING

1.5.1 Transition metal oxide compounds

To improve the activity of TMO-based electrocatalysts, studies have investigated the creation of metal oxide compounds using the synergistic effect of different metal species [93]. For example, in 1980, Bennett [94] developed poorly crystallized MnO_2 as an anode material for seawater electrolysis, which was further decorated with metal oxides by Bigiani *et al.* [95]. The materials were prepared by a three-step strategy, in which a plasma-enhanced chemical vapor deposition (PE-CVD) process was used to cover MnO_x on a fluorine-doped tin oxide (FTO)-coated glass substrate. A radio frequency sputtering process was applied to subsequently disperse Fe_2O_3 or Co_3O_4, then a thermal process under air or inert atmospheres was performed to yield MnO_2- or MnO_3-based electrocatalysts with a high active area and inherent oxygen defectivity (shown in **Figure 1.11a**). The direct growth of materials on a conductive substrate ensured chemically intimate contact between their constituents to reduce charge resistance, thereby enhancing the OER activity and improving electrode stability. As a result, MnO_2 decorated by Co_3O_4 possessed the best performance in alkaline seawater splitting, achieving an overpotential of 450 mV at 10 mA cm^{-2} with the ability to eliminate chlorine evolution.

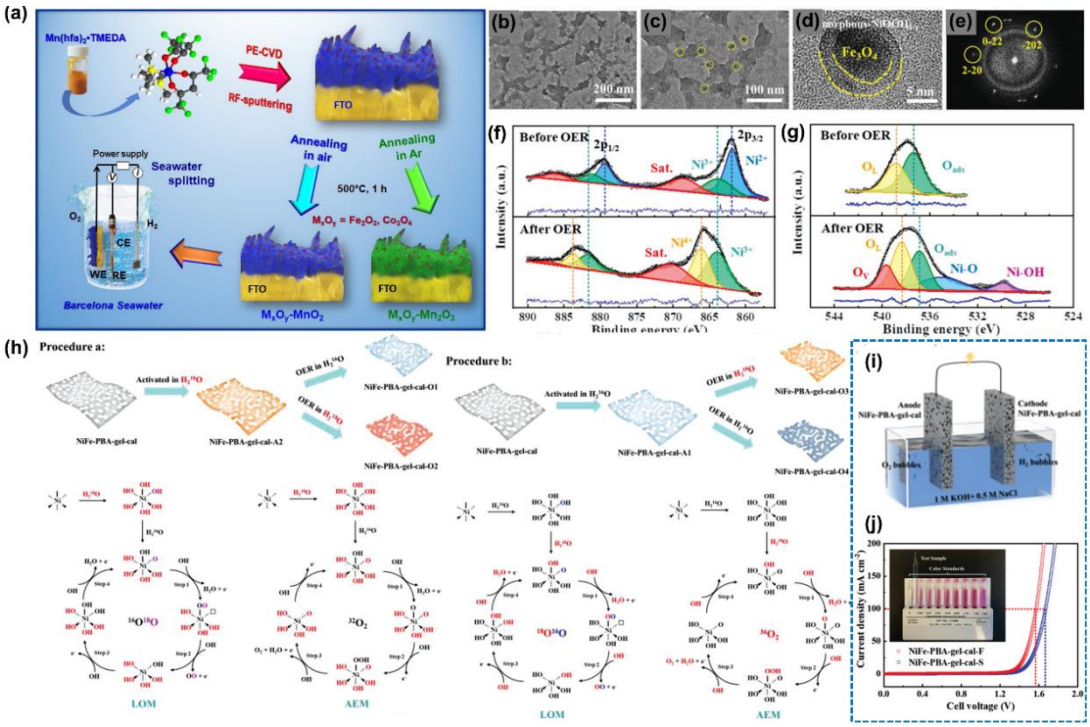

Figure 1.11 (a) Sketch of the fabrication procedure for MnO_2 and Mn_2O_3 electrodes, functionalized with Fe_2O_3 or Co_3O_4 for seawater splitting [95]. (b-d), TEM images of NiFe-PBA-gel-cal after OER test. (e) SAED pattern of d. (f) Ni *2p* edge and (g) O*1s* edge of NiFe-PBA-gel-cal before and after OER test. (h) OER mechanism with concerted and nonconcerted proton-electron transfer. Procedure a: H_218O was used to active the catalyst and $H_2{}^{16}O$ served as electrolyte for the O_2 evolution; Procedure b: $H_2{}^{16}O$ was used to active the catalyst and $H_2{}^{18}O$ served as electrolyte for the O_2 evolution. (i) Schematic illustration of the water-splitting electrolyzer and (j) overall water-splitting performance of NiFe-PBA-gel-cal//NiFe-PBA-gel-cal electrode couple in alkaline freshwater and simulated seawater (inset: hypochlorite detection result of the electrolyte after seawater splitting stability test) [100].

Constructing a heterostructure is an effective method for reducing the internal resistance of TMOs and improving electrical conductivity. For example, Li *et al*. [96] used a facile dipping and heating (DAH) method to synthesize a Fe_2O_3/NiO heterostructure catalyst grown on nickel foam, named FNE300, in which the interface between Fe_2O_3 and NiO could promote charge transfer, while the interaction of Fe with oxygen intermediates could be optimized by e^--e^- repulsion between Ni^{2+} and O

intermediates, thereby improving the OER kinetics of the active sites. Consequently, it exhibited remarkable OER activity and stability in alkaline natural seawater, requiring an overpotential of 291 mV to deliver a high current density of 1000 mA cm^{-2}. Moreover, by coupling FNE300 and $MoNi_4/MoO_2$-based electrodes, the two-electrode electrolyzer met the industrial requirement of 500 mA cm^{-2} at a low voltage of about 1.75 V with high stability. Another Fe_3O_4/NiC_x composite material, NiFe-PBA-gel-cal, with an ultrahigh surface area was also prepared using a Prussian blue precursor obtained from a sol-gel method, which also exhibited excellent seawater splitting performance [97]. According to the details of post-mortem characterizations after the OER test **(Figure 1.11b-e**), Fe_3O_4@$NiOOH_{2-x}$ was *in situ* generated on Fe_3O_4/NiC_x with a core-shell structure due to the conversion of NiC_x during the OER process, which contained abundant oxygen defects and high-valence Ni^{3+}/Ni^{4+} ions. In particular, the high valence states of the Ni species caused the generation of O *2p* electron vacancies as electrophilic centers to achieve the OER redox reaction (**Figure 1.11f** and **g**). Meanwhile, the *in site* ^{18}O isotope labelling (**Figure 1.11h**) revealed that the OER route over NiFe-PBA-gel-cal should be dominated by the lattice oxygen oxidation mechanism (LOM) pathway. As a result, when the NiFe-PBA-gel-cal was used as both cathode and anode material (**Figure 1.11i**), low cell voltages of 1.57 V and 1.66 V to achieve a high current density of 100 mA cm^{-2} were achieved in alkaline freshwater and simulated seawater solutions, respectively (**Figure 1.11j**). In addition, Cl_2 or hypochlorite acid was not formed in the reaction solution, as indicated in the inset of **Figure 1.11j**. Huang and Lin [98] prepared $FePO_4$ on $CaFeO_x$ using an electrodeposition method to reduce the effect of Mg^{2+} ions in natural seawater and inhibit the oxidation of chloride to produce corrosive hypochlorite. As a result, the material worked for more than 12 h at a current density of 10 mA cm^{-2} in a neutral

seawater-based electrolyte. Metal oxide compounds can easily combine oxides with other materials (e. g. sulfides, phosphides, nitrides, and hydroxides) to improve their performance, including conductivity, intrinsic activity, selectivity, and stability parameters, in the seawater splitting process.

1.5.2 Performances of electrocatalyst based electrocatalysts at high current density

Commercial water electrolyzers require a high current density with a low overpotential (j > 500 mA cm^{-2} and η < 300 mV) to realize large-scale hydrogen production from seawater electrolysis. Generally, with a high current density, the gas generation reactions on the surfaces of both the anode and cathode are vigorous. During the reaction process, the electrocatalysts could be peeled off from the electrodes owing to the rapidly generated gas bubbles [99]. Compared with the powder-state electrocatalysts that were adhered to the electrode with various binders, the self-supported electrocatalysts *in-situ* growing on the conductivity substrate could greatly prolong the service life of the electrocatalysts. In addition, in alkaline seawater-based electrolytes, hypochlorite was generated at an overpotential of approximately 480 mV. Therefore, the prepared high activity and selectivity should reach high current densities (more than 500 and 1000 mA cm^{-2}) at overpotentials lower than 480 mV to avoid the chlorine oxidation reaction [100].

In 2000, Fujimura *et al.* [101] reported a series of MnO_2-type Mn-Mo bimetal oxides anodically deposited on IrO_2-coated titanium substrates under various conditions. When they were used for seawater electrolysis, the oxides containing ≥ 8 mol% of Mo in cationic percentage exhibited an initial O_2 evolution efficiency of almost 100% at a continuous current density of 1000 mA cm^{-2} in 0.5 M NaCl containing simulated seawater at a pH of 12 and at a temperature 30 °C. The addition of Mo to MnO_2 significantly increased the overpotential for chlorine evolution. However, the OER

efficiency gradually decreased with time because the deposited Mn-Mo oxides were partly peeled off from the IrO_2-coated titanium substrate. In particular, the oxides were electrochemically dissolved as permanganate ions at a current density of 1000 mA cm^{-2}. However, as the deposition temperature was increased to 90 °C, such dissolution was avoided because the potential at the anode exceeded ~ 3 V, which was greater than the equilibrium potential of the generation of permanganate ions from manganese oxides.

To further improve the stability of the manganese oxides, Mn-Mo-W and Mn-Mo-Fe ternary oxides on IrO_2-coated titanium substrates were prepared by Matsui [102] and Ghany [103], respectively. These two electrodes showed almost 100% oxygen evolution efficiency at a high current density (1000 mA cm^{-2}) in a solution containing NaCl (0.5 M) at 90 °C. However, the Mn-Mo-Fe ternary oxide anode remained stable at 30-90 ℃ while the Mn-Mo-W oxide was gradually oxidized, resulting in dissolution occurring during electrolysis in the NaCl solution when the temperature was lower than 90 °C due to the formation of imperfect crystalline oxides. In addition, El-Moneim [104] studied the deposition method of a Mn-Mo-W-triple oxide electrocatalyst for Cl^- less oxygen-generating electrodes for seawater electrolysis. The durability of the electrodes was examined at a high current density of 1000 mA cm^{-2} in 0.5 M NaCl solution. Using a repeated deposition method for 2×30 min and 3×30 min, the two electrodes exhibited O_2 evolution efficiencies higher than 99% for more than 1500 and 2600 h, respectively. By using a continuous deposition method for 60 and 90 min, the two electrodes obtained displayed 480 and 120 h stability under the same conditions, respectively. In that study, the repeated deposition method not only resulted in the formation of compact, thin, and single-phase oxides with an optimized structure and composition, but also increased the adhesion of the oxide deposited on the conductive substrate.

Because gas bubbles accumulated on the electrode surface at a high current density could block the active sites and decrease the effective mass transfer, it has been necessary to develop electrocatalysts that favor the desorption of gas bubbles by creating superoleophobicity and superhydrophobic surfaces between the gas and liquid–solid interfaces. In one study, the heterointerface between Fe_3O_4 and Fe (Cr)OOH on NF was constructed using a scalable method [105]. The as-prepared Fe (Cr)OOH/ Fe_3O_4/NF possessed a hydrophilic surface. Consequently, a high anodic current density of 500 mA cm^{-2} with a low overpotential of 241 mV was achieved. DFT calculations revealed that the introduction of Cr and its coupling with Fe_3O_4 could significantly lower the energy barriers for the OER and increase the electrical conductivity. In addition, the as-prepared Fe (Cr)OOH/Fe_3O_4/NF-based electrolyzer also exhibited robust stability at a high current density (400 mA cm^{-2}) for 100 h with a minor current attenuation of 8% in alkaline seawater.

1.5.3 Perspectives of the seawater splitting

Hydrogen energy has drawn widespread attention due to the high energy density and nearly zero pollution. Although significant advances have been achieved in the development of various transition metal-based electrocatalysts for the OER in seawater electrolysis, some important issues should be addressed in the future.

(i) Deeper exploration of the seawater electrolysis mechanism is necessary. To date, overcoming the competition between the OER and ClER remains a bottleneck for the successful application of natural seawater electrolysis for hydrogen production. However, the effect of Cl^- ions on OER selectivity over the various TMO-based electrocatalysts remains unclear. In particular, the competitive adsorption of intermediates on the active sites of electrocatalysts and their conversion processes should be investigated in more detail using *in situ* characterization methods and theoretical calculations. The diffusion kinetics of various ions in the electrolytes and

electrodes should be studied along with the reaction mechanisms, which is important for establishing a rational catalysis system for industrial-level applications.

(ii) For fundamental laboratory studies, natural seawater should also be used in addition to simulated seawater (0.5 M NaCl + 1 M KOH) because the composition of natural seawater is much more complicated, with various co-existing ions besides Cl^-, including metal ions such as Li^+, Na^+, Mg^{2+} and Ca^{2+} and anions such as Br^- and I^-, which could affect the activity, selectivity, and stability of electrocatalysts. In particular, in an alkaline electrolyte, Mg $(OH)_2$ and Ca $(OH)_2$ precipitates can be formed and adhere to the surface of the electrocatalysts, affecting their performance. Therefore, the development of effective electrocatalysts for neutral seawater electrolytes is becoming increasingly important. Effective pretreatment of natural seawater for the removal of precipitates and batteries could be a facile way to prevent the blockage of active sites and ensure the long-term stability of electrocatalysis in the seawater splitting process.

(iii) More attention should be paid to the measurement of Faradaic efficiency. The Faradaic efficiency of O_2 is vital for determining the OER selectivity during seawater splitting, which should be a bridge between fundamental and real-world applications.

(iv) For the evaluation of other electrocatalysts, it is necessary to consider universal descriptors in this field to compare the activity and selectivity of various electrocatalysts in different groups for the OER in seawater splitting because different measurement methods could result in different results. For example, the catalyst loading amounts were not reported in the published literature, and the windows for the overpotential measurements differed among research groups. Thus, there is an urgent need to develop universal descriptors with higher accuracy for the evaluation of the developed electrocatalysts.

(v) Taking more attentions on the computational issues in alkaline seawater splitting. Most computational methods apply the scheme of the computational hydrogen electrode (CHE), but the studies do not really tackle the alkaline environment. In contrast, the computation for the acidic seawater splitting is more reliable because the CHE approach is a good approximation for such reaction energetics. That is to say, the computational method should be consistent with the real experimental and theoretical conditions, avoiding any potentially "imitated" alkaline conditions.

(vi) *In situ* characterization of catalytic reactions in seawater electrolysis should be considered. It was found that most of the TMOs undergo phase transformation during the OER process so that the catalyst structure, coordination environment of active sites, and valence states of those active species are always altered. Nowadays, characterizations before and after the OER stability test have been performed by many researchers. However, the structural evolution during the OER process in seawater electrolysis is still not well understood. It is necessary to use various *in situ* characterization techniques such as *in situ* Raman, *in situ* XPS and XRD, and *in situ* TEM to detect the intermediates and adsorption/desorption behaviors of reactants and intermediates. Combining these *in situ* characterizations, theoretical calculations, and electrochemical measurements could reveal the OER reaction mechanism more effectively and rationally so that better electrocatalysts can be developed efficiently for industrial-level applications.

1.6 OBJECTIVE OF THIS STUDY

As reviewed above, searching for cost-effective and earth-abundant electrocatalysts with high activity and stability is the crucial factor to improve the efficiency of water and seawater splitting. Various efforts have been made to enhance the performance of electrocatalysts including designing and preparing the catalysts with

the unique morphology and large surface area to generate more active sites, tuning the crystal structure to create numerous defects, or doping heteroatoms to adjust the electron structure configuration. Although many non-noble HER and OER electrocatalysts have been reported, the activity and stability of reported catalysts are still low, and the preparation process of electrocatalysts are also complex and time-consuming. Especially for the seawater splitting process, the chloride corrosion is a tough issue since it will gradually affect the application life of a catalyst. Thus, the objectives of this study are the development of low-cost and high-efficient OER and HER electrocatalysts, which should possess low overpotential, small Tafel slope, high stability and near 100% Faradic efficiency. Especially, developing corrosion resistant electrocatalysts for the seawater splitting will be considered. Moreover, the reaction mechanisms and the surface adsorption and desorption properties will be clarified.

1.7 SCOPE OF THIS DESSERTATION

Chapter 1 summarizes the fundamentals of both HER, OER in the fresh water and seawater, elucidates the key parameters in water splitting process, summarizes the preparation methods on the electrocatalysts, introduces the trends of anode/cathode materials in the fresh water and seawater. Finally, the objects in this study are mentioned.

In **Chapter 2**, a novel HER electrocatalyst was developed. In this work, to achieve effective interface construction, epitaxial growth of NiS on the surface of one-dimensional (1D) Ni_3S_2 nanowire on nickel foam (NF) was performed, in which a Ni_3S_2/NiS electrocatalyst with a heterojunction structure was constructed via a solid-state phase transformation. Benefiting from the strong charge transfer at the Ni_3S_2/NiS heterojunction interface, the d-band center was downshifted compared to the single component (Ni_3S_2 or NiS), which effectively optimized the valence state and the H adsorption of Ni, thus improved the HER activity. The obtained Ni_3S_2@NiS-250/NF

showed the robust HER catalytic performance with a low overpotential of 129 mV to deliver the current density of 10 mA cm^{-2} with a small Tafel slope (75.5 mV dec^{-1}) in 1 M KOH media. Moreover, it exhibited superior durability for at least 50 h. This work provides a novel strategy for designing nickel sulphide-based catalysts for HER with high performance.

In **Chapter 3**, a novel catalyst composed of Zn-VO_x-Co two-dimensional (2D) nanosheets with well-integrated heterostructure was successfully synthesized on carbon fiber paper (CFP) by a facile electrodeposition approach. Interestingly, the obtained nanosheets composed of amorphous VOx-Co and Zn-Co crystalline phases with a heterostructure. Density functional theory (DFT) calculations revealed that the dual-doping of Zn and VO_x optimized d-band center of Co and balanced adsorption and desorption of H, which enhanced intrinsic electrocatalytic HER activity. As a result, the optimum catalyst achieved a current density of 10 mA cm^{-2} at an overpotential as low as 46 mV and long-term electrochemical stability over 36 h in 1 M KOH solution. This work opens a new avenue for designing electrocatalysts with unique crystalline-amorphous heterostructure by dual-doping to achieve tuneable surface properties as well as d-band structure.

In **Chapter 4,** for effective seawater splitting, a Boron (B) doped $MnFe_2O_4$ spinel-type electrocatalyst with a heterostructure was derived from MnFe-MOF-74 precursor and applied for seawater electrolysis. It is found that the introduction of B species can effectively optimize the electronic configuration of $MnFe_2O_4$ with the promoted electron transfer ability between neighbouring O to Fe_{Oh}, thereby significantly reducing the energy barrier of the electron transfer and boosting the reaction process. As expected, in the real seawater environment, it required a low overpotential of 330 mV for OER to drive a current density of 100 mA cm^{-2} at 60 °C, and exhibited high stability for over

200-h continuing test without producing hypochlorite and corrosion. This work provides a new strategy for enhancing the intrinsic activity of spinel-type oxides in seawater splitting.

Chapter 5 summarized the research results of this dissertation and an outlook was given for the future researches in this field.

Reference

[1] K. Xu, H. Cheng, H. Lv, J. Wang, L. Liu, S. Liu, X. Wu, W. Chu, C. Wu, Y. Xie, Controllable surface reorganization engineering on cobalt phosphide nanowire arrays for efficient alkaline hydrogen evolution reaction, Adv. Mater. 30 (2018) 1703322.

[2] T. Liu, P. Li, N. Yao, G. Cheng, S. Chen, W. Luo, Y. Yin, CoP-doped MOF-based electrocatalyst for pH-universal hydrogen evolution reaction, Angew. Chem. Int. Ed. 131 (2019) 4727-4732.

[3] T. Haq, Y. Haik, Strategies of anode design for seawater electrolysis: recent development and future perspective. Small Science, 2 (2022) 2200030.

[4] X. Xiao, L. Yang, W. Sun, Y. Chen, H. Yu, K. Li, B. Jia, L. Zhang, T. Ma, Electrocatalytic water splitting: from harsh and mild conditions to natural seawater, Small 18 (2022) 2105830.

[5] C. Wang, H. Shang, L. Jin, H. Xu, Y. Du, Advances in hydrogen production from electrocatalytic seawater splitting, Nanoscale 13 (2021) 7897-7912.

[6] M. Chen, J. Liu, N. Kitiphatpiboon, X. Li, J. Wang, X. Hao, A. Abudula, Y. Ma, G. Guan, Zn-VO_x-Co nanosheets with amorphous/crystalline heterostructure for highly efficient hydrogen evolution reaction, Chem. Eng. J. 432 (2022) 134329.

[7] Y. Ma, M. Chen, H. Geng, H. Dong, P. Wu, X. Li, G. Guan, T. Wang, Synergistically tuning electronic structure of porous β-Mo_2C spheres by Co doping and Mo-vacancies defect engineering for optimizing hydrogen evolution reaction activity, Adv. Funct. Mater. 30 (2020) 2000561.

[8] P. C. K. Vesborg, B. Seger, I. Chorkendorff, Recent development in hydrogen evolution reaction catalysts and their practical implementation, J. Phys. Chem. Lett. 6 (2015) 951-957.

[9] J. A. Turner, Sustainable hydrogen production, Science 305 (2004) 972-974.

[10] C. C. Weng, J. T. Ren, Z. Y. Yuan, Transition metal phosphide-based materials for

efficient electrochemical hydrogen evolution: a critical review, ChemSusChem 13 (2020) 3357-3375.

[11] S. Khatun, H. Hirani, P. Roy, Seawater electrocatalysis: activity and selectivity, J. Mater. Chem. A. 9 (2021) 74-86.

[12] J. Wang, S. J. Kim, J. Liu, Y. Gao, S. Choi, J. Han, H. Shin, S. Jo, J. Kim, F. Ciucci, H. Kim, Q. Li, W. Yang, X. Long, S. Yang, S. P. Cho, K. H. Chae, M. G. Kim, H. Kim, J. Lim, Redirecting dynamic surface restructuring of a layered transition metal oxide catalyst for superior water oxidation, Nat Catal. 4 (2021) 212-222.

[13] X. Zuo, K. Chang, J. Zhao, Z. Xie, H. Tang, B. Li, Z. Chang, Bubble-template-assisted synthesis of hollow fullerene-like MoS_2 nanocages as a lithium-ion battery anode material, J. Mater. Chem. A 4 (2016) 51-58.

[14] F. Zhang, L. Yu, L. Wu, D. Luo, Z. Ren, Rational design of oxygen evolution reaction catalysts for seawater electrolysis, Trends in Chemistry 3 (2021) 485-498.

[15] Y. Song, G. Jiang, Y. Chen, P. Zhao, Y. Tian, Effects of chloride ions on corrosion of ductile iron and carbon steel in soil environments, Sci. Rep. 7 (2017) 6865.

[16] S. Dresp, F. Dionigi, S. Loos, J. F. Araujo, C. Spöri, M. Gliech, H. Dau, P. Strasser, Direct electrolytic splitting of seawater: activity, selectivity, degradation, and recovery studied from the molecular catalyst structure to the electrolyzer cell level, Adv. Energy Mater. 8 (2018) 1800338.

[17] X. Wang, X. Zhai, Q. Yu, X. Liu, X. Meng, X. Wang, L. Wang, Strategies of designing electrocatalysts for seawater splitting, J. Solid State Chem. 306 (2022) 122799.

[18] F. Sun, J. Qin, Z. Wang, M. Yu, X. Wu, X. Sun, J. Qiu, Nat. Commun. 12 (2021) 1-11.

[19] J. N. Hausmann, R. Schlögl, P. W. Menezes, M. Driess, Energy Environ. Sci. 14

(2021) 3679-3685.

[20] Z. Y. Yu, Y. Duan, X. Y Feng, X. Yu, M. R. Gao, S. H. Yu, Clean and affordable hydrogen fuel from alkaline water splitting: past, recent progress, and future prospects, Adv. Mater. 33 (2021) 2007100.

[21] H. Wang, K. H. L. Zhang, J. P. Hofmann, V. A. de la Peña O'Shea, F. E. Oropeza, The electronic structure of transition metal oxides for oxygen evolution reaction, *J. Mater. Chem. A* 9 (2021) 19465.

[22] J. Liu, S. Duan, H. Shi, T. Wang, X. Yang, Y. Huang, G. Wu, Q. Li, Rationally designing efficient electrocatalysts for direct seawater splitting: challenges, achievements, and promises, Angew. Chem. Int. Ed. (2022) 202210753.

[23] F. Dionigi, T. Reier, Z. Pawolek, M. Gliech, P. Strasser, Design criteria, operating conditions, and nickel-iron hydroxide catalyst materials for selective seawater electrolysis, ChemSusChem 9 (2016) 962-972.

[24] K. S. Exner, Controlling stability and selectivity in the competing chlorine and oxygen evolution reaction over transition metal oxide electrodes, ChemElectroChem 6 (2019) 3401-3409.

[25] L. J. J. Janssen, L. M. C. Starmans, J. G. Visser, E. Barendrecht, Mechanism of the chlorine evolution on a ruthenium oxide/titanium oxide electrode and on a ruthenium electrode, Electrochim. Acta 22 (1977) 1093-1100.

[26] K. S. Exner, J. Anton, T. Jacob, H. Over, Full kinetics from first principles of the chlorine evolution reaction over a RuO_2 (110) model electrode, Angew. Chem. Int. Ed. 55 (2016) 7501-7504.

[27] K. S. Exner, I. Sohrabnejad-Eskan, H. Over, A universal approach to determine the free energy diagram of an electrocatalytic reaction, ACS Catal. 8 (2018) 1864-1879.

[28] J. Rossmeisl, Z. W. Qu, H. Zhu, G. J. Kroes, J. K. Nørskov, Electrolysis of water

on oxide surfaces, J. Electroanal. Chem. 607 (2007) 83-89.

[29] K. S. Exner, J. Anton, T. Jacob, H. Over, Controlling selectivity in the chlorine evolution reaction over RuO_2-Based Catalysts, Angew. Chem. Int. Ed. 126 (2014) 11212-11215.

[30] T. Ma, W. Xu, B. Li, X. Chen, J. Zhao, S. Wan, K. Jiang, S. Zhang, Z. Wang, Z. Tian, Z. Lu, L. Chen, The critical role of additive sulfate for stable alkaline seawater oxidation on nickel-based electrodes, Angew. Chem. Int. Ed. 133 (2021) 22922-22926.

[31] S. Gupta, M. Forster, A. Yadav, A. J. Cowan, N. Patel, M. Patel, Highly efficient and selective metal oxy-boride electrocatalysts for oxygen evolution from alkali and saline solutions, ACS Appl. Energy Mater. 3 (2020) 7619-7628.

[32] W. Tong, M. Forster, F. Dionigi, S. Dresp, R. S. Erami, P. Strasser, A. J. Cowan, P. Farràs, Electrolysis of low-grade and saline surface water, Nat. Energy. 5 (2020) 367-377.

[33] M. Tahir, L. Pan, F. Idrees, X. Zhang, L. Wang, J. J. Zou, Z. L. Wang, Electrocatalytic oxygen evolution reaction for energy conversion and storage: a comprehensive review, Nano Energy 37 (2017) 136-157.

[34] E. Alizadeh-Gheshlaghi, B. Shaabani, A. Khodayari, Y. Azizian-Kalandaragh, R. Rahimi, Investigation of the catalytic activity of nano-sized CuO, Co_3O_4 and $CuCo_2O_4$ powders on thermal decomposition of ammonium perchlorate, Powder Technol. 217 (2012) 330-339.

[35] W. Jin, X. Han, Y. He, B. Zhang, P. Xu, Y. Du, Galvanic replacement mediated synthesis of rGO-Mn_3O_4-Pt nanocomposites for the oxygen reduction reaction, RSC Adv. 6 (2016) 89124-89129.

[36] Z. Chen, S. Ren, M. Wang, L. Chen, X. Li, J. Li, J. Yang, Q. Liu, Structure-activity strategy comparison of $(NH_4)_2CO_3$ and NH_4OH precipitants on MnO_x catalyst for low-

temperature NO abatement. Mol. Catal. 531 (2022) 112693.

[37] H. S. Jadhav, R. S. Kalubarme, A. H. Jadhav, J. G. Seo, Iron-nickel spinel oxide as an electrocatalyst for non-aqueous rechargeable lithium-oxygen batteries, J. Alloys Compd. 666 (2016) 476-481.

[38] G. Gnana kumar, C. J. Kirubaharan, D. J. Yoo, A. R. Kim, Graphene/poly (3,4-ethylenedioxythiophene)/Fe_3O_4 nanocomposite- an efficient oxygen reduction catalyst for the continuous electricity production from wastewater treatment microbial fuel cells, Int. J. Hydrog. Energy 41 (2016) 13208-13219.

[39] R. Amrousse, A. Tsutsumi, A. Bachar, D. Lahcene, N_2O catalytic decomposition over nano-sized particles of Co-substituted Fe_3O_4 substrates, Appl. Catal. A Gen. 450 (2013) 253-260.

[40] C. W. Cady, G. Gardner, Z. O. Maron, M. Retuerto, Y. B. Go, S. Segan, M. Greenblatt, G. C. Dismukes, Tuning the electrocatalytic water oxidation properties of AB_2O_4 spinel nanocrystals: A (Li, Mg, Zn) and B (Mn, Co) site variants of $LiMn_2O_4$, ACS Catal. 5 (2015) 3403-3410.

[41] A. Amri, X. Duan, C. Y. Yin, Z. T. Jiang, M. M. Rahman, T. Pryor, Solar absorptance of copper-cobalt oxide thin film coatings with nano-size, grain-like morphology: optimization and synchrotron radiation XPS studies, Appl. Surf. Sci. 275 (2013) 127-135.

[42] D. G. Shchukin, A. A. Yaremchenko, M. G. S. Ferreira, V. V. Kharton, Polymer gel templating synthesis of nanocrystalline oxide anodes, Chem. Mater. 17 (2005) 5124-5129.

[43] D. Bokov, A. T. Jalil, S. Chupradit, W. Suksatan, M. J. Ansari, I. H. Shewael, G. H. Valiev, E. Kianfar, Nanomaterial by sol-gel Method: Synthesis and application, Adv. Mater. Sci. Eng. 2021 (2021) 2102014.

[44] N. Wen, Y. Xia, H. Wang, D. Zhang, H. Wang, X. Wang, X. Jiao, D. Chen, Large-scale synthesis of spinel $Ni_xMn_{3-x}O_4$ solid solution immobilized with iridium single atoms for efficient alkaline seawater electrolysis, Adv. Sci. 9 (2022) 2200529.

[45] S. Naz, S. K. Durrani, M. Mehmood, M. Nadeem, Hydrothermal synthesis, structural and impedance studies of nanocrystalline zinc chromite spinel oxide material, J. Saudi Chem. Soc. 20 (2016) 585-593.

[46] Q. Yang, Z. Lu, J. Liu, X. Lei, Z. Chang, L. Luo, X. Sun, Metal oxide and hydroxide nanoarrays: hydrothermal synthesis and applications as supercapacitors and nanocatalysts, Prog. Nat. Sci. 23 (2013) 351-366.

[47] Q. Yang, Z. Lu, Z. Chang, W. Zhu, J. Sun, J. Liu, X. Sun, X. Duan, Hierarchical Co_3O_4 nanosheet@ nanowire arrays with enhanced pseudocapacitive performance, RSC Adv. 2 (2012) 1663-1668.

[48] Z. Lu, Q. Yang, W. Zhu, Z. Chang, J. Liu, X. Sun, D. G. Evans, X. Duan, Hierarchical Co_3O_4@Ni-Co-O supercapacitor electrodes with ultrahigh specific capacitance per area, Nano Res. 5 (2012) 369-378.

[49] J. Sun, Y. Li, X. Liu, Q. Yang, J. Liu, X. Sun, D. G. Evans, X. Duan, Hierarchical cobalt iron oxide nanoarrays as structured catalysts, Chem. Commun. 48 (2012) 3379.

[50] S. N. Nayak, C. P. Bhasin, M. G. Nayak, A review on microwave-assisted transesterification processes using various catalytic and non-catalytic systems, Renew. Energ. 143 (2019) 1366-1387.

[51] J. X. Feng, S. H. Ye, H. Xu, Y. X. Tong, G. R. Li, Design and synthesis of FeOOH/CeO_2 heterolayered nanotube electrocatalysts for the oxygen evolution reaction, Adv. Mater. 28 (2016) 4698-4703.

[52] L. Xu, Q. Jiang, Z. Xiao, X. Li, J. Huo, S. Wang, L. Dai, Plasma-engraved Co_3O_4 nanosheets with oxygen vacancies and high surface area for the oxygen evolution

reaction, Angew. Chem. Int. Ed. 128 (2016) 5363-5367.

[53] D. E. Brown, M. N. Mahmood, M. C. M. Man, A. K. Turner, Preparation and characterization of low overvoltage transition metal alloy electrocatalysts for hydrogen evolution in alkaline solutions. Electrochim. Acta 29 (1984): 1551-1556.

[54] M. Fang, W. Gao, G. Dong, Z. Xia, S. Yip, Y. Qin, Y. Qu, J. C. Ho, Hierarchical NiMo-based 3D electrocatalysts for highly-efficient hydrogen evolution in alkaline conditions. Nano Energy 27 (2016) 247-254.

[55] J. Deng, P. Ren, D. Deng, L. Yu, F. Yang, X. Bao, Highly active and durable non-precious-metal catalysts encapsulated in carbon nanotubes for hydrogen evolution reaction. Energy Environ. Sci. 7 (2014): 1919-1923.

[56] J. Deng, P. Ren, D. Deng, X. Bao, Enhanced electron penetration through an ultrathin graphene layer for highly efficient catalysis of the hydrogen evolution reaction. Angew. Chem. Int. Ed. Engl. 54 (2015) 2100-2104.

[57] X. Chia, A. Y. S. Eng, A. Ambrosi, A. M. Tan, M. Pumera, Electrochemistry of nanostructured layered transition-metal dichalcogenides. Chem. Rev. 115 (2015) 11941-11966.

[58] R. Sun, M. K. Y. Chan, G. Ceder, First-principles electronic structure and relative stability of pyrite and marcasite: Implications for photovoltaic performance. Phys. Rev. B 83 (2011) 235311.

[59] N. Jiang, Q. Tang, M. Sheng, B. You, D. Jiang, Y. Sun, Nickel sulfides for electrocatalytic hydrogen evolution under alkaline conditions: a case study of crystalline NiS, NiS_2, and Ni_3S_2 nanoparticles. Catal. Sci. Technol. 6 (2016) 1077-1084.

[60] X. Shang, K. L. Xiao, Y. Rao, B. Dong, J. Q. Chi, Y. R. Liu, X. Li, Y. M. Chai, C. G. Liu, In situ cathodic activation of V-incorporated Ni_xS_y nanowires for enhanced hydrogen evolution. Nanoscale 9 (2017): 12353-12363.

[61] H. Du, R. Kong, F. Qu, L. Lu, Enhanced electrocatalysis for alkaline hydrogen evolution by Mn doping in a Ni_3S_2 nanosheet array. Chem. Commun. 54 (2018) 10100-10103.

[62] H. Vrubel, X. Hu, Molybdenum boride and carbide catalyze hydrogen evolution in both acidic and basic solutions." Angew. Chem. Int. Ed. Engl. 51 (2012) 12703-12706.

[63] G. Giordano, C. Erpen, W. Yao, M. Antonietti, Synthesis of Mo and W carbide and nitride nanoparticles via a simple “urea glass” route. Nano lett. 8 (2008) 4659-4663.

[64] K. A. Stoerzinger, O. Diaz-Morales, M. Kolb, R. R. Rao, R. Frydendal, L. Qiao, X. R. Wang, N. B. Halck, J. Rossmeisl, H. A. Hansen, T. Vegge, I. E. L. Stephens, M. T. M. Koper, Y. Shao-Horn, Orientation-dependent oxygen evolution on RuO_2 without lattice exchange, ACS Energy Lett. 2 (2017) 876-881.

[65] H. Y. Wang, C. C. Weng, J. T. Ren, Z. Y. Yuan, An overview and recent advances in electrocatalysts for direct seawater splitting, Front. Chem. Sci. Eng. 15 (2021) 1408-1426.

[66] K. Kishor, S. Saha, A. Parashtekar, R. G. S. Pala, Increasing chlorine selectivity through weakening of oxygen adsorbates at surface in Cu doped RuO_2 during seawater electrolysis, J. Electrochem. Soc. 165 (2018) J3276-J3280.

[67] X. Zheng, M. Qin, S. Ma, Y. Chen, H. Ning, R. Yang, S. Mao, Y. Wang, Strong oxide-support interaction over IrO_2/V_2O_5 for efficient pH-universal water splitting, Adv. Sci. 9 (2022) 2104636.

[68] P. K. L. Tran, D. T. Tran, D. Malhotra, S. Prabhakaran, D. H. Kim, N. H. Kim, J. H. Lee, Highly effective freshwater and seawater electrolysis enabled by atomic Rh-modulated Co-CoO lateral heterostructures, Small 17 (2021) 2103826.

[69] Y. Zhu, X. Liu, S. Jin, H. Chen, W. Lee, M. Liu, Y. Chen, Anionic defect engineering of transition metal oxides for oxygen reduction and evolution reactions, J.

Mater. Chem. A 7 (2019) 5875-5897.

[70] F. Jiao, H. Frei, Nanostructured manganese oxide clusters supported on mesoporous silica as efficient oxygen-evolving catalysts, Chem. Commun. 46 (2010) 2920.

[71] M. S. El-Deab, M. I. Awad, A. M. Mohammad, T. Ohsaka, Enhanced water electrolysis: Electrocatalytic generation of oxygen gas at manganese oxide nanorods modified electrodes, Electrochem. Commun. 9 (2007) 2082-2087.

[72] K. Mette, A. Bergmann, J. P. Tessonnier, M. Hävecker, L. Yao, T. Ressler, R. Schlögl, P. Strasser, M. Behrens, Nanostructured manganese oxide supported on carbon nanotubes for electrocatalytic water splitting, ChemCatChem 4 (2012) 851-862.

[73] H. Wang, J. Ying, Y. X. Xiao, J. B. Chen, J. H. Li, Z. Z. He, H. J. Yang, X. Y. Yang, Ultrafast synthesis of Cu_2O octahedrons inlaid in Ni foam for efficient alkaline water/seawater electrolysis, Electrochem. Commun. 134 (2022) 107177.

[74] Q. Zhao, Z. Yan, C. Chen, J. Chen, Spinels: controlled preparation, oxygen reduction/evolution reaction application, and beyond, Chem. Rev. 117 (2017) 10121-10211.

[75] T. Maiyalagan, K. A. Jarvis, S. Therese, P. J. Ferreira, A. Manthiram, Spinel-type lithium cobalt oxide as a bifunctional electrocatalyst for the oxygen evolution and oxygen reduction reactions, Nat. Commun. 5 (2014) 3949.

[76] C. Wei, Z. Feng, G. G. Scherer, J. Barber, Y. Shao-Horn, Z. J. Xu, Cations in octahedral sites: a descriptor for oxygen electrocatalysis on transition-metal spinels, Adv. Mater. 29 (2017) 1606800.

[77] K. Huang, Y. Sun, Y. Zhang, X. Wang, W. Zhang, S. Feng, Hollow-structured metal oxides as oxygen-related catalysts, Adv. Mater. 31 (2019) 1801430.

[78] Yang, Y. Wang, J. Yang, Y. Pang, X. Zhu, Y. Lu, Y. Wu, J. Wang, H. Chen, Z. Kou,

Z. Shen, Z. Pan, J. Wang, Quench-induced surface engineering boosts alkaline freshwater and seawater oxygen evolution reaction of porous $NiCo_2O_4$ nanowires, Small 18 (2022) 2106187.

[79] B. Debnath, S. Parvin, H. Dixit, S. Bhattacharyya, Oxygen-defect-rich cobalt ferrite nanoparticles for practical water electrolysis with high activity and durability, ChemSusChem 13 (2020) 3875-3886.

[80] N. Han, M. Race, W. Zhang, R. Marotta, C. Zhang, A. Bokhari, J. J. Klemeš, Perovskite and related oxide-based electrodes for water splitting, J. Clean. Prod. 318 (2021) 128544.

[81] C. Sun, J. A. Alonso, J. Bian, Recent advances in perovskite-type oxides for energy conversion and storage applications, Adv. Energy Mater. 11 (2021) 2000459.

[82] J. Suntivich, K. J. May, H. A. Gasteiger, J. B. Goodenough, Y. Shao-Horn, A perovskite oxide optimized for oxygen evolution catalysis from molecular orbital principles, Science 334 (2011) 1383-1385.

[83] S. Chen, X. Zhang, J. Zhao, Y. Zhang, G. Kong, Q. Li, N. Li, Y. Yu, N. Xu, J. Zhang, K. Liu, Q. Zhao, J. Cao, J. Feng, X. Li, J. Qi, D. Yu, J. Li, P. Gao, Atomic scale insights into structure instability and decomposition pathway of methylammonium lead iodide perovskite, Nat. Commun. 9 (2018) 4807.

[84] S. Liu, C. Sun, J. Chen, J. Xiao, J. L. Luo, A high-performance Ruddlesden-popper perovskite for bifunctional oxygen electrocatalysis, ACS Catal. 10 (2020) 13437-13444.

[85] Y. Zhu, Q. Lin, Z. Hu, Y. Chen, Y. Yin, H. A. Tahini, H. Lin, C. Chen, X. Zhang, Z. Shao, H. Wang, Self-assembled Ruddlesden-popper/perovskite hybrid with lattice-oxygen activation as a superior oxygen evolution electrocatalyst, Small 16 (2020) 2001204.

[86] H. Zhang, D. Guan, Z. Hu, Y. C. Huang, X. Wu, J. Dai, C. L. Dong, X. Xu, H. J.

Lin, C. T. Chen, W. Zhou, Z. Shao, Exceptional lattice-oxygen participation on artificially controllable electrochemistry-induced crystalline-amorphous phase to boost oxygen-evolving performance, Appl. Catal. B 297 (2021) 120484.

[87] F. Liu, R. Hu, H. Qiu, H. Miao, Q. Wang, J. Yuan, Constructing high-activity Cobalt-based Perovskite hybrid by a top-down phase evolution method for the direct seawater electrolysis anode, J. Alloys and Compd. 913 (2022) 165342.

[88] C. Luan, G. Liu, Y. Liu, L. Yu, Y. Wang, Y. Xiao, H. Qiao, X. Dai, X. Zhang, Structure effects of 2D materials on α-nickel hydroxide for oxygen evolution reaction. ACS Nano. 12 (2018) 3875-3885.

[89] L. Chen, H. Zhang, L. Chen, X. Wei, J. Shi, M. He, Facile synthesis of Cu doped cobalt hydroxide (Cu-$Co(OH)_2$) nano-sheets for efficient electrocatalytic oxygen evolution. J. Mater. Chem. A 5 (2017) 22568-22575.

[90] L. Trotochaud, S. L. Young, J. K. Ranney, S. W. Boettcher, Nickel-iron oxyhydroxide oxygen-evolution electrocatalysts: the role of intentional and incidental iron incorporation. J. Am. Chem. Soc. 136 (2014) 6744-6753.

[91] D. Friebel, Daniel, M. W. Louie, M. Bajdich, K. E. Sanwald, Y. Cai, A. M. Wise, M. J. Cheng, D. Sokaras, T. C. Weng, R. Alonso-Mori, R. C. Davis, J. R. Bargar, J. K. Nørskov, A. Nilsson, A. T. Bell, Identification of highly active Fe sites in (Ni, Fe) OOH for electrocatalytic water splitting." J. Am. Chem. Soc. 137 (2015) 1305-1313.

[92] M. B. Stevens, C. D. M. Trang, L. J. Enman, J. Deng, S. W. Boettcher, Reactive Fe-sites in Ni/Fe (oxy)hydroxide are responsible for exceptional oxygen electrocatalysis activity. J. Am. Chem. Soc. 139 (2017) 11361-11364.

[93] Z. S. Wu, G. Zhou, L. C. Yin, W. Ren, F. Li, H. M. Cheng, Graphene/metal oxide composite electrode materials for energy storage, Nano Energy 1 (2012) 107-131.

[94] J. E. Bennett, Electrodes for generation of hydrogen and oxygen from seawater,

Int. J. Hydrog. Energy 5 (1980) 401-408.

[95] L. Bigiani, D. Barreca, A. Gasparotto, T. Andreu, J. Verbeeck, C. Sada, E. Modin, O. I. Lebedev, J. R. Morante, C. Maccato, Selective anodes for seawater splitting via functionalization of manganese oxides by a plasma-assisted process, Appl. Catal. B 284 (2021) 119684.

[96] L. Li, G. Zhang, B. Wang, D. Zhu, D. Liu, Y. Liu, S. Yang, Fe_2O_3/NiO interface for the electrochemical oxygen evolution in seawater and domestic sewage, ACS Appl. Mater. Interfaces 13 (2021) 37152-37161.

[97] H. Zhang, S. Geng, M. Ouyang, H. Yadegari, F. Xie, D. J. Riley, A self-reconstructed bifunctional electrocatalyst of pseudo-amorphous nickel carbide@iron oxide network for seawater splitting, Adv. Sci. 9 (2022) 2200146.

[98] W. H. Huang, C. Y. Lin, Iron phosphate modified calcium iron oxide as an efficient and robust catalyst in electrocatalyzing oxygen evolution from seawater, Faraday Discuss. 215 (2019) 205-215.

[99] Q. Zhou, L. Liao, H. Zhou, D. Li, D. Tang, F. Yu, Innovative strategies in design of transition metal-based catalysts for large-current-density alkaline water/seawater electrolysis, Mater. Today Phys. 26 (2022) 100727.

[100] G. Liu, Y. Xu, T. Yang, L. Jiang, Recent advances in electrocatalysts for seawater splitting, Nano Materials Science (2020).

[101] K. Fujimura, T. Matsui, H. Habazaki, A. Kawashima, N. Kumagai, K. Hashimoto, The durability of manganese-molybdenum oxide anodes for oxygen evolution in seawater electrolysis, Electrochim. Acta 45 (2000) 2297-2303.

[102] T. Matsui, H. Habazaki, A. Kawashima, K. Asami, N. Kumagai, K. Hashimoto, Anodically deposited manganese-molybdenum-tungsten oxide anodes for oxygen evolution in seawater electrolysis, J. Appl. Electrochem. 32 (2002) 993-1000.

[103] N. A. A. Ghany, N. Kumagai, S. Meguro, K. Asami, K. Hashimoto, Oxygen evolution anodes composed of anodically deposited Mn-Mo-Fe oxides for seawater electrolysis, Electrochim. Acta 48 (2002) 21-28.

[104] A. A. El-Moneim, Mn-Mo-W-oxide anodes for oxygen evolution during seawater electrolysis for hydrogen production: effect of repeated anodic deposition, Int. J. Hydrog. Energy 36 (2011) 13398-13406.

[105] L. Li, G. Zhang, B. Wang, S. Yang, Constructing the Fe/Cr double (oxy) hydroxides on Fe_3O_4 for boosting the electrochemical oxygen evolution in alkaline seawater and domestic sewage, Appl. Catal. B 302 (2022) 120847.

CHAPTER 2 Heterojunction engineering of Ni_3S_2/NiS nanowire for electrochemical hydrogen evolution

2.1. Introduction

The rapid consumption and fast dwindling of traditional fossil fuels for energy is resulting in the critical energy and environmental problems throughout the world [1, 2]. As a clean energy resource, hydrogen has drawn great attention for its potential to replace the traditional fossil fuel [3-6]. Currently, hydrogen is mainly extracted from the reforming of traditional hydrocarbons such as diesel, methane and methanol, coal gasification and other processes relating to the fossil fuels [7, 8]. However, among those processes, massive environmentally-unfriendly by-products such as CO, CO_2 and NO_2 are usually generated along the hydrogen production. Currently, electrocatalytic water splitting is competitive owing to its high efficiency with the applications of renewable energy from wind and solar panel. Especially, alkaline water electrolysis has been receiving special attention due to its unique advantages, including reactant availability, good manufacturing safety, stable operation, and high production capacity [9-12].

In the alkaline media, hydrogen evolution reaction (HER) is the cathode reaction in the water splitting [13, 14], in which a Volmer step ($H_2O+e^- \rightarrow H_{ads}+ OH^-$) always occurs by the reduction of a water molecule, adsorbed on the surface of the electrode, into an adsorbed hydrogen atom and a negatively-charged hydroxide anion. Subsequently, the adsorbed hydrogen atom either combines with another adsorbed hydrogen atom to generate a hydrogen molecule, leading to the surface reaction as $H_{ads} +H_{ads} \rightarrow H_2$ (Tafel step), or is attacked by another water molecule to produce a hydroxide anion and a hydrogen molecule as $H_{ads}+H_2O+ e- \rightarrow H_2+OH^-$ (Heyrovsky step). Herein, the electrocatalytic HER through either the Volmer-Heyrovsky or the Volmer-Tafel

mechanisms depends on the catalyst surface state. Although the HER in alkaline solution involves simple reactants with only two electrons for each hydrogen molecule, multiple elemental reactions always induce an accumulation of energy barriers and result in slow kinetics [15-17]. It is already known that the platinum (Pt)-based materials are the most superb electrocatalysts for HER, standing out among all HER catalysts with almost no overpotential at the onset and rapid current increase over the voltage increment [18, 19]. However, the scarcity and high cost of Pt significantly limit their widespread application. Thus, it is imperative to develop economical and efficient electrocatalysts with comparable electrocatalytic HER performance as the Pt-based materials.

Various non-noble active materials such as sulfides [20, 21], carbides [22, 23], selenides [24, 25] and phosphides [26, 27] have been attracting immense interests due to the earth abundance and high catalytic performance and excellent HER activity under alkaline conditions. Among them, nanostructured transition metal sulfides (TMSs) have been reported as one family of attractive electrocatalysts due to their unique electronic properties [28-30]. As a representative of TMSs, nickel sulfide-based nanomaterials always exhibit excellent catalytic properties. However, nickel sulfides contain several different crystalline structures as well as atomic configurations, which include NiS, Ni_3S_4, NiS_2, Ni_3S_4, Ni_7S_6, Ni_9S_8, and so on [31-33]. In order to further improve their catalytic performances for HER, massive efforts including creating more active sites via increasing phase boundaries among different components and boosting the H atom adsorption and desorption kinetics on the surface via adjusting the charge distribution between the components have been made [34, 35]. For example, Xiao *et al.* [36] created the NiS/Ni_2P nanosheet array heterostructure via interface engineering, which showed outstanding electrochemical activity attributing to the strong electronic

interaction between the NiS and Ni_2P. Zheng *et al.* [37] prepared NiS_2/MoS_2 catalysts with a nanoflake-nanowire heterostructure, in which MoS_2 was highly dispersed inside NiS_2 framework. Its unique heterostructure significantly enhanced the HER activity due to the abundant nano-interface and defects. Therefore, it is important to obtain heterostructure in the electrocatalysts. Our previous work proved that the surface engineering could improve the catalysis performance [38, 39]. In this study, one-dimensional (1D) nickel sulfide nanowire was firstly grown on the nickel foam (NF), and then epitaxial growth of NiS on the surface of 1D Ni_3S_2 nanowire was performed to construct a Ni_3S_2/NiS heterojunction interface for exposing more crystal planes and active sites via a solid-state phase transformation strategy. Based on the results of density functional theory (DFT) calculation, it is found that the Ni_3S_2/NiS heterostructure leads to a favorable down-shifting of the d-band center owing to the strong charge transfer between the interface of the Ni_3S_2/NiS. Moreover, benefitting from the strong electronic interaction in Ni_3S_2/NiS, the intrinsic activity and durability of the electrocatalyst were both improved. As expected, the fabricated Ni_3S_2@NiS-250/NF electrode showed a robust HER catalytic performance with a low overpotential of 129 mV to deliver the current density of 10 mA cm^{-2} with a small Tafel slope (75.5 mV dec^{-1}) in 1 M KOH solution, and superior durability for at least 50 h.

2.2 Experimental section

2.2.1 Chemicals and Materials

Nickel (II) nitrate ($Ni(NO_3)_2{\cdot}6H_2O$, 98%), urea ($CO(NH_2)_2$, ≥ 99.0%), potassium hydroxide (KOH, 85.0%), ammonium fluoride (NH_4F, ≥96%), sulfur powder (S, ≥98.0%) and concentrated hydrochloric acid (HCl, 37%) were purchased from Wako, Japan. Commercial 20% Pt/C and Nafion perfluorinated resin solution (45% containing water) were obtained from Aldrich. The NF (thickness: 1.5 mm, number of pores per inch: 110 and the bulk density: 0.23 g/cm^3) was purchased from MTI, Japan.

Preparation of Ni_3S_2 nanowire-based electrode

Prior to the hydrothermal synthesis process, the NF (2×2 cm^2) was firstly ultrasonicated in 3 M HCl solution for 1 h to move out nickel oxide on the surface, then rinsed with deionized (DI) water and ethanol successively for several times and finally dried in a vacuum oven at 60 ℃ overnight.

Typically, 0.2 mmol of Ni $(NO_3)_2 \cdot 6H_2O$, 0.8 mmol of NH_4F and 1 mmol of urea were dissolved in 20 ml of DI water with magnetically stirring for 1 h and then the transparent solution was transferred to a Teflon-lined stainless-steel autoclave with a capacity of 50 ml. After reacting at 120 ℃ for 24 h, the nickel hydroxide precursor was formed on the NF substrate. Thereafter, the nickel hydroxide coated NF was sealed in a quartz boat with 0.1 g of sulfur powder, and then heated at 350 ℃ for 2 h. As such, Ni_3S_2 nanowires coated NF (Ni_3S_2/NF) electrode was obtained.

Preparation of Ni_3S_2 nanowire @NiS/NF electrode

Epitaxial growth of NiS on the surface of 1D Ni_3S_2 nanowire on NF was performed by direct calcination of Ni_3S_2/NF electrode in air at different temperatures, i.e., 200 ℃, 250 ℃ and 300 ℃. The obtained electrodes are denoted as Ni_3S_2@NiS-200/NF, Ni_3S_2@NiS-250/NF and Ni_3S_2@NiS-300/NF. The mass loadings of all as-prepared sample are 123 ± 5.6 mg.

2.2.2 Material Characterizations

Crystalline structure of the prepared electrocatalyst was determined by X-ray diffraction (Rigaku Smartlab Diffractometer, Japan) with a Cu-Kα as the radiation source. The scanning rate was 8° min^{-1} in the range of 10° to 80° and the phase identification was verified through Joint Committee on Powder Diffraction Stander (JCPDS). Morphology and nanostructure were characterized by a scanning electron microscope (SEM, SU-8100, Hitachi, Japan) and a transmission electron microscope

(TEM, JEM-2100F, JEOL, Tokyo, Japan). X-ray photoelectron spectrum (XPS) was obtained by a VG Scientific ESCALab250i-XL instrument with an Al Kα source and C *1s* (284.8 eV) was used as reference.

2.2.3 Electrochemical performance tests

Electrochemical measurement was conducted on a three-electrode electrochemical workstation (Versa STAT4, Princeton, USA) in 1 M KOH solution (pH=14). The surface area exposed to electrolyte is 1×1 cm^2. Linear sweep voltammetry (LSV) curve was conducted with a scan rate of 2 mV/s using a Hg/HgO electrode and a carbon rod electrode were used as the reference and counter electrodes, respectively. All potentials were referenced to a reversible hydrogen electron (RHE) and calculated by $E_{RHE}= E_{Hg/HgO} + (0.098 +0.0592\ pH)$ V. Electrochemical impedance spectroscopy (EIS) was performed at η=200 mV with a frequency range from 0.01 to 100 kHz and an amplitude of 10 mV. While, electrochemical double-layer capacitances (C_{dl}) were obtained by measuring the cyclic voltammetry (CVs) at different scan rates (5, 10, 15 and 20 mV/s) at the applied potential in the range of 0.3~0.5 V (vs. RHE).

2.2.4 Computational method

The present first principle DFT calculations were performed by Vienna Ab initio Simulation Package (VASP) with the projector augmented wave (PAW) method. The exchange-functional was treated using the generalized gradient approximation (GGA) of Perdew-Burke-Ernzerhof (PBE) function. The energy cutoff for the plane wave basis expansion was set to 450 eV and the force on each atom less than 0.05 eV/Å was set for convergence criterion of geometry relaxation. 20 Å vacuum was added along the c direction for all systems in order to avoid the interaction between periodic structures. The Hubbard U (DFT+U) correction for a 3d-transition metal was set as a value of 3.0 eV in all calculation. The Brillouin zone integration was performed using 3×3×1. The self-consistent calculations applied a convergence energy threshold of 10^{-4} eV.

The Free energies of the adsorption atomic hydrogen (ΔGH*) was calculated by using equation:

$\Delta G_{H^*}=\Delta E_{DFT}+\Delta E_{ZPE}-T\Delta S$

where ΔE_{DFT} is the DFT energy difference and the ΔE_{ZPE} and $T\Delta S$ terms were obtained based on vibration analysis.

2.3. Results and discission

2.3.1 Synthesis and characterization of Ni_3S_2@NiS-250/NF electrode

The fabrication strategy of Ni_3S_2@NiS-250/NF involves three steps as illustrated in **Figure 2.1**. Typically, the hydrothermal treatment of the solution containing Ni ions with the NF substrate at 120 ºC for 24 h led to the formation of nanowire-like nickel hydroxide precursor on the NF. Then, the Ni_3S_2 nanowire coated on NF electrode was obtained by a vulcanization process with sulfur powder. Finally, the epitaxial growth of NiS on the surface of 1D Ni_3S_2 nanowire was realized by controlling the calcination temperature in the air. As such, the Ni_3S_2/NiS electrocatalyst with a heterojunction structure was obtained.

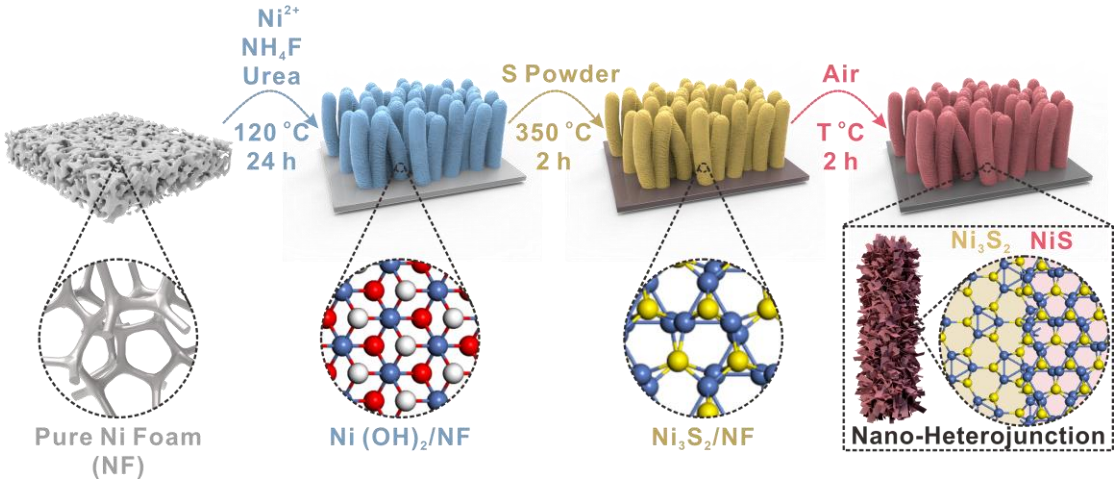

Figure 2.1 Schematic depiction of the fabrication of Ni_3S_2/NF and Ni_3S_2@NiS/NF electrodes

The crystal structure and phase of as-prepared samples were determined by X-ray diffraction (XRD). **Figure 2.2** displays XRD patterns of Ni_3S_2/NF, Ni_3S_2@NiS-200/NF, Ni_3S_2@NiS-250/NF, and Ni_3S_2@NiS-300/NF electrodes. Herein, three strong diffraction peaks at 44.3°, 51.7°, 76.5° correspond to the NF substrate (JCPDS No. 04-0850, **Figure 2.3 a**). For the Ni_3S_2/NF electrode, the characteristic diffraction peaks at 2θ=21.75°, 31.10°, 38.27°, 49.73°, 50.12°, 55.16°, and 55.34° are well assigned to (101), (110), (021), (113), (211), (122), and (300) facets of Ni_3S_2 (JCPDS No. 44-1418), indicating the successful synthesis of Ni_3S_2. It should be noticed that no additional peaks correspond to Ni $(OH)_2$ precursor (**Figure 2.3 b)**, demonstrating that the Ni $(OH)_2$ precursor was completely transformed to Ni_3S_2 during vulcanization. After calcined in the air, from the XRD analysis results of Ni_3S_2@NiS-200/NF, Ni_3S_2@NiS-250/NF and Ni_3S_2@NiS-300/NF, the peaks relating to Ni_3S_2 were also observed. While, the additional peaks at 2θ=18.44°, 30.31°, 32.20°, 35.70°, 40.45°, 48.84°, 50.14°, and 52.64° corresponded to the (110), (101), (300), (021), (211), (131), (410) and (401) planes of NiS (JCPDS No. 12-0041), respectively. These results indicate that the Ni_3S_2@NiS-T (T=200, 250 or 300) should be composed of Ni_3S_2 and NiS. Herein, the phase transition from the Ni_3S_2 to NiS should have occurred by the combination of abundant sulfur atoms in the presence of sulfur powder with oxygen in the air during the calcination, which could lead to the re-crystallization to generate the NiS phase on the surface of Ni_3S_2. While, the phase transition from Ni_3S_2 to NiS during the calcination process may generate the unsaturated or imperfect bonding in each phase of the Ni_3S_2/NiS interface, resulting in the exposing of more active edge sites [40].

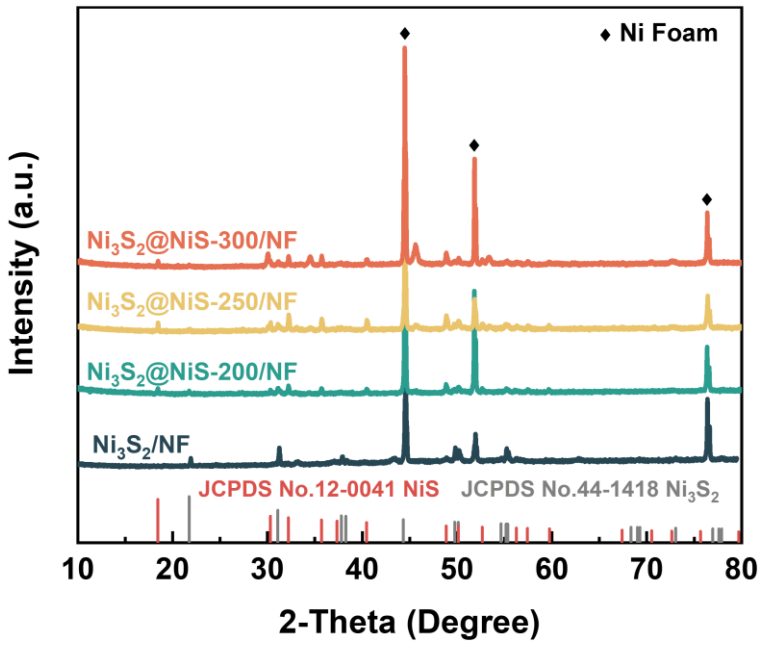

Figure 2.2 XRD patterns of Ni_3S_2/NF, Ni_3S_2@NiS-200/NF, Ni_3S_2@NiS-250/NF and Ni_3S_2@NiS-300/NF electrodes

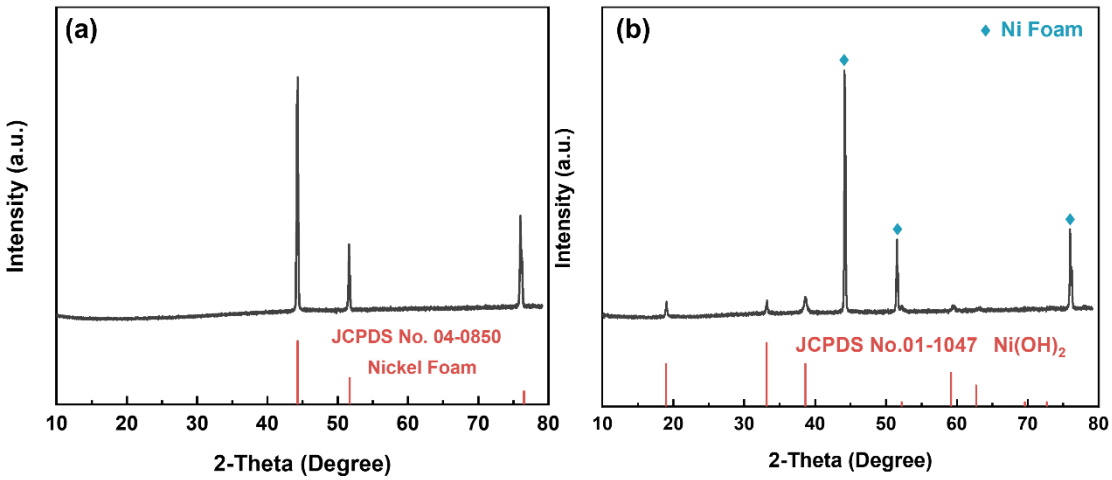

Figure 2.3 XRD pattern of (a) pure nickel foam substrate and (b) $Ni(OH)_2$

Figure 2.4 shows morphologies with different magnifications of as-obtained samples. Comparing the scanning electron microscope (SEM) image of pure NF (**Figure 2.5a**), it is obvious that the morphologies of Ni_3S_2, Ni_3S_2@NiS-200 and Ni_3S_2@NiS-300 also show uniform wire-like shapes (**Figure 2.5c-e**). These nanowires formed ordered nanoarray with a 3D interconnected network. At the same time, ordered nano-arrays of Ni_3S_2@NiS-250/NF were well supported on the surface of NF substrate

(Figure 2.4a and **Figure 2.5b**). An enlarged view (Figure 2.4b) revealed that the diameter of 1D Ni_3S_2 nanowire was about 150 nm. Such a nanowire array structure could expose more active sites and facilitate the mass and electron transfers. In addition, the EDS analysis results shown in Figure 2.4c-e indicated the existence of Ni and S elements, which are distributed uniformly on the Ni_3S_2@NiS-250/NF electrode surface.

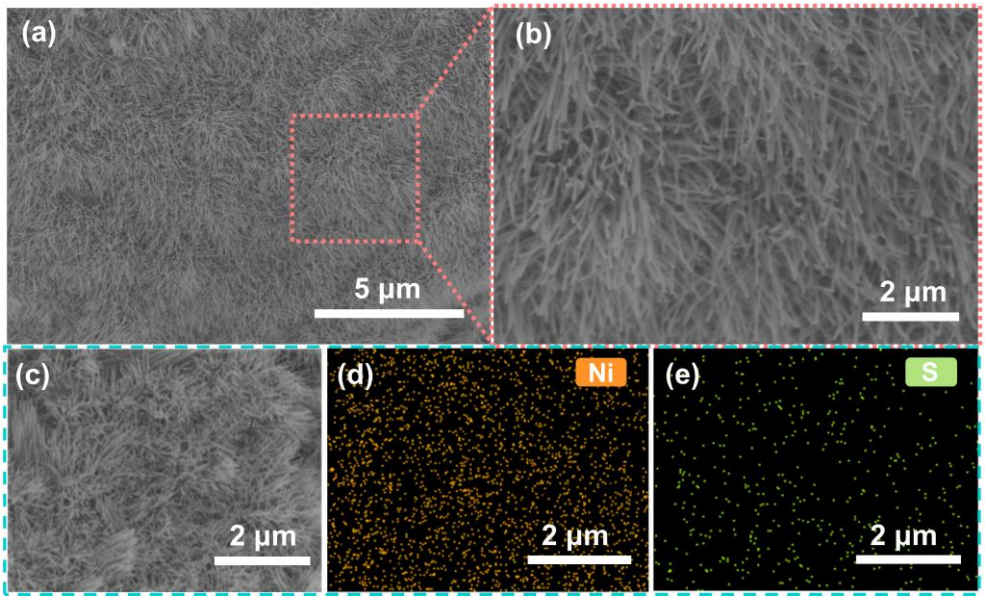

Figure 2.4 (a-b) SEM images of Ni_3S_2@NiS-250/NF and (c-f) corresponding elemental mappings of Ni and S on the Ni_3S_2@NiS-250/NF surface

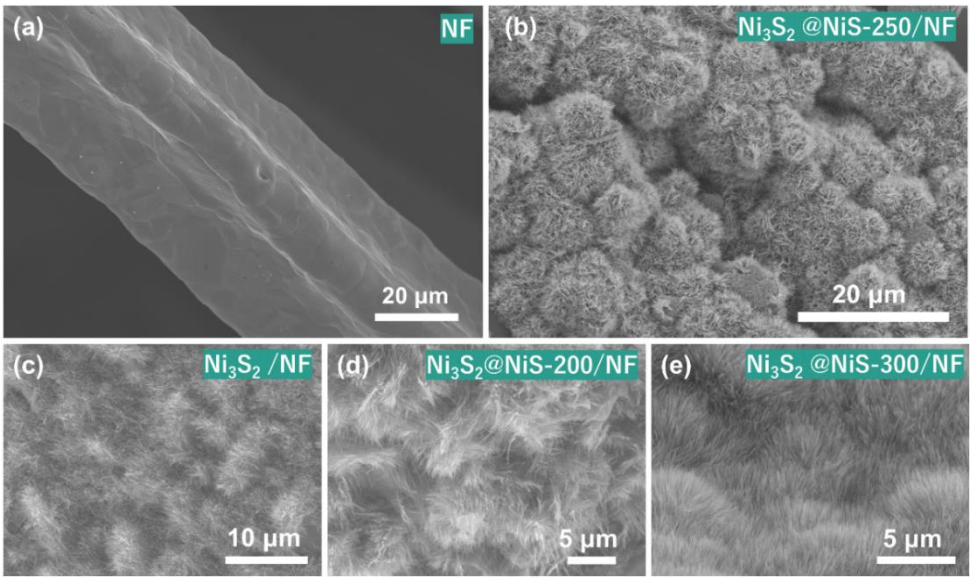

Figure 2.5 SEM images of (a) pure nickel foam, (b) Ni_3S_2@NiS-250/NF in a large scale, (c) Ni_3S_2/NF and (d) Ni_3S_2@NiS-200/NF and (e) Ni_3S_2@NiS-300/NF.

Figure 2.6a-c shows the TEM and high-resolution TEM (HR-TEM) images of the Ni_3S_2@NiS-250/NF electrocatalyst. It exhibited a nanowire structure with a diameter about 150 nm, which is consistent with the results of SEM observation. Besides, Figure 2.6b shows the nanoparticles with about 10-15 nm in size were grown on the surface of the nanowire, which could expose more active sites. The image intensity alone L (in Figure 2.6c) as shown in the profile of Figure 2.6h indicated clearly that the lattice fringes with an interplanar distance of 0.407 nm corresponded to the (101) plane of Ni_3S_2. However, on the edge of Ni_3S_2, the fringes became curvy and disordered due to the lattice reorganization during the calcination process, which could increase the S unsaturated bonds on the interface [41, 42]. Moreover, the interplanar distances of ~0.25 and ~0.22 nm should correspond to the (021) and (211) crystal planes of NiS, respectively, indicating the formation of NiS phase. It is noteworthy that the Ni_3S_2/NiS heterojunction structure should be constructed by the epitaxial growing of NiS on the surface of Ni_3S_2 with the formation of heterojunction interface between Ni_3S_2 and NiS. The EDS analysis further confirmed that the main elements on the electrode were Ni and S (Figure 2.6i) with an atom ratio of Ni and S at 1.266, which is between 1(NiS) and 1.5 (Ni_3S_2), further proving that the Ni_3S_2/NiS heterostructure was formed. Besides, the corresponding elemental mappings also showed that the Ni and S were uniformly distributed on the electrode surface (Figure 2.6 d-g), which indicated that the phase transfer occurred between the Ni_3S_2 and NiS instead of single element (S or Ni) detachment during the calcination process.

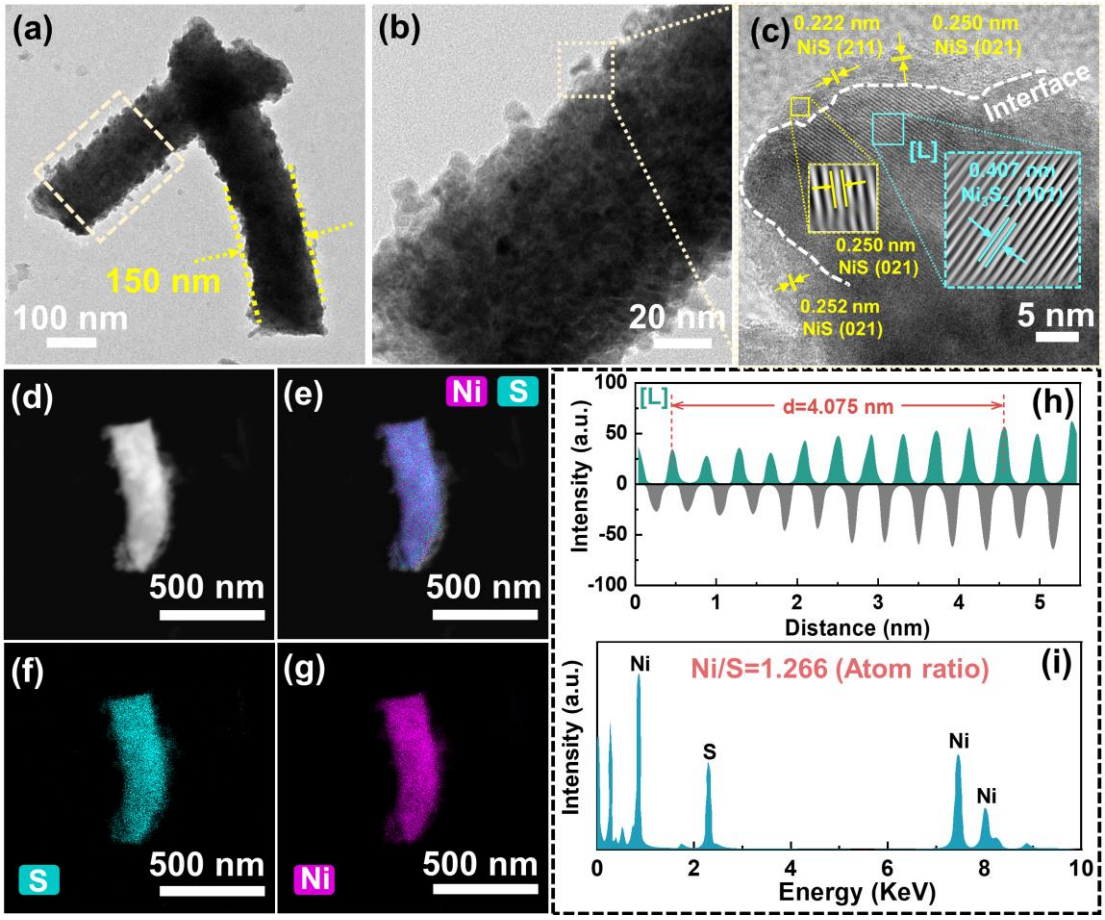

Figure 2.6 (a-b) TEM and (c) HR-TEM images of Ni_3S_2@NiS-250/NF electrocatalyst; (d-g) TEM-EDS mappings of Ni_3S_2@NiS-250/NF electrocatalyst; (h) Image intensity line profiles taken alone the yellow line in Figure 2.6c; (i) the EDS spectrum of Ni_3S_2@NiS-250/NF electrocatalyst.

To further confirm the surface chemical states, XPS spectrum was analyzed (**Figure 2.7**). From the full XPS spectra of Ni_3S_2, Ni_3S_2@NiS-200, Ni_3S_2@NiS-250, and Ni_3S_2@NiS-300 (Figure 2.7a), the C *1s*, S *2p*, and Ni *2p* were observed at about 285, 162, and 855 eV, respectively, indicating that the core levels of Ni and S should exist in the electrocatalysts, which are consistence with the EDS analysis results. The high-resolution Ni *2p* spectra of Ni_3S_2 (b_1), Ni_3S_2@NiS-200 (b_2), Ni_3S_2@NiS-250 (b_3), and Ni_3S_2@NiS-300 (b_4) are shown in Figure 2.7b. Two spin-orbit doublets have a splitting of ~17 eV with a Ni $2p_{3/2}$ to Ni $2p_{1/2}$ ration of 2:1. The species state distributions were analyzed by the deconvolution. As a result, the profiles of Ni *2p* can

be deconvoluted into three peaks, including two species peaks and one satellite peak. It indicated that two different states for Ni were formed on the surface [43, 44]. The peak positions in the interval from 855.55 to 855.91 eV are assigned to Ni^{3+}, which correspond to the Ni_3S_2 [45, 46]. The peaks located at the range of banding energies in the range from about 852.79 to 853.83 eV are related to Ni $2p_{3/2}$ peaks of Ni^{2+}, belonging to the NiS [47, 48]. The binding energies of the corresponding Ni $2p_{3/2}$ peaks are summarized in **Table 2.1**.

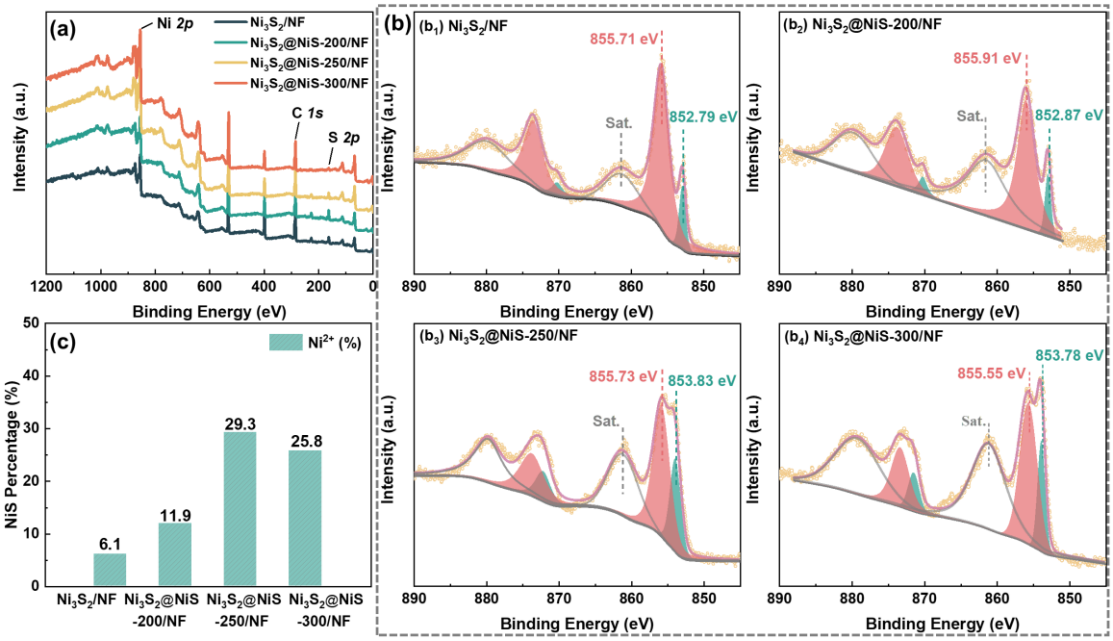

Figure 2.7 (a) Full XPS profiles of Ni_3S_2/NF, Ni_3S_2@NiS-200/NF, Ni_3S_2@NiS-250/NF and Ni_3S_2@NiS-300/NF electrocatalysts; (b) High resolution XPS spectra of Ni *2p* of (b_1) Ni_3S_2/NF, (b_2) Ni_3S_2@NiS-200/NF, (b_3) Ni_3S_2@NiS-250/NF and (b_4) Ni_3S_2@NiS-300/NF electrocatalyst

Moreover, it should be noted that the concentration of the surface Ni^{2+} was increased by the increasing of the calcination temperature in the air, e.g., from 6.1% for Ni_3S_2 to 29.3% for Ni_3S_2@NiS-250/NF as shown in Figure 2.7c. It also indicated that the phase transition can affect the element content as well as the electron density on the surface of nickel sulfide. As the high-resolution S *2p* spectrum of as-prepared samples

shown in **Figure 2.8**, the peaks located at 161.90~162.42 eV are attributed to the S-Ni bonding (Ni_3S_2) and the peak position of S *2p*$_{3/2}$ in the interval from 161.39 to 161.90 eV is assigned to S^{2-}, which is corresponding to the NiS and should be attributed to the surface NiS epitaxial grown on the Ni_3S_2 [49]. Additionally, the extra S *2p* characteristic peaks at 162.53~162.78 eV in Ni_3S_2@NiS-200/NF, Ni_3S_2@NiS-250/NF and Ni_3S_2@NiS-300/NF can be assigned to the unsaturated S atoms in Ni_3S_2/NiS system [41, 50, 51], which could serve as active sites for enriching hydrogen protons and boosting the active process.

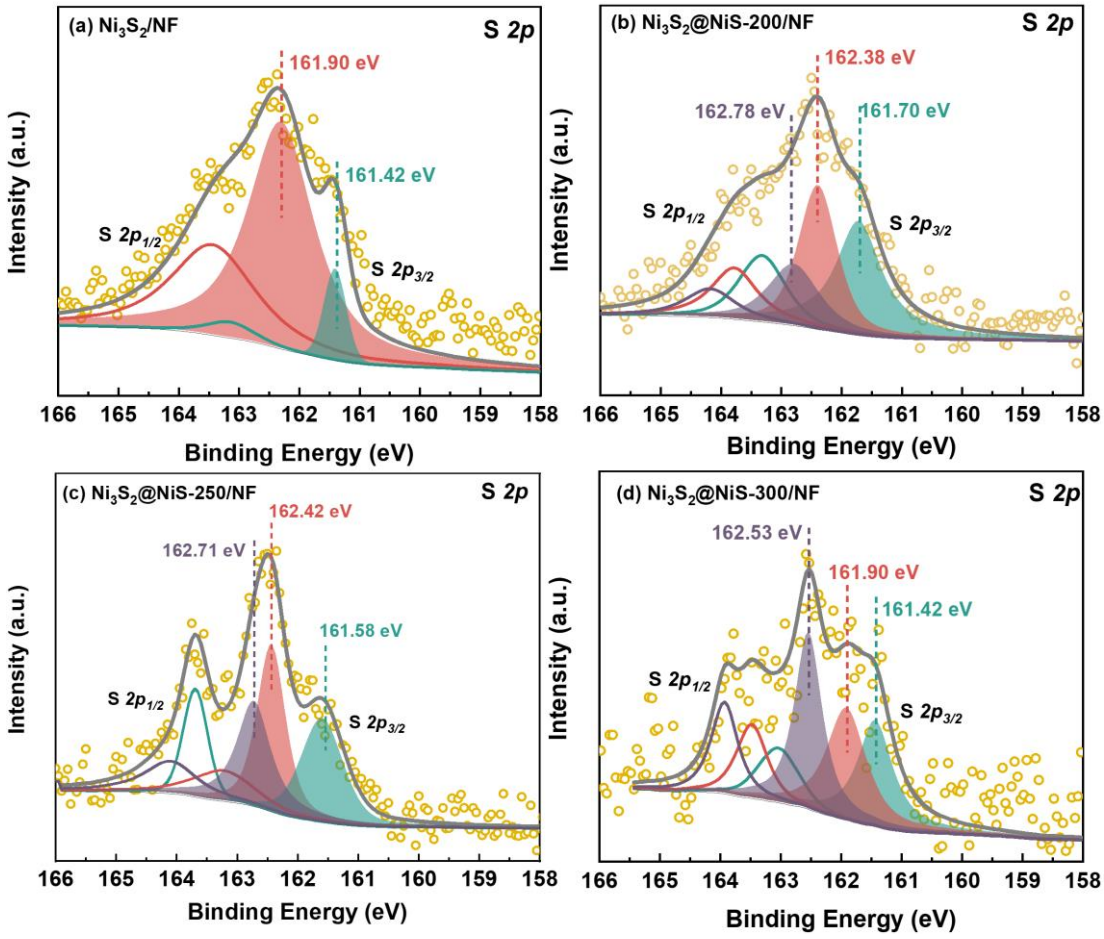

Figure 2.8 High resolution XPS spectra of S *2p* of (a) Ni_3S_2; (b) Ni_3S_2@NiS-200; (c) Ni_3S_2@NiS-250 and (d) Ni_3S_2@NiS-300.

Table 2.1 Ni $2p_{3/2}$ binding energies of Ni_3S_2/NF, Ni_3S_2@NiS-200/NF, Ni_3S_2@NiS-250/NF and Ni_3S_2@NiS-300/NF

Catalysts	Ni $2p_{3/2}$ (eV)		S $2p_{3/2}$ (eV)		
	Ni (III)	Ni (II)	S (II)	S (III)	Unsaturated S
Ni_3S_2/NF	855.71	852.79	161.42	161.90	-
Ni_3S_2@NiS-200/NF	855.91	852.87	161.70	162.38	162.78
Ni_3S_2@NiS-250/NF	855.73	853.83	161.58	162.42	162.71
Ni_3S_2@NiS-300/NF	855.55	853.78	161.42	161.90	162.53

2.3.2 HER performance

Electrocatalytic HER performances of the pure NF, Ni_3S_2/NF, Ni_3S_2@NiS-200/NF, Ni_3S_2@NiS-250/NF, Ni_3S_2@NiS-300/NF and commercial 20 wt% Pt-C were measured in 1 M KOH solution. As shown in **Figures 2.9**a and b, the commercial Pt-C shows excellent activity with ultra-low overpotential while pure nickel foam has poor HER activity. Notably, the Ni_3S_2@NiS-250/NF exhibited the outstanding HER activity, by which the standard current density of 10 mA cm^{-2} was achieved at an overpotential as low as 129 mV, which is smaller than those of the Ni_3S_2/NF (η_{10}=298 mV), Ni_3S_2@NiS-200/NF (η_{10}=227 mV), and Ni_3S_2@NiS-300/NF (η_{10}=187 mV) electrodes, indicating that the ratio of NiS and Ni_3S_2 in the heterostructure could affect the activity. And the corresponding results are summarized in **Table 2.2** Meanwhile, the Ni_3S_2@NiS-250 ranked the top level among those reported Ni-based catalysts (**Table 2.3**).

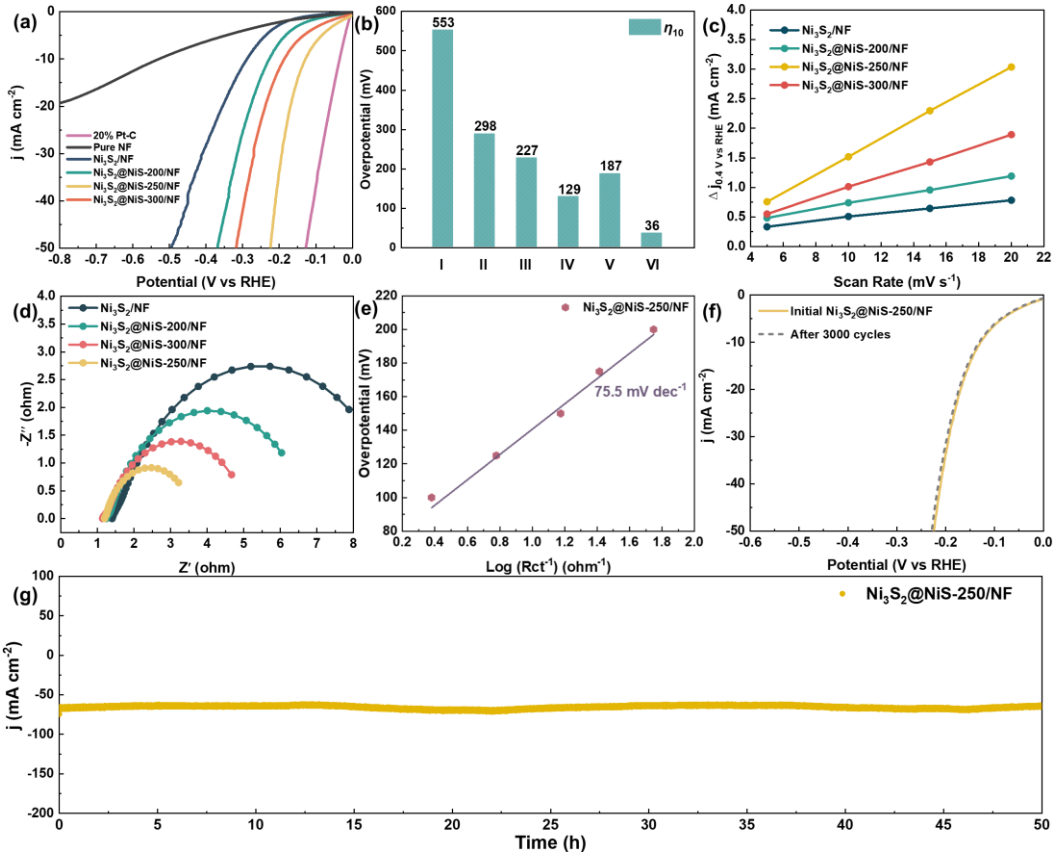

Figure 2.9 (a) Polarization curves of the samples; (b) relationship between overpotentials of NF (I), Ni_3S_2/NF (II), Ni_3S_2@NiS-200/NF (III), Ni_3S_2@NiS-250/NF (IV) Ni_3S_2@NiS-300/NF (V) and Pt-C (VI); (c) Estimation of C_{dl}, data obtained from **Figure 2.10**; (d) the Nyquist plots of electrodes with an applied potential of 200 mV; (e) Tafel plots derived from overpotential and log (R_{ct}), data obtained from **Figure 2.11** (f) durability of the Ni_3S_2@NiS-250/NF modified electrode with an initial polarization curve and after 3000 cycles and (g) Operation stability of the Ni_3S_2@NiS-250/NF electrode running at -250 mV in 1 M KOH solution for 50 h.

Table 2.2 Summary of the HER performances of Ni_3S_2/NF, Ni_3S_2@NiS-200/NF, Ni_3S_2@NiS-250/NF and Ni_3S_2@NiS-300/NF

Catalysts	η_{10} (mV)	Tafel (mV dec^{-1})	C_{dl} (mF cm^{-2})	R_{ct} (Ω)
Ni_3S_2/NF	298	-	29.68	7.7
Ni_3S_2@NiS-200/NF	227	-	46.81	5.5
Ni_3S_2@NiS-250/NF	129	75.5	152.43	2.4
Ni_3S_2@NiS-300/NF	187	-	89	3.9

Table 2.3 Comparison of HER catalytic activities with the reported HER catalysts from Ni-based materials in 1M KOH.

Catalysts	Substrate	η_{10} (mV)	Reference
Ni_3S_2@NiS-250/NF	**NF**	**129**	**This work**
NiS_2 HMSs	GCE	219	*J. Mater. Chem. A* **2017**, *5*, 20985.
$NiMo_3S_4$ hollow nanoplates	GCE	257	*Angew. Chem. Int. Ed.* **2016,** *128*, 15466.
N-C@CoP/Ni_2P	GCE	176	*Int. J. Hydrog. Energy* **2021,** *46*, 8431.
NiS_2 nanosheets	CFP	225	*Int. J. Hydrog. Energy* **2017,** *42*, 17038.
$NiCo_2S_4$ NW/NF	NF	210	*Adv. Funct. Mater.* **2016,** *26*, 4661.
$NiCo_2P_x$/CF	CF	58	*Adv. Mater.* **2017,** *29*, 1605502.
NiO/Co_3O_4	CFP	169.5	*Chem. Commun.* **2019,** *55*, 6515.
$NiCo_2S_4$/Ni_3S_2/NF	NF	111	*Int. J. Hydrog. Energy* **2021,** *46*, 39226.
CuNiS@Ni_2P/NF	NF	144	*Int. J. Hydrog. Energy* **2021,** *46*, 33078.
NiS-$Ni_2P_2S_6$/NF	NF	140	*J. Mater. Chem. A* **2017,** *5*, 22131.
NiS@ NiO /NF	NF	150	*Int. J. Electrochem Sci.* **2020,** *15*, 3563.
NiS/NF	NF	122	*ACS Sustain. Chem. Eng.* **2017,** *5*, 7203.
NiFeVS/NF	NF	161	*Electrochim. Acta.* **2017,** *256*, 241.
NiS_2/CoS_2/MoS_2	NF	112	*Sci. Bull.* **2020,** *65*, 359.
Sn-doped Ni_3S_2	NF	137	*ChemElectroChem* **2017**, *4*, 594.
Ni/Co-S	NF	102	*Electrochim Acta* **2018**, *260*, 82.

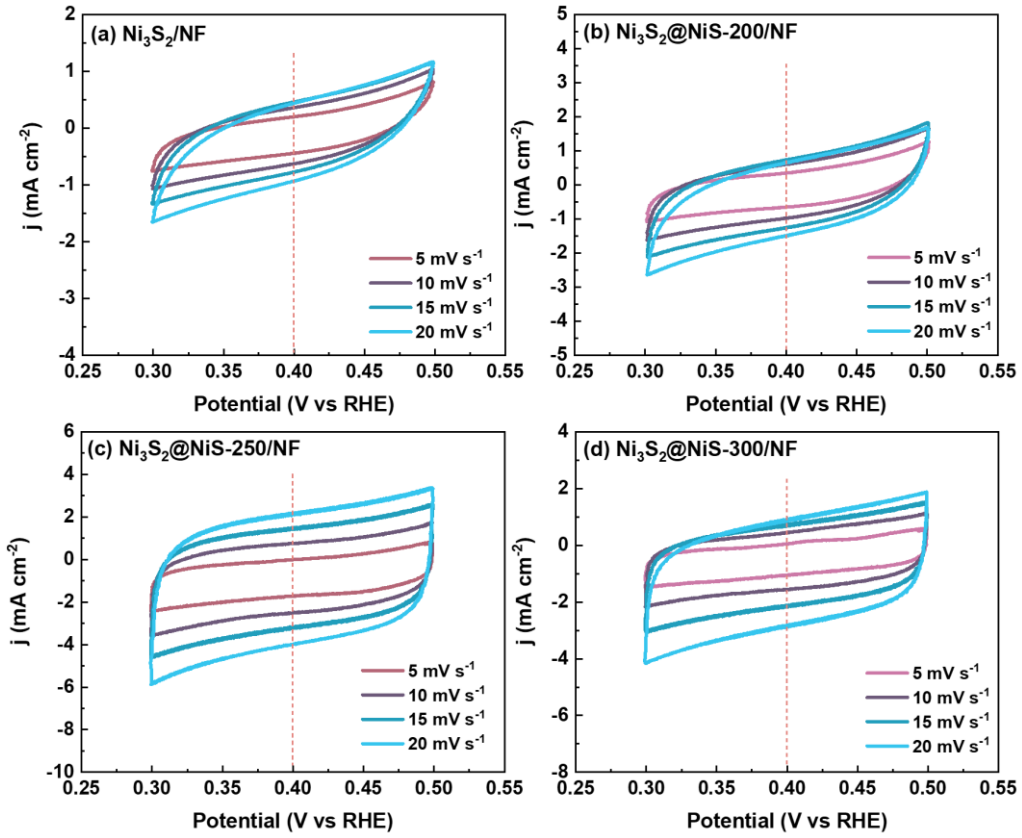

Figure 2.10 Cyclic voltammograms of (a) Ni_3S_2; (b) Ni_3S_2-NiS-200/NF; (c) Ni_3S_2-NiS-250/NF and (d) Ni_3S_2-NiS-300/NF based electrodes with various scan rates in 1 M KOH solution

Estimation of C_{dl} by plotting the current density variation ($\Delta j=(j_a-j_c)/2$ at 400 mV) versus RHE based on the data obtained from **Figure 2.10** was performed for comparison (Figure 2.9c). As a result, Ni_3S_2@NiS-250/NF had the largest C_{dl} value (152.43 mF cm^{-2}) among the all as-prepared electrodes (89 mF cm^{-2} for Ni_3S_2@NiS-300/NF, 46.81 mF cm^{-2} for Ni_3S_2@NiS-200/NF and 29.68 mF cm^{-2} for Ni_3S_2/NF), indicating that the Ni_3S_2@NiS-250/NF could expose more catalytic active sites on the surface. In addition, the electrochemical impedance spectroscopy (EIS) performance was evaluated, as shown in Figure 2.9d. The size of the semicircle on the Z′-axis represented the value of R_{ct}, which is related to the charge transfer resistance, indicating the conductivity of electrocatalysts. It can be observed that the Ni_3S_2@NiS-250/NF

possessed the minimal R_{ct} of about 2.4 Ω among the as-prepared electrodes, followed by Ni_3S_2@NiS-300/NF (3.9 Ω), Ni_3S_2@NiS-200/NF (5.5 Ω), and Ni_3S_2/NF (7.7 Ω). A smaller R_{ct} value could result in a faster reaction rate for HER. Thus, the Ni_3S_2@NiS-250/NF should be more beneficial for the fast electrocatalytic Faradaic process.

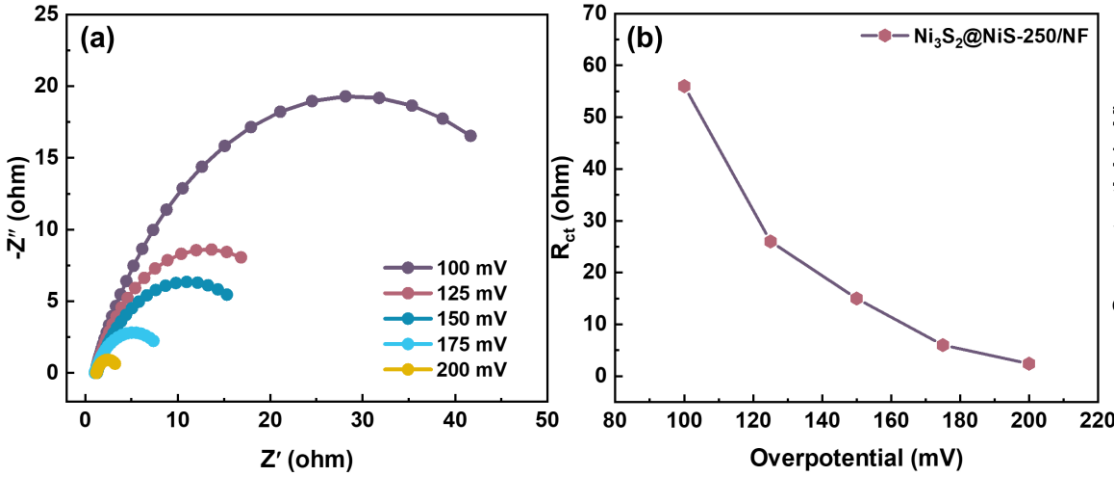

Figure 2.11 (a) Nyquist plots of the Ni_3S_2@NiS-250/NF measured at various overpotential (100, 125, 150, 175 and 200 mV); (b) Dependence of the charge transfer resistance (R_{ct}) on the overpotential.

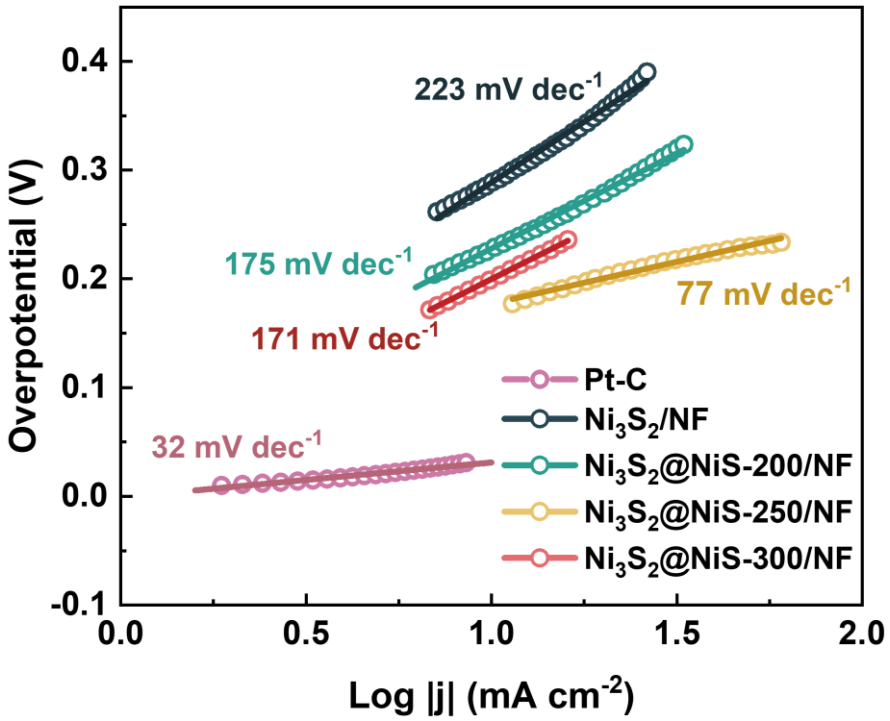

Figure 2.12 Tafel slope of as-prepared samples and Pt/C.

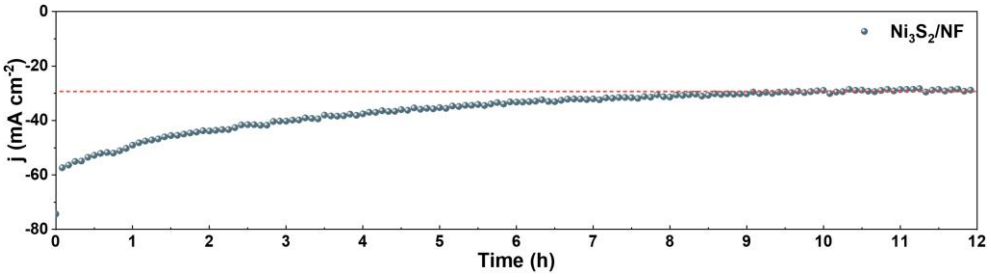

Figure 2.13 Operation stability of the Ni_3S_2/NF running in 1M KOH solution for 12h

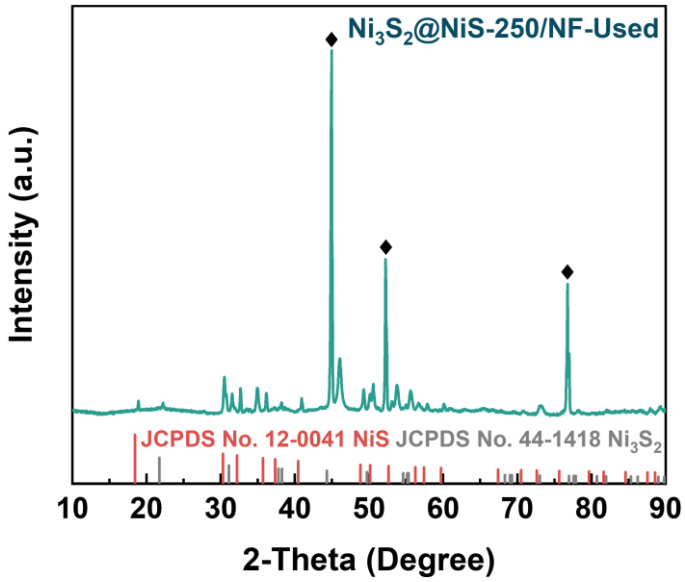

Figure 2.14 the XRD pattern of Ni_3S_2@NiS-250/NF after the stability test in 1 M KOH solution for 50 h

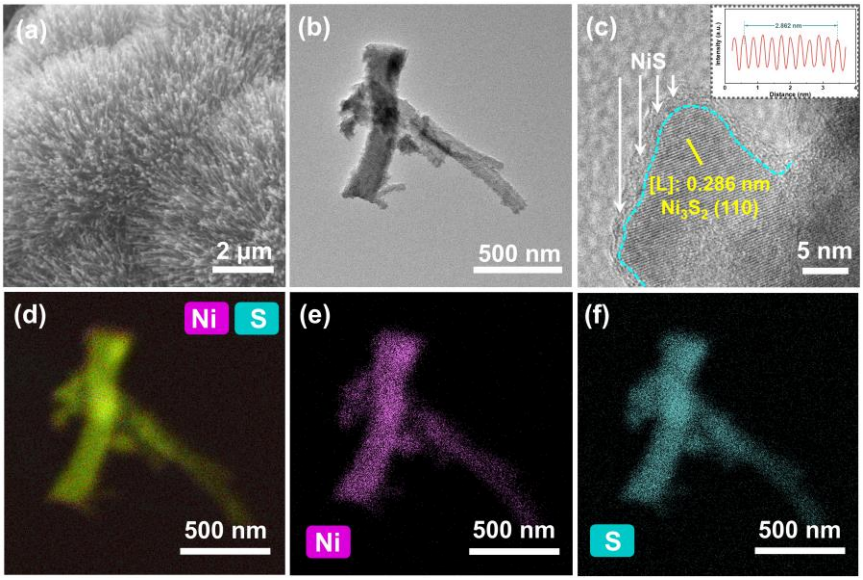

Figure 2.15 (a) SEM; (b) TEM; (c) HR-TEM; (d)-(f) the EDS spectrum of Ni_3S_2@NiS-250/NF after the stability test in 1 M KOH solution for 50 h

In addition, the Tafel slope of Ni_3S_2@NiS-250/NF was also measured by EIS method, which derived from the plot of function of the overpotential applied (100, 120, 150, 175 and 200 mV) versus log (Rct^{-1}) (**Figure 2.11**). In Figure 2.9e, the Ni_3S_2@NiS-250/NF depicted a Tafel slope of 75.5 mV dec^{-1}, which demonstrated that the electrocatalysis over Ni_3S_2@NiS-250/NF electrode should follow a Volmer-Heyrovsky mechanism, that is, the rate determining step is Heyrovsky step, which is similar as the result based on LSV method (**Figure 2.12**). The stability of Ni_3S_2@NiS-250/NF electrode was evaluated by continuous cycling for 3000 cycles in 1 M KOH solution at first (Figure 2.9f). Obviously, at the end of cycle, the Ni_3S_2@NiS-250/NF electrode still afforded a similar *j*-V curve as the initial one. Besides, the long-term stability at η=-250 mV was further examined for the Ni_3S_2@NiS-250/NF electrode. As shown in Figure 2.9g, after 50 h test, there was no obvious attenuation phenomenon detected, also confirming its outstanding durability in the basic solution. For comparison, the stability of Ni_3S_2/NF was measured in **Figure 2.13**. One can see that the activity of Ni_3S_2/NF was decreased in the first 12h. In addition, after the stability test for the Ni_3S_2@NiS-250/NF electrode, XRD, SEM and TEM analyses were also performed. As shown in **Figures 2.14** and **2.15**, obviously, the spent catalyst was also composed of NiS and Ni_3S_2 as the fresh one, and the nanowire structure was still maintained. While, the HR-TEM image also clearly showed a two-phase heterojunction structure with the inter-planar distance of 0.286 nm affiliated to the (110) facet of Ni_3S_2. As such, it could be reasonably inferred that the NiS formed on the surface of Ni_3S_2 served as the main active sites. Besides, the electron transfer was also observed from the XPS analysis results, indicating a strong interaction between Ni_3S_2 and NiS. Thus, the excellent catalytic activity and stability may be resulted from the interface interaction between the Ni_3S_2 and NiS phases. In addition, as shown in Figure 2.15 d-f, the Ni and S

elements were still distributed uniformly on the Ni_3S_2@NiS-250/NF electrode.

2.3.3 DFT calculations

Density functional theory (DFT) calculations were carried out to investigate the mechanism of the enhanced HER performance of Ni_3S_2/NiS heterostructure formed from epitaxial growth of NiS on the Ni_3S_2. Herein, three optimized structure models (Ni_3S_2 (101), NiS (021) and Ni_3S_2/NiS) were designed based on the characterization results (XRD and HR-TEM), and the corresponding top and side views are shown in **Figure 2.16**. The conductivities of Ni_3S_2, NiS, and Ni_3S_2/NiS were evaluated by density of states (DOSs) shown in **Figure 2.17**. One can see that the DOS value of Ni_3S_2/NiS calculated is 9.00 eV, which is stronger than those of Ni_3S_2 (3.35 eV) and NiS (4.24 eV), indicating that the Ni_3S_2/NiS heterostructure should have superior electrical conductivity, which is consistent with the EIS results. It indicates that the formation of NiS phase could improve the conductivity in the NiS/Ni_3S_2 heterostructure system.

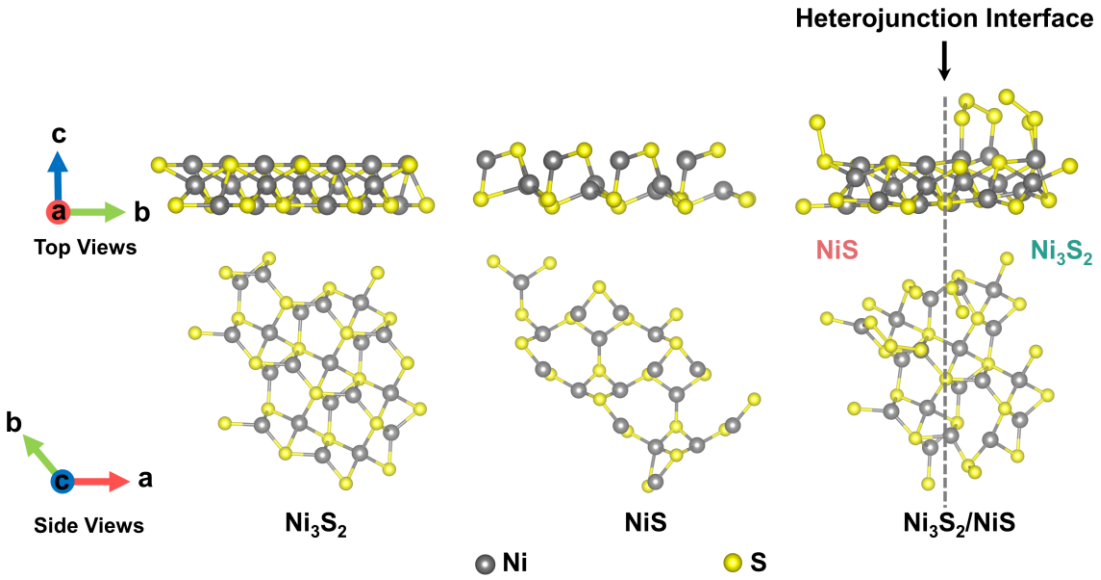

Figure 2.16 Top and side views of the optimized structures of Ni_3S_2 (101), NiS (021) and Ni_3S_2/NiS

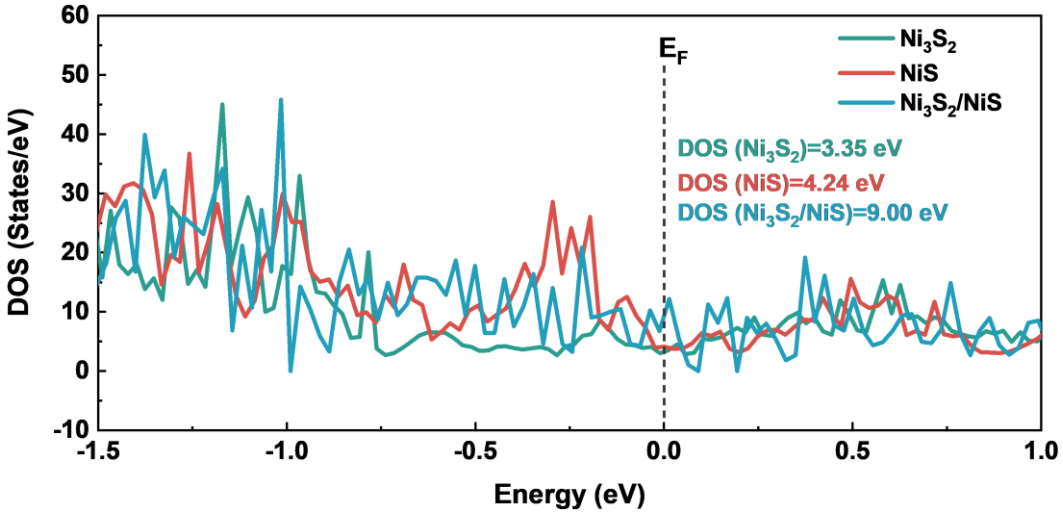

Figure 2.17 Density of states (DOS) of Ni_3S_2, NiS and Ni_3S_2/NiS

Moreover, the charge transfer at the interface of the Ni_3S_2/NiS heterojunction can optimize the electronic properties of Ni and well-adjust the d-band center (ε_d) relative to Fermi level (F_E) [52]. As a result of projected density of states (*p*DOS), the surface d-band center relative to the Fermi level was calculated to be -0.506, -0.551 and -0.563 eV for Ni_3S_2, NiS, and Ni_3S_2/NiS, respectively. The d-band center theory is extensively used to predict the surface strength between the adsorbates and electrode. The ε_d, which is closer to the Fermi level, demonstrates a stronger binding interaction between the catalyst surface and reaction intermediates. Figures 2.18b, c and d show the *p*DOS results of Ni_3S_2, NiS, and Ni_3S_2/NiS, respectively. For the Ni_3S_2, the highest ε_d value (-0.506 eV) indicates the lowest HER kinetics. Obviously, the d-band center of Ni_3S_2/NiS (-0.563 eV) shows a significant downshift compared with those of Ni_3S_2 and NiS, indicating that the interaction between H adsorption and Ni_3S_2/NiS surface should be weakened. Therefore, it could be inferred that the heterostructure should have a positive effect on tuning electronic structure. Combining with the experiment results, the shift of d-band center could be attributed to the charge transfer at the interface of Ni_3S_2/NiS heterojunction. Additionally, the free energy of hydrogen adsorption (ΔG_{H^*}) is another

criterion to evaluate the HER activity of the electrocatalysts. Figures 2.18a and **2.19** display the side and top views of the optimized structure of adsorbed H on the Ni_3S_2, NiS, and Ni_3S_2/NiS, and the corresponding calculation results of ΔG_{H^*} are shown in Figure 2.18e and summarized in **Table 2.4**. The free energy of H (H*) on the Ni_3S_2/NiS surface is closer to the zero compared with those of Ni_3S_2 and NiS, indicating that the Ni_3S_2/NiS heterostructure should possess a positive effect on tuning electronic structure, thereby balancing the adsorption and desorption of H to boost the HER process.

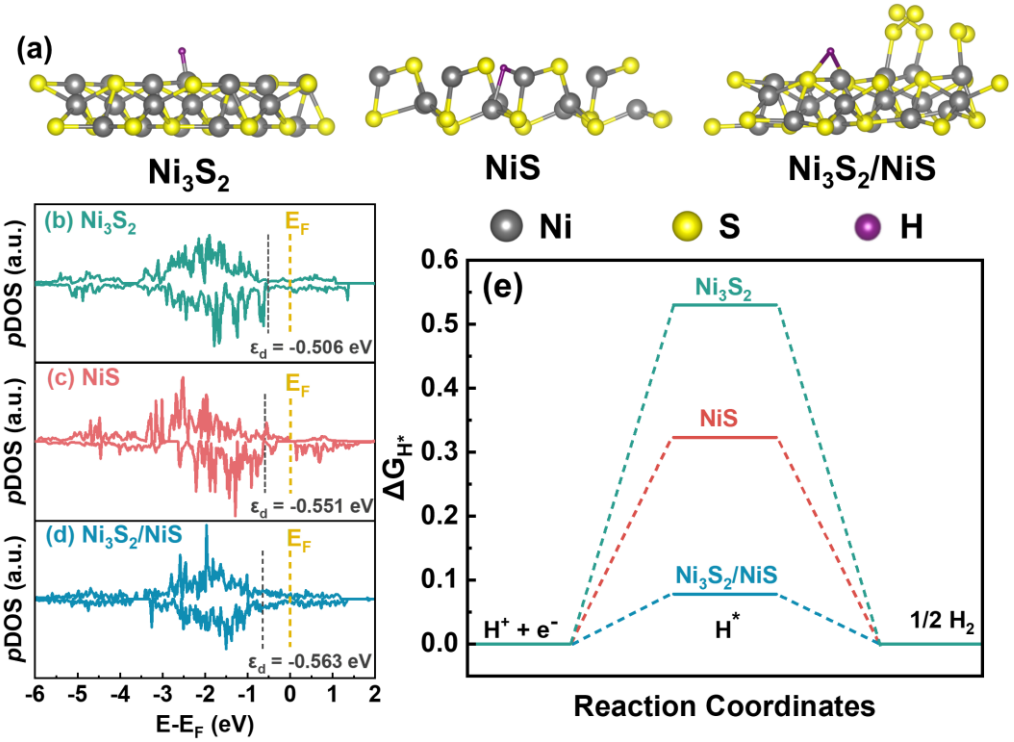

Figure 2.18 (a) Optimized structure of adsorbed H; (b-c) *p*DOS of d-states and (e) free energies of adsorption on the Ni_3S_2, NiS and Ni_3S_2/NiS heterostructures

Table 2.4 Summary of the values of d band center (ε_d) and the free energies of hydrogen adsorption (ΔGH*) for Ni_3S_2 (101), NiS (021) and Ni_3S_2/NiS.

Catalysts	ε_d (eV)	ΔG_{H^*} (eV)
Ni_3S_2	-0.506	0.530
NiS	-0.551	0.323
Ni_3S_2/NiS	-0.563	0.078

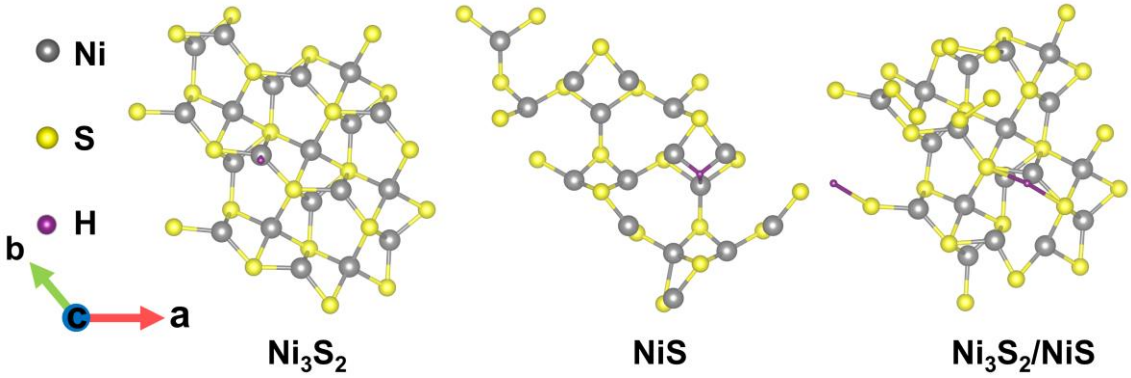

Figure 2.19 Top views of the optimized structures of adsorbed H on Ni_3S_2 (101), NiS (021) and Ni_3S_2/NiS

2.4 Conclusions

In summary, a facile method was developed for the preparation of nanowire-like Ni_3S_2@NiS-250/NF electrocatalysts with a heterojunction structure on the NF substrate. It is found that the calcination temperature, in the solid-state phase transformation strategy, could affect the degree of epitaxial growing of NiS layer on the surface of the Ni_3S_2 nanowire, creating Ni_3S_2/NiS interface with abundant active unsaturated S sites to increase the conductivity and to expose more active sites. Moreover, it is found that the strong charge transfer at the Ni_3S_2/NiS heterojunction interface could modulate the d band center so that the Ni-H bond is reasonably optimized, thereby boosting the HER performance. The obtained Ni_3S_2@NiS-250/NF electrode exhibited outstanding HER performance, achieving a low overpotentials of 129 mV to deliver the standard current density of 10 mA cm^{-2} with a small Tafel slope (75.5 mV dec^{-1}) in 1 M KOH media, as well as long-term stability. This study is expected to provide a method to develop lower-cost electrocatalysts with higher HER performance via morphology and phase transition.

References

[1] J. E. Lee, K. J. Jeon, P. L. Show, I. H. Lee, S. C. Jung, Y. J. Choi, G. H. Rhee, K. Y. A. Lin, Y. K. Park, Mini review on H_2 production from electrochemical water splitting according to special nanostructured morphology of electrocatalysts, Fuel 308 (2022) 122048.

[2] A. Huang, Y. Ma, J. Peng, L. Li, S. L. Chou, S. Ramakrishna, S. Peng, Tailoring the structure of silicon-based materials for lithium-ion batteries via electrospinning technology, eScience 1 (2021) 141-162.

[3] X. Li, B. Lv, X. P. Zhang, X. Jin, K. Guo, D. Zhou, H. Bian, W. Zhang, U. P. Apfel, R. Cao, Introducing water-network-assisted proton transfer for boosted electrocatalytic hydrogen evolution with cobalt corrole, Angew. Chem. Int. Ed. 61 (2022) e202114310.

[4] H. Huang, D. Yu, F. Hu, S. C. Huang, J. Song, H. Y. Chen, L. Li, S. Peng, Clusters induced electron redistribution to tune oxygen reduction activity of transition metal single-atom for metal-air batteries, Angew. Chem. Int. Ed. 134 (2022) e202116068.

[5] L. Xie, J. Tian, Y. Ouyang, X. Guo, W. Zhang, U. P. Apfel, W. Zhang, R. Cao, Water-soluble polymers with appending porphyrins as bioinspired catalysts for the hydrogen evolution reaction, Angew. Chem. Int. Ed. 59 (2020) 15844-15848.

[6] E. Lee, H. Park, H. Joo, B. P. T. Fokwa, Unexpected correlation between boron chain condensation and hydrogen evolution reaction (HER) activity in highly active vanadium borides: enabling predictions, Angew. Chem. Int. Ed. 59 (2020) 11774-11778.

[7] C. Gong, Z. Li, L. Yi, K. Huang, F. Liu, Research on the performance of a hydrogen/methanol dual-injection assisted spark-ignition engine using late-injection strategy for methanol, Fuel 260 (2020) 116403.

[8] F. Zhang, Y. Zhu, Y. Chen, Y. Lu, Q. Lin, L. Zhang, S. Tao, X. Zhang, H. Wang, RuCo alloy bimodal nanoparticles embedded in N-doped carbon: a superior pH-

universal electrocatalyst outperforms benchmark Pt for the hydrogen evolution reaction, J. Mater. Chem. A 8 (2020) 12810-12820.

[9] L. Li, D. Yu, P. Li, H. Huang, D. Xie, C. C. Lin, F. Hu, H. Y. Chen, S. Peng, Interfacial electronic coupling of ultrathin transition-metal hydroxide nanosheets with layered MXenes as a new prototype for platinum-like hydrogen evolution, Energy Environ. Sci. 14 (2021) 6419-6427.

[10] K. L. Zhou, Z. Wang, C. B. Han, X. Ke, C. Wang, Y. Jin, Q. Zhang, J. Liu, H. Wang, H. Yan, Platinum single-atom catalyst coupled with transition metal/metal oxide heterostructure for accelerating alkaline hydrogen evolution reaction, Nat. Commun. 12 (2021) 1-10.

[11] J. Jin, J. Yin, H. Liu, B. Huang, Y. Hu, H. Zhang, M. Sun, Y. Peng, P. Xi, C. H. Yan, Atomic sulfur filling oxygen vacancies optimizes H absorption and boosts the hydrogen evolution reaction in alkaline media, Angew. Chem. Int. Ed. 133 (2021) 14236-14242.

[12] J. X. Feng, H. Xu, Y. T. Dong, X. F. Lu, Y. X. Tong, G. R. Li, Efficient hydrogen evolution electrocatalysis using cobalt nanotubes decorated with titanium dioxide nanodots, Angew. Chem. Int. Ed. 56 (2017) 2960-2964.

[13] M. Chen, J. Liu, N. Kitiphatpiboon, X. Li, J. Wang, X. Hao, A. Abudula, Y. Ma, G. Guan, Zn-VO_x-Co nanosheets with amorphous/crystalline heterostructure for highly efficient hydrogen evolution reaction, Chem. Eng. J. 432 (2022) 134329.

[14] F. Hu, D. Yu, M. Ye, H. Wang, Y. Hao, L. Wang, L. Li, Lattice-matching formed mesoporous transition metal oxide heterostructures advance water splitting by active Fe-O-Cu bridges, Adv. Energy Mater. 12 (2022) 2200067.

[15] L. Deng, F. Hu, M. Ma, S. C. Huang, Y. Xiong, H. Y. Chen, L. Li, S. Peng, Electronic modulation caused by interfacial Ni-O-M (M=Ru, Ir, Pd) bonding for accelerating hydrogen evolution kinetics, Angew. Chem. Int. Ed. 133 (2021) 22450-

22456.

[16] X. Gao, Y. Chen, T. Sun, J. Huang, W. Zhang, Q. Wang, R. Cao, Karst landform-featured monolithic electrode for water electrolysis in neutral media, Energy Environ. Sci. 13 (2020) 174-182.

[17] J. X. Feng, H. Xu, S. H. Ye, G. Ouyang, Y. X. Tong, G. R. Li, Silica-polypyrrole hybrids as high-performance metal-free electrocatalysts for the hydrogen evolution reaction in neutral media, Angew. Chem. Int. Ed. 129 (2017) 8232-8236.

[18] J. X. Feng, S. Y. Tong, Y. X. Tong, G. R. Li, Pt-like hydrogen evolution electrocatalysis on PANI/CoP hybrid nanowires by weakening the shackles of hydrogen ions on the surfaces of catalysts, J. Am. Chem. Soc. 140 (2018) 5118-5126.

[19] W. Hua, H. H. Sun, F. Xu, J. G. Wang, A review and perspective on molybdenum-based electrocatalysts for hydrogen evolution reaction. Rare Metals 39 (2020) 335-351.

[20] X. Gao, J. Qi, S. Wan, W. Zhang, Q. Wang, R. Cao, Conductive molybdenum sulfide for efficient electrocatalytic hydrogen evolution, Small 14 (2018) 1803361.

[21] Y. Rao, H. Ning, X. Ma, Y. Liu, Y. Wang, H. Liu, J. Liu, Q. Zhao, M. Wu, Template-free synthesis of coral-like nitrogen-doped carbon dots/Ni_3S_2/Ni foam composites as highly efficient electrodes for water splitting, Carbon 129 (2018) 335-341.

[22] C. Yang, K. Shen, R. Zhao, H. Xiang, J. Wu, W. Zhong, Q. Zhang, X. Li, N. Yang, Balance effect: A universal strategy for transition metal carbides to enhance hydrogen evolution, Adv. Funct. Mater. 32 (2022) 2108167.

[23] S. Wu, M. Chen, W. Wang, J. Zhou, X. Tang, D. Zhou, C. Liu, Molybdenum carbide nanoparticles assembling in diverse heteroatoms doped carbon matrix as efficient hydrogen evolution electrocatalysts in acidic and alkaline medium, Carbon 171 (2021) 385-394.

[24] W. Feng, W. Pang, Y. Xu, A. Guo, X. Gao, X. Qiu, W. Chen, Transition metal

selenides for electrocatalytic hydrogen evolution reaction, ChemElectroChem. 7 (2020) 31-54.

[25] S. Shen, Z. Lin, K. Song, Z. Wang, L. Huang, L. Yan, F. Meng, Q. Zhang, L. Gu, W. Zhong, Reversed active sites boost the intrinsic activity of graphene-like cobalt selenide for hydrogen evolution, Angew. Chem. Int. Ed. 60 (2021) 12360-12365.

[26] J. Song, S. Qiu, F. Hu, Y. Ding, S. Han, L. Li, H. Y. Chen, X. Han, C. Sun, S. Peng, Sub-2 nm thiophosphate nanosheets with heteroatom doping for enhanced oxygen electrocatalysis, Adv. Funct. Mater. 31 (2021) 2100618.

[27] H. Yang, P. Guo, R. Wang, Z. Chen, H. Xu, H. Pan, D. Sun, F. Fang, R. Wu, Sequential phase conversion-induced phosphides heteronanorod arrays for superior hydrogen evolution performance to Pt in wide pH media, Adv. Mater. (2022) 2107548.

[28] T. F. Hung, Z. W. Yin, S. B. Betzler, W. Zheng, J. Yang, H. Zheng, Nickel sulfide nanostructures prepared by laser irradiation for efficient electrocatalytic hydrogen evolution reaction and supercapacitors, Chem. Eng. J. 367 (2019) 115-122.

[29] H. Xu, Y. Jiao, S. Li, H. Meng, J. Wu, X. Shi, Z. Du, R. Wang, G. Tian, Ultrathin-layered MoS_2 hollow nanospheres decorating Ni_3S_2 nanowires as high effective self-supporting electrode for hydrogen evolution reaction, Int. J. Hydrog Energy 45 (2020) 13149-13162.

[30] B. Li, Z. Li, Q. Pang, J. Z. Zhang, Core/shell cable-like Ni_3S_2 nanowires/N-doped graphene-like carbon layers as composite electrocatalyst for overall electrocatalytic water splitting, Chem. Eng. J. 401 (2020) 126045.

[31] Z. Qin, Y. Chen, Z. Huang, J. Su, Z. Diao, L. Guo, Composition-dependent catalytic activities of noble-metal-free NiS/Ni_3S_4 for hydrogen evolution reaction, J. Phys. Chem. C 120 (2016) 14581-14589.

[32] K. Jayaramulu, J. Masa, O. Tomanec, D. Peeters, V. Ranc, A. Schneemann, R.

Zboril, W. Schuhmann, R. A. Fischer, Nanoporous nitrogen-doped graphene oxide/nickel sulfide composite sheets derived from a metal-organic framework as an efficient electrocatalyst for hydrogen and oxygen evolution, Adv. Funct. Mater. 27 (2017) 1700451.

[33] A. Khalil, Q. Liu, Z. Muhammad, M. Habib, R. Khan, Q. He, Q. Fang, H. T. Masood, Z. Rehman, T. Xiang, C. Q. Wu, L. Song, Synthesis of Ni_9S_8/MoS_2 heterocatalyst for enhanced hydrogen evolution reaction, Langmuir 33 (2017) 5148-5153.

[34] L. Sha, T. Liu, K. Ye, K. Zhu, J. Yan, J. Yin, G. Wang, D. Cao, A heterogeneous interface on $NiS@Ni_3S_2/NiMoO_4$ heterostructures for efficient urea electrolysis, J. Mater. Chem. A 8 (2020) 18055-18063.

[35] A. Yan, X. Shi, F. Huang, M. Fujitsuka, T. Majima, Efficient photocatalytic H_2 evolution using $NiS/ZnIn_2S_4$ heterostructures with enhanced charge separation and interfacial charge transfer, Appl. Catal. B 250 (2019) 163-170.

[36] X. Xiao, D. Huang, Y. Fu, M. Wen, X. Jiang, X. Lv, M. Li, L. Gao, S. Liu, M. Wang, C. Zhao, Y. Shen, Engineering NiS/Ni_2P heterostructures for efficient electrocatalytic water splitting, ACS Appl. Mater. Inter. 10 (2018) 4689-4696.

[37] T. An, Y. Wang, J. Tang, W. Wei, X. Cui, A. M. Alenizi, L. Zhang, G. Zheng, Interlaced NiS_2-MoS_2 nanoflake-nanowires as efficient hydrogen evolution electrocatalysts in basic solutions, J. Mater. Chem. A 4 (2016) 13439-13443.

[38] Y. Ma, M. Chen, H. Geng, H. Dong, P. Wu, X. Li, G. Guan, T. Wang, Synergistically tuning electronic structure of porous β-Mo_2C spheres by Co doping and Mo-vacancies defect engineering for optimizing hydrogen evolution reaction activity, Adv. Funct. Mater. 30 (2020) 2000561.

[39] Y. Ma, J. Liu, M. Chen, Q. Yang, H. Chen, G. Guan, Y. Qin, T. Wang, Selective

hydrogenation of naphthalene to decalin over surface-engineered α-MoC based on synergy between Pd doping and Mo vacancy generation, Adv. Funct. Mater. (2022) 2112435.

[40] L. Dong, P. Wang, H. Yu, EDTA-assisted synthesis of amorphous BiS_x nanodots for improving photocatalytic hydrogen-evolution rate of TiO_2, J. Alloys Compd. 887 (2021) 161425.

[41] W. Zhong, X. Wu, Y. Liu, X. Wang, J. Fan, H. Yu, Simultaneous realization of sulfur-rich surface and amorphous nanocluster of NiS_{1+x} cocatalyst for efficient photocatalytic H_2 evolution, Appl. Catal. B 280 (2021) 119455.

[42] Y. Wu, J. Lian, Y. Wang, J. Sun, Z. He, Z. Gu, Potentiostatic electrodeposition of self-supported NiS electrocatalyst supported on Ni foam for efficient hydrogen evolution, Mater. Des. 198 (2021) 109316.

[43] Z. Qin, Y. Chen, Z. Huang, J. Su, Z. Diao, L. Guo, Composition-dependent catalytic activities of noble-metal-free NiS/Ni_3S_4 for hydrogen evolution reaction, J. Phys. Chem. C 120 (2016) 14581-14589.

[44] Y. Yang, Y. Zhang, Y. Zhou, C. Zhu, Y. Xie, L. Lv, W. Chen, Y. He, Z. Hu, Design and synthesis of NiS@ CoS@ CC with abundant heterointerfaces as high-efficiency hydrogen evolution electrocatalyst, Int. J. Hydrog. Energy 44 (2019) 26753-26763.

[45] C. Ouyang, X. Wang, C. Wang, X. Zhang, J. Wu, Z. Ma, S. Dou, S. Wang, Hierarchically porous Ni_3S_2 nanorod array foam as highly efficient electrocatalyst for hydrogen evolution reaction and oxygen evolution reaction, Electrochim. Acta 174 (2015) 297-301.

[46] S. Y. Lu, S. Li, M. Jin, J. Gao, Y. Zhang, Greatly boosting electrochemical hydrogen evolution reaction over Ni_3S_2 nanosheets rationally decorated by $Ni_3Sn_2S_2$ quantum dots, Appl. Catal. B 267 (2020) 118675.

[47] Z. Qin, Y. Chen, Z. Huang, J. Su, Z. Diao, L. Guo, Composition-dependent catalytic activities of noble-metal-free NiS/Ni_3S_4 for hydrogen evolution reaction, J. Phys. Chem. C 120 (2016) 14581-14589.

[48] J. Wen, J. Xie, H. Zhang, A. Zhang, Y. Liu, X. Chen, X. Li, Constructing multifunctional metallic Ni interface layers in the g-C_3N_4 nanosheets/amorphous NiS heterojunctions for efficient photocatalytic H_2 generation, ACS Appl. Mater. Inter. 9 (2017) 14031-14042.

[49] J. Xie, H. Qu, J. Xin, X. Zhang, G. Cui, X. Zhang, J. Bao, B. Tang, Y. Xie, Defect-rich MoS_2 nanowall catalyst for efficient hydrogen evolution reaction, Nano Res. 10 (2017) 1178-1188.

[50] Y. Zhang, W. Zhou, Y. Tang, Y. Guo, Z. Geng, L. Liu, X. Tan, H. Wang, T. Yu, J. Ye, Unravelling unsaturated edge S in amorphous NiS_x for boosting photocatalytic H_2 evolution of metastable phase CdS confined inside hydrophilic beads, Appl. Catal. B 305 (2022) 121055.

[51] P. F. Cheng, T. Feng, Z. W. Liu, D. Y. Wu, J. Yang, Laser-direct-writing of 3D self-supported NiS_2/MoS_2 heterostructures as an efficient electrocatalyst for hydrogen evolution reaction in alkaline and neutral electrolytes, Chinese J. Catal. 40 (2019) 1147-1152.

[52] S. Shen, Z. Wang, Z. Lin, K. Song, Q. Zhang, F. Meng, L. Gu, W. Zhong, Crystalline-amorphous interfaces coupling of $CoSe_2$/CoP with optimized d-band center and boosted electrocatalytic hydrogen evolution, Adv. Mater. 34 (2022) 2110631.

CHAPTER 3 Zn-VO_x-Co nanosheets with amorphous/ crystalline heterostructure for highly efficient hydrogen evolution reaction

3.1 Introduction

To realize carbon neutrality in the near future, green growth strategy has been announced by many countries, in which using those green energies such as hydrogen energy to replace the traditional fossil fuel has been considered widely [1-3]. Among the different strategies for production of hydrogen [4-6], water electrolysis is deemed as an indispensable and effective approach due to its unique advantages including unlimited reactant availability, outstanding manufacturing safety, stable output and high product purity [7-10].

In the water electrolysis process, designing of cost-effective electrocatalysts with high-activity and ultra-stability to replace those noble-metal-based ones for hydrogen evolution reaction (HER) is one of important tasks in the scaling-up of it for hydrogen production [11-13]. Cobalt, one of the most abundant elements in nature, has been widely used in the catalysis of HER process [14-16]. However, its catalysis performance cannot reach those of noble metal-based ones because of the lower reaction rate in the generation of H_2 resulting from the excessive adsorption energy for the hydrogen atoms [17, 18]. To solve this issue, massive efforts have been made to facilitate the HER kinetics, which including the morphology designing [19, 20], heterostructure constructing [21, 22], heteroatom doping [23, 24], and so on.

Currently, compared with zero-dimensional (0D) nanoparticles [25, 26] and one-dimensional (1D) nanowires [27, 28], two-dimensional (2D) materials attracted intense interests owing to their large specific surface areas and abundant active site exposed on

the surface by the atomically thin nature of nanosheets [29-31]. Constructing of the 2D heterostructure materials is an efficient method to further increase the active sites. Typically, the heterostructure could provide sufficient adsorption sites from the refined nanostructures with substantially exposed edges for the intermediates generated in the HER process [22]. To date, various heterostructure structure catalysts such as MOF-based heterojunctions [32-34], transition metal phosphides-based heterojunctions [26], sulfides-based heterostructures [35, 36], metal-oxide based heterostructures [37, 38] and so on have been reported. Recently, some heterostructure catalysts have been found to have outstanding HER performance. For instance, CoP/Co-MOF heterostructure nanosheets prepared via a partially controlled phosphorization method only required an overpotential as low as 26 mV at 10 mA cm^{-2} in basic solution [34]. CoS_2/MoS_2 hetero-nanosheet array (HNSAs) with vertically aligned flower-like architectures synthesized through the sulfurization of $CoMoO_4$ nanosheet precursor exhibited an outstanding HER performance with a low overpotential of 50 mV at 10 mA cm^{-2} and a small Tafel slope of 76 mV/dec in basic solution [36]. Mo-$NiCo_2O_4/Co_{5.47}N$ with a heterostructure nanosheet array prepared via depositing on the nickel foam (NF) also exhibited an outstanding HER performance in basic solution with an overpotential of 81 mV at 10 mA cm^{-2} and excellent durability [37].

As a special phase engineering method, creating amorphous structure in the transition metal-based catalysts could result in unique activity properties. Liu *et al.* doped vanadium species on the Co-based catalysts, and found that the rigid conformations of crystalline Co phase to the amorphous Co phase effectively enhanced the catalytic activity, achieving outstanding long-term stability [39]. Li *et al.* doped VO_x cluster on Co-based catalysts, named as Co (VO_x), in which VO_x cluster modified the Co lattice structure to endow metallic Co phase with a highly disordered lattice

(amorphous phase). As such, the electron can be more easily transferred from Co to VO_x, which effectively decreased the hydrogen atom adsorption energy on the Co surface [40]. As a result, the appropriate VO_x doped metallic Co catalyst (Co (VO_x)-3%) displayed much higher HER activity in the basic solution than the pure metallic Co catalyst. However, although the amorphous material with distinctive molecular structure can arouse abundant unsaturated coordination atoms to provide more active sites for HER, it always has low electrical conductivity, which will hinder the charge transfer [41, 42]. To solve this issue, the concept of amorphous-crystalline heterostructure was proposed, in which the combination of two phases could demonstrate unique properties with high electrical conductivity to improve the catalysis performance [43, 44].

It has been demonstrated that alloying two distinct metals is an effective way to enhance the catalytic activity as well as conductivity due to the synergistically electronic effect of two elements [45-47]. In our previous work, the synergistic effect of second metal (such as Mo, Ni, Mn and Fe) and Co elements was found to effectively tune the electronic structure of Co species for enhancing the HER activity [10, 48]. Herein, it is considered to incorporate Zn into metallic Co phase to form a Zn-Co alloy crystalline heterostructure to effectively improve the electrical conductivity, and doping VO_x to generate more interphase structures (Co amorphous) to further enhance the catalytic performance of Co-based electrocatalysts. As such, a newly interphase-engineered Zn-VO_x-Co ultrathin 2D film with abundant amorphous/ crystalline heterostructures was grown on the carbon fiber paper (CFP) by a facile electrodeposition approach for the first time. Based on the experimental characterizations and DFT calculations, it is indicated that dual-doped Zn and VO_x could optimize the d-band center, which can make the amorphous Co phase with

abundant unsaturated bonds, thereby facilitating the H-adsorption and fast hydrogen release to significantly enhance the HER activity and stability.

3.2 Experimental section

3.2.1 Chemical and Materials

Cobalt (II) sulfate heptahydrate ($CoSO_4 \cdot 7H_2O$, 99.0%), boric acid (H_3BO_3, 99.5%), zinc (II) sulfate heptahydrate ($ZnSO_4 \cdot 7H_2O$, 99.5%), ammonium vanadate (V) (NH_4VO_3, 99%), nitric acid (HNO_3, 69%) and potassium hydroxide (KOH, 85%) were purchased from Wako, Japan. Platinum on graphitized carbon (20 wt.% loading) and Nafion perfluorinated resin solution (containing 45% water) were provided from Aldrich. CFP (TGP-H-060, thickness: 190 μm) was purchased from Toray, Japan.

3.2.2 Preparation of Zn-VO_x-Co Nanosheet Based Electrode

The electrode was prepared by a one-step electrodeposition process. Prior to the electrodeposition, the CFP (2×2 cm^2) was firstly ultrasonicated in 6 M HNO_3 solution for 3 h, and then rinsed with deionized (DI) water and ethanol, and finally dried in a vacuum oven at 60 ℃ overnight. In a typical synthesis process, a solution containing 0.5 M $CoSO_4 \cdot 7H_2O$, 0.5 M H_3BO_3, 10 mM NH_4VO_3 and 10 mM $ZnSO_4 \cdot 7H_2O$ was prepared by dissolving the chemicals in 50 mL of DI water (pH =5.54) with magnetically stirring for 2 h before transferring it into a standard three-electrode electrochemical cell. The electrodeposition was carried out at a fixed potential -1.7 V (vs. Ag/AgCl) for 1200 s with the pretreated CFP as the working electrode and a standard Ag/AgCl and a Pt wire as the reference and counter electrodes, respectively. After the electrodeposition(pH =5.35), the electrode was rinsed with DI water before it was dried in a vacuum oven at 60 ℃ overnight. Based on the preliminary experiments, the optimum catalyst mass loading amount of Zn-VO_x-Co on the CFP was 5.0 ± 0.5 mg cm^{-2}, and for the single metal catalysts, the mass loading amounts were ~4.67 mg cm^{-2}

for Co, ~0.14 mg cm^{-2} for V and ~0.19 mg cm^{-2} for Zn in the composite based on the molar amounts determined by an inductively coupled plasma mass spectrometry (ICP-MS-7700).

3.2.3 Material Characterizations

X-ray diffraction (XRD, Rigaku Smartlab diffractometer, Japan) with a Cu-Kα as the radiation source (λ=0.15406 nm) was employed to determine the crystal structure of sample at a scanning rate of 8.0° min^{-1} in the range of 10°-80°. Morphology of the sample was characterized by a scanning electron microscope (SEM, SU8010, Hitachi, Japan). Nanostructure and elemental distribution of the sample were determined by a transmission electron microscopy (TEM, JEM-2100F, Japan) with an energy dispersive X-ray spectroscopy (EDX). X-ray photoelectron spectrum (XPS) was obtained by a VG Scientific ESCALab250i-XL instrument with a monochromate Al Kα source. The water contact angle on the surface of electrode was measured by a contact angle analysis machine (DMe-201, Japan).

3.2.4 Electrochemical measurements

Electrochemical properties of the obtained electrocatalysts were evaluated in either 1 M KOH (pH=14) solution and 1 M phosphate buffer solution (pH=7.0) respectively using a three-electrode setup on an electrochemical workstation (Versa STAT4, Princeton, USA). A RE-61AP type Hg/HgO electrode purchased from the ALS, Tokyo, Japan and a graphite rod with 6 mm in diameter were used as the reference and counter electrodes, respectively. Linear sweep voltammetry (LSV) curves were obtained with a scan rate of 1 mV s^{-1} in potential ranges of -0.8~-2.0 V vs. the reversible hydrogen electrode (RHE) in the alkaline solution and -0.2~-1.5 V vs. RHE in the natural solution. All potentials referenced to RHE were calculated by $E_{RHE} = E_{Hg/HgO} + (0.118 + 0.0592\ pH)$ V. Electrochemical double-layer capacitances (C_{dl}) were

investigated by measuring cyclic voltammetries (CVs) at scan rates of 10, 25, 50, 75, 100, 125 and 150 mV s^{-1} in a potential range of 0.3~0.5 V (vs. RHE). Besides, the measured current densities were also normalized by the ECSA value. Herein, the ECSA was calculated from the double-layer capacitance according to the follow equation (Eq. 3.1):

$$ECSA=C_{dl}/C_s \quad \text{(Eq. 3.1)}$$

Where, C_s presents the specific capacitance, and based on the literature, its value is 0.040 mF cm^{-2} in 1 M KOH solution. Electrochemical impedance spectroscopy (EIS) measurement was performed at an overpotential (η) of -150 mV with an amplitude of 10 mV and a frequency range from 0.01 to 100000 Hz. Stability test was carried out by a continuous CV measurement for 3000 cycles in the 1 M KOH solution. While, chronoamperometry measurement at a fixed overpotential of -100 mV and a test with multi-step chronoamperometric overpotentials from 10 to 300 mV with an increment of 20 mV every 1 h were also performed.

3.2.5 DFT calculation

Density functional theory (DFT) calculations were carried out by Vienna Ab initio Simulation Package (VASP) under the projected augmented wave (PAW) method. The generalized gradient approximation (GGA) of Perdew-Burke-Ernzerhof (PBE) were used to treat the exchange-function. The energy cutoff for the plane wave basis expansion was set as 450 eV. To convergence criterion of geometry relaxation, the force on each atom less than 0.03 eV/Å was set. For the whole system, 20 Å vacumm was added along with the c direction to avoid the interaction between the periodic structure. The energy converge criteria was 10^{-5} eV for self-consistent calculations and the Brillouin zone integration was performed using 3×3×1.

The free energies of the adsorption atomic hydrogen (ΔG_H^*) is defined by the following equation (Eq. 3.2) :

$$\Delta G_{H^*}=\Delta E_{DFT}+\Delta E_{ZPE}-T\Delta S \quad \text{(Eq. 3.2)}$$

where ΔE_{DFT} is the DFT energy difference, ΔE_{ZPE} is the zero-point energy difference between adsorbed hydrogen and gaseous hydrogen and the $T\Delta S$ term was obtained based on vibration analysis.

The center of d-band was calculated according to the following equation (Eq. 3.3):

$$\mu=\frac{\int N(\varepsilon)\varepsilon\, d\varepsilon}{\int N(\varepsilon)\, d\varepsilon} \quad \text{(Eq. 3.3)}$$

where N(ε) is the DOS, μ the center of d-band, and ε the bonding energy.

3.3 Results and discussion

3.3.1 Characteristics of Zn-VO_x-Co 2D ultrathin nanosheets

The procedure for the preparation of 2D Zn-VO_x-Co ultrathin nanosheets on the CFP by a facile electrodeposition method is schematically illustrated in **Figure 3.1**. From the digital photographs of pure Co, Zn-Co and VO_x-Co based films (**Figure 3.2**), one can see that the CFP was covered by the electrodeposited films with different color.

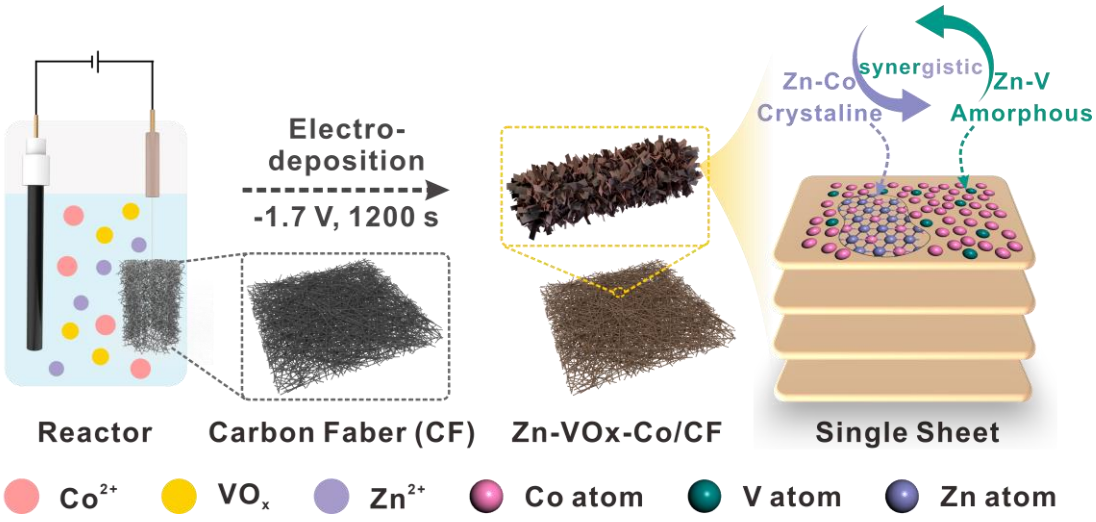

Figure 3.1 Schematic illustration of the preparation of Zn-VOx-Co 2D nanosheets.

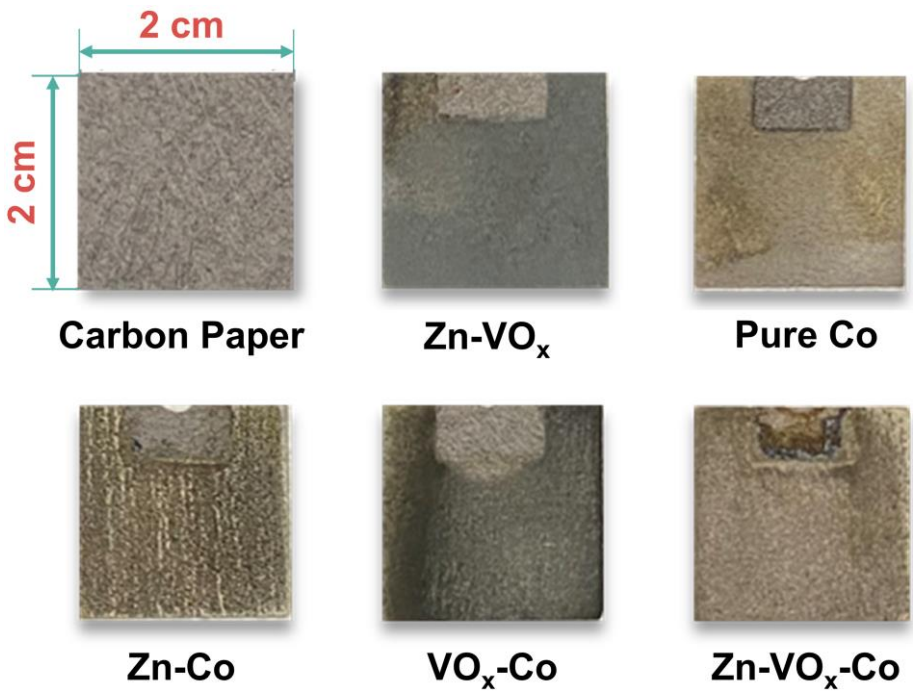

Figure 3.2 Optical images of the prepared electrodes

Figure 3.3 shows XRD patterns of the pure Co, Zn-Co, VO_x-Co and Zn-VO_x-Co coated CFP electrodes. For the pure Co and Zn-Co based samples, four diffraction peaks at $2\theta = 41.78°$, 44.37°, 47.30° and 76.08° assigned to the (100), (002), (101) and (220) planes of hexagonal close packed (hcp) metallic Co (JCPDS, No. 01-1254). Generally, it is easy to form alloy structure with similar metal atomic radius [49]. Herein, since the radii of Co (125 pm) and Zn (134 pm) are similar, the Zn-Co alloy could be easily formed. The Co unit cell volume will be increased to some extent when the Zn atom replaces Co atom or inserts into the framework of Co unit cell during the electrodeposition. In this case, the corresponding interplanar spacing of cobalt could be also expanded. Thence, comparing with the pure Co based one, as shown in **Figure 3.3**b, the Co (100) and Co (002) peaks were slightly shifted to the lower angle direction. In comparison, for the XRD patterns of VO_x-Co and Zn-VO_x-Co coated CFP electrodes, no intense diffraction peak except those relating to the CFP (**Figure 3.4a**) was observed.

While, the XRD patterns of VO_x-Co and Zn-VO_x-Co powders scraped from the electrode were also measured. As shown in **Figure 3.4b**, the crystallinity of either VO_x-Co or Zn-VO_x-Co was low. From the XRD patterns of pure Zn and Zn-VO_x samples (**Figure 3.4c**), one can see that the peak intensity relating to Zn species had no obvious change after the doping of VO_x, indicating that the VO_x doping only had a significantly influence on the crystalline structure of the Co species rather than Zn species.

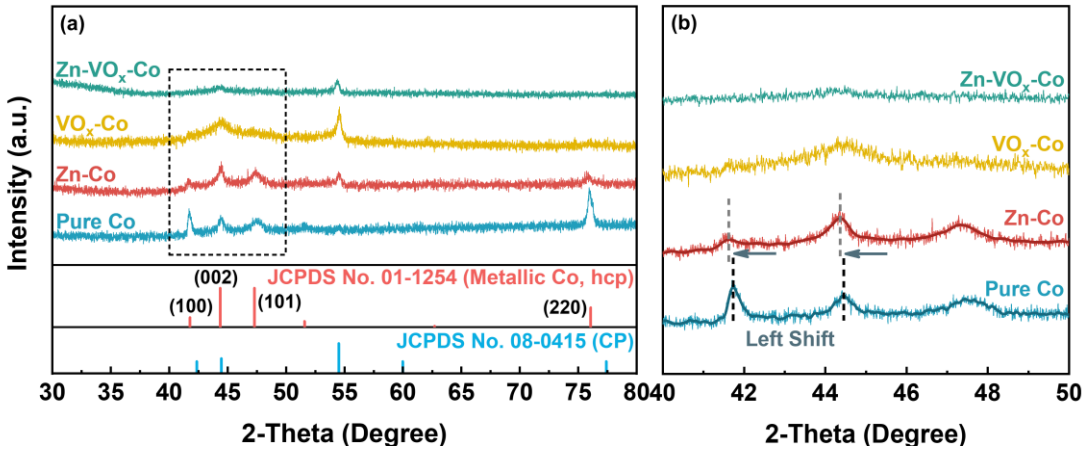

Figure 3.3 XRD patterns of pure Co, Zn-Co, VOx-Co and Zn-VO_x-Co electrodes. (a) Full spectrum; (b) Corresponding zoom-in regions between 2θ of 40° and 50°.

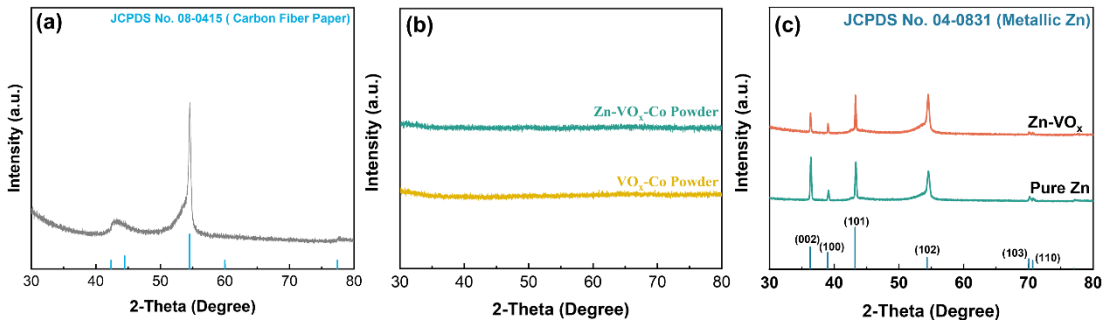

Figure 3.4 XRD pattern of (a) pristine CFB substrate; (b) VO_x-Co and Zn-VO_x-Co powders and (c) pure Zn and Zn-VO_x.

The morphologies of CFP and Zn-VO_x, pure Co, Zn-Co, VO_x-Co and Zn-VO_x-Co coated CFP electrodes were investigated by SEM. It is found that only some bulk Zn-VO_x particles (**Figure 3.5**) were grown on the smooth surface of pristine CFP (**Figure**

3.6), and for the pure Co film, the whole surface of CFP was covered by the nanoflakes with random shapes (**Figure 3.7**). However, for the Zn-Co (**Figure 3.8**) and VO_x-Co samples (**Figure 3.9**), the formed nanosheet arrays became more uniform and tighter. **Figure 3.10**a-c shows the morphologies of Zn-VO_x-Co at different scales. One can see that the Zn-VO_x-Co film was composed of numerous overlapped 2D ultra-thin nanosheets with lateral sizes of about 1~3 μm, which could provide larger active surface area and expose more active sites, and simultaneously, the 3D structure made of nanosheets could facilitate the electrolyte penetration and charge transport effectively. Herein, it should be noted that the morphologies of Zn-Co, VO_x-Co and Zn-VO_x-Co were similar with the nanosheet of pure Co sample, indicating that the Co species played a dominant role in the formation of film during the electrodeposition process. In addition, the EDS analysis (**Figure 3.10**d) indicated the existence of Zn, V, O and Co elements, which distributed uniformly on the Zn-VO_x-Co film (**Figure 3.10**e-i).

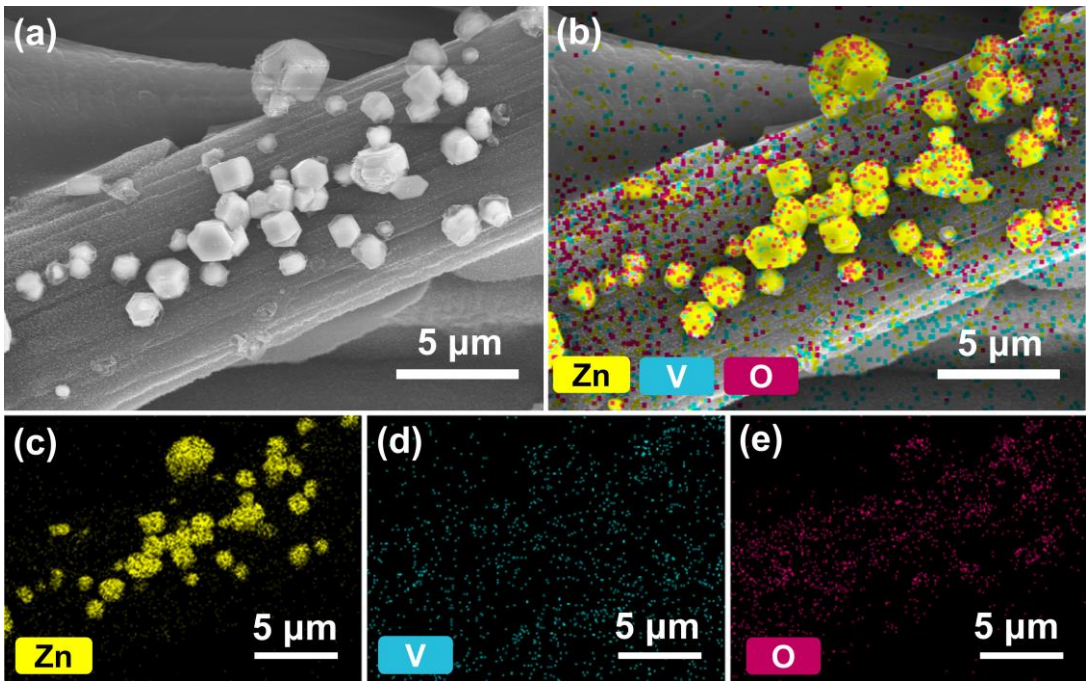

Figure 3.5 SEM images of Zn-VOx on CFP; (b-e) Corresponding EDX elemental mappings of Zn, V and O in Zn-VOx based electrode.

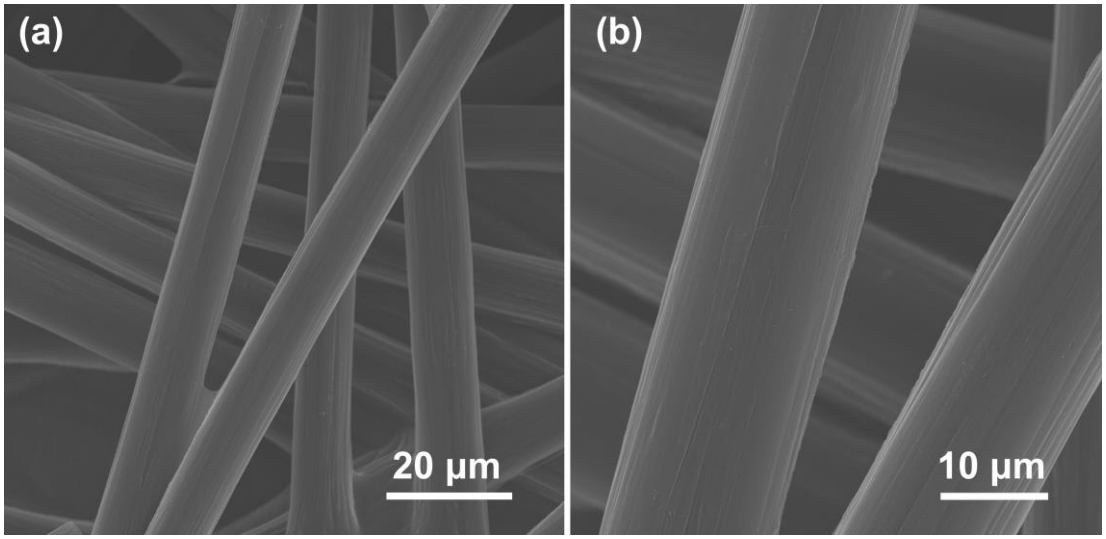

Figure 3.6 SEM images of a pristine carbon fiber paper substrate.

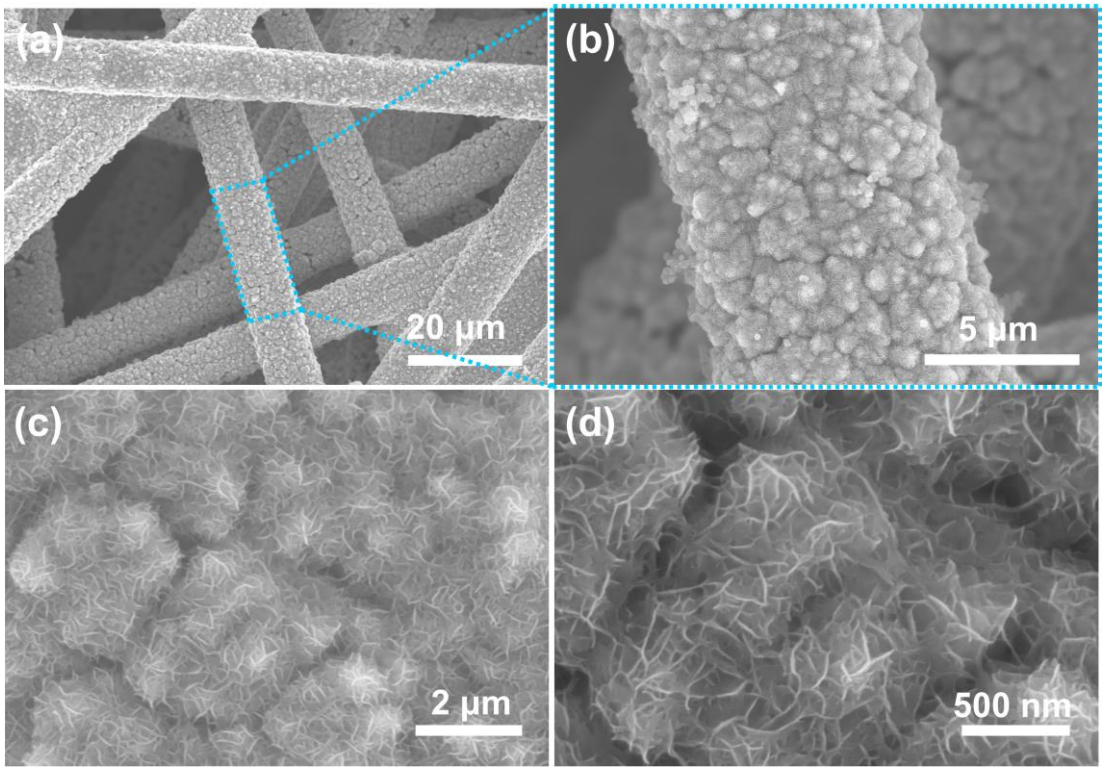

Figure 3.7 (a)-(d) SEM images of pure Co based electrode.

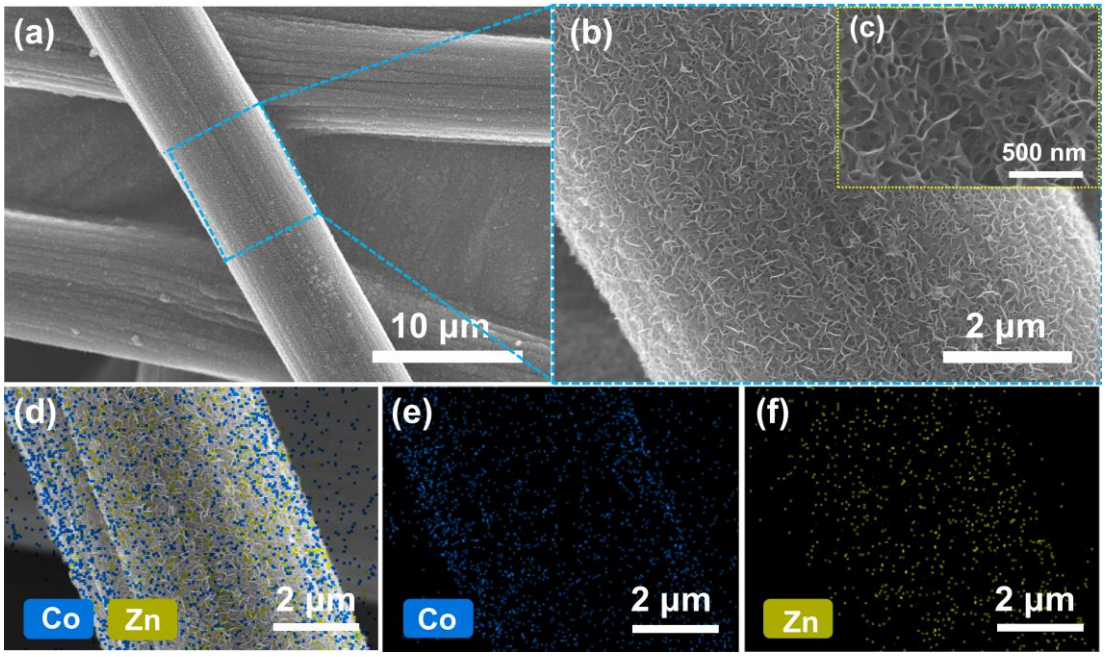

Figure 3.8 (a)-(c) SEM images of Zn-Co based electrode; (d)-(f) Corresponding EDX elemental mappings of Co and Zn in Zn-Co based electrode.

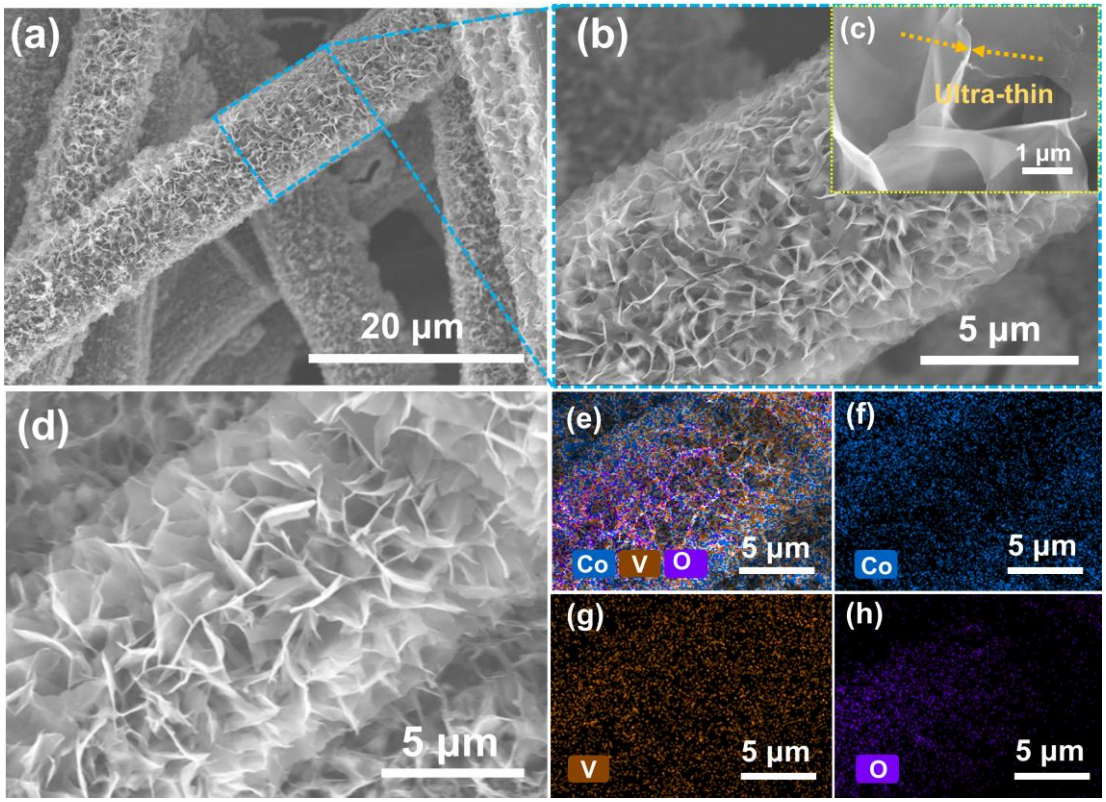

Figure 3.9 (a)-(d) SEM images of VO_x-Co based electrode; (e)-(h) Corresponding EDX elemental mappings of Co, V and O in VO_x-Co based electrode.

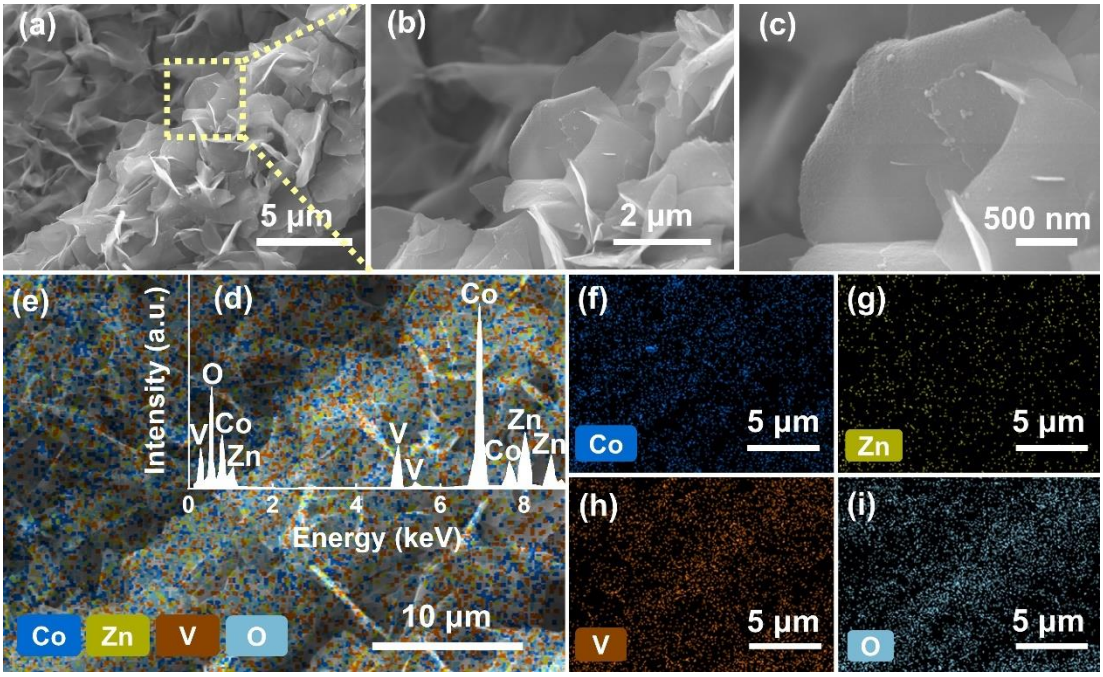

Figure 3.10 (a), (b) and (c) Representative SEM images of Zn-VO_x-Co on CFP; (d) EDS spectrum of Zn-VO_x-Co; (e)-(i) Corresponding EDX elemental mappings of Co, Zn, V and O on Zn-VO_x-Co surface.

Figure 3.13 (a-c) shows TEM and HRTEM images of Zn-VO_x-Co sample. One can see that the thickness of the nanosheet was about 6 nm (**Figure 3.13**a). Moreover, it is observed that the nanosheet was composed of both crystalline (**Figure 3.13**b, marked by the dashed white curves) and amorphous areas, which can be further identified by the corresponding diffuse ring (b_1) and bright spots (b_2) in the selected area from the fast Fourier transform (FFT) patterns. It is noteworthy that the connection of bright spots showed an irregular hexagon shape (dashed blue in b_2), indicating the partial heteroatom doping into the lattice of Co in the crystallized domain of the Zn-VO_x-Co. To be clearer, the crystalline area (dashed yellow cube in **Figure 3.13**b) was enlarged (shown in **Figure 3.13**c), and the image intensity L_1 is shown in the profile of **Figure 3.13**h. Herein, the fringe lattice spacing of 0.219 nm can be indexed, which is slightly larger than the interplanar distance of metallic Co (100) plane (0.216 nm). Moreover, the obvious heterojunction interface between crystalline and amorphous phases is

shown in **Figure 3.11**, in which the area was divided into two parts by blue dash line. In the left area, the clear lattice fringes were observed. To be clearly, the area of the interface was enlarged and shown in **Figure 3.11**b. It depicted the fringe with an interplanar distance of 0.203 nm, which is accordance with the interplanar distance of metallic cobalt (111). Meanwhile, it is almost no visible lattice in the top right region, indicating the existence of amorphous VO_x-Co phase. Overall, the analysis demonstrated that the 2D nanosheets were composed by amorphous VO_x-Co and crystalline Zn-Co phases. Moreover, based on the HR-TEM image, it can be found that the Co (or Co-Zn) crystals were confined in nanosheets with smaller size (< 5 nm), which is much smaller than those of pure Co and Zn-Co alloy (17.83 nm and 16.80 nm) calculated by Scherrer equation based on XRD analysis results. From the tiny nano-crystal of Zn-VO_x-Co, it could be induced that abundant unsaturated coordination atoms can be exposed on the interface of amorphous and crystalline phases, providing rich active sites. For comparison, the TEM and HR-HRTEM images of VO_x-Co sample are displayed in **Figure 3.12**. One can see that no obvious lattice structure was observed on the VO_x-Co surface, which is also demonstrated that the doping VO_x cluster could endow the metallic Co highly disorder lattice [39, 40], enhancing the formation of amorphous phase. On the other hand, based on the TEM and XRD analyses, it is found that the doping of Zn could prevent the amorphization of Co species. Thus, doping Zn and VO_x together can generate suitable crystalline/amorphous structure with rich interfaces between the amorphous VO_x-Co and crystalline Zn-Co phases, which could play an important role in boosting the reaction kinetics since the amorphous VO_x-Co phase is propitious to the adsorption of water molecules due to the existence of unsaturated bonds while the crystalline Zn-Co phase can remedy the poor electrical conductivity of amorphous area [22, 43]. While, the elemental mapping results are

shown in **Figure 3.13**d-g, which manifested that the Zn, V, Co elements were uniformly distributed in a large scale. In addition, EDS line scanning (L_2) spectra are displayed in **Figure 3.13**i, which further confirmed the homogeneous distribution of elements in a relatively accurate range.

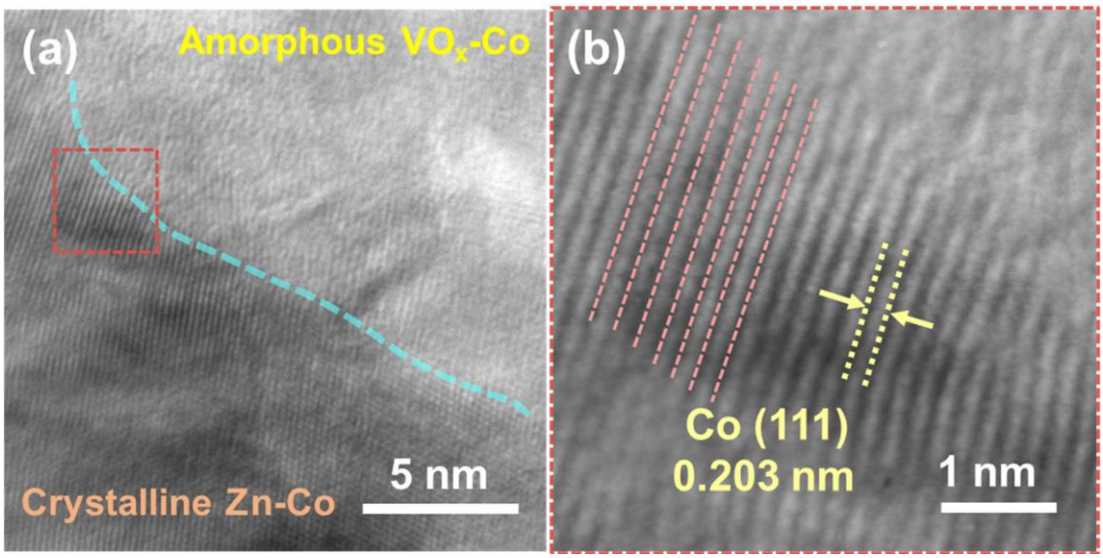

Figure 3.11 (a) TEM image of Zn-VO_x-Co; (b) HRTEM image of Zn-VO_x-Co.

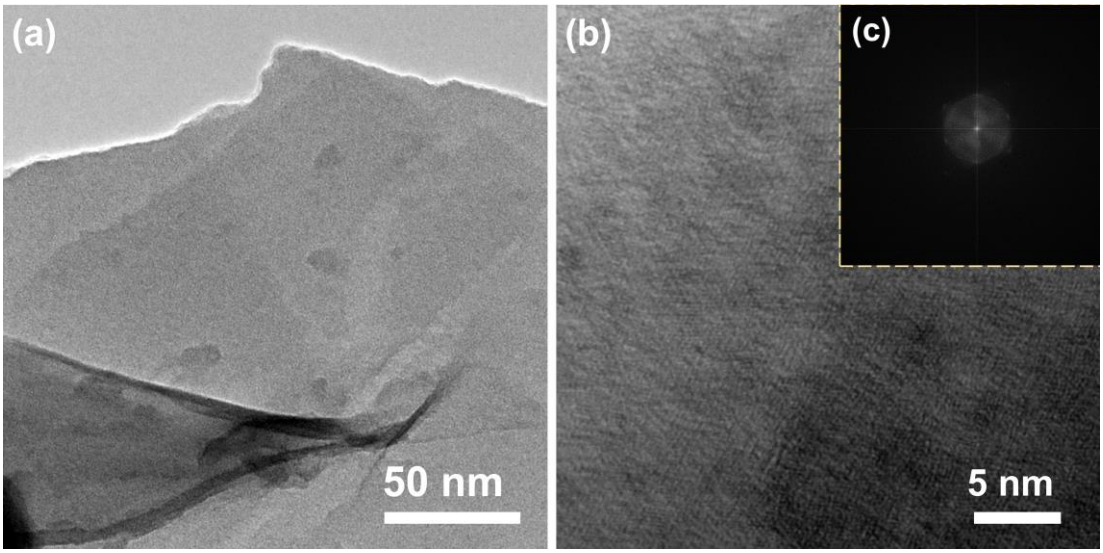

Figure 3.12 (a) TEM image of VO_x-Co; (b) HRTEM image and FFT pattern (inset) of VO_x-Co.

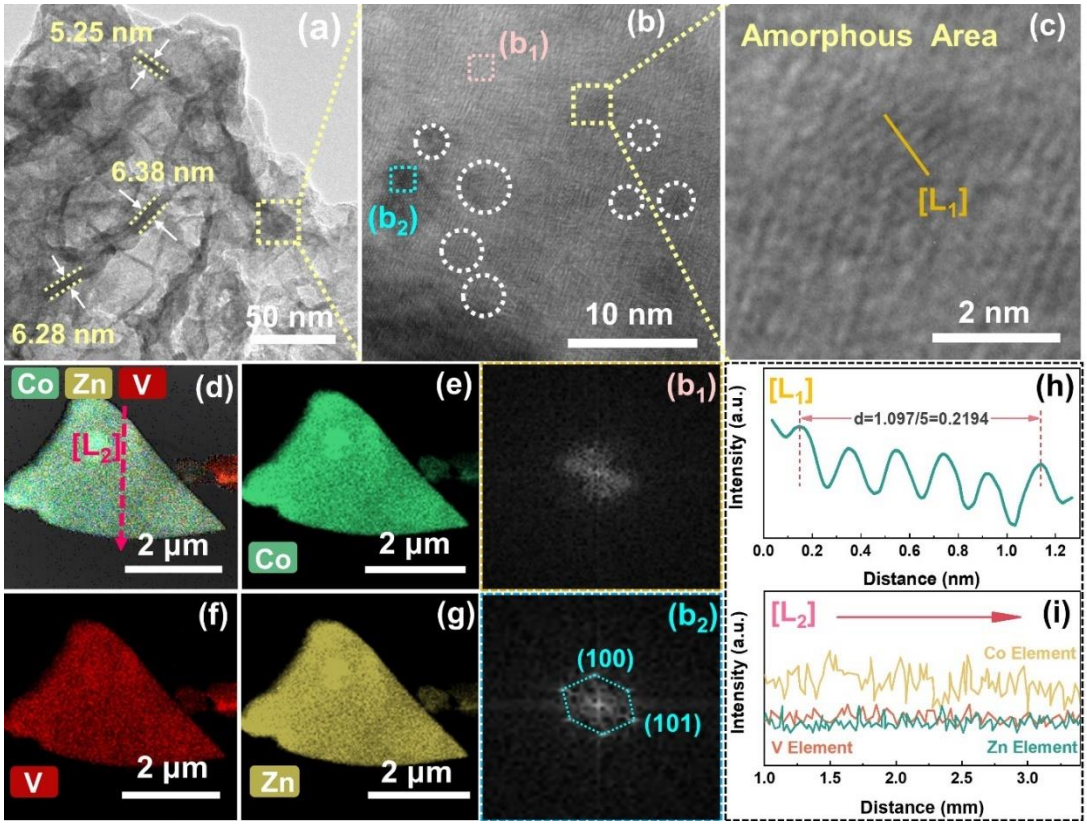

Figure 3.13 (a) TEM image of Zn-VO_x-Co 2D ultrathin nanosheets; (b) HR-TEM image showing the hetero-phase structure, in which the crystalline domains are marked by the dashed white curves. (b_1), (b_2) Corresponding FFT patterns of the selected regions marked by pink and blue squares, respectively; (c) HETEM image enlarged in (b) image; (d)-(g) TEM-EDS mappings of Zn-VO_x-Co; (h) Image intensity line profiles taken alone the yellow line in Figure c; (i) EDS line scanning spectra of Zn-VO_x-Co 2D ultrathin nanosheets in Figure d.

Figure 3.15 displays the full XPS spectra of the as-prepared samples, in which the C *1s*, V *2p*, O *1s*, Co *2p* and Zn *2p* were observed at about 285, 517, 532, 782 and 1022 eV, respectively. It revealed that the core levels of Co, Zn, V, O existed in the Zn-VO_x-Co sample, further proving that the V and Zn elements were doped on the Co based material, which is consisted with the result of EDS. High-resolution Co *2p* spectra of the samples were fitted (**Figure 3.15**b_1-b_4), in which two spin-orbit doublets at binding energies of about ~781.3 and ~797.1 eV with the spin-orbit splitting energy of around 15.8 eV can be assigned to the Co $2p_{3/2}$ and Co $2p_{1/2}$, respectively. The peak position of Co $2p_{3/2}$ in the interval from 781.08 to 781.71 eV is assigned to Co^{3+}, which is

corresponding to the Co oxide [39, 50]. Herein, the existence of oxide species should be attributed to the surface oxides formed when exposing to the atmosphere. Comparing with the binding energy of pure Co (781.26 eV, shown in **Figure 3.15**b_1), a slightly negative energy shift (781.08 eV, displayed in **Figure 3.15**b_3) of VO_x-Co was observed due to the higher oxidation degree of doping VO_x cluster [51]. Furthermore, the Co $2p_{3/2}$ peak located at 782.58 eV for VO_x- Co assigned to the Co^{2+} species, which indicated that the doped VO_x significantly affected the electron distribution of Co species [52]. It is noticed that the peak relating to Co^{2+} in Zn-VO_x-Co was positively shifted ~0.1 eV relative to that of VO_x-Co, as displayed in **Figures 3.15**b_4 and b_3, indicating that the introduction of Zn species modified the electron structure of Co species. Besides, **Figure 3.15**c shows the high-resolution XPS spectrum of V *2p*$_{3/2}$, which was distinguished at ~516 and 517.16 eV assigning to V^{4+} and V^{5+}, respectively [23, 53], revealing that the VO_x species in these two samples were at lower vanadium oxidation state. Comparing with the corresponding V^{4+} and V^{5+} peaks of VO_x-Co, those of Zn-VO_x-Co had an obvious negative shift, indicating that the Zn doping affected the valence of V element (the binding energies of Co and V elements were summarized in **Table 3.1**). In addition, as shown in **Figure 3.14**, four fitting peaks of O *1s* of Zn-VO_x-Co sample were obtained. They are the peaks at 592.82, 530.5, 531.79 and 533.09 eV, corresponding to Co-O bond, Zn-O bond, VO_x cluster and H-O bond relating to the adsorbed H_2O molecule, respectively. Based on these results, it can be deduced that the electron structures of Co, VO_x and Zn species should interact with each other, which were further proved by the charge density distribution. For the Zn-Co (**Figure 3.15**d), it showed weak electron transfer between Zn and Co atoms. After doping VO_x cluster (**Figure 3.15**e), numerous electrons could transfer from the Co atom to VO_x. Moreover, for the dual-doping of Zn and VO_x (**Figure 3.15**f), the transfer of electrons from Co to

both Zn and VO_x species could occur [54, 55]. That is, the co-existence of VO_x and Zn could reduce the electron density on the Co surface, leading to the reduced electrons in the bonding orbitals, which will weaken the Co-H bond and in turn favor the H_{ads} desorption, and thereby improving the HER activity. Combining with the XRD and TEM results, the amorphous phase composed of Co and VO_x species with abundant variable valences should provide a large amount of unsaturated chemical bonds to balance the adsorption and desorption processes of hydrogen atoms. Meanwhile, since the introduced Zn species could combine with the Co to form alloy, which can improve the conductivity of sample for the faster electron transfer. Thus, the synergy between the amorphous and crystalline phases could significantly boost the intrinsic electrocatalytic performance of Zn-VO_x-Co based electrode. Besides, the valence-band spectra of as-prepared catalysts were measured. As shown in **Figure 3.14b**, the maximum values of valance bands for pure Co, Zn-Co VO_x-Co and Zn-VO_x-Co were nearly 0.28, 1.08, 0.68 and 0.78 eV, respectively. Since the valance electrons close to Fermi level mainly contribute to the d-state, the d-band center could be adjusted by doping Zn or VO_x heteroatom atoms.

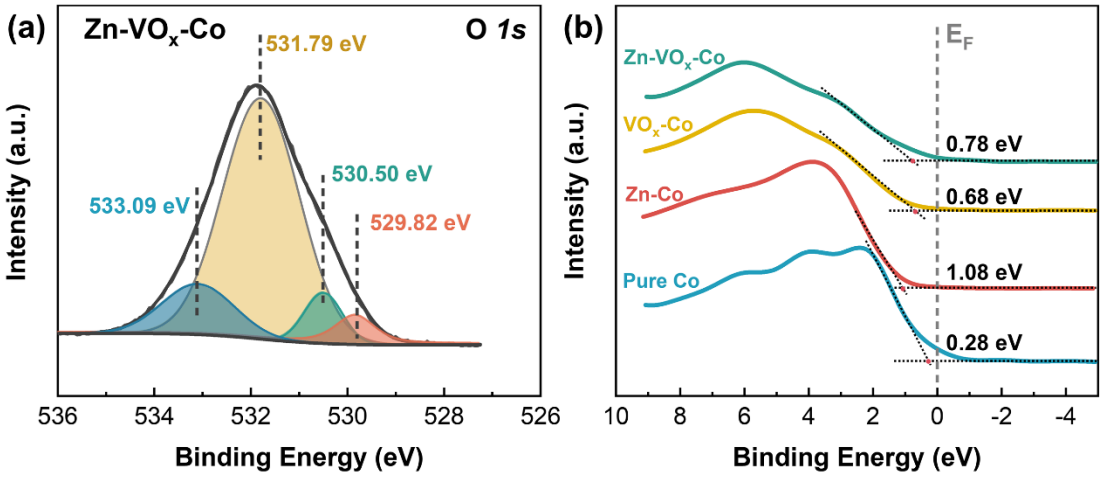

Figure 3.14 (a) High resolution XPS spectrum of O *1s* in Zn-VO_x-Co electrocatalyst and (b) Valence-band spectra of pure Co, Zn-Co, VO_x-Co and Zn-VO_x-Co.

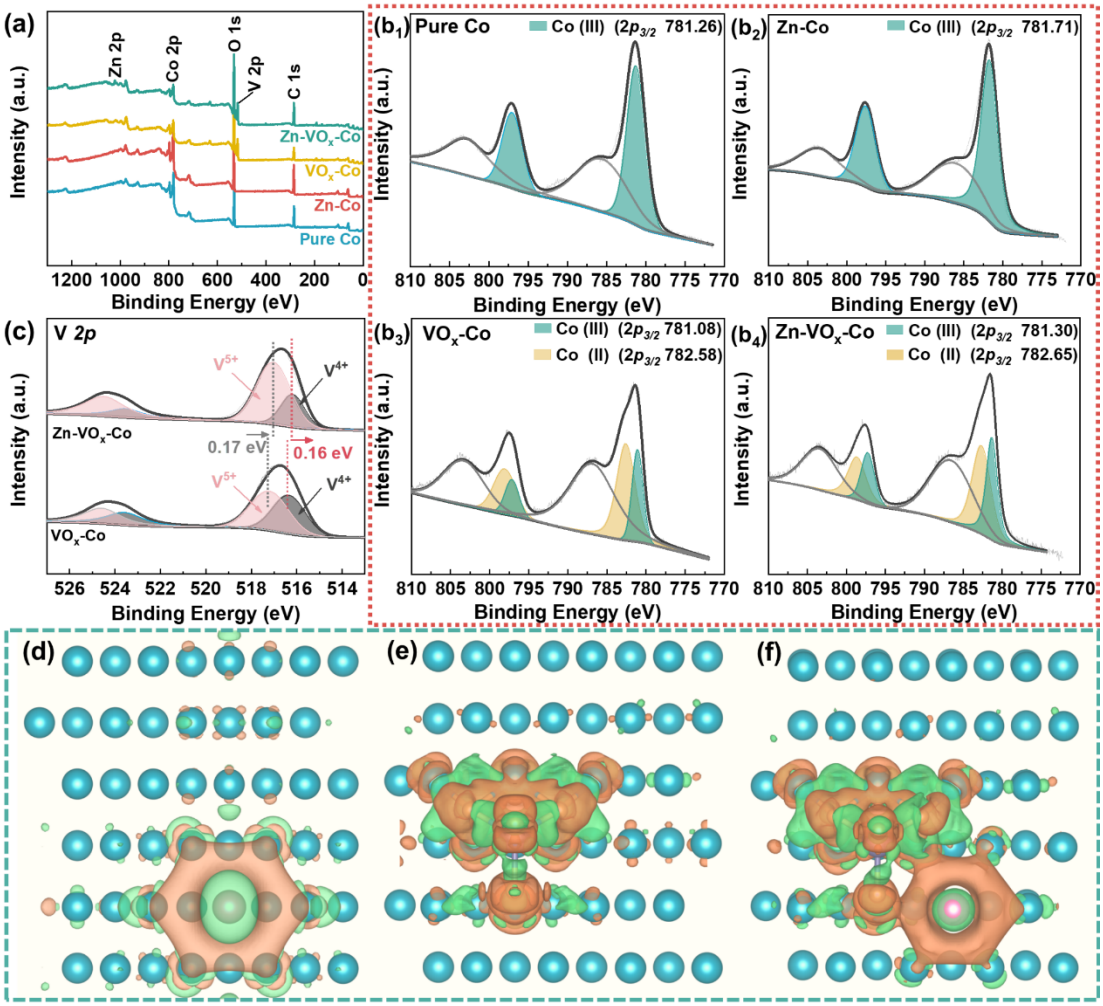

Figure 3.15 (a) Full XPS profiles of pure Co, Zn-Co, VO_x-Co and Zn-VO_x-Co electrocatalysts; (b) High resolution XPS spectra of Co *2p* of pure Co (b_1), Zn-Co (b_2), VO_x-Co (b_3) and Zn-VO_x-Co (b_4); (c) High resolution XPS spectra of V *2p* of VO_x-Co and Zn-VO_x-Co; and the charge distributions in (d) Zn-Co, (e) VO_x-Co and (f) Zn-VO_x-Co, respectively.

Table 3.1 Co $2p_{3/2}$ and V $2p_{3/2}$ binding energies of pure Co, Zn-Co, VO_x-Co and Zn-VO_x-Co electrocatalysts.

Catalysts	**Co $2p_{3/2}$ (eV)**		**V $2p_{3/2}$ (eV)**	
	Co (III)	**Co (II)**	**V (IV)**	**V (V)**
Pure Co	781.26		-	-
Zn-Co	781.71		-	-
VO_x-Co	781.08	782.58	516.33	517.19
Zn-VO_x-Co	781.30	782.65	516.17	517.02

Additionally, the surface wettability of as-prepared electrodes was also investigated. Generally, different catalysts coated on the CFP could result in diverse surface roughness, which can affect the surface wettability [56]. As shown in **Figure 3.16**, comparing with the water contact angle on the surface of pure Co film (the left is 132.3° and the right is 132.7°), the average water contact angles of the left and right on the surface of Zn-Co film were increased a little to 134.3° and 134.5°, respectively, indicating the hydrophobic nature of both pure Co and Zn-Co based electrodes. In contrast, for the VO_x-Co film, the average water contact angle significantly reduced (52.8°), and especially, for the Zn-VO_x-Co film, the average water contact angles were further reduced to 29.6° (left) and 29.5° (right), suggesting that Zn-VO_x-Co film had a hydrophilic surface, which should be more favorable for the aqueous electrolyte solution contacting with the electrocatalyst, facilitating the HER kinetics and finally enhancing the catalysis performance.

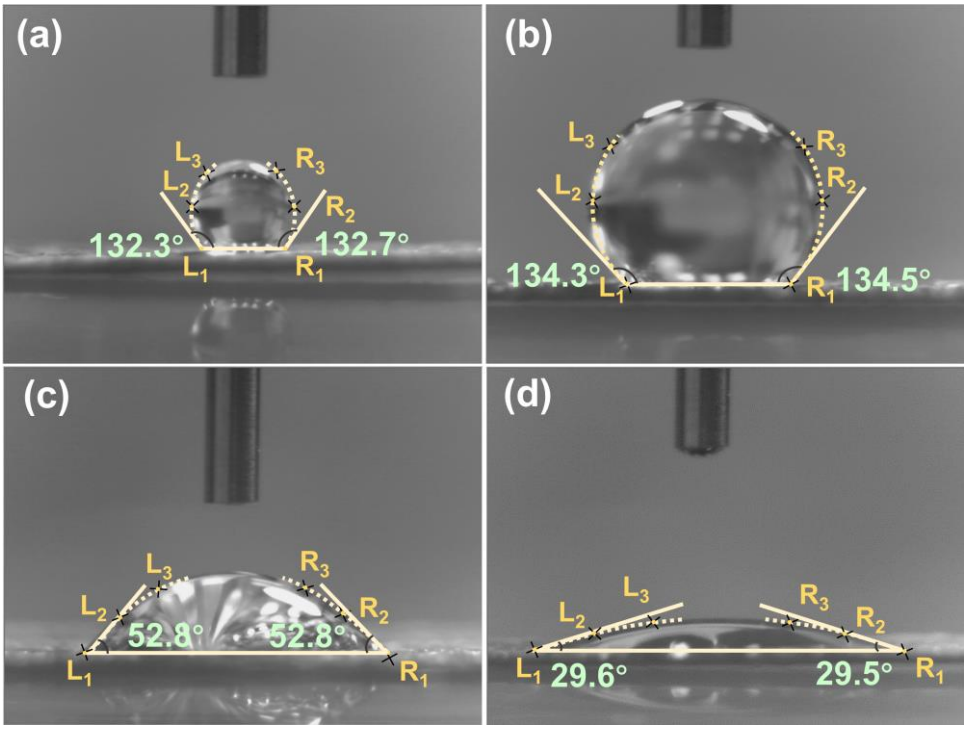

Figure 3.16 Water contact angles on (a) pure Co; (b)Zn-Co; (c) VO_x-Co and (d) Zn-V O_x-Co surfaces.

3.3.2 Electrocatalytic property

HER performances of as-prepared electrocatalysts were evaluated by monitoring the polarization curve in 1 M KOH solution. Firstly, to investigate the effect of doping amounts of Zn and VO_x, a series of electrodes were prepared by changing the concentrations of $ZnSO_4 \cdot 7H_2O$ (5, 8, 10, 12 mM) and NH_4VO_3 (5, 8, 10, 12 mM). As shown in **Figures 3.17a** and **3.17b**, the Zn-VO_x-Co electrocatalyst synthesized with a solution containing 10 mM $ZnSO_4 \cdot 7H_2O$ and 10 mM NH_4VO_3 exhibited the best performance, which further demonstrated that the ratio of amorphous and crystalline phases could affect the activity of HER. For comparison, the HER performances of Zn-VO_x, pure Co, Zn-Co, VO_x-Co prepared with the same molar concentration for each element as those in the best Zn-VO_x-Co electrocatalyst were also tested under the same condition, and the results are shown in **Figure 3.18**a. While, **Figure 3.18**b compares the overpotentials at j=-10 mA cm^{-2} (the orange column) and j=-50 mA cm^{-2} (the green column). Obviously, the Zn-VO_x-Co electrocatalyst showed much remarkable HER performance, achieving the standard current density of 10 mA cm^{-2} at an overpotential as low as 72 mV (without iR correction), which is quite smaller than those of VO_x-Co (137 mV), Zn-Co (213 mV), pure Co (336 mV) and Zn-VO_x (792 mV) electrocatalysts. For comparison, the LSV curve of the Zn-VO_x-Co electrocatalyst with iR-compensation is also shown as the red dash line in **Figure 3.18**a, in which the overpotential was only 46 mV, which is even lower than that of 20 % commercial Pt-C (62 mV). Meanwhile, the Zn-VO_x-Co ranked the top level among those reported catalysts (**Figure 3.18**c and **Table 3.2**). **Figure 3.18**d shows the corresponding Tafel plots. For the Zn-VO_x-Co electrocatalyst, the Tafel slope was as low as 75 mV dec^{-1}, which is much smaller than those of VO_x-Co (115 mV dec^{-1}), Zn-Co (117 mV dec^{-1}), pure Co (170 mV dec^{-1}) and Zn-VO_x (339 mV dec^{-1}) electrocatalysts, indicating the

faster kinetics. It also suggested that the HER over Zn-VO_x-Co electrocatalyst should follow a Volmer-Heyrovsky mechanism with a first step of $H_2O+e^-=H_{ads}+ OH^-$ and a secondary step of $H_2O+e^-+H_{ads}=H_2+OH^-$ (H_{ads} means the adsorbed hydrogen atoms). To evaluate the HER intrinsic performance, the exchange current density (j_0) was calculated by extrapolating the Tafel curve to zero overpotential. As summarized in **Table 3.3**, the j_0 of Zn-VO_x-Co was 1.3 mA cm^{-2}, which is much higher than those of VO_x-Co (0.63 mA cm^{-2}), Zn-Co (0.13 mA cm^{-2}), pure Co (0.10 mA cm^{-2}) and Zn-VO_x (0.05 mA cm^{-2}) electrocatalysts. The higher j_0 means a higher intrinsic electron transfer rate between the electrode and electrolyte [55]. Thus, the lower Tafel slope and the higher j_0 for Zn-VO_x-Co sample indicated that it had more excellent HER performance, which should be attributed to its special heterostructure with the distinctive 2D ultra-thin nanosheets combined with amorphous and crystalline phases as stated above.

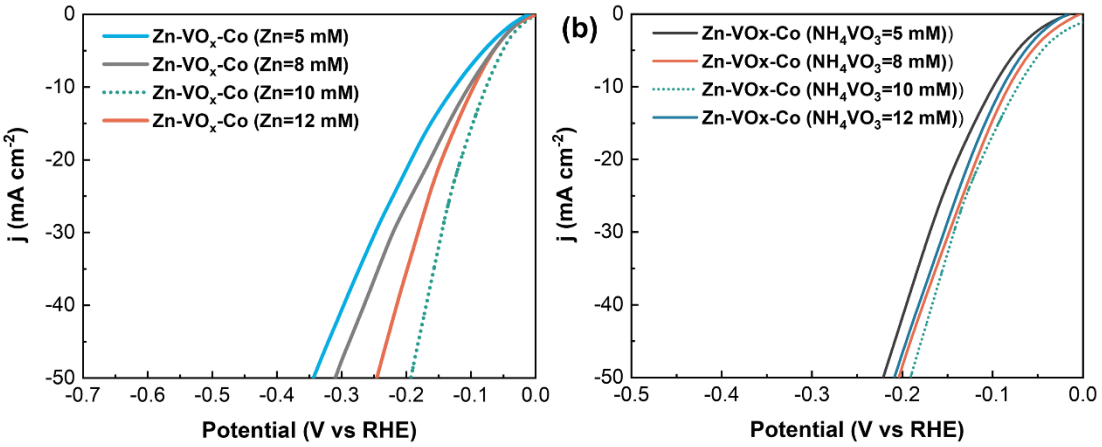

Figure 3.17 LSV curves of (a) Zn-VO_x-Co based electrodes prepared by using different amounts of Zn precursor (molar amount) during the electrodeposition. And (b) Zn-VO_x-Co based electrodes prepared by using different amounts of NH_4VO_3 precursor (molar amount) during the electrodeposition.

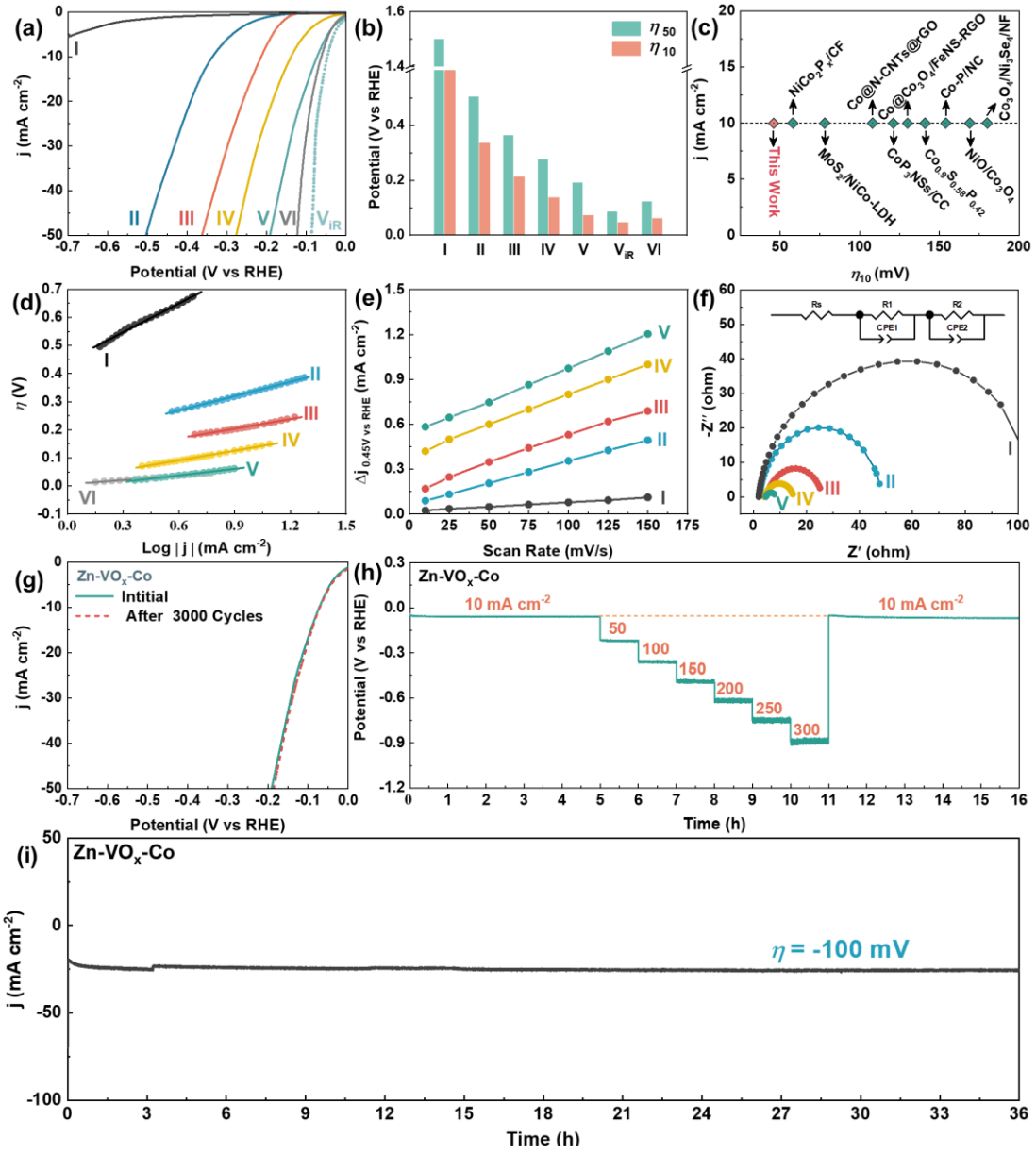

Figure 3.18 (a) Polarization curves of Zn-VO_x (I), pure Co (II), Zn-Co (III), VO_x-Co (IV), Zn-VO_x-Co (V) , 20% Pt-C (VI), and Zn-VOx-Co based electrodes after iR compensation; (b) Relationship between overpotential; (c) Comparison of Zn-VO_x-Co with other works; (d) Tafel plots for HER; (e) Estimation of C_{dl} by plotting the current density variation, data obtained from **Figure 3.19**; (f) Nyquist plots of as-prepared electrodes; (g) Durability of the Zn-VO_x-Co with an initial polarization curve and after 3000 cycles in 1 M KOH solution; (h) Multi-current step test of Zn-VO_x-Co based electrode at current densities of 10, 50, 100, 150, 200, 250 and 300 mA cm^{-2}; (i) the stable operation of the Zn-VO_x-Co based electrode running at -100 mV for 36 h.

Table 3.2 Comparison of HER catalytic activities with the reported HER catalysts from Co-based materials after iR-correction in 1M KOH.

Catalysts	Substrate	η_{10}	Reference
Zn-VO_x-Co	CFP	46	This work
CoO_x@CN	GCE	232	*J. Am. Chem. Soc.* **2015**, *137*, 2688.
Co-P/NC	RDE	154	*Chem. Mater.* **2015**, *27*, 76367642.
Co-NRCNTs	GCE	370	*Nano Res.* **2018**, *11*, 323.
Co@N-CNTs@rGO	GCE	108	*Adv. Mater.* **2018**, *30*, 1802011.
Fe-Co_3O_4/CNTs	GCE	210	*Int. J. Hydrog. Energy* **2018**, *43,*
$NiCo_2S_4$ NW/NF	NF	210	*Adv. Funct. Mater.* **2016**, *26*, 4661.
Co-S-FTO	FTO	480	*J. Am. Chem. Soc.* **2013**, *135,*
CoP_3NS_s/CC	CC	121	*J. Alloys Compd.* **2017,** *729*, 203.
$Co_{0.9}S_{0.5}8P_{0.42}$	GCE	141	*ACS Nano* **2017**, *11,* 11031.
$NiCo_2P_x$/CF	CF	58	*Adv. Mater.* **2017**, *29,* 1605502.
ECA-CoNPs@C	CC	58	*J. Mater. Chem. A* **2016**, *4,* 10014.
MoS_2/NiCo-LDH	GCE	78	*Joule* **2017**, *1,* 220.
NiO/Co_3O_4	CFP	169.5	*Chem. Commun.* **2019**, *55***,** 6515.
Co@Co_3O_4/FeNS-GO	GCE	130	*Electrochim. Acta* **2019***, 323,*
Co_3O_4@Ni_3Se_4/NF	NF	180	*ChemNanoMat.* **2019***, 5*, 814.

Table 3.3 Summary of the HER performances of Zn-VO_x, pure Co, Zn-Co, VO_x-Co and Zn-VO_x-Co in 1 M KOH solution.

Catalysts	η_{10}	η_{50}	Tafel	j_0	C_{dl}	R_{ct}
Zn-VO_x	792	-	339	0.05	0.601	67.35
Pure Co	336	504	170	0.10	2.91	46.26
Zn-Co	213	362	117	0.13	3.70	18.69
VO_x-Co	137	276	115	0.63	4.08	10.82
Zn-VO_x-Co	72	191	75	1.30	4.44	4.59
Zn-VO_x-Co (iR-Correction)	46	84	-	-	-	-

Furthermore, the electrochemical surface areas (ECSAs) of the as-prepared electrocatalysts were also determined by using the double-layer capacitance (C_{dl}) [55], which was calculated by the liner relationship of Δj ($\Delta j=(j_a-j_c)/2$ at 450 mV versus RHE and the scan rate at the Faradaic silence potential (**Figure 3.18**e). Herein, the values of C_{dl} were obtained from **Figure 3.19** and summarized in **Table 3.2**. As a result, the C_{dl} values of Zn-VO_x-Co, VO_x-Co, Zn-Co, pure Co and Zn-VO_x electrocatalysts were 4.44, 4.04, 3.70, 2.91 and 0.60 mF cm^{-2}, respectively. The high C_{dl} value of Zn-VO_x-Co electrocatalyst further indicated that the combination of amorphous and crystalline structures induced more exposed active edge sites, which can facilitate the transfer of electrons and significantly boost the HER performance [10]. To further determine the intrinsic activity of individual active site, j_{ECSA}-normalized polarization curves were also obtained. As shown in **Figure 3.20**, the Zn-VO_x-Co electrocatalysts exhibited larger j_{ECSA} value when compared with Zn-VO_x, pure Co, Zn-Co and VO_x-Co electrocatalysts, further confirming that it had higher intrinsic activity. In addition, the electrochemical impedance spectroscopy (EIS) performance was evaluated by the charge transfer resistance (R_{ct}), which is controlled by measuring the size of the semicircle on the Z′-axis in the high-frequency range. **Figure 3.18**f shows the corresponding Nyquist plots. One can see that Zn-VO_x-Co based electrode possessed the minimal R_{ct} of 4.59 Ω among all the prepared electrodes. Herein, it should be noted that the R_{ct} value of VO_x-Co based electrode was as high as 10.82 Ω, however, after doping Zn with an adequate amount, the conductivity was obviously increased. Meanwhile, the small R_{ct} value of Zn-VO_x-Co based electrode should be also benefit for the fast electrocatalytic Faradaic process with superior HER kinetics [8, 24]. Obviously, the results relating to R_{ct} are consistent with the trends of activity performances, Tafel slopes and the values of C_{dl}. In addition, the theoretical and

experimental H_2 evolution amounts over Zn-VO_x-Co were measured and shown in **Figure 3.21**, the experimental H_2 evolution exhibited nearly 100% Faradic efficiency, which indicated that the electrical energy could be efficiently converted to chemical energy.

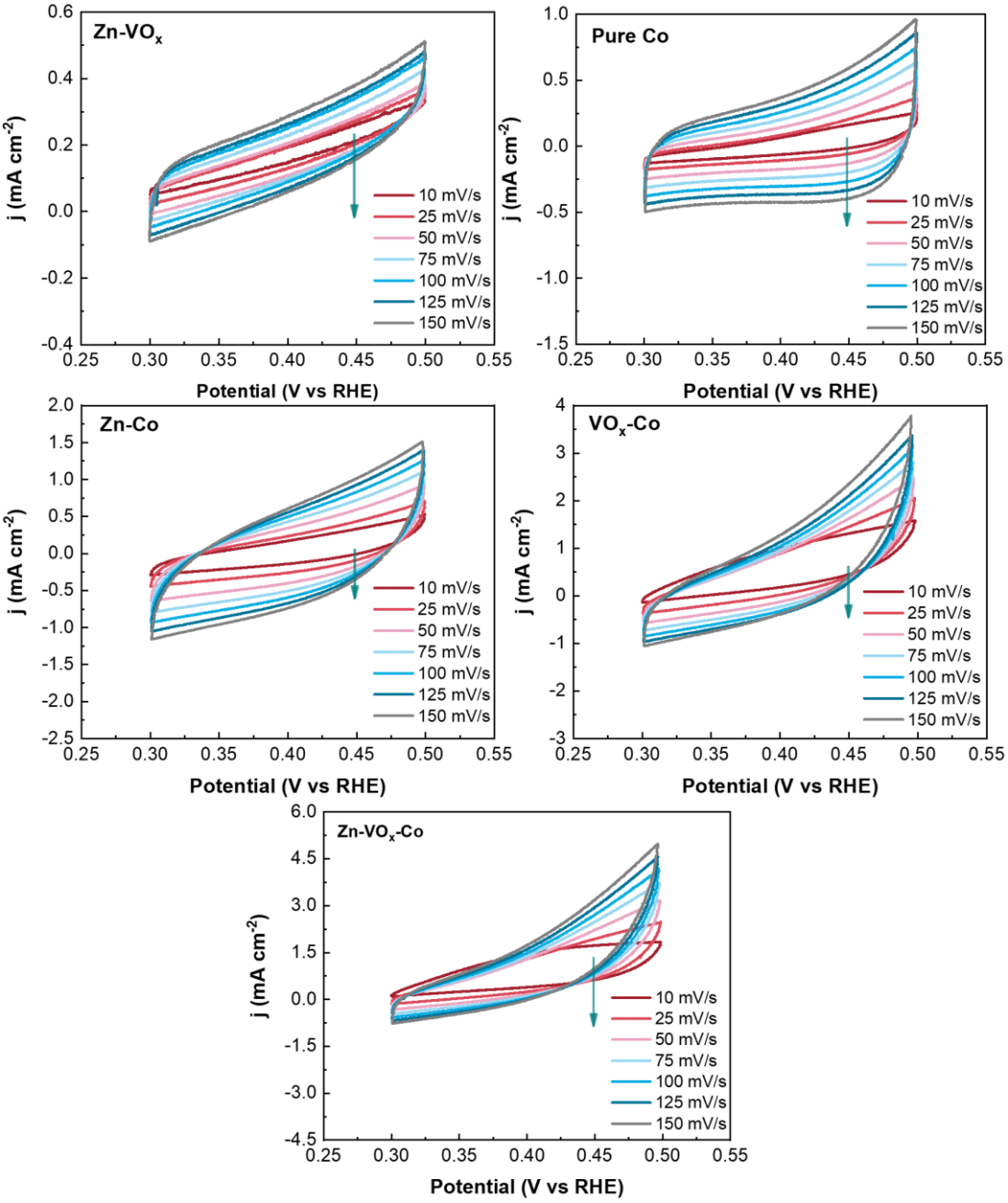

Figure 3.19 Cyclic voltammograms of (a) Zn-VO_x; (b) pure Co; (c)Zn-Co; (d) VO_x-Co and (e) Zn-VO_x-Co based electrodes with various scan rates in 1M KOH solution.

Long-term stability of the Zn-VO_x-Co electrocatalyst coated electrode was firstly examined via a continuous cycling test for 3000 cycles in 1 M KOH solution. As shown in **Figure 3.18**g, after the 3000th cycle test, the electrode afforded a similar *j*-V curve as that in the initial cycle. Then, a multi-step chronopotentiometry test was also performed for this electrode, in which the test was carried out at 10 mA cm^{-2} for 5 h at first and then the tests from 10 to 300 mA cm^{-2} with the increasement of 50 mA cm^{-2} every 1 h were continued, and finally the current density was set back to 10 mA cm^{-2} after the examination at 300 mA cm^{-2} and kept for 5 h. As shown in **Figure 3.18**h, the potential maintained constantly under each step. In addition, a long-term stability at η =-100 mV was also measured for the Zn-VO_x-Co electrocatalyst based electrode. As displayed in **Figure 3.18**i, a steady HER performance without obvious decrease over 36 h was obtained. These three kinds of stability tests indicated the outstanding stability and mechanical robustness of Zn-VO_x-Co electrocatalyst coated electrode in 1 M KOH solution. After 36 h stability test for Zn-VO_x-Co sample, the HR-TEM images, TEM-EDS mappings and the corresponding element line scans were observed. As shown in **Figure 3.22**, the robust crystalline/amorphous heterostructure still maintained. Besides, the Co, Zn and V elements also distributed uniformly on the spent Zn-VO_x-Co electrocatalyst. The full XPS spectrum (**Figure 3.23**a) confirmed the similar existence of Zn, Co and V elements as the fresh one. Moreover, it is obvious that two additional spin-orbit doublets at binding energies of about ~778.6 and ~793.1 eV appeared in Co *2p* spectra (**Figure 3.23**b), which corresponds to the metallic Co species, indicating that after the stability testing, partial of surface cobalt oxide was reduced to the metallic Co, which is consistent with the structure of catalyst. Besides, the valence band spectrum after 36-h stability test for the Zn-VO_x-Co sample was also investigated. As shown in **Figure 3.24**, the maximum value of valance band was 0.75 eV, which was almost the

similar as the fresh one (0.78 eV). It means that the d-band center had no obvious shift, which further indicated the outstanding stability for Zn-VO_x-Co.

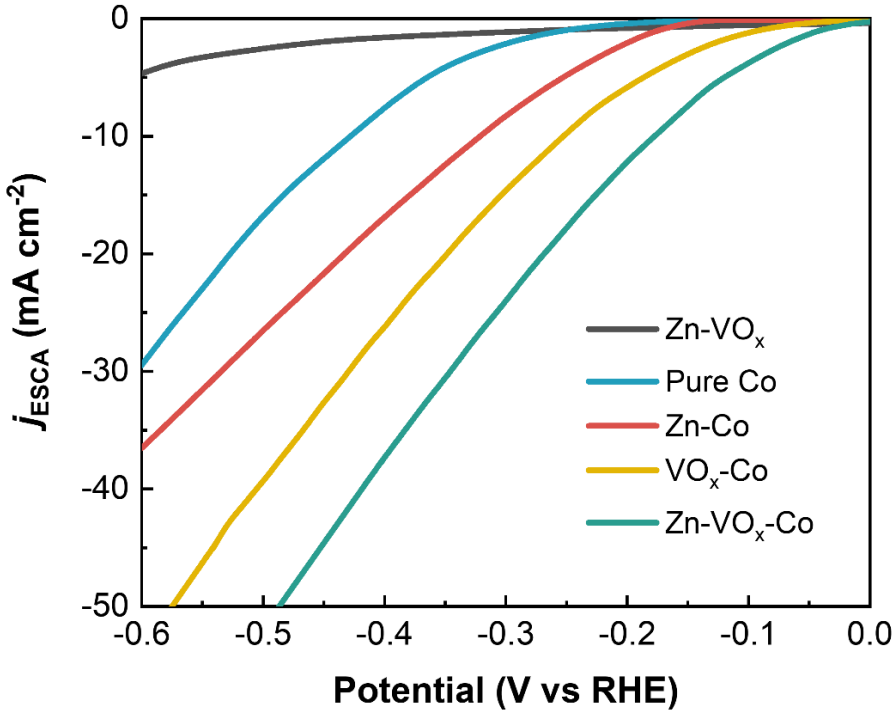

Figure 3.20 HER ECSA-normalized LSV curves of Zn-VO_x, pure Co, Zn-Co, VO_x-Co and Zn-VO_x-Co.

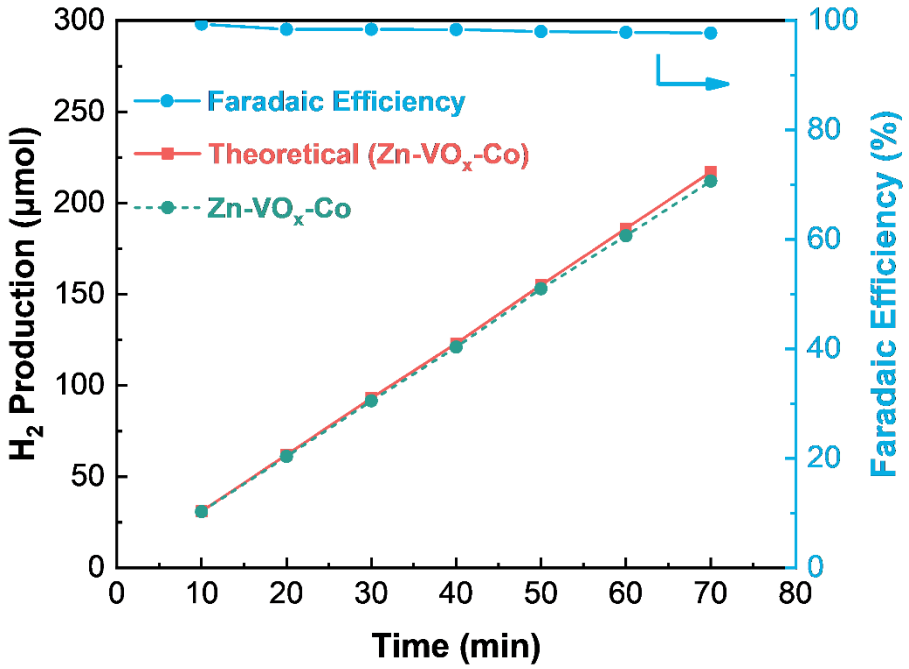

Figure 3.21 Time dependence of H_2 production over Zn-VO_x-Co catalyst

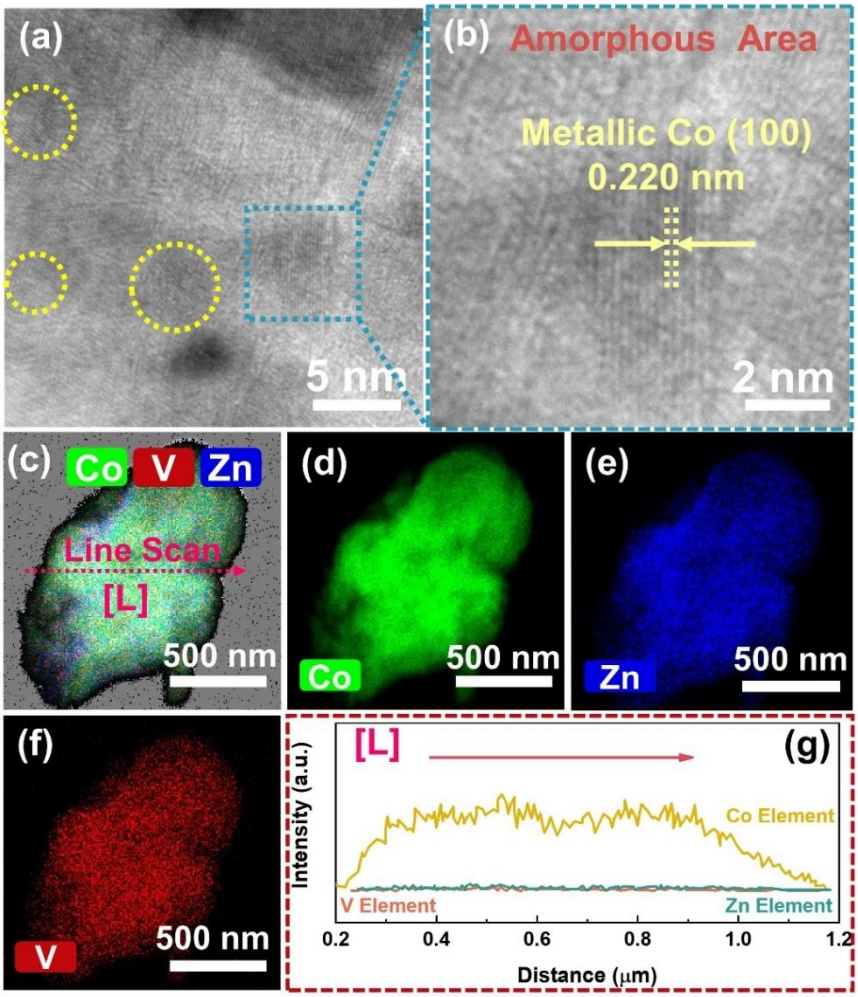

Figure 3.22 (a) and (b) TEM images; (c)-(f) TEM-EDS mapping images of Co, Zn, V and (g) Corresponding EDS line scanning spectra of Zn-VO_x-Co after stability test.

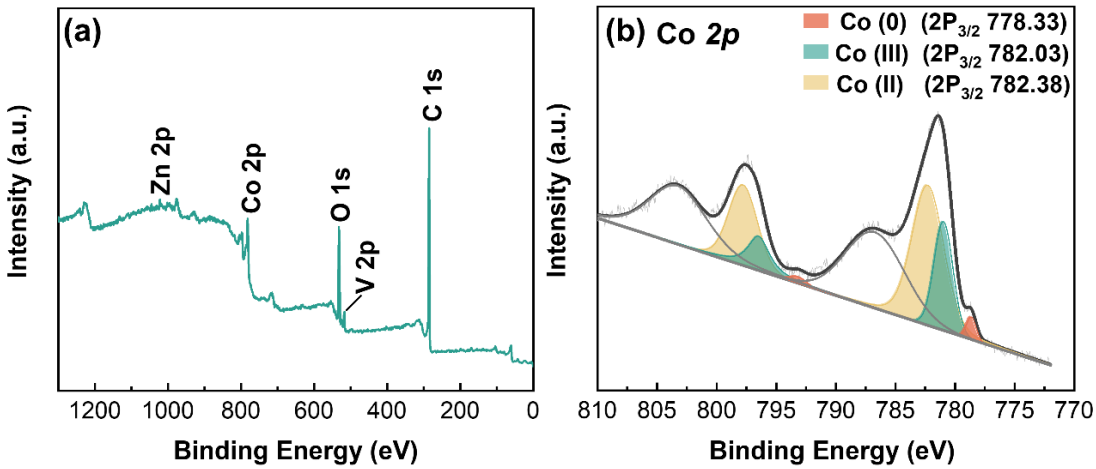

Figure 3.23 (a) Full XPS profiles and high resolution XPS spectra of (b) Co *2p* in Zn-VO_x-Co electrocatalysts after the stability test.

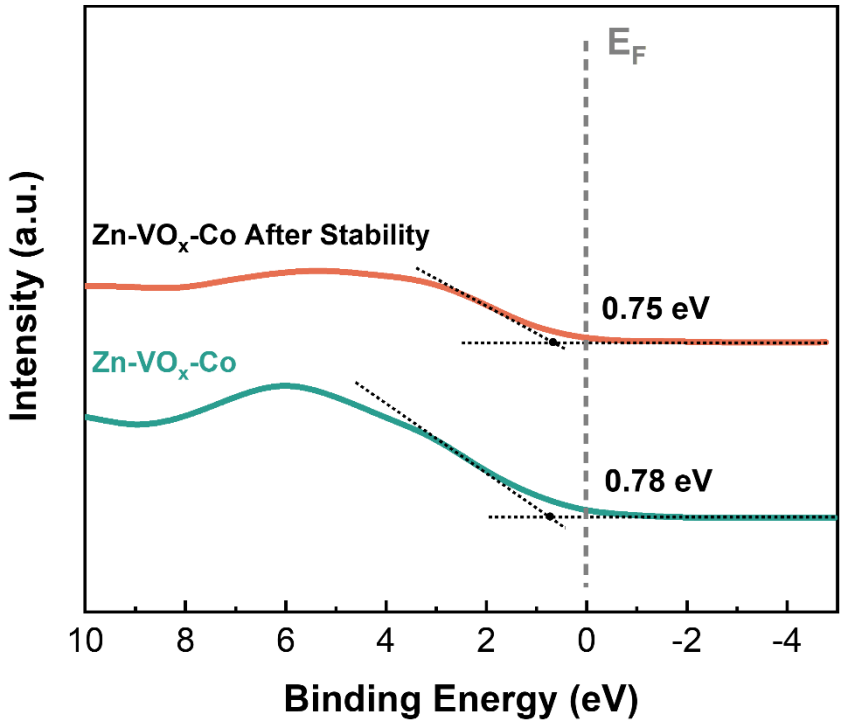

Figure 3.24 Valence-band spectra of Zn-VO_x-Co and Zn-VO_x-Co electrocatalysts after the stability test.

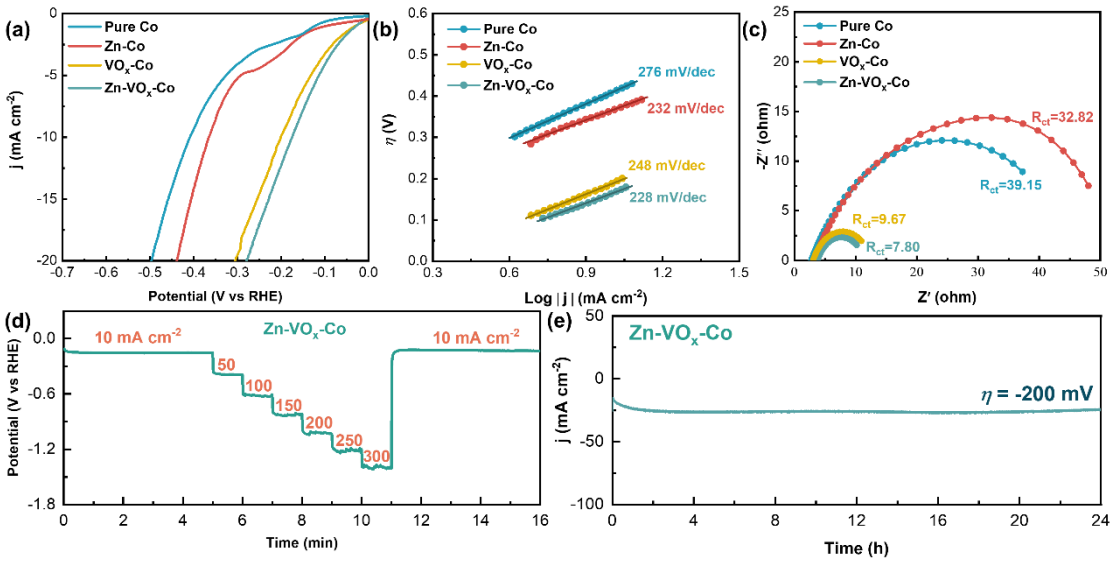

Figure 3.25 (a) Polarization curves, (b) Tafel plots, (c) Nyquist plots of pure Co, Zn-Co, Zn-VO_x and Zn-VO_x-Co based electrodes; (d) multi-current step test of Zn-VO_x-Co based electrode at current densities of 10, 50, 100, 150, 200, 250 and 300 mA cm^{-2}; (e) stable operation of Zn-VO_x-Co running at -200 mV in 1 M PBS solution for 24 h.

The HER performances of these electrocatalysts in the neutral 1 M PBS solution were also evaluated via the same method without iR-correction. As shown in **Figure 3.25**a, the Zn-VO_x-Co based electrode required an overpotential of 174 mV to drive a current density of 10 mA cm^{-2}, which is lower than those of other electrodes of VO_x-Co (200 mV), Zn-Co (365 mV) and pure Co (408 mV). Meanwhile, the corresponding Tafel slopes (**Figure 3.25** (b)) also indicated that the Zn-VO_x-Co based electrode owned the minimum Tafel slope of 228 mV dec^{-1}, lower than those of VO_x-Co (248 mV dec^{-1}), Zn-Co (232 mV dec^{-1}) and the pure Co (276 mV dec^{-1}) based electrodes. The corresponding Nyquist plots illustrated in **Figure 3.25**c exhibited that the Zn-VO_x-Co based electrode had a R_{ct} of as low as 7.8 Ω, suggesting the rapid electron transfer ability during the HER even in the neutral solution. In addition, a multi-step chronopotentiometry test was also performed for this electrode, in which the test was carried out at 10 mA cm^{-2} for 5 h at first and then the tests from 10 to 300 mA cm^{-2} with the increasement of 50 mA cm^{-2} every 1 h were continued, and finally the current density was set back to 10 mA cm^{-2} after the examination at 300 mA cm^{-2} and kept for 5 h. As shown in **Figure 3.25**d, the current density promptly leveled out at every current density value, indicating its stability at different current densities. Meanwhile, the HER durability test at a stable η=-200 mV (**Figure 3.25**e) also showed no obvious attenuation in 24 h of operation, suggesting the outstanding stability of Zn-VO_x-Co based electrode in the neutral electrolyte solution.

3.3.3 DFT calculations

DFT calculations were employed to fundamentally explore the intrinsic electrocatalytic activity of as-prepared catalysts in this study. Due to the short-range order of amorphous structure and similar chemical bond between amorphous and crystal counterparts [57], the crystalline models were adopted to understand the

intrinsic electrocatalytic activity. Herein, the conductivities of pure Co and Zn-Co were evaluated via DOS as shown in **Figure 3.26.** One can see that the Zn-Co exhibited a stronger DOS intensity near the Fermi level when compared with that of pure Co, suggesting that the Zn-Co possessed superior electrical conductivity.

Besides, based on the characterization results, the top and side views of the optimized catalyst models of pure Co (100), Zn-Co, VO_x-Co and Zn-VO_x-Co are illustrated in **Figure 3.27**. The incorporation of Zn or VO_x on the metallic cobalt surface resulted in a change of state within the cobalt, which can adjust the value of the d-band center (ε_d) relative to Fermi level (E_F). According to the d-band center theory, ε_d closer to the Fermi level indicates the stronger binding interaction between the electrode and adsorbates. From the results of projected density of states (*p*DOS) calculation (**Figure 3.29** a-d), the surface d-band center relative to the Fermi level was calculated to be -1.37 eV for pure Co, higher than those of -1.47, -1.41 and -1.43 eV for Zn-Co, VO_x-Co and Zn-VO_x-Co, respectively, which is corresponding to the results of valence-band spectra (**Figure 3.14b**). For the pure Co, the highest ε_d value is consistent with the conclusion of lower reaction rate. After doping Zn or VO_x, the ε_d was far away from the Fermi level, which indicated that the interaction between H adsorption and Co surface of Zn-Co, VO_x-Co or Zn-VO_x-Co should be weakened, which is coincided to the conclusion of XPS results. On the one hand, **Figure 3.28** shows the models of pure Co and VO_x-Co samples with serial numbers, where the numbers 3, 19, 20 were selected to calculate the distance and the angle (the details are shown in **Table 3.4**) between Co atoms. It is obvious that the distance between Co atoms was changed significantly (e.g., the distance of Co_3 to Co_{19} is 2.39587 Å for pure Co and 2.47092 Å for VO_x-Co; the angles of Co_{19}-Co_{20}-Co_3 are 59.245° for pure Co and 61.0499° for VO_x-Co), which means that the doping of VO_x cluster changed the lattice structure of

Co species. For the VO_x-Co (ε_d =-1.41 eV), the ε_d was close to that of Co (ε_d =-1.37 eV), indicating that the Co-H bond was too strong to facilitate the desorption of H atoms. After the dual-doping of Zn and VO_x, partial amorphous phases were replaced by crystalline ones, which can enhance the transfer of electrons on the metallic Co surface, resulting in the ε_d located at the optimal position (ε_d =-1.43 eV). For contrast, ε_d of the crystalline Zn-Co (-1.47 eV) was too far from the Fermi level. In this case, it is hard to form stable reaction intermediates (Co-H) because of the too weak bonding between H and Co on the surface, which can decrease the intrinsic HER activity. On the other hand, the side views of charge density distributions of Zn-Co and Zn-VO_x-Co are displayed in **Figure 3.30**, in which Zn element shows the discrete effect for the electrons on the Co surface since the doped Zn element could affect a huge range (until the 6th layer of Co atoms). In addition, the strong electron transfer might result in the over desorption of Co-H, thereby leading to the over shift-down of ε_d. However, the electron transfer of Zn-Co was obviously decreased by the doping of VO_x (only had the effect to the first 4 layers of Co atom). As such, the VO_x could weaken the degree of electron transfer and make the ε_d located at an optimal position. Thus, the dual-doping of Zn and VO_x resulted in a highest intrinsic activity as corrected by ECSA (**Figure 3.29**f). Additionally, the free energy of hydrogen adsorption (ΔG_{H^*}) is also a crucial criterion to evaluate the HER performance of the electrode. According the side (**Figure 3.29**e) and top views (**Figure 3.31**) of the optimized structure of adsorption H on the four models, the calculation results of ΔG_{H^*} are displayed in **Figure 3.29**g. It is revealed that the free energy of H (H*) on the Zn-VO_x-Co surface closed to zero, which means that Zn-VO_x-Co could balance the adsorption and desorption of H to facilitate the HER process.

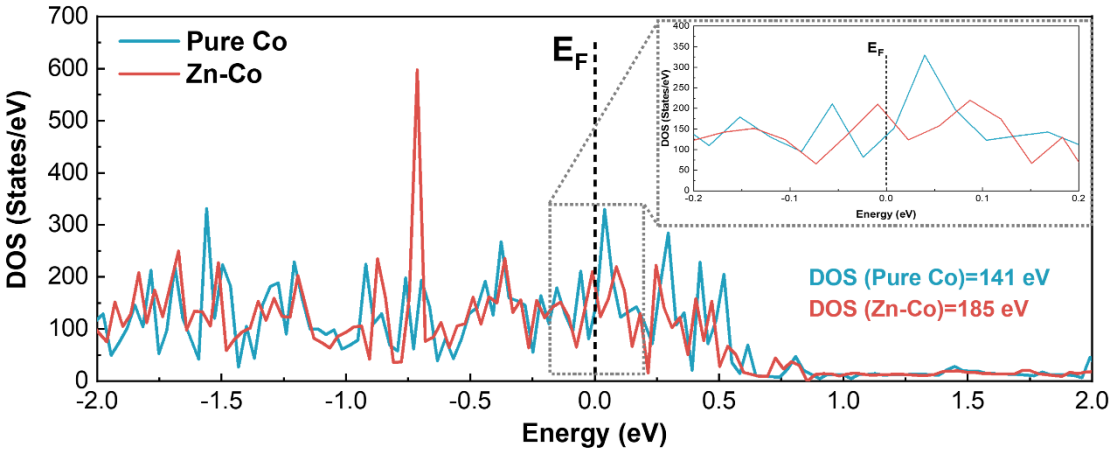

Figure 3.26 Density of states (DOS) of pure Co and Zn-Co

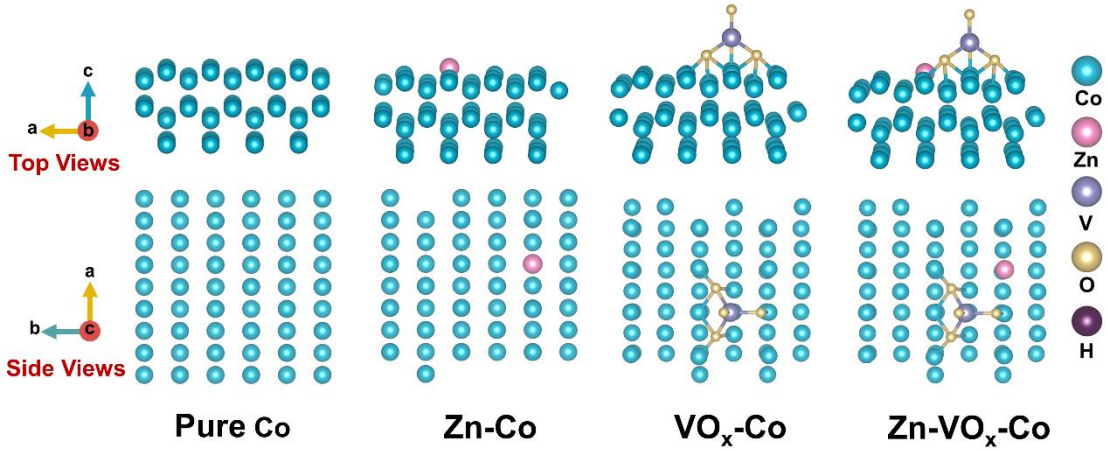

Figure 3.27 Top (upper) and side (lower) views of the optimized structures of pure Co, Zn-Co, VO_x-Co and Zn-VO_x-Co.

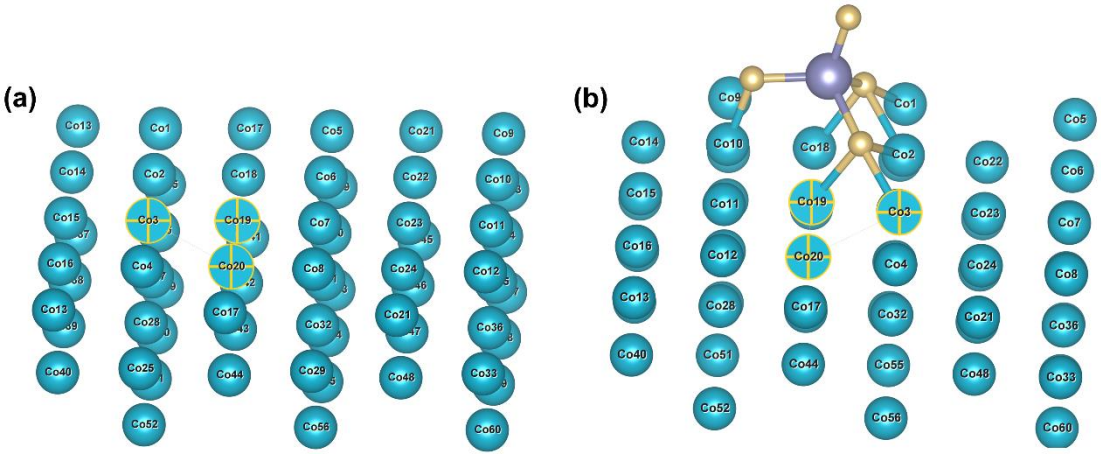

Figure 3.28 (a) Pure Co and (b) VO_x-Co models with serial numbers

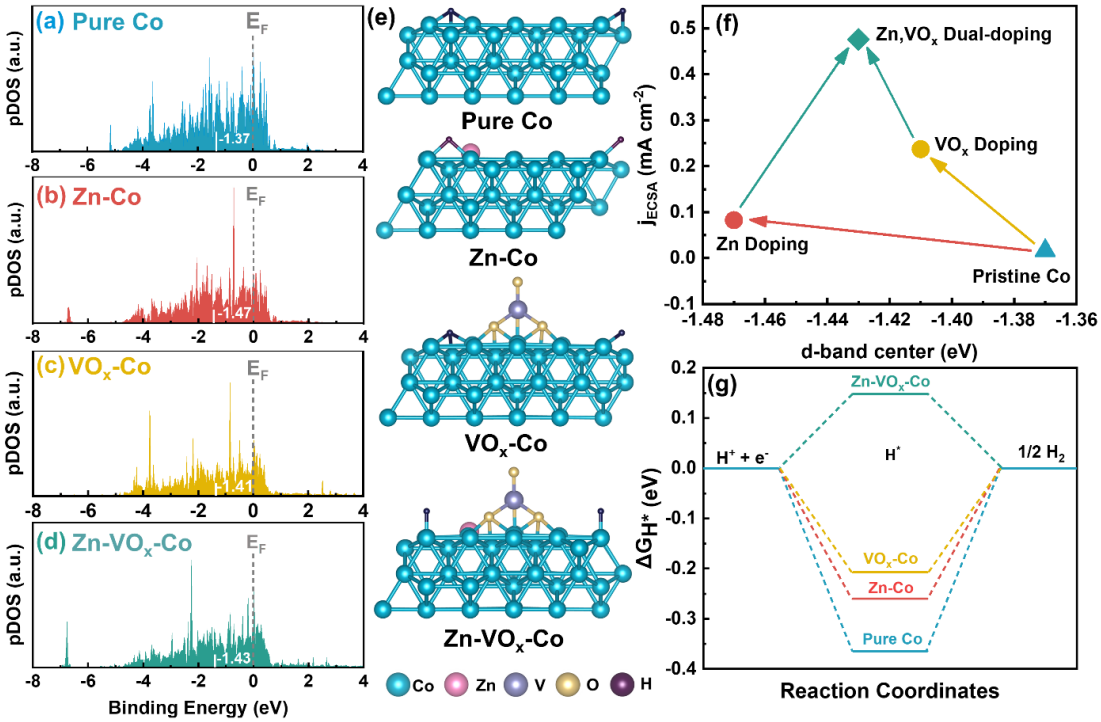

Figure 3.29 (a-d) *p*DOS of d-states of model structures of pure Co, Zn-Co, VO_x-Co and Co-VO_x-Co, respectively; (e) optimized structure of adsorbed H on the four models; (f) relationship between the HER overpotential versus d-band center; (g) free energies of H adsorptions on the pure Co, Zn-Co, VO_x-Co and Co-VO_x-Co.

Based on the above results of the characterizations, the performance tests and DFT calculations, the outstanding HER performance of the Zn-VO_x-Co electrocatalyst should be mainly attributed to its unique nanostructures and related electronic structure: (1) 2D ultra-thin nanosheets increased the active sites and facilitated the electrolyte penetration. Meanwhile, the overlapped nanosheet structure enhanced the mechanical intensity and ensured the endurance of the hydrogen generation and release process. (2) The unique crystalline/amorphous heterostructure was beneficial for either hydrogen adsorption or desorption processes. Typically, VO_x cluster doping into metallic cobalt resulted in the formation of the amorphous structure with abundant variable valences and a large amount of unsaturated chemical bonds, which can enhance the adsorption of water. Meanwhile, the introduction of Zn species increased the conductivity, which

can effectively promote the electron transfer. Especially, the synergy of crystalline and amorphous phases ensured the balance of the adsorption and desorption during the HER process, which significantly lowered the overpotential. (3) Using the facile and binder-free electrodeposition method promoted the interfacial electron transfer between the Zn-VO_x-Co nanosheets and the bare CFP, reducing the resistance of Zn-VO_x-Co based electrode and finally improving the catalysis efficiency.

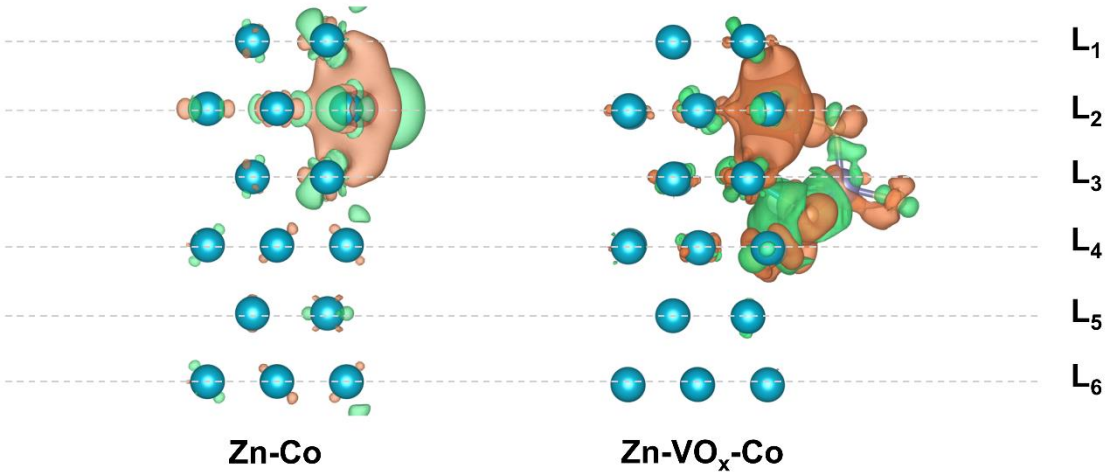

Figure 3.30 Side views of charge density distributions in Zn-Co and Zn-VO_x-Co.

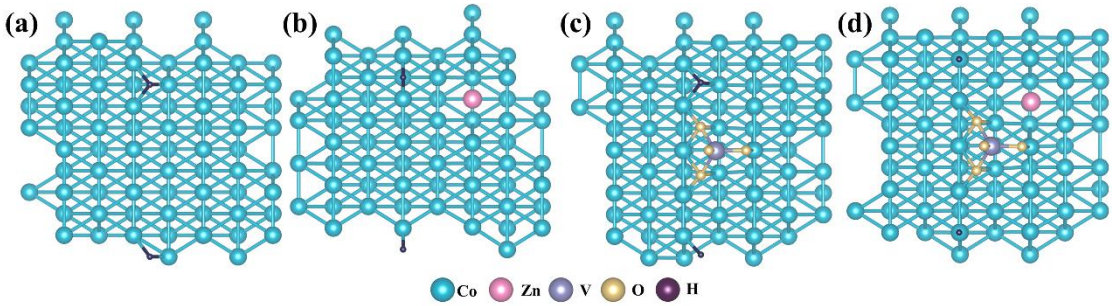

Figure 3.31 Top views of the optimized structures of adsorbed H on (a) pure Co, (b) Zn-Co, (c) VO_x-Co and (d) Zn-VO_x-Co.

Table 3.4 Summary of the distance and angles between Co atoms in pure Co and VO_x-Co samples

Catalysts	Distance (Å)			Angle (°)
	Co_3-Co_{19}	Co_{19}-Co_{20}	Co_{20}-Co_3	∠Co_{19} Co_{20} Co_3
Pure Co	2.39587	2.45033	2.39587	59.245
VO_x-Co	2.47092	2.42902	2.43581	61.0499

3.4 Conclusions

In summary, 2D ultrathin Zn-VO_x-Co nanosheets were successfully coated on CFP substrate by a facile electrodeposition method for the first time. The obtained Zn-VO_x-Co electrocatalysts had unique heterostructure combined with the amorphous Co metal phase and crystalline Zn-Co alloy phase. DFT calculations revealed that the dual-doping of Zn and VO_x could optimize the d-band center, significantly balance the adsorption and desorption of hydrogen species. As a result, the optimum catalyst demonstrated a superior HER performance with an overpotential as low as 46 mV to deliver the standard current density of 10 mA cm^{-2} with a small Tafel slope of 75 mV dec^{-1} and long-term electrochemical stability over 36 h in 1 M KOH solution. While, it also exhibited excellent HER performance in the neutral electrolyte solution. This study provides a facile approach to synthesize electrocatalysts working in a wide pH range with high catalytic activity and stability, which could be applied in the water electrolysis industry.

References

[1] J. A. Turner, Sustainable hydrogen production, Science 305 (2004) 972-974.

[2] W. Yang, S. Chen, Recent progress in electrode fabrication for electrocatalytic hydrogen evolution reaction: a mini review, Chem. Eng. J. 393 (2020) 124726.

[3] C. Dai, X, Tian, Y. Nie, C. Tian, C. Yang, Z. Zhou, Y. Li, X. Gao, Successful synthesis of 3D $CoSe_2$ hollow microspheres with high surface roughness and its excellent performance in catalytic hydrogen evolution reaction, Chem. Eng. J. 321 (2017) 105-112.

[4] J. Mahmood, F. Li, S. M. Jung, M. S. Okyay, I. Ahmad, S. J. Kim, N. Park, H. Y. Jeong, J. B. Baek, An efficient and pH-universal ruthenium-based catalyst for the hydrogen evolution reaction, Nature nanotech. 12 (2017) 441-446.

[5] X. Zhang, F. Jia, S. Song, Recent advances in structural engineering of molybdenum disulfide for electrocatalytic hydrogen evolution reaction, Chem. Eng. J. 405 (2021) 127013.

[6] X. Cao, D. Jia, D. Li, L. Cui, J. Liu, One-step co-electrodeposition of hierarchical radial Ni_xP nanospheres on Ni foam as highly active flexible electrodes for hydrogen evolution reaction and supercapacitor, Chem. Eng. J. 348 (2018) 310-318.

[7] H. Yin, S. Zhao, K. Zhao, K. Zhao, A. Muqsit, H. Tang, L. Chang, H. Zhao, Y. Gao, Z. Tan, Ultrathin platinum nanowires grown on single-layered nickel hydroxide with high hydrogen evolution activity, Nature Commun. 6 (2015) 1-8.

[8] J. Li, C. Zhang, T. Zhang, Z. Shen, Q. Zhou, J. Pu, H. Ma, T. Wang, H. Zhang, H. Fan, Y. Wang, H. Ma, Multiple-interface relay catalysis: enhancing alkaline hydrogen evolution through a combination of Volmer promoter and electrical-behavior regulation, Chem. Eng. J. 397 (2020) 125457.

[9] J. Jiang, R. Sun, X. Huang, H. Cong, J. Tang, W. Xu, M. Li, Y. Chen, Y. Wang, S. Han, H. Lin, CoS_2 quantum dots modified by ZIF-67 and anchored on reduced graphene oxide as an efficient catalyst for hydrogen evolution reaction, Chem. Eng. J. 430 (2022) 132634.

[10] Y. Ma, M. Chen, H. Geng, H. Dong, P. Wu, X. Li, G. Guan, T. Wang, Synergistically tuning electronic structure of porous β-Mo_2C spheres by Co doping and Mo-vacancies defect engineering for optimizing hydrogen evolution reaction activity, Adv. Funct. Mater. 30 (2020) 2000561.

[11] J. Dong, Q. Wu, C. Huang, W. Yao, Q. Xu, Cost effective Mo rich Mo_2C electrocatalysts for the hydrogen evolution reaction, J. Mater. Chem. A 6 (2018) 10028-10035.

[12] H. Liao, C. Wei, J. Wang, A. Fisher, T. Sritharan, Z. Feng, Z. J. Xu, A multisite strategy for enhancing the hydrogen evolution reaction on a nano-Pd surface in alkaline media, Adv. Energy Mater. 7 (2017) 1701129.

[13] X. Y. Zhang, J. Y. Xie, Y. Ma, B. Dong, C. G. Liu, Y. M. Chai, Catalytic mechanisms and practical activity of the active site in transition metal electrocatalysts for hydrogen evolution reaction, Chem. Eng. J. (2021) 132312.

[14] H. Zhong, C. A. Campos-Roldán, Y. Zhao, S. Zhang, Y. Feng, N. Alonso-Vante, Recent advances of cobalt-based electrocatalysts for oxygen electrode reactions and hydrogen evolution reaction, Catalysts 8 (2018) 559.

[15] S. Baranton, C. Coutanceau, Nickel cobalt hydroxide nanoflakes as catalysts for the hydrogen evolution reaction, Appl. Catal. B: Environ. 136 (2013) 1-8.

[16] B. Huang, L. Chen, Y. Wang, L. Ouyang, J. Ye, Paragenesis of palladium-cobalt nanoparticle in nitrogen-rich carbon nanotubes as a bifunctional electrocatalyst for hydrogen-evolution reaction and oxygen-reduction reaction, Chem. Eur. J. 23 (2017)

7710-7718.

[17] A. R. Zeradjanin, J. Grote, G. Polymeros, K. J. J. Mayrhofer, A critical review on hydrogen evolution electrocatalysis: re-exploring the volcano-relationship, Electroanalysis 28 (2016) 2256-2269.

[18] G. B. Darband, M. Aliofkhazraei, A. S. Rouhaghdam, M. A. Kiani, Three-dimensional Ni-Co Alloy hierarchical nanostructure as efficient non-noble-metal electrocatalyst for hydrogen evolution reaction, Appl. Surf. Sci. 465 (2019) 846-862.

[19] B. A. Yusuf, M. Xie, W. Yaseen, J. Xie, Y. Xu, Hierarchical ultrathin defect-rich $CoFe_2O_4$@BC nanoflowers synthesized via a temperature-regulated strategy with outstanding hydrogen evolution reaction activity, Inorg. Chem. Fron. 8 (2021) 1455-1467.

[20] F. Zhang, R. Ji, Y. Liu, Z. Li, Z. Liu, S. Lu, Y. Wang, X. Wu, H. Jin, B. Cai, Defect-rich engineering and F dopant Co-modulated NiO hollow dendritic skeleton as a self-supported electrode for high-current density hydrogen evolution reaction, Chem. Eng. J. 401 (2020) 126037.

[21] H. Cheng, N. Yang, X. Liu, Q. Yun, M. H. Goh, B. Chen, X. Qi, Q. Lu, X. Chen, W. Liu, L. Gu, H. Zhang, Aging amorphous/crystalline hetero-phase PdCu nanosheets for catalytic reactions, Natl. Sci. Rev. 6 (2019) 955-961.

[22] G. Zhao, K. Rui, S. X. Dou, W. Sun, Heterostructures for electrochemical hydrogen evolution reaction: a review, Adv. Funct. Mater. 28 (2018), 1803291.

[23] Y. Li, X. Tan, R. K. Hocking, X. Bo, H. Ren, B. Johannessen, S. C. Smith, C. Zhao, Implanting Ni-O-VO_x sites into Cu-doped Ni for low-overpotential alkaline hydrogen evolution, Nat. Commun. 11 (2020), 2720.

[24] H. Jin, X. Liu, S. Chen, A. Vasileff, L. Li, Y. Jiao, L. Song, Y. Zheng, S. Z. Qiao, Heteroatom-doped transition metal electrocatalysts for hydrogen evolution reaction, ACS Energy Lett. 4 (2019) 805-810.

[25] D. L. Han, P. L. Yu, X. M. Liu, Y. D. Xu, S. L. Wu, Polydopamine modified CuS@ HKUST for rapid sterilization through enhanced photothermal property and photocatalytic ability, Rare Metals (2021) 1-10.

[26] W. Guan, L. Tan, X. Liu, Z. Cui, Y. Zheng, K. W. K. Yeung, D. Zheng, Y. Liang, Z. Li, S. Zhu, X. Wang, S. Wu, Ultrasonic interfacial engineering of red phosphorous-metal for eradicating MRSA infection effectively, Adv. Mater. 33 (2021) 2006047.

[27] B. A. Yusuf, M. Xie, N. Ullah, C. J. Oluigbo, W. Yaseen, J. Xie, Y. Xu, Facile synthesis of N, S co-doped MoO_2@ C nanorods as an outstanding electrocatalyst for hydrogen evolution reaction, Appl. Surf. Sci. 537 (2021) 147971.

[28] C. J. Oluigbo, Y. Xu, H. Louis, A. B. Yusuf, W. Yaseen, N. Ullah, K. J. Alagarasan, M. Xie, E. E. Ekpenyong, J. Xie, Controllable fabrication of abundant nickel-nitrogen doped CNT electrocatalyst for robust hydrogen evolution reaction, Appl. Surf. Sci. (2021) 150161.

[29] J. Li, Z. Li, X. Liu, C. Li, Y. Zheng, K. W. K. Yeung, Z. Cui, Y. Liang, S. Zhu, W. Hu, Y. Qi, T. Zhang, X. Wang, S. Wu, Interfacial engineering of $Bi_2S_3/Ti_3C_2T_x$ MXene based on work function for rapid photo-excited bacteria-killing, Nature Commun. 12 (2021) 1-10.

[30] X. Kong, X. Liu, Y. Zheng, P. K. Chu, Y. Zhang, S. Wu, Graphitic carbon nitride-based materials for photocatalytic antibacterial application, Mater. Sci. Eng. R Rep. 145 (2021) 100610.

[31] Y. Li, X. Liu, L. Tan, Z. Cui, X. Yang, Y. Zheng, K. W. K. Yeung, P. K. Chu, S. Wu, Rapid sterilization and accelerated wound healing using Zn^{2+} and graphene oxide modified g-C_3N_4 under dual light irradiation, Adv. Funct. Mater. 28 (2018) 1800299.

[32] Y. Luo, X. Liu, L. Tan, Z. Li, K. W. K. Yeung, Y. Zheng, Z. Cui, Y. Liang, S. Zhu, C. Li, X. Wang, S. Wu, Enhanced photocatalytic and photothermal properties of ecofriendly metal-organic framework heterojunction for rapid sterilization, Chem. Eng. J. 405 (2021) 126730.

[33] D. Han, Y. Li, X. Liu, K. W. K. Yeung, Y. Zheng, Z. Cui, Y. Liang, Z. Li, S. Zhu, X. Wang, S. Wu, Photothermy-strengthened photocatalytic activity of polydopamine-modified metal-organic frameworks for rapid therapy of bacteria-infected wounds, J. Mater. Sci. Technol. 62 (2021) 83-95.

[34] Q. Li, Y. Zhou, C. Chen, Q. Liu, J. Huo, H. Yi, Building CoP/Co-MOF heterostructure in 2D nanosheets for improving electrocatalytic hydrogen evolution over a wide pH range, J. Electroanal. Chem. 895 (2021) 895.

[35] H. Ding, D. Han, Y. Han, Y. Liang, X. Liu, Z. Li, S. Zhu, S. Wu, Visible light responsive CuS/protonated g-C_3N_4 heterostructure for rapid sterilization, J. Hazard. Mater. 393 (2020) 122423.

[36] M. Shi, Y. Zhang, Y. Zhu, W. Wang, C. Wang, A. Yu, X. Pu, J. Zhai, A flower-like CoS_2/MoS_2 heteronanosheet array as an active and stable electrocatalyst toward the hydrogen evolution reaction in alkaline media, RSC Adv. 10 (2020) 8973-8981.

[37] W. Liu, L. Yu, R. Yin, X. Xu, J. Feng, X. Jiang, D. Zheng, X. Gao, X. Gao, W. Que, P. Ruan, F. Wu, W. Shi, X. Cao, Non-3d metal modulation of a 2D Ni-Co heterostructure array as multifunctional electrocatalyst for portable overall water splitting, Small 16 (2020) 1906775.

[38] B. A. Yusuf, M. Xie, W. Yaseen, C. J. Oluigbo, J. Xie, Y. Xu, Ni nanoparticles oriented on MoO_2@ BC nanosheets with an outstanding long-term stability for hydrogen evolution reaction, Chem. Eng. Sci. 246 (2021) 116868.

[39] J. Liu, Y. Ji, J. Nai, X. Niu, Y. Luo, L. Guo, S. Yang, Ultrathin amorphous cobalt-vanadium hydr(oxy)oxide catalysts for oxygen evolution reaction, Energ. Environ. Sci. 9 (2013) 1-3.

[40] Y. Li, X. Tan, W. Yang, X. Bo, Z. Su, T. Zhao, S. C. Smith, C. Zhao, Vanadium oxide clusters decorated metallic cobalt catalyst for active alkaline hydrogen evolution, Cell Rep. Phys. Sci. 1 (2020) 100275.

[41] M. Kuang, J. Zhang, D. Liu, H. Tan, K. N. Dinh, L. Yang, H. Ren, W. Huang, W. Fang, J. Yao, X. Hao, J. Xu, C. Liu, L. Song, B. Liu, Q. Yan, Amorphous/crystalline heterostructured cobalt-vanadium-iron (oxy)hydroxides for highly efficient oxygen evolution reaction, Adv. Energy Mater. 10 (2020) 2002215.

[42] Z. Sun, X. Wang, M. Yuan, H. Yang, Y. Su, K. Shi, C. Nan, H. Li, G. Sun, J. Zhu, X. Yang, S. Chen, “Lewis base-hungry” amorphous-crystalline nickel borate-nickel sulfide heterostructures by in situ structural engineering as effective bifunctional electrocatalysts toward overall water splitting, ACS Appl. Mater. Inter. 12 (2020) 23896-23903.

[43] D. Cao, J. Wang, H. Xu, D. Cheng, Growth of highly active amorphous RuCu nanosheets on Cu nanotubes for the hydrogen evolution reaction in wide pH values, Small 16 (2020) 2000924.

[44] X. Zuo, K. Chang, J. Zhao, Z. Xie, H. Tang, B. Li, Z. Chang, Bubble-template-assisted synthesis of hollow fullerene-like MoS_2 nanocages as a lithium-ion battery anode material, J. Mater. Chem. A 4 (2016) 51-58.

[45] L. Zhao, Q. Wei, L. Zhang, Y. Zhao, B. Zhang, NiCo Alloy decorated on porous

N-doped carbon derived from ZnCo-ZIF as highly efficient and magnetically recyclable catalyst for hydrogen evolution from ammonia borane, Renew. Energy. 173 (2021) 273-282.

[46] R. Wang, Q. Yuan, P. Sun, R. Nie, X. Wang, Tuning the active sites in the cobalt-based nitrogen-doped carbon by zinc for enhancing hydrogen evolution reaction, J. Alloy. Compd. 789 (2019) 100-107.

[47] N. Yang, H. Cheng, X. Liu, Q. Yun, Y. Chen, B. Li, B. Chen, Z. Zhang, X. Chen, Q. Lu, J. Huang, Y. Huang, Y. Zong, Y. Yang, L. Gu, H. Zhang, Amorphous/crystalline hetero-phase Pd nanosheets: one-pot synthesis and highly selective hydrogenation reaction, Adv. Mater. 30 (2018) 1803234.

[48] M. Chen, Y. Ma, Y. Zhou, C. Liu, Y. Qin, Y. Fang, G. Guan, X. Li, Z. Zhang, T. Wang, Influence of transition metal on the hydrogen evolution reaction over nano-molybdenum-carbide catalyst, Catalysts 8 (2018) 294.

[49] N. Eliaz, K. Venkatakrishna, A. C. Hegde, Electroplating and characterization of Zn-Ni, Zn-Co and Zn-Ni-Co alloys, Surf. Coat. Tech. 205 (2010) 1969-1978.

[50] P. W. Menezes, A. Indra, A. Bergmann, P. Chernev, C. Walter, H. Dau, P. Strasser, M. Driess, Uncovering the prominent role of metal ions in octahedral versus tetrahedral sites of cobalt-zinc oxide catalysts for efficient oxidation of water, J. Mater. Chem. A 4 (2016) 10014-10022.

[51] K. J. McDonald, K. Choi, Photodeposition of Co-based oxygen evolution catalysts on α-Fe_2O_3 photoanodes, Chem. Mater. 23 (2011), 1686-1693.

[52] N. Bai, Q. Li, D. Mao, D. Li, H. Dong, One-step electrodeposition of Co/CoP film on Ni foam for efficient hydrogen evolution in alkaline solution, ACS Appl. Mater. Inter. 8 (2016) 29400-29407.

[53] Z. Wang, L. Chen, S. Xu, D. Zhang, X. Zhou, X. Wu, X. Xie, X. Qiu, Cobalt

vanadium layered double hydroxide/FeOOH heterostructure catalyst with strong electron interactions for stable oxygen evolution performance, Compos. Commun. 27 (2021) 100780.

[54] B. You, M. T. Tang, C. Tsai, F. Abild-Pedersen, X. Zheng, H. Li, Enhancing electrocatalytic water splitting by strain engineering, Adv. Mater. 31 (2019) 1807001.

[55] H. Lin, N. Liu, Z. Shi, Y. Guo, Y. Tang, Q. Gao, Cobalt-doping in molybdenum-carbide nanowires toward efficient electrocatalytic hydrogen evolution, Adv. Funct. Mater. 26 (2016) 5590-5598.

[56] D. He, L. Cao, J. Huang, K. Kajiyoshi, J. Wu, C. Wang, Q. Liu, D. Yang, L. Feng, In-situ optimizing the valence configuration of vanadium sites in NiV-LDH nanosheet arrays for enhanced hydrogen evolution reaction, J. Energy. Chem. 47 (2020) 263-271.

[57] W. Zhao, T. Xu, T. Li, Y. Wang, H. Liu, J. Feng, S. Ding, Z. Li, M. Wu, Amorphous iron (III)-borate nanolattices as multifunctional electrodes for self-driven overall water splitting and rechargeable zinc-air battery, Small 14 (2018) 1802829.

CHAPTER 4 Tuning octahedron sites in $MnFe_2O_4$ spinel by boron doping for highly efficient seawater splitting

4.1 Introduction

Water splitting with renewable energy such as wind and solar power as well as surplus electricity for hydrogen production should be a sustainable technology to decrease the demand of fossil fuels and solve environmental pollution issues in the future [1-3]. In the overall water splitting process, oxygen evolution reaction (OER) at anode is a four-electron transferring reaction with a sluggish and multi-step proton-coupled process, which will impact the splitting efficiency in energy [4-6]. Considering the growing population and intensified water pollution, fresh water is becoming the limited resource around the world. Fortunately, seawater covers 71% of the earth surface and represents 97% of water resources in the world, which is deemed as an inexhaustible resource for hydrogen production [7-9]. Combining seawater splitting with those ocean energies such as wave, wind and solar energy could realize the goal of producing clean and sustainable hydrogen energy. While, the use of hydrogen can generate pure fresh water for our daily life, which is significant to the creating of a sustainable society, especially for the coastal and arid areas. Therefore, seawater should be considered as an ideal feedstock for electrocatalytic hydrogen production. However, one critical challenge in the direct seawater splitting is to solve the issues relating to high content of chlorine anions (Cl^-), including the chlorine evolution reaction (ClER) at a low pH situation and chlorine oxidation reaction to generate hypochlorite at a high pH condition [10,11]. Compared with the acid or neutral solution, the alkaline water splitting could provide a larger overpotential (η) window limit for OER selectivity. In alkaline conditions, it is found that the potential window could reach up to about 480 mV due to the large equilibrium potential, where the best probability to achieve 100%

Faradaic efficiency of O_2 generation could be realized [12,13]. The other critical challenge is the very complex composition of natural seawater, in which various dissolved ions such as Na^+, Ca^{2+}, Mg^{2+} and so on exist while the bacteria/ microbes and small particles could poison and pollute the electrodes and decay the catalytic performance [13,14].

Numerous studies have been dedicated to explore efficient OER catalysts for seawater splitting. Among them, transition metal oxides (MO_x, M=Fe, Co, Mn, Ni, etc.) hold the promising merits with various nanostructures suitable for catalysis process and high resistance to corrosion [15-17]. In particular, spinel-type metal oxides (AB_2O_4, A, B=transition metal) have been considered as the promising substitute for the noble-metal catalysts due to their high intrinsic OER activities and tunable chemical composition features [18,19]. For the normal spinel, the metal A charged as +2 occupies the center of the tetrahedrally coordinated position while cation B charged as +3 occupies the octahedral position, and the O^{2-} locates at the polyhedral vertexes [20,21]. From the study by Wei and co-workers [22], the metal cations occupied on the octahedral sites play an efficient role in the OER process due to the large overlap of the lying e_g-3d orbital in the octahedrally coordinated metal cations with an orbital of O 2p. Hence, further shifting the charge to catalytically critical octahedral site is essential in boosting OER activity. It is found that non-metal element (e.g., P, F or B) doping is a facile and efficient method for the reconfiguring of the desired surface of spinel for improving OER activity in both alkaline fresh water and seawater media [23,24]. Especially, the incorporation of the electronegative boron into oxides could reduce the oxidation reaction barrier under an applied bias and facilitate the charge transfer [25]. For example, Yu et al. [26] found that coupling of boron and cobalt spinel oxide could tune the surface structure to boost OER activity.

$MnFe_2O_4$ has a unique structure, in which the oxygen atoms constitute a face-centered cubic close-packed structure with multiple distributions of Fe and Mn cations. It is reported that the octahedral Fe sites can easily split water molecule to provide intermediates and Mn-based oxides always present outstanding OER selectivity in the seawater splitting due to the weak chlorine ion adsorption on them by surface polarization [23,27,28]. Thence, in this study, a FeMn bimetal-based nanocrystalline $MnFe_2O_4$ spinel doping with B (B-$MnFe_2O_4$) prepared under ambient condition was considered as the OER electrocatalysts for seawater splitting for the first time. Using in situ conversion of MnFe-MOF-74 precursor coated on nickel foam (NF) by calcination in air followed with alkaline $NaBH_4$ solution treatment, the ultrathin B-$MnFe_2O_4$ nanosheets were formed on amorphous nanowires composed of Mn, Fe, O and C species (denoted as MFOC hereafter). Furthermore, by using XPS analysis and DFT calculations, it is confirmed that the boron-engineering of $MnFe_2O_4$ can configurate the electronic structure, reduce the free energy and promote the OER kinetics. It is expected that such a unique hierarchically-architecture B-$MnFe_2O_4$@MFOC composite could provide abundant active sites, high conductivity and corrosion-resistance in the seawater splitting.

4.2 Experimental section

4.2.1 Chemical and materials

2,5-dihydroxyterephthalic acid (DHTA, 98%) was purchased from TCL, Japan. Iron (II) sulfate heptahydrate ($FeSO_4 \cdot 7H_2O$, 98%), manganese (II) sulfate monohydrate ($MnSO_4 \cdot 7H_2O$, 97%), N, N-dimethylformamide (DMF, deoxidized), sodium borohydride powder ($NaBH_4$, powder, 95%), hydrochloric acid (HCl, 69%), potassium hydroxide (KOH, 85%), sodium chloride (NaCl, 99%) were purchased from Wako, Japan. The ethanol (C_2H_5OH, 99.5%) and the deionized (DI) water (18.2 MΩ·cm@25 ^oC) was used to wash the sample. NF (thickness:1.5mm; number of pores per inch:110;

bulk density:0.23 g/cm^3) was purchased from MTI, Japan.

4.2.2 Synthesis of Samples

Synthesis of MnFe-MOF-74 precursor

A piece of nickel foam was cut into slice-state (2×2 cm^2), ultrasonicated in 3 M HCl solution, ethanol and DI water for one hour, respectively, and then heated at 60 ^{o}C overnight in a vacuum state. In a typical MnFe-MOF-74 precursor synthesis process, 48 mg of DHTA, 78 mg of $FeSO_4 \cdot 7H_2O$ and 13 mg of $MnSO_4 \cdot H_2O$ were dissolved in 25 mL of DMF with stirring for three hours and then sonicating one hour. Thereafter, a piece of the treated NF was immersed into a 50 mL Teflon-lined stainless-steel autoclave containing the above solution, following by a 20-h thermal treatment at 140 ^{o}C. After the autoclave was cooled down to room temperature naturally, the MnFe-MOF-74 precursor coated NF was rinsed with ethanol before heated at 60 ^{o}C overnight in a vacuum state.

Synthesis of MFOC nanowires

MnFe-MOF-74 precursor coated NF was calcined in a Muffle furnace at 250 ^{o}C for two hours with a heating rate of 1 ^{o}C min^{-1} under air atmosphere. After naturally cooled down to room temperature, the amorphous nanowires (composed of Mn, Fe, O and C species, denoted as MFOC) coated NF electrode was obtained.

Synthesis of B-$MnFe_2O_4$@MFOC

The as-prepared amorphous MFOC nanowires coated NF electrode was further treated by a freshly prepared alkaline $NaBH_4$ solution (1 M $NaBH_4$ dissolved in 0.1 M NaOH solution) for 20 minutes at room temperature. Then, the electrode was washed repeatedly with DI water to completely remove those residual ions, and vacuum-dried at 60 ^{o}C for 12 hours. Based on inductively coupled plasma mass spectrometry (ICP-MS-7700) analysis and various preliminary investigation, the optimal element mass

amounts in the electrocatalyst were found to be ~0.17 mg cm^{-2} for Fe, ~0.03 mg cm^{-2} for Mn and ~0.002 mg cm^{-2} for B element in this study.

Synthesis of B-Fe_3O_4@FOC and B-Mn_3O_4@MOC

The B-Fe_3O_4@FOC (FOC: amorphous material composed of Fe, O and C species) and B-Mn_3O_4@MOC (MOC: amorphous material composed of Mn, O and C species) were also prepared with the same method as that of B-$MnFe_2O_4$@MFOC but without Mn or Fe element.

Synthesis of standard $MnFe_2O_4$ spinel

10 ml of mixed metallic salts with a molar ratio of 2:1 (Fe(III)/Mn(II)) were stirred followed by adjusting the pH value to 12 by NaOH. Then, the solution with a piece of treated NF was added into a 50mL Teflon-lined stainless-steel autoclave and heated at 200 ℃ for 12 hours. After the product was washed for several times with DI water and ethanol successively, the $MnFe_2O_4$ spinel sample was obtained after heated at 60 ºC overnight in a vacuum state.

4.2.3 Catalysts characterization

Crystalline structure of the as-prepared sample was tested by an X-ray diffraction (XRD, Smartlab 9KW, Rigaku, Japan) with monochromatized Cu-Kα radiation (λ=0.15406 nm) at an accelerating voltage of 45 kV, a current of 200 mA, a 2θ range of 10°-90° with a scan rate is 10° min^{-1} and a step size of 0.01°. Raman spectrum was obtained in the spectral range of 100-2000 cm^{-1} by a JASCO NRS-5100, employed a He-Ne laser source with an excitation wavelength of 532 nm at 15mW laser powder. Nanostructures and morphology of the samples were determined by a scanning electron microscope (SEM, SU8010, Hitachi, Japan) at an accelerating voltage of 3 kV, the electric current was 10 mA with an energy dispersive X-ray spectroscopy (EDS) equipment. EM-2100F transmission electron microscopy (TEM) and high-resolution TEM (HRTEM) was operated. The surface chemical states were determined by X-ray

photoelectron spectrum (XPS) on a VG Scientific ESCALab250i-XL instrument using Al Kα (1486.6 eV, 10 mA) radiation as the photon source and focus on a 0.2 mm spot surface. The C1s photoelectron line (BE=284.8 eV) was used to calibrate the binding energies of the photoelectron. The binding energies of all the sample were analyzed using the XPSPEAK41 software. Shirley's background type was selected, and Gaussian fitting was used to add the fitting peak. Thermo gravimetric (TGA) curves of samples were obtained under N_2 atmosphere by a TGA instrument (DTG-60H) with a heating rate of 10° min^{-1} from 0-700 ℃. Electron paramagnetic resonance (EPR) spectroscopy was measured using a Bruker A300 spectrometer. The water contact angle was measured by a contact angle meter (DMe-201, Japan). 5μL of DI water was applied on the sample surface for characterization. The contact angle was analyzed by FAMAS software and the surface contact angle were the average value of three measurements made on different positions of the sample surface.

4.2.4 Electrochemical measurements

The electrochemical performance was measured on an electrochemical station (Versa STAT4, Princeton, USA). The OER was carried out in a standard three-electrode system with the prepared sample as a work electrode, a graphite rod with 6mm diameter and a RE-61AP type Hg/HgO purchased from the ALS, Tokyo, Japan, were used as the counter and reference electrodes, respectively. Four different electrolytes were used, including 1 M KOH, 1 M KOH+0.5 M NaCl, 1 M KOH+ natural seawater with a pH value of around 14. The stable polarization of each sample was recorded at a potential range of 0~1.5 V with a scan rate of 2 mV s^{-1} without iR compensation after running at least 50 cyclic voltammetry (CV) cycles for stabilization and activation. All potentials referenced to the revisable hydrogen electrode (RHE) were calculated using the equation (Eq. 4.1) and the overpotential (η) was calculated by equation (Eq. 4.2):

$E_{RHE} = E_{Hg/HgO} + (0.098 + 0.059\ pH)\ V$ (Eq. 4.1)

$\eta(V) = E_{RHE} - 1.23V$ (Eq. 4.2)

The Tafel slope (b) was obtained by $\eta = a + b \log(j)$, in which j is the current density. Electrochemical impedance spectrum (EIS) was tested at an overpotential of 200 mV with a frequency range from 0.01 to 100kHz and an amplitude of 10 mV. The double-layer capacitance (C_{dl}) was obtained by measuring cyclic voltammetries (CVs) at a scan rate of 5, 10, 20, 50, 75, 100 and 150 mV s^{-1} in the potential range of 1.1~1.3 V (vs. RHE). The measured current densities were also normalized by the ECSA value evaluate the electrochemically active surface area (ECSA), the ECSA was calculated from the double-layer capacitance according to the follow equation (Eq. 4.3):

$ECSA = C_{dl}/C_s$ (Eq. 4.3)

Where C_s presents the specific capacitance for a flat surface (40 μF cm^{-2}).

For the durability testing, 3000 CV cycles were performed with a scan rate of 50 mV s^{-1}, and the corresponding polarization curves were recorded before and after CV cycling. Chrono-potentiometric measurements were measured at the current densities of 100 and 500 mA cm^{-2} in the 1M KOH+0.5M NaCl and 1M KOH+ seawater solution, respectively. Corrosion testing was conducted on the work-station in natural seawater-based electrolyte. For the two-electrode seawater electrolysis, the B-$MnFe_2O_4$@MFOC composite was used as the bifunctional electrocatalyst on both cathode and anode.

Hypochlorite titration analysis

Iodometric titration was used to identify the possible hypochlorite species generation during seawater splitting OER process. After chrono-potentiometric curves at 100 mA cm^{-2} for 24 h measurement, 45mL of the used seawater solution were transferred from the electrochemical cell to a beaker. Subsequently, 0.13g of potassium iodide (KI), 8 mL of HCl (3.5 M), and 1mL of starch solution as the redox indicator

were introduced under magnetic stirring. In principle, there are two different situations could be observed:

(i) If the target anode material is not 100% selective towards OER, the solution color is pale pink after starch introduction;

(ii) If the anode material is 100% selective toward OER, the solution is colorless ever after starch introduction.

4.2.5 Computational Method

All the calculations were performed in the framework of the density functional theory (DFT) with the projector augmented plane-wave method, as implemented in the Vienna ab initio simulation package (VASP). The generalized gradient approximation (GGA) proposed by Perdew, Burke, and Ernzerhof (PBE) was selected for the exchange-correlation potential. The cut-off energy for plane wave was set at 520 eV. The energy criterion was set to 10^{-6} eV in iterative solution of the Kohn-Sham equation. The Brillouin zone integration was performed using a 5x5x1 k-mesh. All the structures were relaxed until the residual forces on the atoms had declined to less than 10^{-2} eV/Å.

4.3 Results and discussion

4.3.1 Characterization of B-$MnFe_2O_4$@MFOC electrocatalyst

The fabrication of B-$MnFe_2O_4$@MFOC composite-coated NF electrode mainly contains three steps. First, the MnFe-MOF-74 precursor is prepared by using a solvothermal method with the dissolved Fe, Mn salts and organic linkers in the DMF solution. Subsequently, by annealing MnFe-MOF-74 nanowires precursor at 250 ºC for two hours, the amorphous MnFeOC compound electrode is obtained. Finally, the B-$MnFe_2O_4$@ MFOC coated on NF electrode is prepared by using $NaBH_4$ as the reductant and boron source at the ambient temperature. Herein, the H^- originated from $NaBH_4$ has a strong reducing ability, which also serves as the oxygen scavenger to generate oxygen

defects and simultaneously change the crystallinity of sample [29]. Moreover, during the reducing process, lattice reconstruction of the randomly arranged structural units in amorphous MFOC also occurs, resulting in the transformation of amorphous MFOC into crystalline $MnFe_2O_4$ spinel owing to its lower activation energy barrier [30]. In addition, some oxygen species of $MnFe_2O_4$ spinel could be replaced by B species, leading to B doping in the spinel framework. The existence of amorphous MFOC layer between B-$MnFe_2O_4$ spinel and NF surface is expected to facilitate the interfacial contact and solid-state diffusion due to the short diffusion distance as well as the large surface area. **Figure 4.1** shows the optical photographs of different materials coated on NF substrate. In the macroscopic scale, the color of NF is changed from silver gray to black for the coating of FeMn-MOF-74 precursor on the NF, reddish-brown color for the MFOC generation, and dark brown color after the B-$MnFe_2O_4$ formation on MFOC.

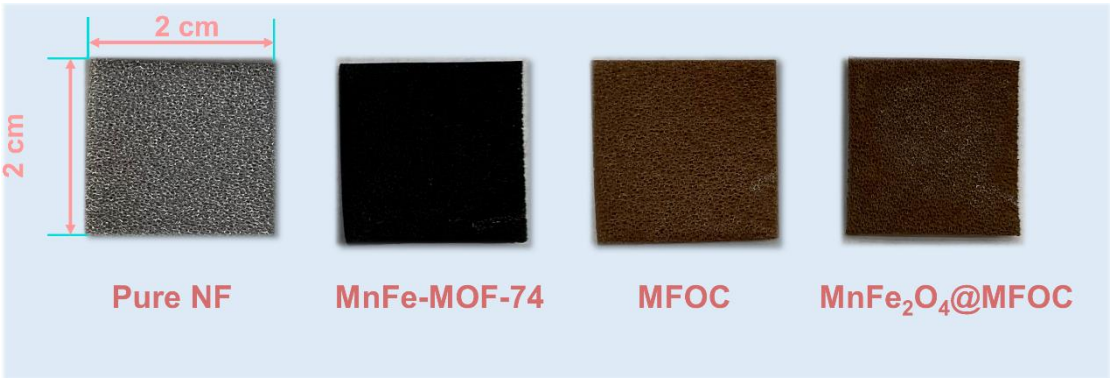

Figure 4.1 Optical images of the as-prepared electrodes

X-ray diffraction (XRD) patterns of all obtained precursors (**Figure 4.3**) have two well-defined and strong diffraction peaks at 2θ between 6 and 15°, which are consistence with the (110) and (300) planes of simulated MOF-74 crystalline structure, indicating the successful syntheses of Mn-MOF-74, Fe-MOF-74 and Mn-Fe-MOF-74 [31]. The different peak intensities also prove the successful doping of Mn and Fe elements into the MOF-74 framework successfully. However, no evident characteristic

peaks of the MOF-74 phase are observed in the XRD pattern of MFOC (**Figure 4.2**b), indicating its amorphous structural feature. **Figure 4.2**c displays XRD pattern of the final as-prepared B-$MnFe_2O_4$@MFOC, confirming the formation of $MnFe_2O_4$ spinel phase (JCPDS, No. 10-0319) on MFOC. Additionally, the broadened XRD peaks indicate that the obtained materials have a nanoscale grain size. The same phenomena are also observed from the XRD patterns of B-Fe_3O_4@FOC (FOC: Fe-O-C compound) and B-Mn_3O_4@MOC (MOC: Mn-O-C compound), as shown in **Figure 4.4**.

Raman spectroscopy is widely used to investigate the crystallographic phase as well as local cation distributions in details. Specifically, in the ferrite spinel material, the electron transport property usually depends on the cation distribution in the tetrahedral (A-site) and octahedral (B-site) sites [32]. According to the factor group analysis, the $MnFe_2O_4$ spinel shows four Raman active modes, in which those of A_{1g}, F_{2g} (2) and F_{2g} (1) belong to the tetrahedral A-sites while E_g is related to the octahedral B-sites. **Figure 4.2**d shows the Raman spectroscopy of B-$MnFe_2O_4$@MFOC and MFOC. Compared to a flat curve of MFOC, four Raman modes of B-$MnFe_2O_4$@MFOC are also observed at 607, 495, 410 and 265 cm^{-1} (summarized in **Table 4.1**), which are attributed to A_{1g}, F_{2g} (2), E_g and F_{2g} (1), respectively, indicating that the observed Raman bands are well matched with those of the normal spinel $MnFe_2O_4$ structure [32,33]. It is further proved that the $MnFe_2O_4$ structure has been prepared successfully. **Figure 4.5** shows the thermal behaviors of MFOC and B-$MnFe_2O_4$@MFOC samples. The main weight loss region of B-$MnFe_2O_4$@MFOC is identified in the temperature ranged from room temperature to 550 ℃ whereas the weight of MFOC is decreased continuously with the increase in the temperature. This may be due to that the catalyst surface structure has changed after the chemical reduction by $NaBH_4$.

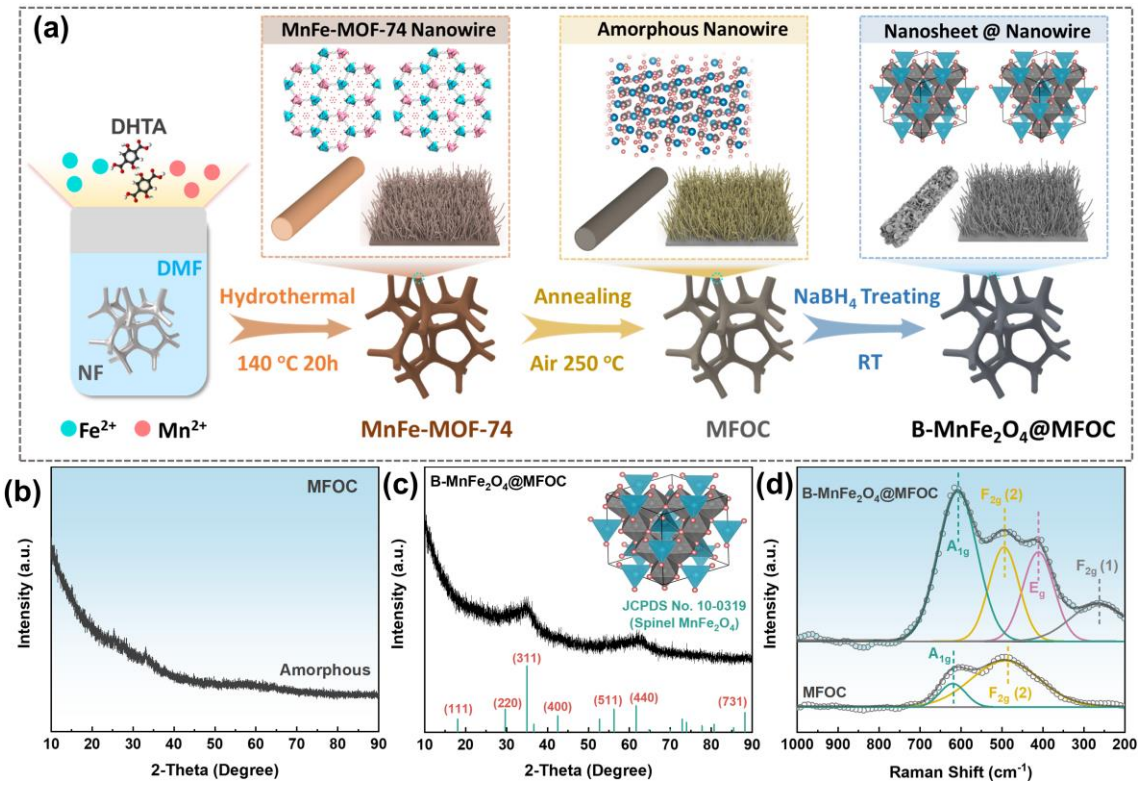

Figure 4.2 (a) Schematic illustration of the preparation of B-$MnFe_2O_4$@MFOC coated NF electrode; (b) XRD pattern of MFOC; (c) XRD pattern of B-$MnFe_2O_4$@MFOC and (d) Raman spectra of MFOC and B-$MnFe_2O_4$@MFOC.

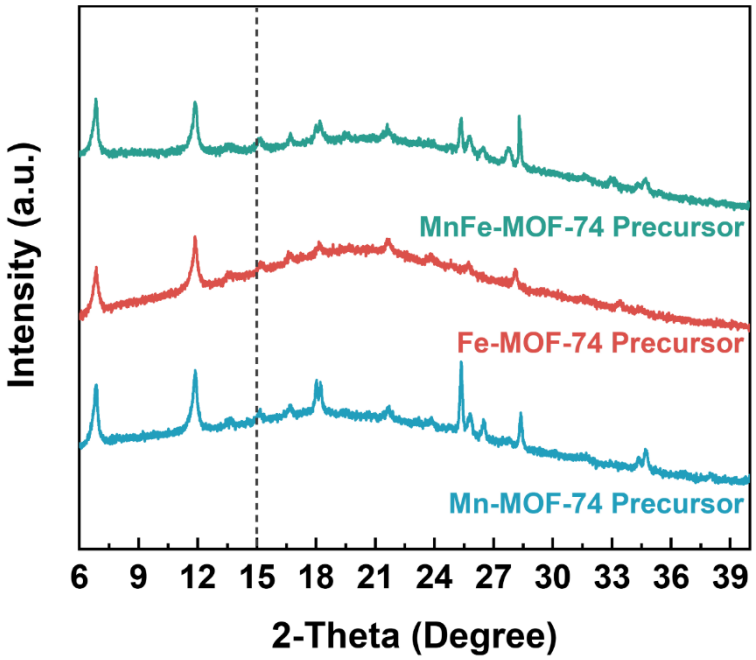

Figure 4.3 XRD patterns of Mn-MOF, Fe-MOF and MnFe-MOF precursors

Table 4.1 Summary of Raman peak positions and areas of samples

Catalyst	Peak	Raman Shift (cm^{-1})	Peak Area	Area (%)
	A_{1g}	607	21472	44
	F_{2g} (2)	495	10443	21
B-$MnFe_2O_4$@MFOC	E_g	410	10330	22
	F_{2g} (1)	265	7750	13
MFOC	A_{1g}	620	11663	84
	F_{2g} (2)	491	2252	16

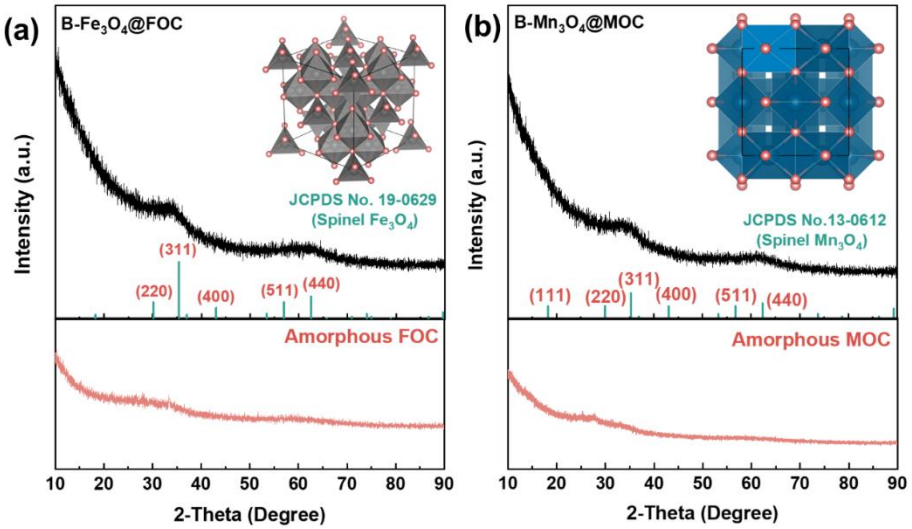

Figure 4.4 XRD patterns of (a) FOC, B-Fe_3O_4@FOC and (b) MOC, B-Mn_3O_4@MOC

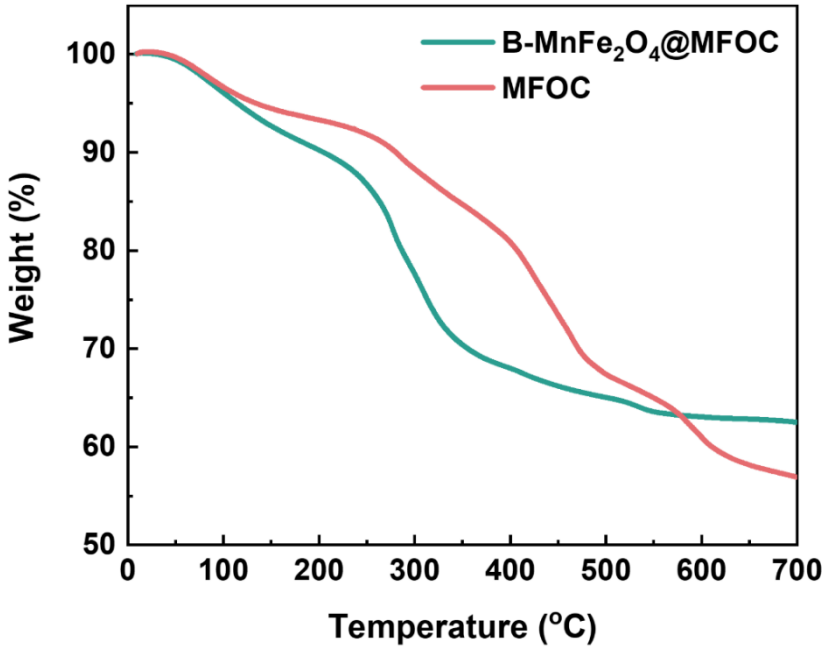

Figure 4.5 TGA patterns of MFOC and B-$MnFe_2O_4$@MFOC

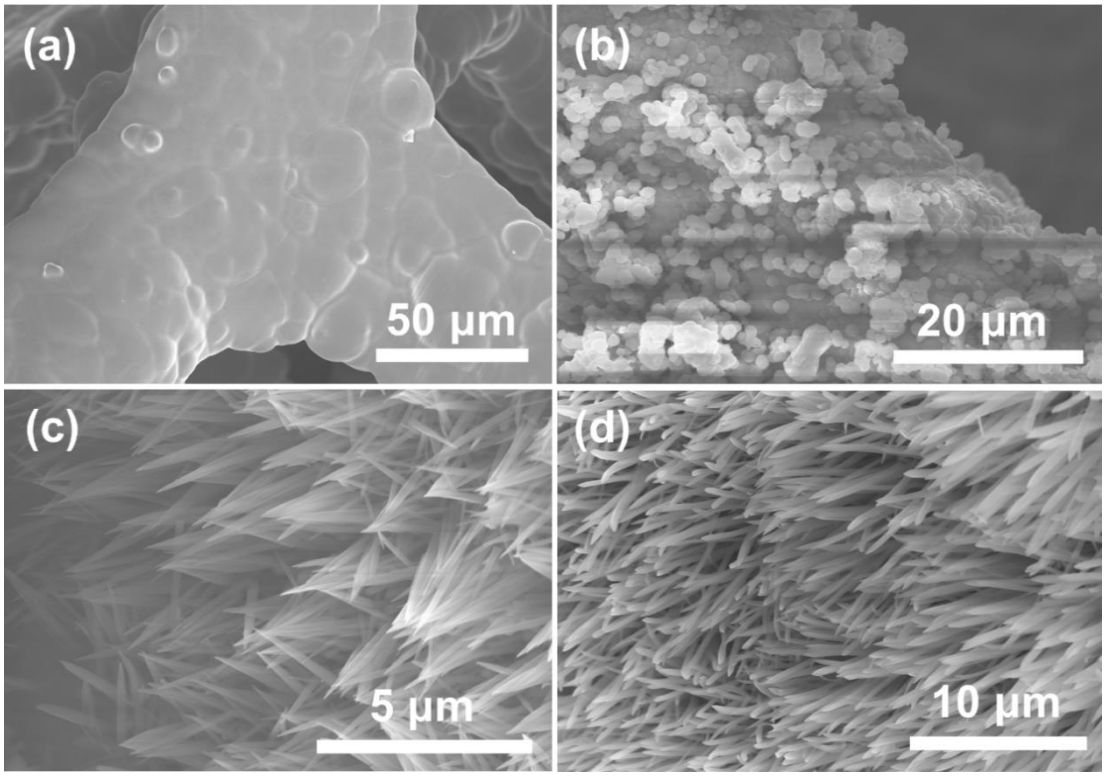

Figure 4.6 SEM images of (a) pure nickel foam; (b) Mn-MOF-74; (c)Fe-MOF-74 and (d) MnFe-MOF-74 precursors

From SEM images, one can see that bulk Mn-MOF-74 particles (**Figure 4.6**b) exist on the NF surface (**Figure 4.6**a). In comparison, Fe-MOF-74 (**Figure 4.6**c) and MnFe-MOF-74 (**Figure 4.6**d) needle-like nanowires with sharp tips are formed on NF. The magnified image of MnFe-MOF-74 (**Figure 4.12**a) reveals that the nanowires have a uniform size with an average diameter of ~150 nm and lengths up to several microns. After annealing in the air, the morphology of MFOC has no obvious change (**Figure 4.12**b). The well-separately grown MFOC nanowires with large open spaces on NF are observed, which could act as the perfect conductive platform for guiding the growth of B-$MnFe_2O_4$ nanosheets in the next step, leading to a large increase of effective surface area. As shown in **Figures 4.12**c and d, the nanowire-state MFOC has been changed to a nanosheet@ nanowire heterostructure B-$MnFe_2O_4$@MFOC with a uniform core@ shell nanostructure after the chemical reduction by alkaline $NaBH_4$ solution. That is,

the surface of the MFOC nanowire is covered by interconnected ultrathin B-$MnFe_2O_4$ nanosheets. Herein, the generated loose porous structure with plentiful free spaces should facilitate the electrolyte infiltration, especially ion diffusion in the electrode, as well as generated gases releasing [34]. To further proved the role of nanosheet @ nanowire heterostructure in the OER process, the contact angle of MFOC and B-$MnFe_2O_4$@MFOC was measured shown in **Figure 4.7**.

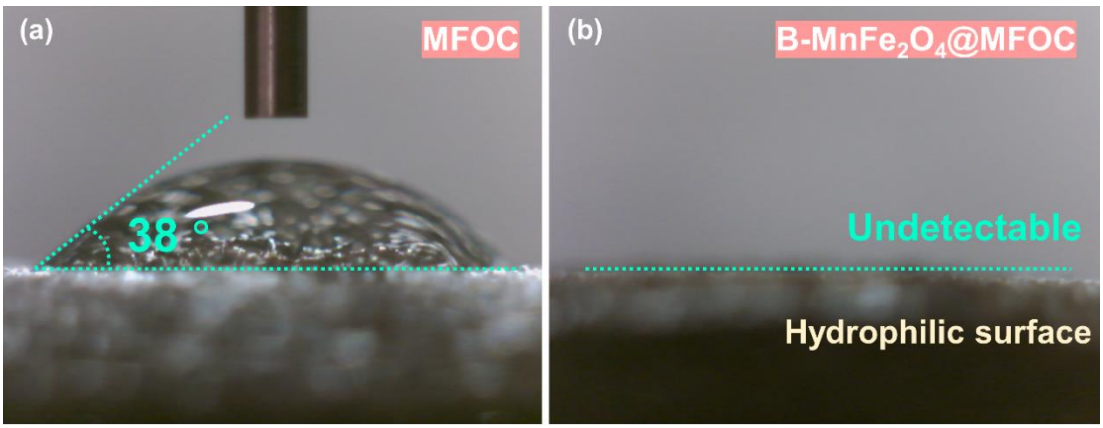

Figure 4.7 Water contact angles on (a) MFOC and (b) B-$MnFe_2O_4$@MFOC

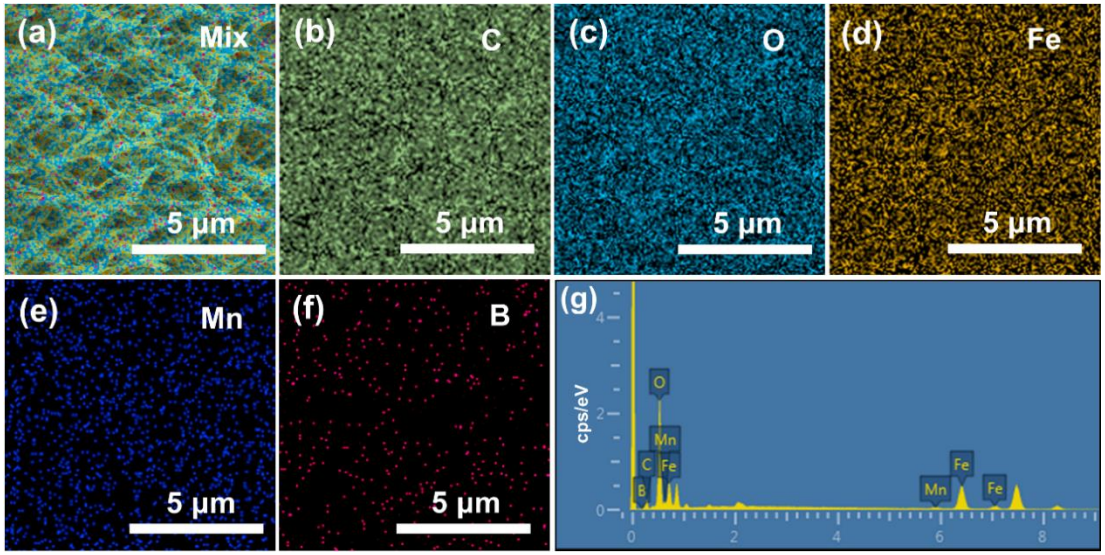

Figure 4.8 (a-f) EDS elemental mappings of C, O, Fe, Mn and B on B-$MnFe_2O_4$@MFOC; (g) corresponding EDS spectrum.

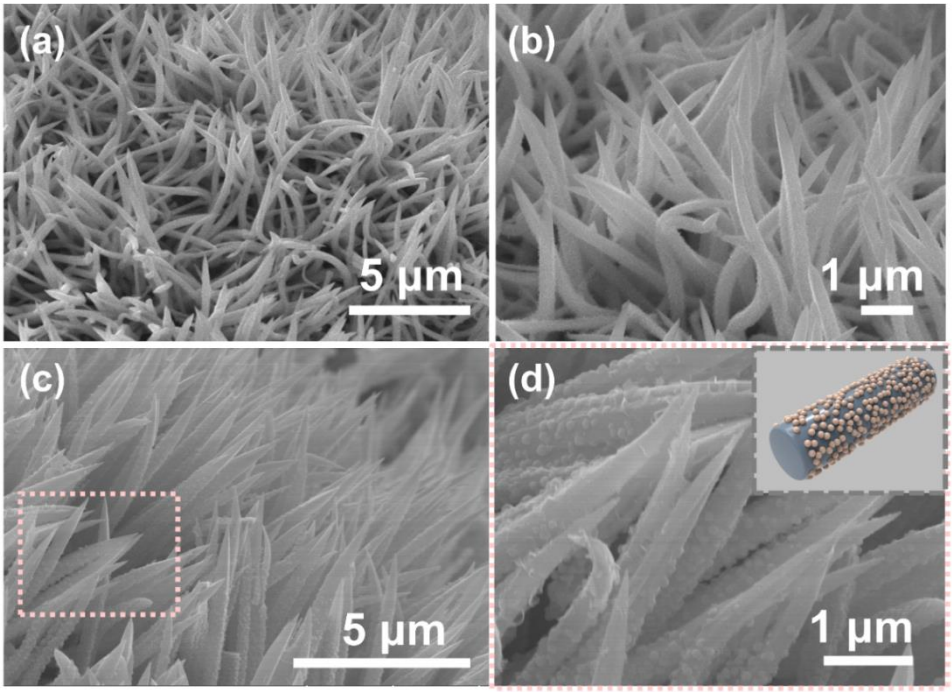

Figure 4.9 SEM images of B-$MnFe_2O_4$@MFOC with (a-b) $NaBH_4$ treating time for 10 min; (c-d) $NaBH_4$ treating time for 40 min.

Compared with the water contact angle on the surface of MFOC (38°), the average water contact angle on the surface of B-$MnFe_2O_4$@MFOC was significantly reduced to 0°, even barely undetected, suggesting the surface of B-$MnFe_2O_4$@MFOC shows excellent hydrophilicity, which should be more favorable for the aqueous electrolyte solution contacting with the electrocatalyst, conducting to the adsorption of water molecules and fast ionic diffusion and finally improving the catalysis performance. EDS analysis (**Figure 4.8**) indicated the existence of C, O, B, Fe, Mn elements, which distributed uniformly on the B-$MnFe_2O_4$@MFOC. Interestingly, when the reduction time by $NaBH_4$ is reduced to 10 minutes, it can be observed that few nanosheets are grown (**Figure 4.9**a and b); however, the nanosheets are replaced by nanoparticles grown on the MFOC (**Figure 4.9**c and d) as the reduction duration for the formation of the B-$MnFe_2O_4$ shell is increased from 20 to 40 minutes. Therefore, the 20-min should be the optimal treatment time since the excessive reduction leads to agglomeration,

reducing the number of active sites and surface area. As displayed in **Figures 4.10** and **4.11**, the nanosheet-state B-Fe_3O_4 and B-Mn_3O_4 are also grown on the FOC and MOC after the reduction by $NaBH_4$ for 20 min, respectively.

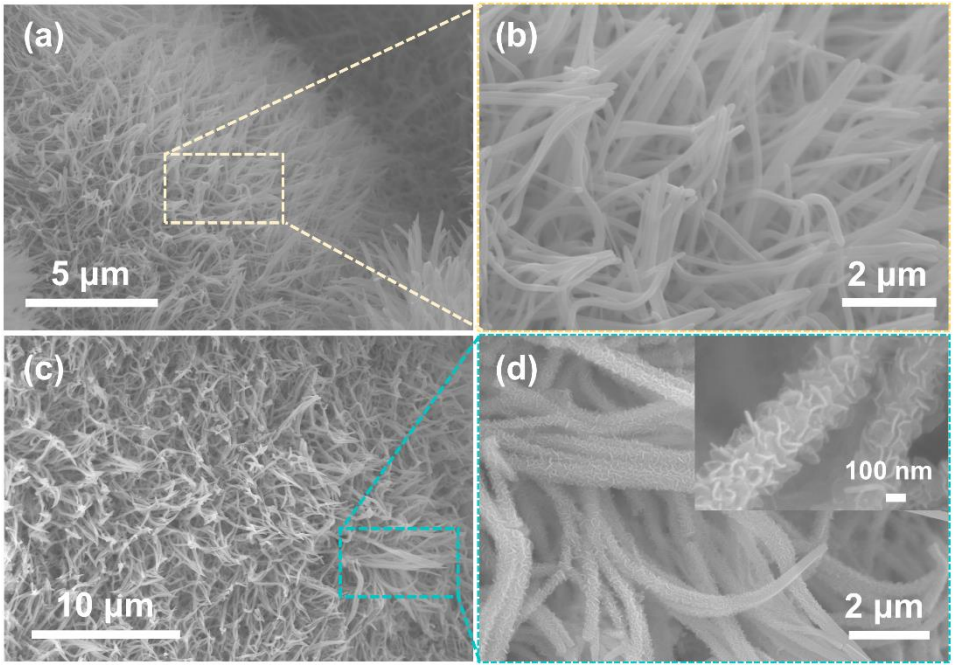

Figure 4.10 SEM images of (a-b) FOC, (c-d) B-Fe_3O_4@FOC formed on NF and high magnification of nanowire of the B-Fe_3O_4@FOC

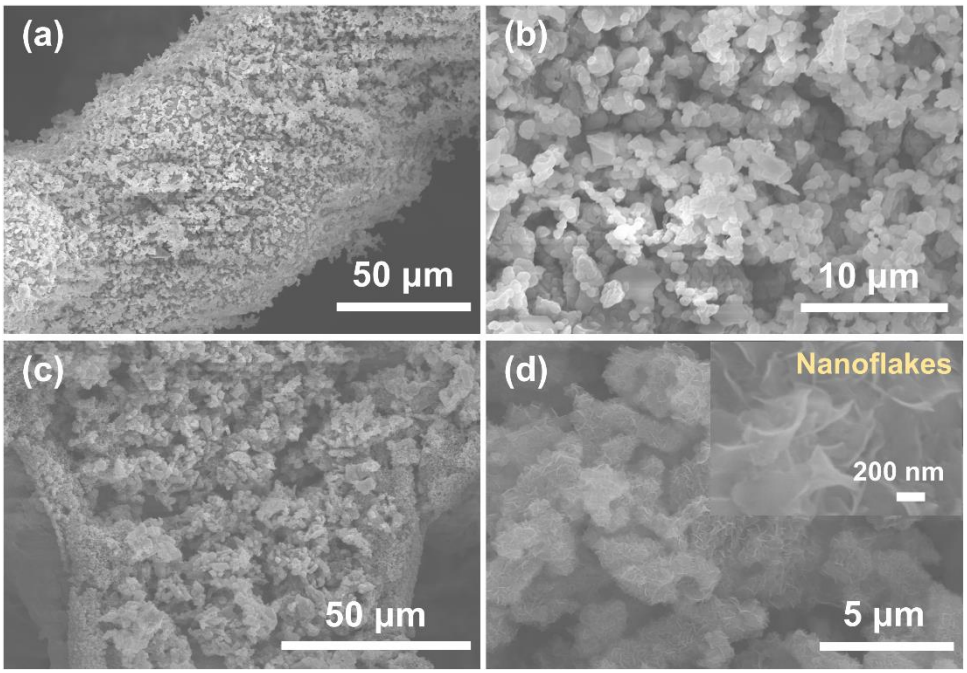

Figure 4.11 SEM images of (a-b) MOC, (c-d) B-Mn_3O_4@FOC formed on NF and high magnification of nanowire of the B-Mn_3O_4@MOC

The B-$MnFe_2O_4$@MFOC was stripped from NF for TEM and HR-TEM observations to obtain the detailed nano-scale morphological and heterointerface information. As illustrated in **Figures 4.12**e and f, the MFOC wire is clearly wrapped by a layer of B-$MnFe_2O_4$ nanosheets to form a core@ shell nanostructure, which is consistent with the SEM results. Noticeably, the inner core material presents an amorphous area (selected with pink square, **Figure 4.12**g), which is further identified by the corresponding diffusion ring (**Figure 4.12**h) with the fast Fourier transform (FFT) pattern. It is also confirmed by the TEM images of MFOC in **Figure 4.13**, in which the selected areas have only weak reflection halos in the diffraction pattern of MFOC sample, demonstrating the amorphous state of nanowire. An interface between B-$MnFe_2O_4$ and MFOC is clearly observed in **Figures 4.12**i and j. The B-$MnFe_2O_4$ nanosheets shell structure reveals a polycrystalline nature, the fringe lattice spacings of 0.298 and 0.491 nm can be indexed to the characteristic (220) and (111) planes of the $MnFe_2O_4$ nanocrystal, respectively, indicating that the nanosheets are composed by the crystalline $MnFe_2O_4$. For comparison, the HR-TEM images of Fe_3O_4@FOC and Mn_3O_4@MOC are also shown in **Figures 4.14** and **4.15**, respectively, in which the interplanar spacings of 0.259 and 0.297 nm are matched well with the (311) and (220) planes of Fe_3O_4 and Mn_3O_4, respectively. Besides, EDS analysis results confirm the existence of element B within the resultant B-$MnFe_2O_4$@MFOC (**Figure 4.16**). Meanwhile, same as the elemental mapping of MFOC (**Figure 4.17**), the B, C, O, Fe and Mn elements are also uniformly distributed on the nanowire (**Figures 4.12** k-p).

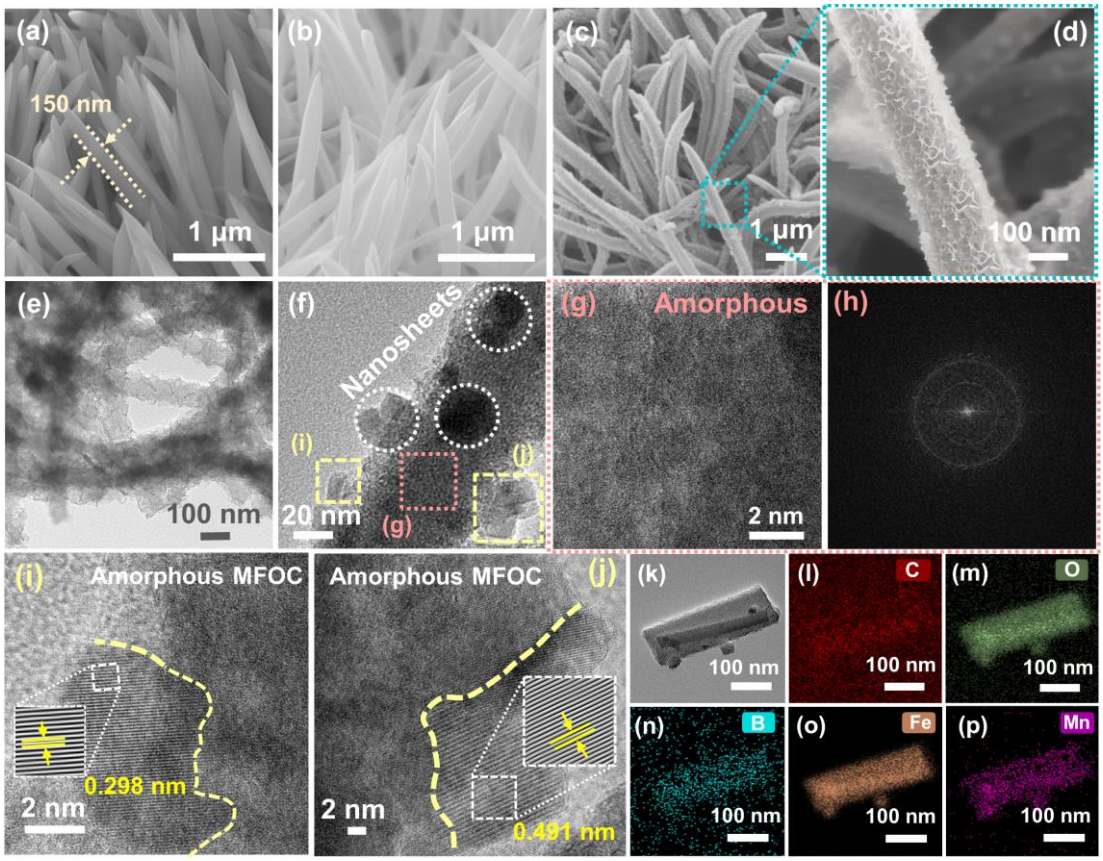

Figure 4.12 SEM images of (a) MnFe-MOF precursor; (b) MFOC and (c-d) B-$MnFe_2O_4$@MFOC; (e) TEM images of B-$MnFe_2O_4$@MFOC; (f) HR-TEM image showing nanosheet@ nanowire heterostructure, in which the nanosheets are marked by white dashed curves; (g) HRTEM image enlarged the pink dashed square in (f) image; (h) corresponding FFT pattern of the (g) image; (i-j) HRTEM images enlarged the yellow dashed square in (f) image; (k-p) TEM-EDS mappings of B-$MnFe_2O_4$@MFOC.

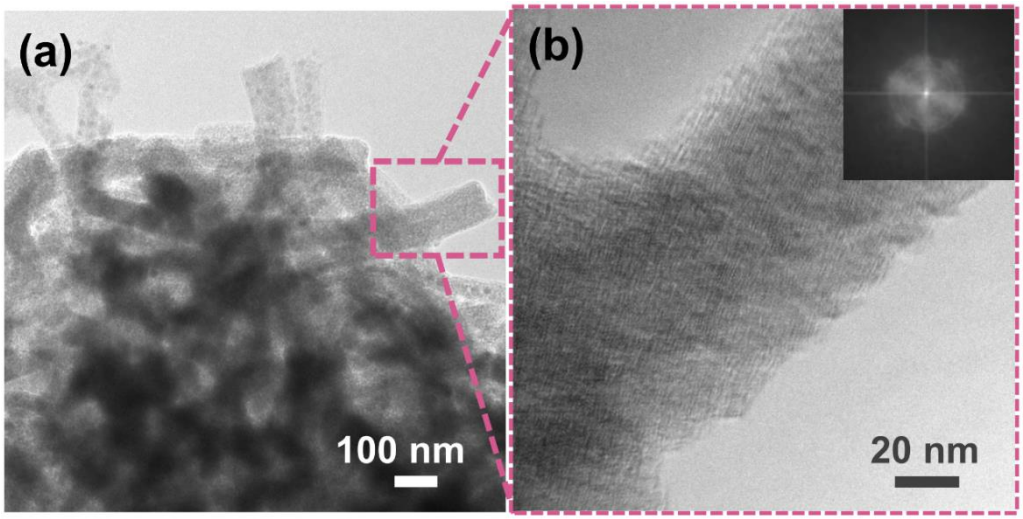

Figure 4.13 (a) TEM image of MFOC; (b) HR-TEM of MFOC (insert: FFT pattern)

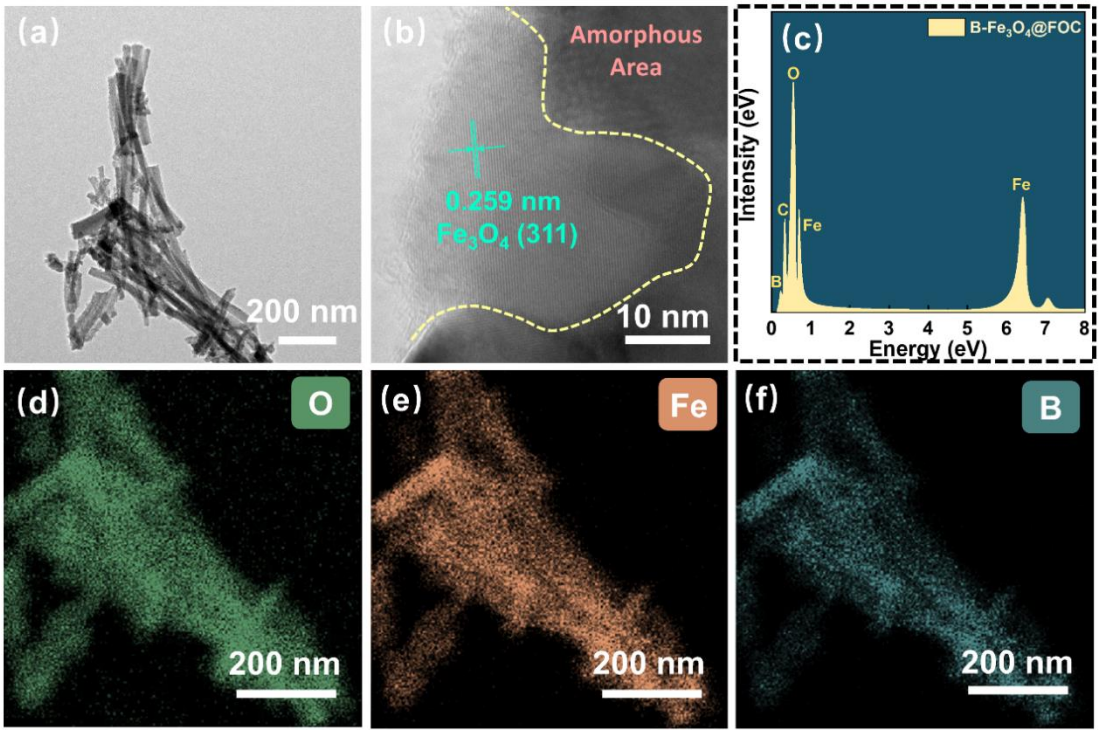

Figure 4.14 (a)TEM image; (b)HR-TEM image; (c)EDS spectrum and (d-f) TEM-EDS mappings of B-Fe_3O_4@FOC

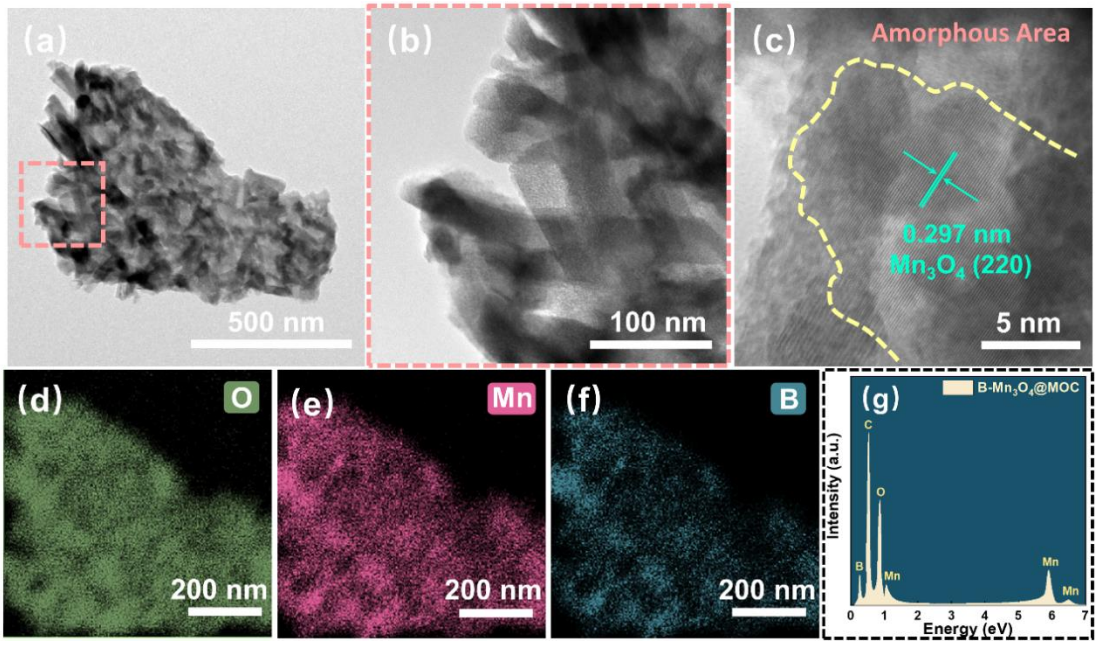

Figure 4.15 (a)TEM image; (b)HR-TEM image; (c)EDS spectrum and (d-f) TEM-EDS mappings of B-Mn_3O_4@MOC

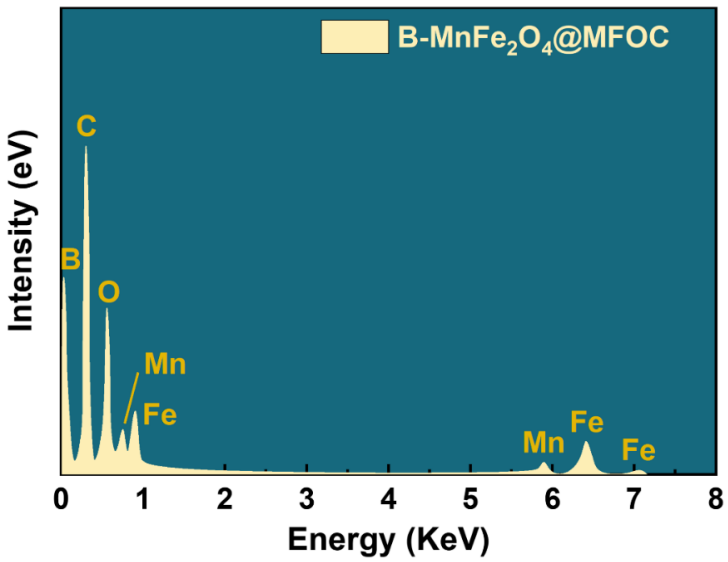

Figure 4.16 EDS spectrum of B-$MnFe_2O_4$@MFOC

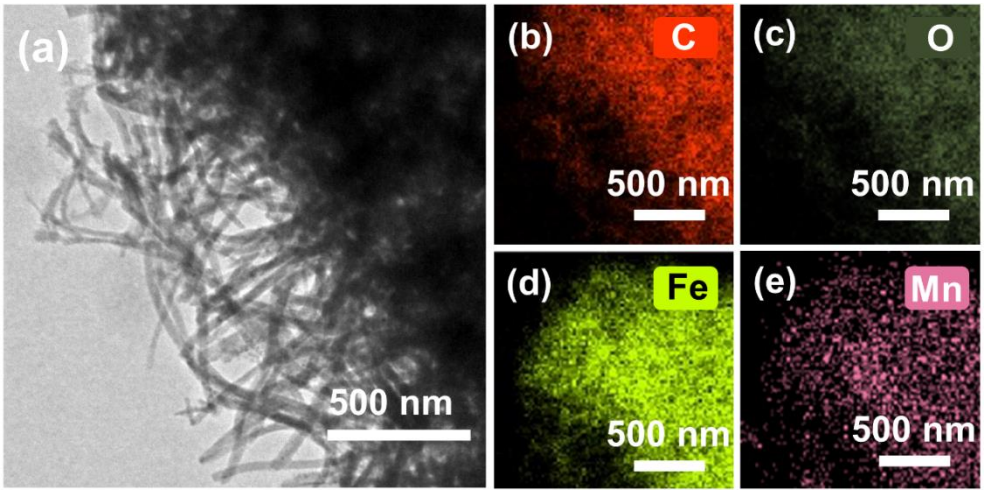

Figure 4.17 TEM-EDS mapping of MFOC

Figure 4.18a shows the wide-scan XPS profiles of the synthesized electrocatalysts, in which Fe *2p*, Mn *2p*, C *1s*, O *1s* and B *1s* are found at 710, 640, 285, 532 and 190 eV, respectively, also indicating the existence of B besides Fe, Mn, C and O on the B-$MnFe_2O_4$@MFOC surface (the elements content details shown in **Table 4.2**). In the Fe *2p* high-resolution XPS spectrum of B-$MnFe_2O_4$@MFOC (**Figure 4.18**b), two spin-orbit doublets at binding energies at ca. 711 and 725 eV can be attributed to the Fe $2p_{3/2}$ and Fe $2p_{1/2}$, respectively. Furthermore, the profile of the Fe $2p_{3/2}$ spectrum can be deconvoluted into four peaks, suggesting four states of Fe species on the surface. That

is, the bonding energies at 710.54, 712.35 and 714.33 eV assign to Fe^{2+}, Fe^{3+} (in spinel octahedron site, Oh) and Fe^{3+} (in spinel tetrahedron site, Td), respectively [35]. It should be noted that an additional peak of Fe-B at ~707 eV is fitted in the high-resolution XPS spectra of Fe, and the same position peak was also observed on the B-Fe_3O_4@FOC surface (**Figure 4.19**b), suggesting that the doping of B can generate a Fe-B bond [36]. The Mn *2p*$_{3/2}$ spectra of B-$MnFe_2O_4$@MFOC and B-Mn_3O_4@MOC are displayed in **Figures 4.18**c and **4.19**d, which are distinguished at ~641.0 and 642.8 eV, assigning to Mn^{2+} and Mn^{3+}, respectively. Similarly, a peak relating to Mn-B at ~637.9 eV can be fitted on either B-$MnFe_2O_4$@MFOC or B-Mn_3O_4@MOC surface. To further confirm the real oxidation of Mn *2p*, the multiple splitting separation of Mn *3s* photopeak was fitted (**Figure 4.20**). The Mn *3s* spectrum splits into a doublet of peaks with a multiple splitting energy of 6.3 eV, higher than that of Mn^{2+} (6.1 eV) [37], which indicates the real oxidation states of Mn *2p* is the mixing of Mn^{2+} and Mn^{3+}.

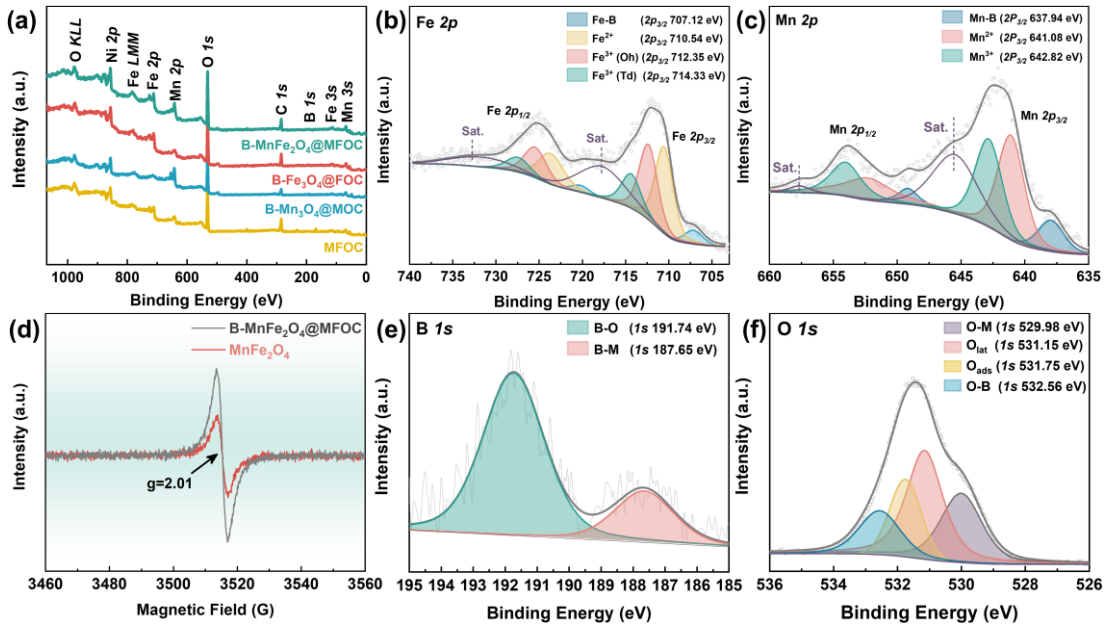

Figure 4.18 (a) Full XPS profiles of B-Fe_3O_4@FOC, B-Mn_3O_4@MOC, MFOC and B-$MnFe_2O_4$@MFOC; High-resolution XPS spectra of (b) Fe *2p*; (c) Mn *2p*; (e) B *1s* and (f) O*1s* of B-$MnFe_2O_4$@MFOC; (d) EPR spectra of $MnFe_2O_4$ and B-$MnFe_2O_4$@MFOC.

To further investigate the change of valence states after doping of B into the $MnFe_2O_4$ structure, a standard spinel $MnFe_2O_4$ sample was also synthesized (**Figure 4.21**), and the standard XPS spectrum was also fitted (**Figure 4.22**). Comparing with the Fe *2p* and Mn *2p* XPS peaks of the standard $MnFe_2O_4$ sample, both of them for the B-$MnFe_2O_4$@MFOC are shifted to a lower binding energy direction, suggesting that electron densities of the Fe and Mn should be increased due to the replacing of O with high electronegativity (3.44 of O) around the Fe and Mn elements by B with lower electronegativity (2.01 of B), which could vary the electronic structure as well as the coordination bond. Thus, B should have replaced parts of oxygen in the lattice structure of $MnFe_2O_4$ spinel [38]. After the doping of B into the lattice of $MnFe_2O_4$ spinel, the localized electrons on the B will favor the generation of higher oxidation states of Fe and Mn metal sites. **Figure 4.18**e displays the B *1s* spectrum of B-$MnFe_2O_4$@MFOC, which can be deconvoluted into three peaks at 191.784 and 187.65 eV, assigning to oxidized borate species, B-Metal bonds, respectively. It also indicates that B atoms could be directly bonded to metal (Fe and Mn) by the metal d-orbitals and/or the hybridization of B *2p* states after $NaBH_4$ reduction treatment [39, 40], and the binding energies of B-Fe and B-Mn for B-Fe_3O_4@FOC and B-Mn_3O_4@MOC are 187.42 and 187.71 eV, respectively (**Figure 4.23**). Herein, it should be noticed that the binding energy of metal-B is higher than that of pure boron (187.0 eV), which should be beneficial for the occurrence of electron transfer from B to Fe/Mn atom. Compared with the non-metal B atom, the d-orbitals of the metal species are filled with more electrons, serving as the catalytic active sites. That is, the B atoms may not serve as the active sites directly to participate in the OER reaction but act as supplementary function to mitigate the over-oxidation of metal-sites, decrease the activation energy barrier and boost the electrocatalytic activity by donating electrons [40]. For the high-resolution O

1s spectrum of B-$MnFe_2O_4$@MFOC (**Figure 4.18**f), comparing with that of MFOC (**Figure 4.24**), three peaks located at 529.98, 531.15 and 531.75 eV are assigned to the lattice O^{2-} species (O_{lat}) within the M-O bonds, adsorption oxygen (O_{ads}) from M-OH^- and minor chemisorbed water on the surface, respectively [41, 42]. In addition, an extra peak located at 532.56 eV is observed, which should belong to the B-O bond. It should be noticed that the area of O_{ads} peak (19.13%) is smaller than that of O_{lat} (39.4%), suggesting that the oxygen in the oxygen-containing groups on the surface of B-$MnFe_2O_4$@MFOC tends to transform into more dense lattice oxygen after the reduction reaction [38]. Moreover, the asymmetric nature of the high energy O_{ads} demonstrates the presence of oxygen vacancy, by which it can be found that the vacancy density is increased after the $NaBH_4$ reduction treating.

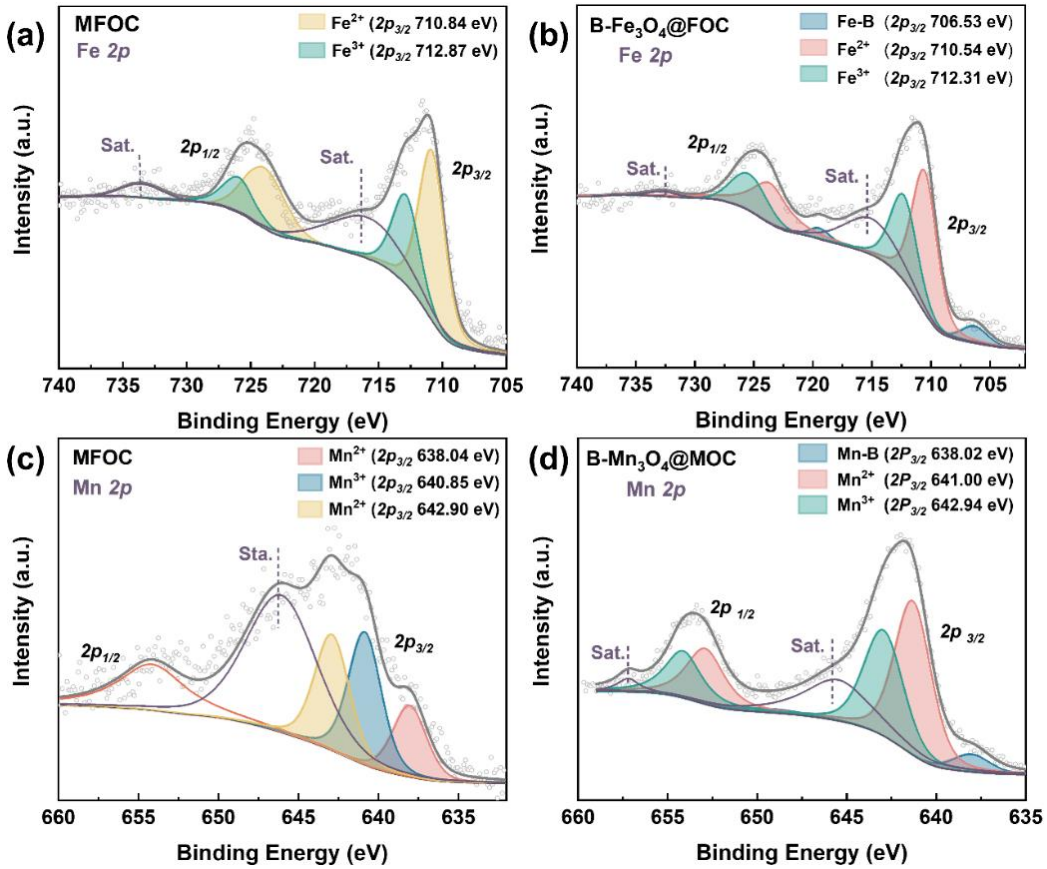

Figure 4.19 High resolution XPS spectra of Fe *2p* in (a) MFOC and (b) B-Fe_3O_4@FOC; Mn *2p* in (c) MFOC and (d) B-Mn_3O_4@MOC

Table 4.2 Summary information details of elements on B-$MnFe_2O_4$@FMOC measured from XPS.

Elements	Start BE	End BE	FWHM (eV)	Area	Atomic (%)
B *1s*	196	180	1.44	4312.92	7
C *1s*	298	279.36	3.25	59416.57	28
O *1s*	539.52	527.39	3.3	256342.44	46.2
Mn *2p*	660	632	6.27	34676.8	5.6
Fe *2p*	740	700	6.08	61602.62	12
Ni *2p*[a]	888	856.12	3.71	119588.28	1.2

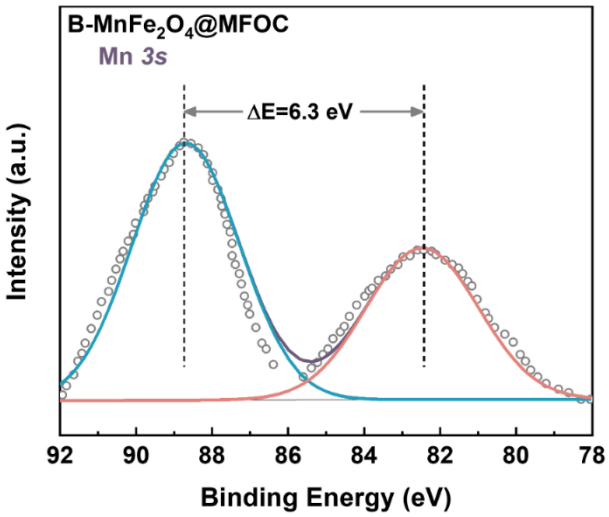

Figure 4.20 Mn *3s* XPS spectra of the B-$MnFe_2O_4$@MFOC

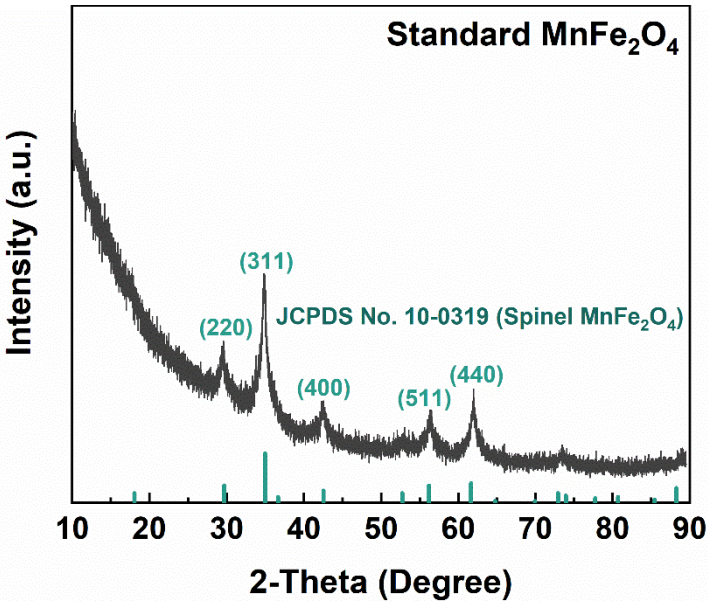

Figure 4.21 XRD pattern of standard $MnFe_2O_4$

Furthermore, the oxygen vacancy density was confirmed by the electron paramagnetic resonance (EPR) measurements of B-$MnFe_2O_4$@MFOC and $MnFe_2O_4$ [43]. As shown in **Figure 4.18**d, there is a stronger magnetic signal at ~3515 G for the B-$MnFe_2O_4$@MFOC, which indicates a higher concentration of unpaired electrons resulted from the oxygen defects [44]. As stated above, due to the replacing of O by B in the spinel, the electrons from the boron could be transferred to the neighboring metal sites so that the metal species such as Fe^{3+} experience a conversion to a more stabilized high spin state, achieving an optimal e_g filling. The corresponding overlap area of oxygen with metal ions is getting concentrated, which may cause the faster charge transfer and thereby improving the catalyst performance.

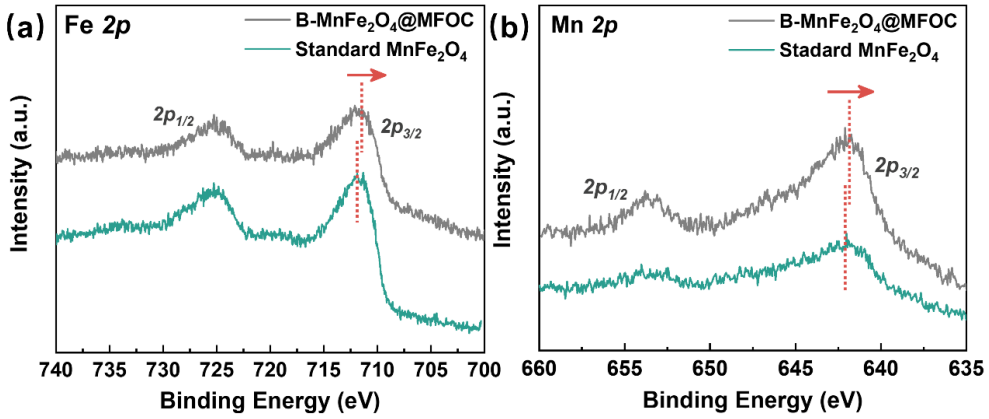

Figure 4.22 High resolution XPS spectra of (a) Fe *2p* and (b) Mn *2p* in B-$MnFe_2O_4$ @FMOC and standard $MnFe_2O_4$.

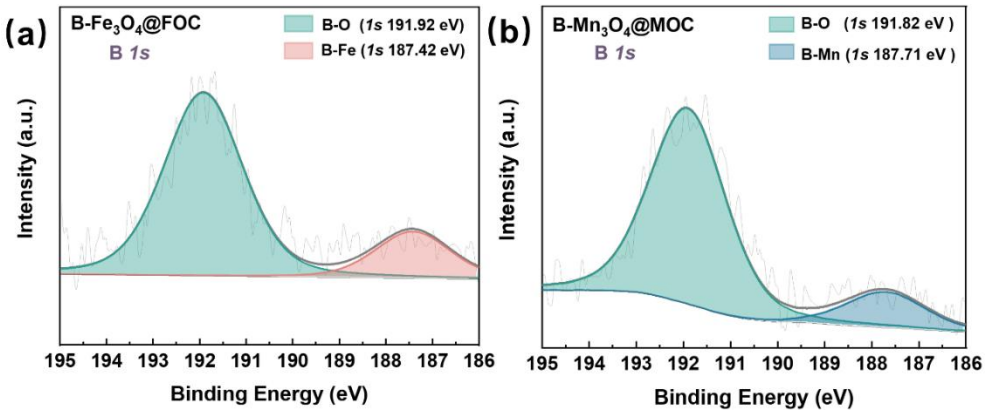

Figure 4.23 XPS spectra of B 1s in (a) B-Fe_3O_4@FOC and (b) B-Mn_3O_4@MOC

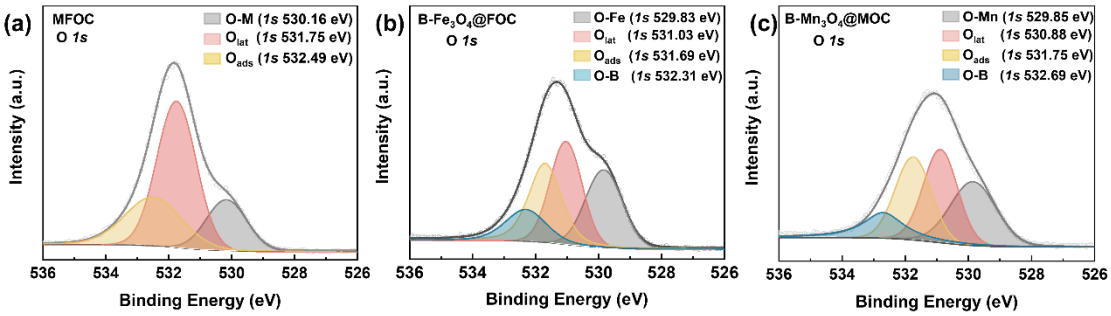

Figure 4.24 High resolution of O *1s* in as-prepared samples

4.3.2 Electrochemical performance for OER

OER linear sweep voltammetry (LSV) curves of the fabricated electrodes were assessed in 1 M KOH containing freshwater based electrolyte at first. As the preliminary experiments, various electrodes were fabricated by adjusting the molar ratio of Fe and Mn (1:10; 2:10; 3:10 and 4:10) in the initial solutions and their LSV performances were evaluated (**Figure 4.25a**). Besides, the effects of other synthesis conditions including annealing temperature (250, 350 and 450 ℃) and $NaBH_4$ reduction time (0, 20 and 40 min) on the LSV performance were also investigated (**Figures 4.25** b and c). As such, it is found that the B-$MnFe_2O_4$@MFOC electrocatalyst with the best OER performance should be synthesized with a Fe: Mn molar ratio of 3:10, an annealing temperature of 250 ℃ and $NaBH_4$ reduction time of 20 minutes, which was further studied in this work in the following. **Figure 4.26**a records the LSV curves without iR-corrections for the as-prepared best B-$MnFe_2O_4$@MFOC, MFOC, B-Fe_3O_4@FOC and B-Mn_3O_4@MOC based electrodes. Specifically, the B-$MnFe_2O_4$@MFOC requires an extremely low overpotential of 298 mV at 100 mA cm^{-2}, which is much lower than those of MFOC (341 mV), B-Fe_3O_4@FOC (377 mV) and B-Mn_3O_4@MOC (452 mV) (**Figure 4.26**b and **Table 4.3**). Meanwhile, the B-$MnFe_2O_4$@MFOC ranked the top level among those reported materials (**Table 4.4**).

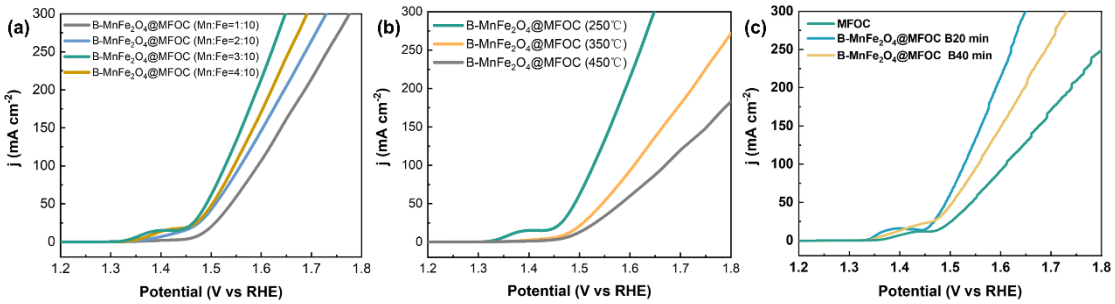

Figure 4.25 LSV curves of B-$MnFe_2O_4$@FMOC based electrodes prepared by (a) using different amounts of $FeSO_4 \cdot 7H_2O$ and $MnSO_4 \cdot H_2O$ precursors (molar amount) (b) using different temperatures and (c) by using different $NaBH_4$ treating time.

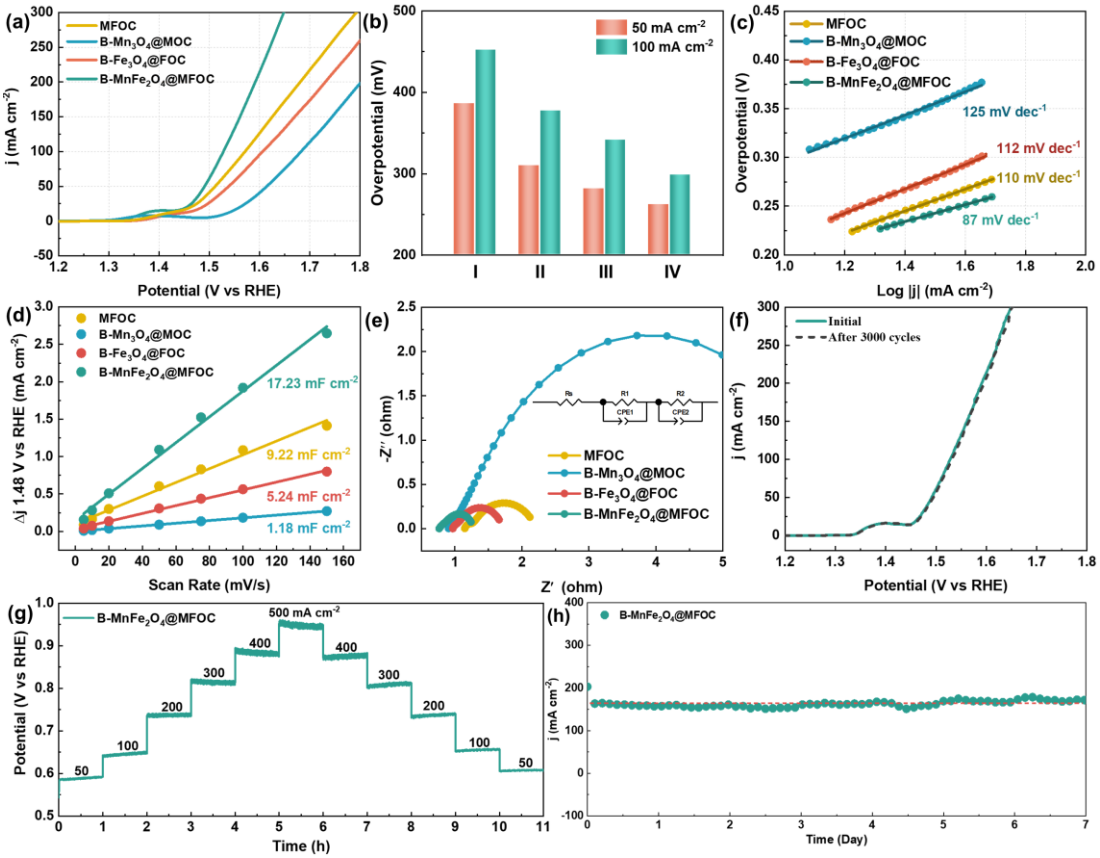

Figure 4.26 OER polarization curves of B-Mn_3O_4@MOC (I), B-Fe_3O_4@FOC (II), MFOC (III) and B-$MnFe_2O_4$@MFOC (IV) in 1 M KOH; (b) related overpotentials; (c)Tafel plots; (d) current density as a function of scan rate derived from the CV curves at; (e) Nyquist plots and equivalent circuit model (inset); (f) polarization curves of the B-$MnFe_2O_4$@MFOC electrode before and after 3000 CV cycles; (g) multi-current step test and (h) the chronoamperometry curves of the B-$MnFe_2O_4$@MFOC electrode at the constant potential corresponding to the current density of 100 mA cm^{-2} for 7 days.

Table 4.3 Summary of the OER performances of B-Mn_3O_4@MOC, B-Fe_3O_4@FOC, MFOC and B-$MnFe_2O_4$@FMOC.

Catalysts	η_{100}	Tafel	C_{dl}	R_{ct}
B-Mn_3O_4@MOC	452	125	1.18	4.51
B-Fe_3O_4@FOC	377	112	5.24	1.15
MFOC	341	110	9.22	0.97
B-$MnFe_2O_4$@FMOC	298	87	17.23	0.77

Table 4.4 Comparison of OER catalytic activities with reported OER catalysts from oxides materials in 1M KOH.

Catalysts	Substrate	η_{100} (mV)	Reference
B-$MnFe_2O_4$@MFOC	NF	298	This work
MoS_2/*r*Fe-$NiCo_2O_4$	CP	320	*J. Am. Chem. Soc.* **2019**,*142*, 50.
CoO/Co_3O_4	Ti foil	315	*Angew. Chem. Int. Ed.* **2020**, *59,* 6929.
MoS_2/NPF-$CoFe_2O_4$	GC	360	*Adv. Energy Mater.* **2018**, *8,* 1800980.
$CoFe_2O_4$/NF	NF	400	*RSC Adv.* **2019**, *9*, 13269.
$Fe_{10}Co_{40}Mn_{50}O$	FTO	280	*Small,* **2022**, 2204520.
NiFeCo oxides	SS	315	*Int. J. Energy Res.* **2020**, *44*, 1789.
Fe_3O_4-NF	NF	310	*J. Alloys Compd.* **2021**, *863*, 158742.
2D (FeCoNi)O_4	CP	305	*Mater. Today Chem.* 2022, *26*, 101214.
FeOOH-$CoMoO_4$	IF	298	*ACS Appl. Mater. Interfaces* **2021***,* 13
Fe-Co_3O_4 HHNPs	GC	303	*Adv. Mater.* **2020***, 32*, 2002235.
Fe-Co_2SiO_4 nanosphere	NF	390	*J. Colloid Interface Sci.* **2022**, *611*, 235.
$NiMoO_4$@Co_3O_4	NF	282	*Adv. Energy Mater.* 2021, 11, 2101324.
FeCoNiPB/$(FeCoNi)_3O_{4-x}$	HEA ribbons	406	*Appl. Surf. Sci.* 549 (2021) 149327.

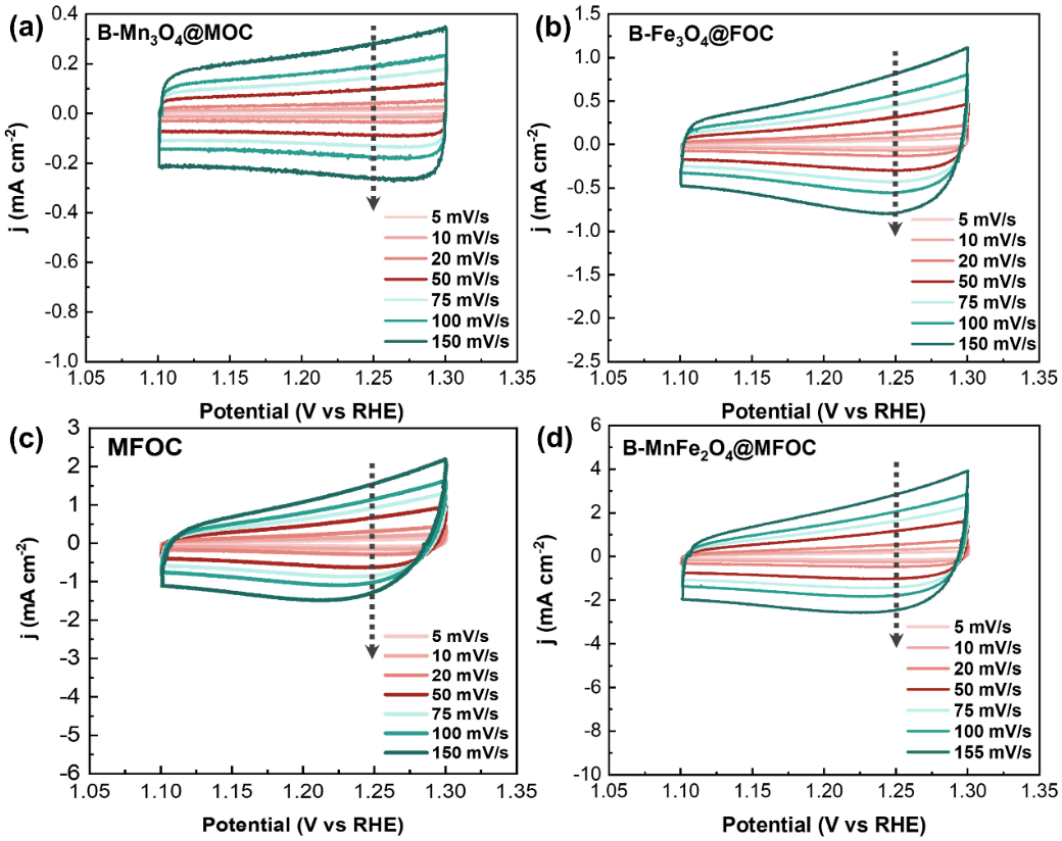

Figure 4.27 Cyclic voltammograms of (a) B-Mn_3O_4@MOC; (b) B-Fe_3O_4@FOC; (c) FMOC and (d) B-$MnFe_2O_4$@FMOC based electrodes with various scan rates in 1 M KOH solution.

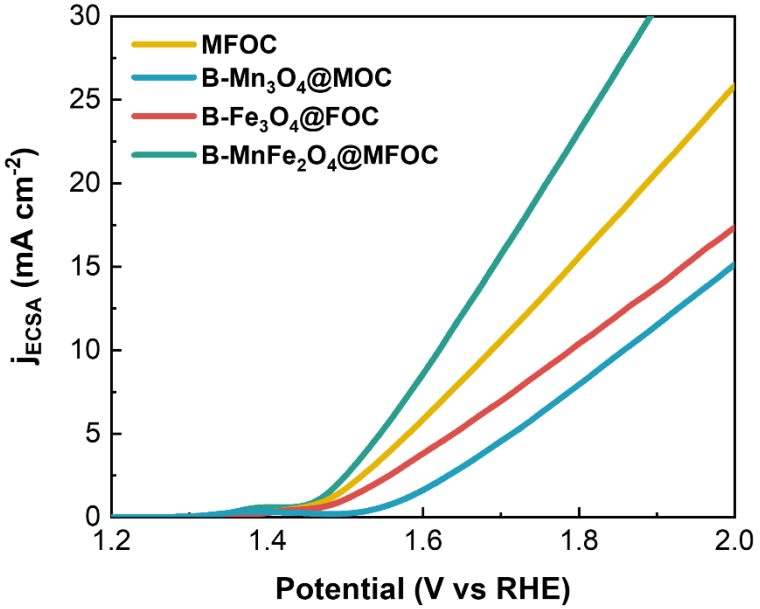

Figure 4.28 OER ECSA-normalized LSV curves of B-Mn_3O_4@MOC; (b) B-Fe_3O_4@FOC; (c) FMOC and (d) B-$MnFe_2O_4$@FMOC

While, the catalytic kinetics of the above electrocatalysts were evaluated by the Tafel slope. As shown in **Figure 4.26**c, the Tafel slope of the B-$MnFe_2O_4$@MFOC is only as low as 87 mV dec^{-1}, which is much lower than those of MFOC (110 mV dec^{-1}), B-Fe_3O_4@FOC (112 mV dec^{-1}) and B-Mn_3O_4@MOC (125 mV dec^{-1}), demonstrating a fastest electrocatalytic kinetics of OER. Herein, it is conjectured that the outstanding OER performance of B-$MnFe_2O_4$@MFOC electrode should be mainly originated from the B-$MnFe_2O_4$, where MFOC possibly only serves as a conductor and support as discussed above. Furthermore, the electrochemical double-layer capacitances (C_{dl}) were evaluated based on the cyclic voltammetry curves (**Figure 4.27**). As displayed in **Figure 4.26**d, the C_{dl} of B-$MnFe_2O_4$@MFOC electrode is about 17.23 mF cm^{-1}, which is significantly higher than those of MFOC (9.22 mF cm^{-1}), B-Fe_3O_4@FOC (5.24 mF cm^{-1}) and B-Mn_3O_4@MOC (1.18 mF cm^{-1}), indicating that the B-$MnFe_2O_4$@MFOC possesses higher electrocatalytically active surface area, which may be due to that more active sites could be created by growing the spinel nanosheets. In addition, the intrinsic catalytic activity was evaluated by the overpotential required to achieve a certain density, which can be further normalized to the effective electrochemical surface area (ECSA). **Figure 4.28** exhibits the j_{ECSA}-normalized polarization curves, which indicates that the B-$MnFe_2O_4$@MFOC has the highest inherent catalytic activity. The reaction kinetics and charge transfer resistance of as-prepared electrode were further explored by electrochemical impedance spectroscopy (EIS) analysis. As shown in **Figure 4.26**e, the B-$MnFe_2O_4$@MFOC electrode displays a smaller charge transfer resistance (R_{ct}) of 0.77 Ω than those of MFOC (0.97 Ω), B-Fe_3O_4@FOC (1.15 Ω) and B-Mn_3O_4@MOC (4.51 Ω) electrodes. As such, it can infer that the B-$MnFe_2O_4$@MFOC should have a fast charge transfer kinetics, which accounts for its enhanced OER performance. The stability of B-$MnFe_2O_4$@MFOC/NF electrode was further tested. As shown in **Figure**

4.26f, the current density is retained well with no obvious decrease compared to the initial one even after 3000-cycle testing. Furthermore, the multi-step chrono-potentiometric curve of B-$MnFe_2O_4$@MFOC/NF electrode was measured and shown in **Figure 4.26**g, where the current density was changed from 50 to 500 mA cm^{-2} and then returned to 50 mA cm^{-2}. A sharp voltage response with the current density changes manifests that the composite structure has outstanding mass transport property as well as mechanical robustness for OER. Obviously, in the time interval of one hour, the potential maintains constantly under each step, indicating the excellent stability at different voltages. In addition, an electrochemical long-term stability for the B-$MnFe_2O_4$@MFOC electrode was evaluated via a chrono potentiometric curve testing. As shown in **Figure 4.26**h, a steady OER performance without obvious decrease over 7 days is achieved. Therefore, the obtained B-$MnFe_2O_4$@MFOC/NF electrode should have outstanding mechanical robustness as well as excellent catalytic stability in 1 M KOH containing freshwater based electrolyte.

4.3.3 DFT Calculations

DFT calculation was employed to establish the close relationship between OER performance and electronic structure on the catalyst surface [16]. At first, the conductivities of pure carbon and Mn, Fe oxides doped into carbon species were evaluated by total density of states (DOS) calculations (**Figure 4.29**). It is found that the metal doped carbon species has a higher DOS intensity around Fermi level, indicating that it owns superior electrical conductivity, which further proves that the MFOC in the B-$MnFe_2O_4$@MFOC could provide a good conductive environment for the whole catalysts during the OER process. Then, on the basis of above characterizations, the top and side views of atomic structure models of $MnFe_2O_4$ and B-$MnFe_2O_4$ are established, in which Fe^{3+} and Mn^{2+} are coordinated with six and four

oxygen atoms, respectively, and the B atoms replace the O atoms bonding with Fe or Mn. (**Figure 4.30**). After the structure optimization, it is obvious that most Fe-O bond lengths decrease significantly while Mn-O bond length basically maintains after the doping of B atoms (**Figure 4.31 and Table 4.5**), indicating that the doping of B atoms can distort the octahedral structure, which is in agreement with the XPS analysis results as discussed above.

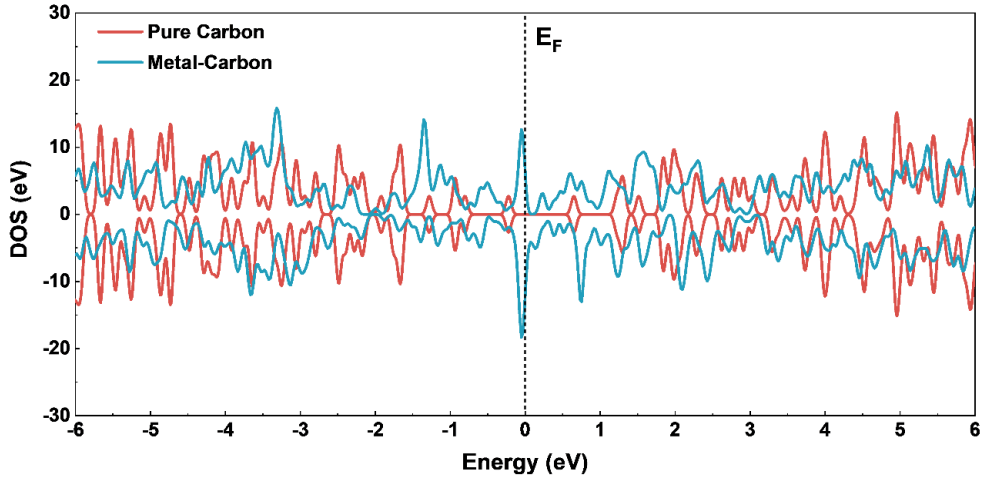

Figure 4.29 Density of states (DOS) of pure carbon and Mn, Fe oxides doped into carbon species

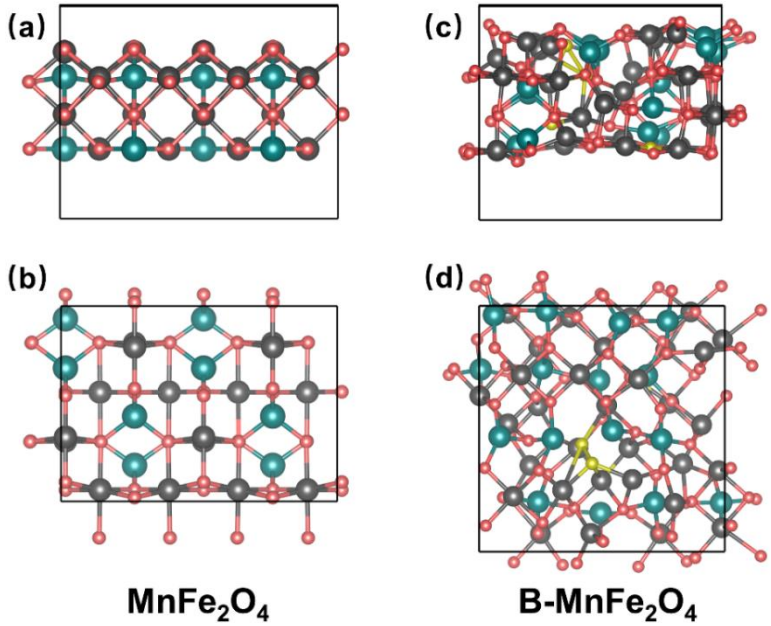

Figure 4.30 Top (upper) and side (lower) views of the optimized structures of $MnFe_2O_4$ and $B\text{-}MnFe_2O_4$

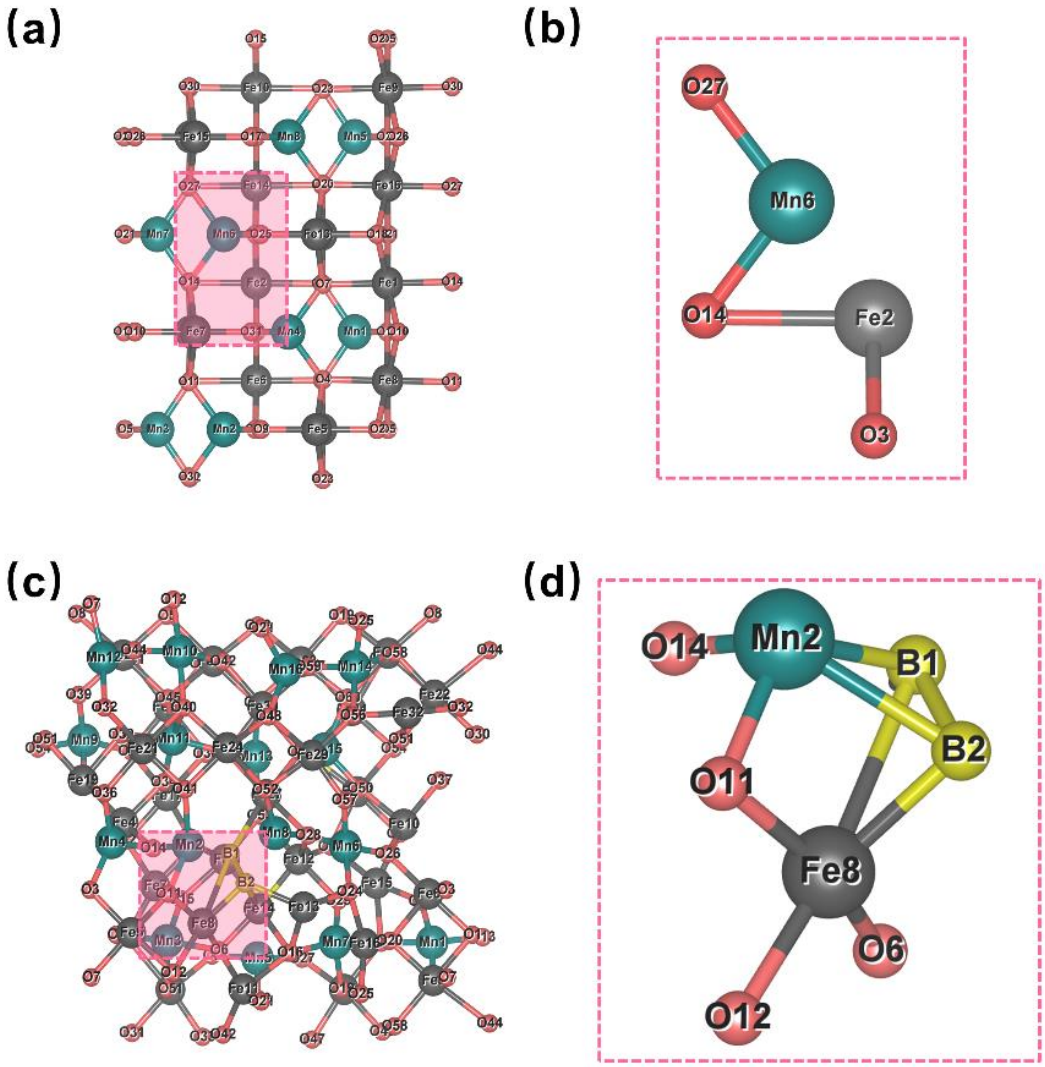

Figure 4.31 (a), (b) $MnFe_2O_4$ and (c), (b) B-$MnFe_2O_4$ models with serial numbers

Table 4.5 Summary of the distance and angles between Fe-O and Mn-O atoms in $MnFe_2O_4$ and B-$MnFe_2O_4$.

Catalysts	**Distance (Å)**			
$MnFe_2O_4$	Fe_2-O_{14}	Fe_2-O_3	Mn_6-O_{27}	Mn_6-O_{14}
	2.12423	2.12420	1.84210	1.82110
B-$MnFe_2O_4$	Fe_8-O_{12}	Fe_8-O_6	Mn_2-O_{14}	Mn_2-O_{11}
	1.95890	1.87468	1.85001	1.88486

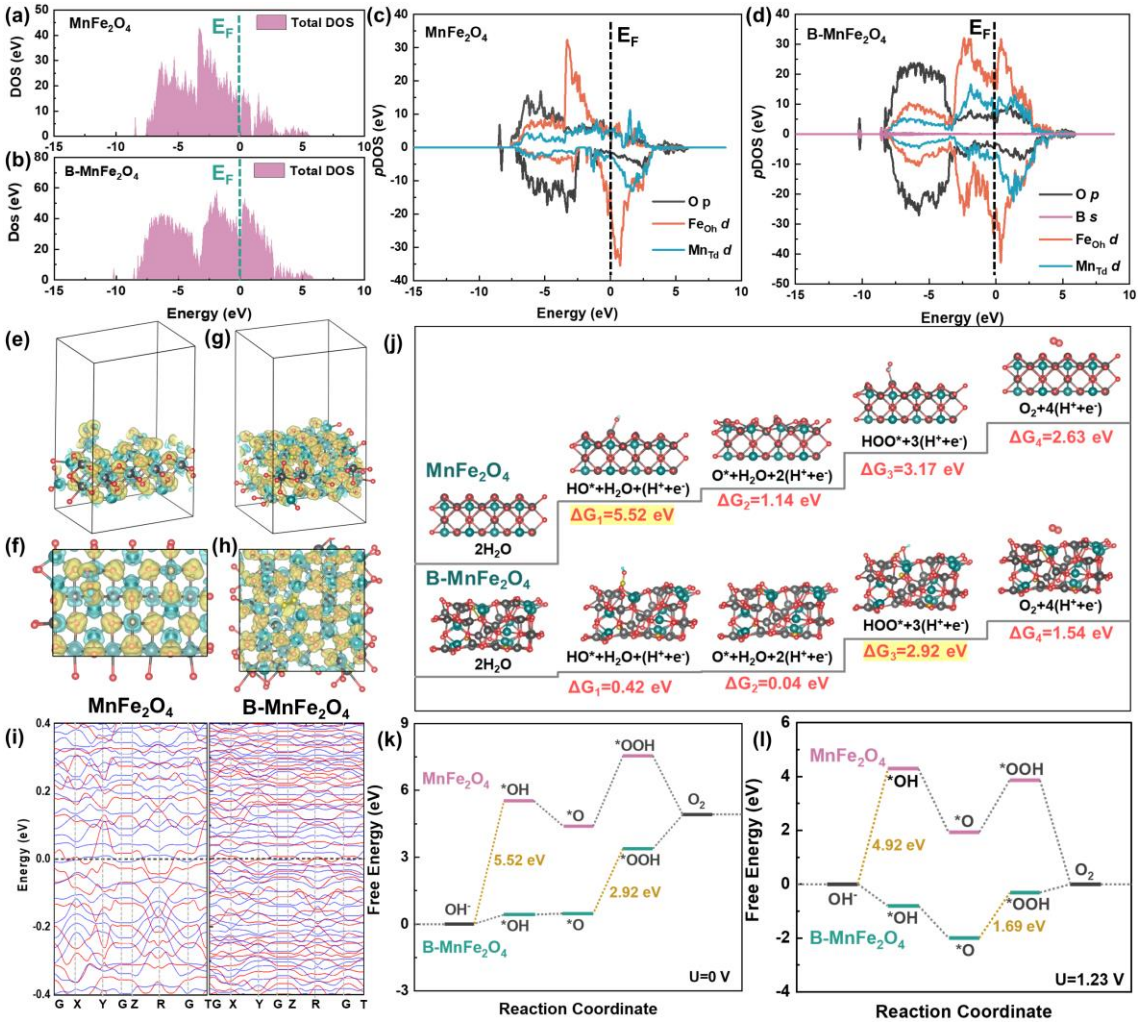

Figure 4.32 Total DOSs of (a) $MnFe_2O_4$ and (b) B-$MnFe_2O_4$; pDOSs of (c) $MnFe_2O_4$ and (d) B-$MnFe_2O_4$; charge distributions in (e-f) $MnFe_2O_4$ and (g-h) B-$MnFe_2O_4$; (i) band structures of $MnFe_2O_4$ and B-$MnFe_2O_4$; (j) elementary steps; Gibbs free energy diagrams of $MnFe_2O_4$ and B-$MnFe_2O_4$ for OER process at (k) U=0 V and (l) U=1.23 V.

The effect of B introduction into $MnFe_2O_4$ structure was further analyzed by DOS and partial density of states (*p*DOS) calculations. It is found that the DOSs of both $MnFe_2O_4$ and B-$MnFe_2O_4$ are cross the Fermi level (E_F) (**Figures 4.32**a-b), and the introduction of B shifts the DOS projected on Fe and Mn orbitals to near the Fermi level (**Figure 4.33**), demonstrating that $MnFe_2O_4$ possesses the metallic properties in the electrical conductivity after the doping of B. From the *p*DOSs of $MnFe_2O_4$ and B-$MnFe_2O_4$ (**Figures 4.32**c and d), the d orbitals of both Td sites of Mn and Oh sites of

Fe overlap with the p orbitals of O, indicating that O has obvious interactions with both Mn_{Td} and Fe_{Oh}. After the O-site is substituted by B atoms, the overlap area of the Fe_{Oh} with O is increased obviously, suggesting that the introduction of B atoms could significantly promote the charge transfer between O and Fe_{Oh}. Moreover, compared with those in $MnFe_2O_4$, the orbitals of Fe *d* and O *p* centers get closer in B-$MnFe_2O_4$, indicating that the B-$MnFe_2O_4$ structure possesses greater Fe-O covalency. Herein, the larger Fe-O covalency could promote the electron transfer between metal cations and oxygen adsorbates (e.g., O_2^{2-}, O^{2-}), thereby accelerating the OER kinetics [45]. **Figures 4.32** e-h display the charge density distributions of $MnFe_2O_4$ and B-$MnFe_2O_4$ with top and side views, where yellow area presents positive electronic clouds accepted from others while cyan indicates the negative electronic clouds donated to others. It is clearly observed that the charge density rearrangement occurs after the introduction of B atoms. In addition, as illustrated in **Figure 4.32**i, comparing with that of $MnFe_2O_4$, the band structure of B-$MnFe_2O_4$ is more concentrated around the Fermi level. Thus, the B-$MnFe_2O_4$ should have a more continuous electronic structure, expanding the range of adsorption energy, which is in agreement well with the results of DOS.

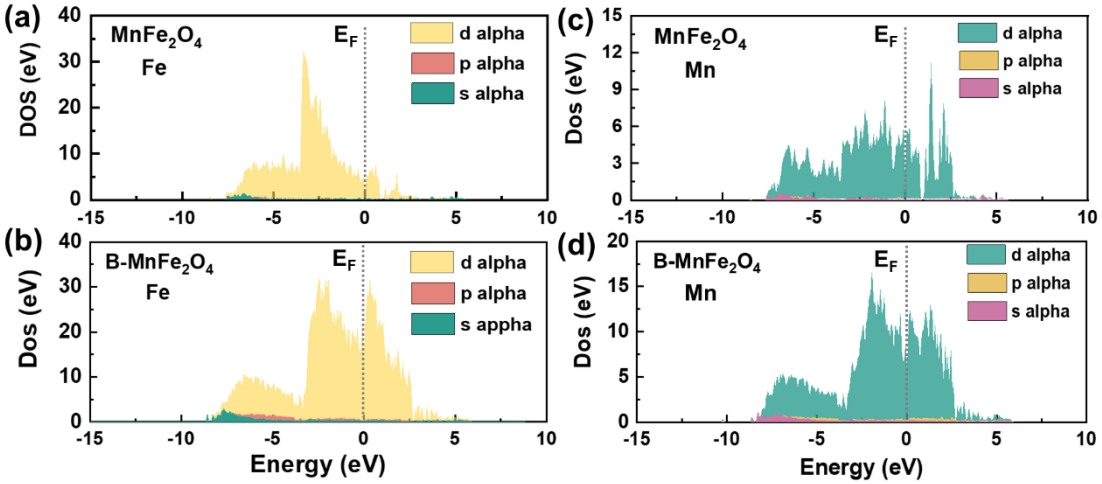

Figure 4.33 (a) Fe density states of $MnFe_2O_4$ and (b) Fe density states of B-$MnFe_2O_4$; (c) Mn density states of $MnFe_2O_4$ and (d) Mn density states of B-$MnFe_2O_4$.

It is already identified that the OER performance of spinel type oxide is closely related to the adsorption energies of intermediates [46]. Herein, the adsorption energies of *OH, *O and *OOH species on $MnFe_2O_4$ and B-$MnFe_2O_4$ were calculated. The optimized configurations of the adsorption of intermediates on the catalytic surface during the OER process and the change of each step are presented in **Figure 4.32**j. As a result, the rate-determine step (RDS) on the pristine $MnFe_2O_4$ should be the first step of the adsorption and discharge of OH^-, and the free energy (ΔG_1) reaches up to 5.52 eV. Surprisingly, for the B-$MnFe_2O_4$, the RDS seems to be the formation of *OOH since its free energy (ΔG_3) is as low as 2.92 eV. When U=1.23 V (**Figure 4.32**l), the reaction limiting barrier on B-$MnFe_2O_4$ (1.69 eV) is much lower than that on B-$MnFe_2O_4$ (4.92 eV). The dramatic decrease of ΔG indicates the enhancement of reaction kinetics, which is in good agreement with the highest intrinsic activity for B-$MnFe_2O_4$ in the OER process as discussed above.

4.3.4 Electrochemical performance for OER in seawater solution

Due to the high OER performance and stability for B-$MnFe_2O_4$@MFOC in the 1 M KOH containing freshwater based electrolyte, whose OER performance in the seawater-based electrolyte was also evaluated. As stated in the introduction section, the most critical challenge for seawater splitting is the competition between OER and chlorine oxidation reaction (ClER) at a low pH situation and chlorine oxidation reaction to generate hypochlorite at a high pH condition, which could significantly lower the efficiency of seawater oxidation. Herein, the catalytic activities of B-$MnFe_2O_4$@MFOC in both alkaline simulated seawater (1 M KOH+0.5 M NaCl) and alkaline natural seawater solution (1 M KOH+ natural seawater, collected from Aomori Bay, Japan (**Figure 4.34**)) were investigated. As shown in **Figure 4.35**a, the B-$MnFe_2O_4$@MFOC electrode requires an overpotential of 334 mV to achieve a current density of 100 mA

cm^{-2}, which is higher than that in the freshwater-based electrolyte, but much lower than those of MFOC (360 mV), B-Fe_3O_4@FOC (414 mV) and B-Mn_3O_4@MOC (449 mV) based electrodes. In the case using the natural seawater, as displayed in **Figure 4.35**b, at room temperature (25℃), the B-$MnFe_2O_4$@MFOC electrode exhibits a slight decay performance with an overpotential of 405 mV at 100 mA cm^{-2} when compared with the cases using freshwater and simulated seawater (**Figure 4.35**c), which may be due to the generations of some insoluble precipitates such as Ca $(OH)_2$ and Mg $(OH)_2$ in alkaline environment, which could deposit on the electrode surface. To boost the OER activity, the electrolyte temperature was increased (**Figure 4.35**b). As a result, the overpotentials are decreased to 380, 350 and 330 mV at 100 mA cm^{-2} by heating the electrolyte to 40, 50 and 60 ℃, respectively. It should be noted that such high temperatures could be easily achieved by a solar heating system on the sea. In addition, the Faradaic efficiency of B-$MnFe_2O_4$@MFOC/NF electrode for the electrolysis of 1 M KOH containing natural seawater-based electrolyte was evaluated by a drainage method. As illustrated in **Figure 4.35**d, the measured O_2 production is matched well with the theoretical one, indicating that the Faradic efficiency is nearly 100%, which confirms the high OER selectivity of B-$MnFe_2O_4$@MFOC electrocatalyst in the alkaline seawater electrolyte.

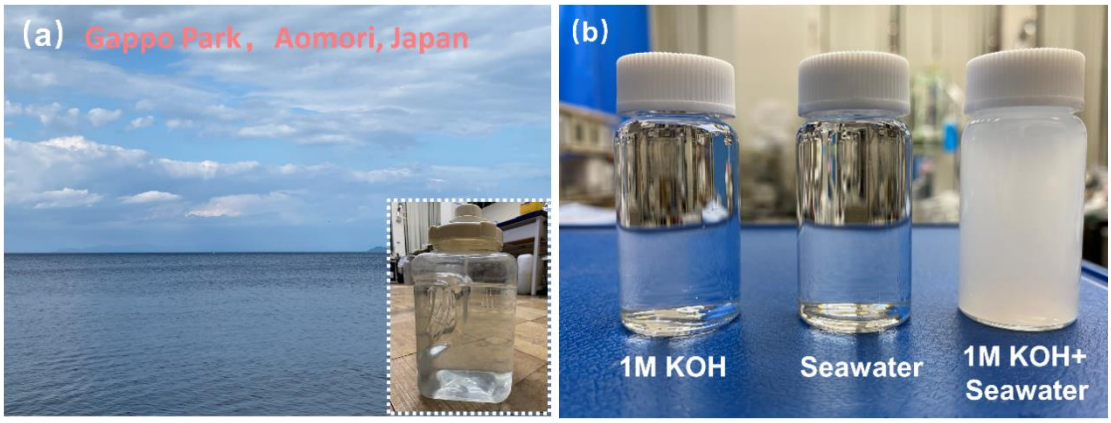

Figure 4.34 Photograph of (a) seawater collected from Aomori Bay near Aomori, Japan; (b) 1 M KOH, seawater and 1 M KOH+ seawater electrolysis

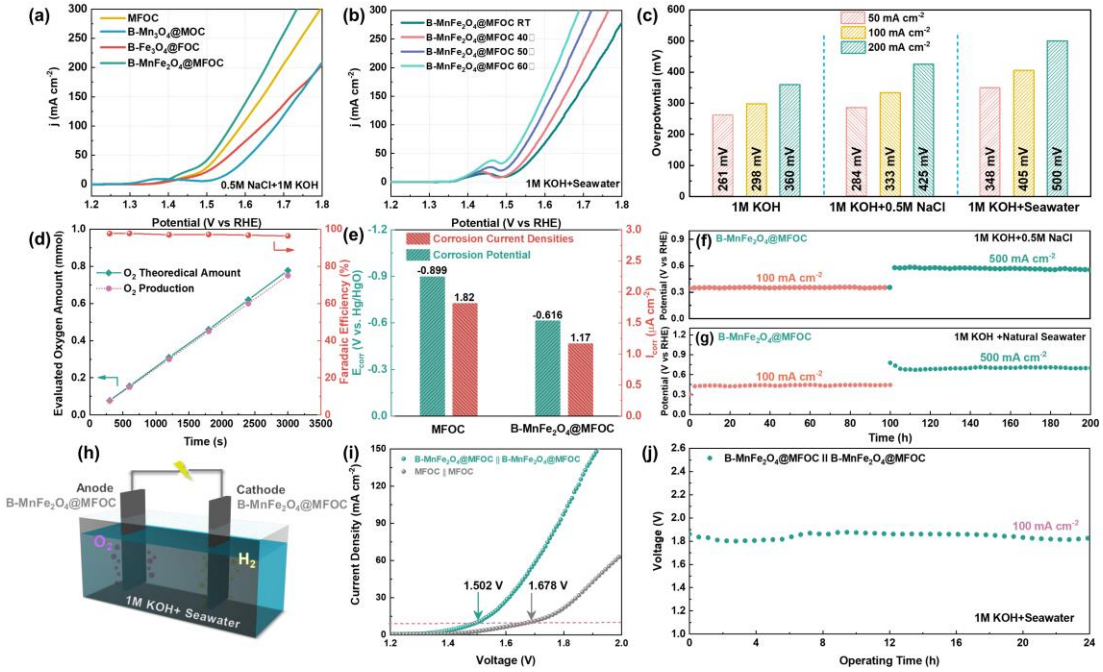

Figure 4.35 OER polarization curves of as-prepared sample in (a) simulated seawater (0.5 M NaCl+1M KOH solution) and (b) 1M KOH+ natural seawater solution under different temperatures; (c) Comparison of the overpotentials for B-$MnFe_2O_4$@MFOC electrode; (d) measured and theoretical gaseous products over B-$MnFe_2O_4$@MFOC electrocatalyst; (e) Corrosion potentials (green) and corrosion current densities (red) of B-$MnFe_2O_4$@MFOC electrode in natural seawater; Chrono potentiometric curves of B-$MnFe_2O_4$@MFOC electrode for 200 h in (f) 1M KOH+0.5M NaCl and (g) 1M KOH+ seawater; (h) Schematic illustration of a seawater-splitting electrolyzer using B-$MnFe_2O_4$@MFOC for both electrodes; (i) Overall seawater splitting performance of MFOC‖MFOC and B-$MnFe_2O_4$@MFOC‖B-$MnFe_2O_4$@MFOC couples in 1M KOH+ natural seawater; (j) Chrono-potentiometric curves at 100 mA cm^{-2} for 24 h.

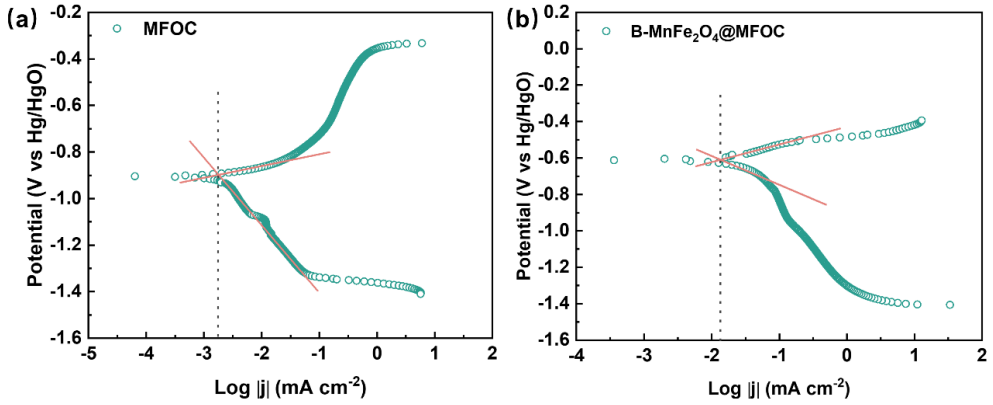

Figure 4.36 Corrosion polarization curves of (a) FMOC and (b) B-$MnFe_2O_4$@FMOC.

Table 4.6 Comparison of OER catalytic activities with reported OER catalysts

Electrolyzer	Electrolyte	Cell voltage	Reference
B-$MnFe_2O_4$@MFOC|| B-$MnFe_2O_4$@MFOC	1M KOH+ Seawater	1.502V@ 10 mA cm^{-2}	This work
P-NiFe@$NiMoO_4$|| P-NiMoO	1M KOH+ Seawater	~1.63V@100 mA cm^{-2}	47
NiFe-PBA-gel-cal|| NiFe-PBA-gel-cal	Simulated Seawater	1.66V @100 mA cm^{-2}	48
Fe (Cr)OOH/Fe_3O_4|| $MoNi_4/MoO_2$	1M KOH+ Seawater	1.57V@100 mA cm^{-2}	49
$MnCo_2O_4$@NiFe-LDH (-) || $MnCo_2O_4$@NiFe-LDH	1M KOH+ Seawater	1.56V @10 mA cm^{-2}	50
NiFe LDH||FeOOH	Simulated Seawater	1.55V@10 mA cm^{-2}	51
MoN-Co_2N|| MoN-Co_2N	1M KOH+ Seawater	1.70V@100 mA cm^{-2}	52
$CoSe_2$-NCF|| $CoSe_2$-NCF	1M KOH+ Seawater	1.671 V@100 mA cm^{-2} (80℃)	53
Er-MoO_2|| Er-MoO_2	1M KOH+ Seawater	1.67 V@100 mA cm^{-2}	54
NiMoN||NiMoN@NiFeN	1M KOH+ Seawater	1.581V@100 mA cm^{-2}	55
Ni_2P-Fe_2P/NF|| Ni_2P-Fe_2P/NF	1M KOH+ Seawater	1.811V@100 mA cm^{-2}	56

Chloride corrosion is another tough issue in the field of seawater electrolysis since it will gradually affect the application life of a catalyst. However, the effect of chloride effect is hard to determine during the electrolysis process. In order to specifically analyze the corrosion resistance of the as-prepared electrocatalysts, the corrosion polarization curves of MFOC and B-$MnFe_2O_4$@MFOC were measured (**Figure 4.36**), and the corresponding data are summarized in **Figure 4.35**e. One can see that the B-

$MnFe_2O_4$@MFOC exhibits a higher corrosion potential (-0.616 V) and a lower corrosion current density (1.17 μA cm^{-2}) than those of MFOC (-0.899 V and 1.82 μA cm^{-2}), indicating that the B-$MnFe_2O_4$@MFOC has higher chloride corrosion resistance ability than the MFOC. Furthermore, the durability of B-$MnFe_2O_4$@MFOC in the simulated seawater and natural seawater was also determined by a two-step chron-potentiometric method sequentially at the current densities of 100 and 500 mA cm^{-2}. As shown in **Figures 4.35**f and g, no obvious voltage elevations are observed at the current densities of 100 and 500 mA cm^{-2} in 100-h continuous test, demonstrating the outstanding durability of B-$MnFe_2O_4$@MFOC under a high current density in both simulated seawater- and natural seawater-based electrolytes. The changes of component and structure of B- $MnFe_2O_4$@MFOC after the OER stability test in seawater-based electrolyte were also characterized by TEM and XPS analyses. As illustrated in **Figures 4.37**a-c, the morphology of nanosheet@ nanowire heterostructure has no obvious change, and the overall hierarchical nanosheet@ nanowire structure also maintains in the micro scale. Furthermore, the fringe lattice spacings of 0.295 and 0.297 nm are indexed clearly, both of which are consistent with the interplanar distances of spinel $MnFe_2O_4$ (220) plane, which confirms the outstanding chlorine corrosion resistance of the B-$MnFe_2O_4$@MFOC catalyst. In addition, EDS-mappings also indicate the existence of boron element in the spent catalyst. While, the XPS spectra of B-$MnFe_2O_4$@MFOC after the OER stability test (**Figure 4.38**) show that the peaks of Fe *2p* and Mn *2p* remain unchanged after the OER test, demonstrating that the crystalline $MnFe_2O_4$ is relatively stable during seawater oxidation. Also, the specific peak of B is still maintained, indicating that more boron atoms have been doped into $MnFe_2O_4$ crystalline to form a metallic boride than the existence on the surface.

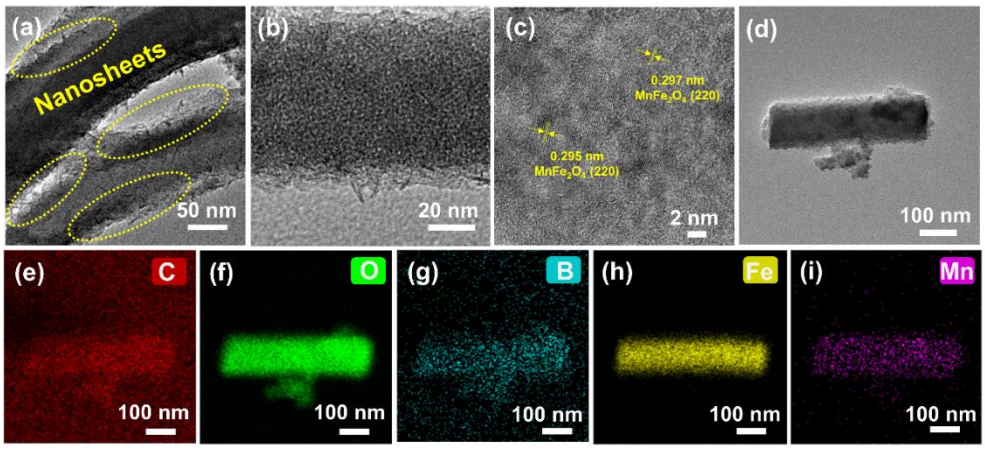

Figure 4.37 (a) TEM and (b)HR-TEM images; (c)-(h) TEM-EDS mapping images of C, O, B, Fe and Mn of B-$MnFe_2O_4$@FMOC after the stability test.

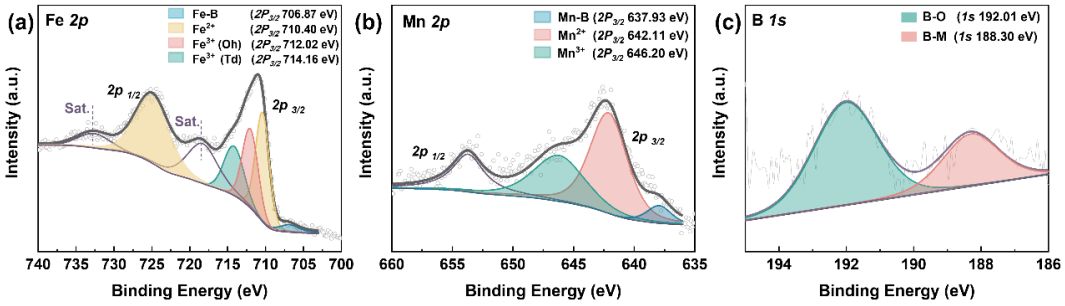

Figure 4.38 High-resolution XPS spectra of (a) Fe *2p*; (b) Mn *2p* and (c) B *1s* in B-$MnFe_2O_4$@MFOC after the stability test

HER performances of the B-$MnFe_2O_4$@MFOC composite and MFOC were also tested in natural seawater (**Figure 4.39**). As a result, the η_{10} values of 64 and 210 mV are required with Tafel slopes of 77 and 150 mV dec^{-1} for B-$MnFe_2O_4$@MFOC and MFOC, respectively. Due to the outstanding OER and HER activities of B-$MnFe_2O_4$@MFOC composite, the overall alkaline seawater splitting performance was investigated by integrating it as the bifunctional electrocatalyst on both anode and cathode into a two-electrode electrolyzer, as illustrated in **Figure 4.35**h. Consequently, the B-$MnFe_2O_4$@MFOC||B-$MnFe_2O_4$@MFOC and MFOC||MFOC cell voltages required to achieve a current density of 10 mA cm^{-2} are 1.502 and 1.678V in the natural

seawater-based electrolyte, respectively (**Figure 4.35**i). It should be noticed that the B-$MnFe_2O_4$@MFOC||B-$MnFe_2O_4$@MFOC is superior to the most of the recent reported catalysts, which can be seen in **Table 4.6**. More importantly, the electrolyzer retains the outstanding durability with no obvious degradation over 24-h chronopotentiometry operation at a current density of 100 mA cm^{-2} (**Figure 4.35**j). In addition, the possible generation of Cl^- oxidation products (e.g., ClO^-) during seawater splitting was measured by the iodometric titrations method shown in **Figure 4.40,** it can be seen that no obvious pink color in the solution, clearly indicated the absence of any hypochlorite trace, which confirmed the high OER detectivity in the tested systems.

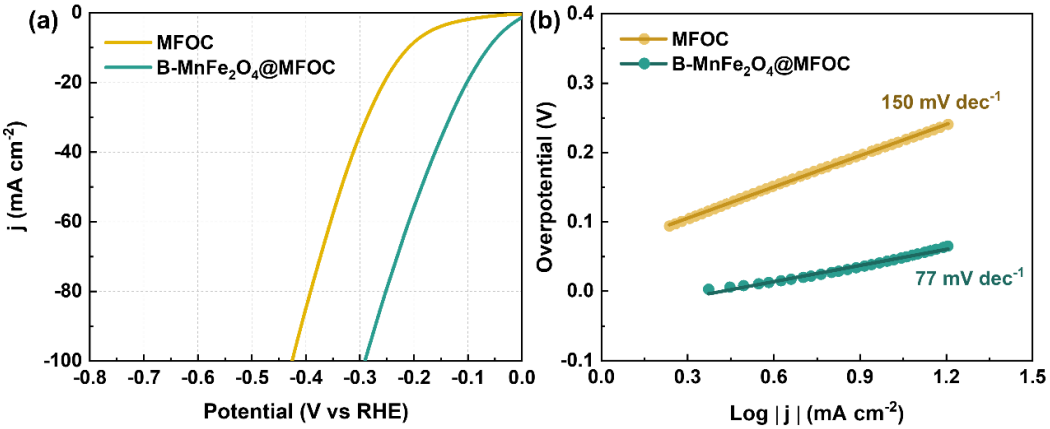

Figure 4.39 Polarization curves of MFOC and B-$MnFe_2O_4$@MFOC; (b) Tafel plots of MFOC and B-$MnFe_2O_4$@MFOC in 1M KOH+ natural seawater solution

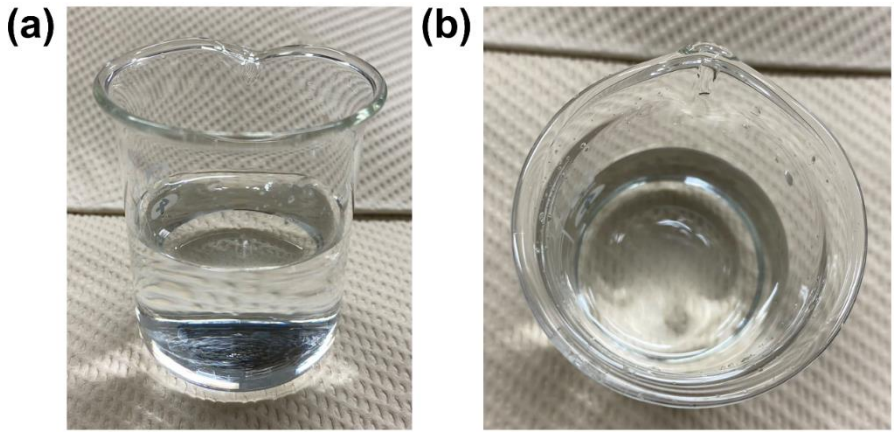

Figure 4.40 Side (a) and top (b) views of the digital photographs of the OER solutions for the iodometric titration, showing the absence of ClO^- production in this case.

4.4 Conclusions

In summary, we have successfully synthesized a nanocrystalline boron doped $MnFe_2O_4$ spinel at room temperature realized using a reduction-crystallization method with amorphous MFOC. Its hierarchical nanosheet@ nanowire structure and hydrophilic feature make the B-$MnFe_2O_4$@MFOC possess the favorable synergistic effects for seawater splitting. More important, boron-doped $MnFe_2O_4$ could induce the formation of oxygen vacancies and significantly promote the charge transfer between O and Fe_{Oh}. As a result, the optimum B-$MnFe_2O_4$@MFOC exhibited a superior OER activity with an overpotential as low as 298 mV cm^{-2} at 100 mA cm^{-2} and a long-stability over 7 days in freshwater-based electrolyte. Meanwhile, it also showed an excellent OER performance and high corrosion-resistance in the alkaline natural seawater. This work provides a facile method to prepare electrocatalysts suitable for different electrolytes with high stability in the seawater splitting industry.

References

[1] L. Li, G. Zhang, B. Wang, S. Yang, Constructing the Fe/Cr double (oxy)hydroxides on Fe_3O_4 for boosting the electrochemical oxygen evolution in alkaline seawater and domestic sewage, Appl. Catal. B Environ. 302 (2022) 120847.

[2] H. Zhang, D. Guan, Z. Hu, Y. C. Huang, X. Wu, J. Dai, C. L. Dong, X. Xu, H. J. Lin, C. T. Chen, W. Zhou, Z. Shao, Exceptional lattice-oxygen participation on artificially controllable electrochemistry-induced crystalline-amorphous phase to boost oxygen-evolving performance, Appl. Catal. B Environ. 297 (2021) 120484.

[3] Z. Feng, E. Wang, S. Huang, J. Liu, A bifunctional nanoporous Ni-Co-Se electrocatalyst with a superaerophobic surface for water and hydrazine oxidation, Nanoscale, 12(2020) 4426-4434.

[4] K. Deng, Q. Mao, W. Wang, P. Wang, Z. Wang, Y. Xu, X. Li, H. Wang, L. Wang,

Defect-rich low-crystalline Rh metallene for efficient chlorine-free H_2 production by hydrazine-assisted seawater splitting, Appl. Catal. B Environ. 310 (2022) 121338.

[5] Z. Feng, T. Shi, W. Liu, W. Zhang, H. Zhang, Highly active bifunctional electrocatalyst: Nanoporous $(Ni, Co)_{0.85}Se$ anchored on rGO for water and hydrazine oxidation, Int. J. Energy Res. 46 (2022) 15938-15947.

[6] W. Liu, T. Shi, Z. Feng, Bifunctional zeolitic imidazolate framework-67 coupling with CoNiSe electrocatalyst for efficient hydrazine-assisted water splitting, J. Colloid Interface Sci. 630 (2023) 888-899.

[7] J. Li, G. Zheng, One-dimensional earth-abundant nanomaterials for water-splitting electrocatalysts, Adv. Sci. 4 (2017) 1600380.

[8] X. Xiao, L. Yang, W. Sun, Y. Chen, H. Yu, K. Li, B. Jia, L. Zhang, T. Ma, Electrocatalytic water splitting: from harsh and mild conditions to natural seawater, Small 18 (2022) 2105830.

[9] J. Liu, X. Liu, H. Shi, J. Luo, L. Wang, J. Liang, S. Li, L. M. Yang, T. Wang, Y. Huang, Q. Li, Breaking the scaling relations of oxygen evolution reaction on amorphous NiFeP nanostructures with enhanced activity for overall seawater splitting, Appl. Catal. B Environ. 302 (2022) 120862.

[10] C. Wang, H. Shang, L. Jin, H. Xu, Y. Du, Advances in hydrogen production from electrocatalytic seawater splitting, Nanoscale 13 (2021) 7897-7912.

[11] B. Cui, Z. Hu, C. Liu, S. Liu, F. Chen, S. Hu, J. Zhang, W. Zhou, Y. Deng, Z. Qin, Z. Wu, Y. Chen, L. Cui, W. Hu, Heterogeneous lamellar-edged Fe-Ni $(OH)_2/Ni_3S_2$ nanoarray for efficient and stable seawater oxidation, Nano Res. 14 (2021) 1149-1155.

[12] K. S. Exner, J. Anton, T. Jacob, H. Over, Full kinetics from first principles of the chlorine evolution reaction over a RuO_2 (110) model electrode, Angew. Chem. Int. Ed. 55 (2016) 7501-7504.

[13] J. Liu, S. Duan, H. Shi, T. Wang, X. Yang, Y. Huang, G. Wu, Q. Li, Rationally designing efficient electrocatalysts for direct seawater splitting: challenges, achievements, and Promises, Angew. Chem. Int. Ed. (2022) 202210753.

[14] H. Y. Wang, C. C. Weng, J. T. Ren, Z. Y. Yuan, An overview and recent advances in electrocatalysts for direct seawater splitting, Front. Chem. Sci. Eng. 15 (2021) 1408-1426.

[15] Q. Zhao, Z. Yan, C. Chen, J. Chen, Spinels: Controlled Preparation, Oxygen reduction/evolution reaction application, and beyond, Chem. Rev. 117 (2017) 10121-10211.

[16] J. Sun, N. Guo, Z. Shao, K. Huang, Y. Li, F. He, Q. Wang, A facile strategy to construct amorphous spinel-based electrocatalysts with massive oxygen vacancies using ionic liquid dopant, Adv. Energy Mater. 8 (2018) 1800980.

[17] L. Xu, Q. Jiang, Z. Xiao, X. Li, J. Huo, S. Wang, L. Dai, Plasma-engraved Co_3O_4 nanosheets with oxygen vacancies and high surface area for the oxygen evolution reaction, Angew. Chem. Int. Ed. 128 (2016) 5363-5367.

[18] D. Wang, Y. Chen, L. Fan, T. Xiao, T. Meng, Z. Xing, X. Yang, Bulk and surface dual modification of nickel-cobalt spinel with ruthenium toward highly efficient overall water splitting, Appl. Catal. B Environ. 305 (2022) 121081.

[19] S. Chen, D. Huang, D. Liu, H. Sun, W. Yan, J. Wang, M. Dong, X. Tong, W. Fan, Hollow and porous $NiCo_2O_4$ nanospheres for enhanced methanol oxidation reaction and oxygen reduction reaction by oxygen vacancies engineering, Appl. Catal. B Environ. 291 (2021) 120065.

[20] C. Mu, J. Mao, J. Guo, Q. Guo, Z. Li, W. Qin, Z. Hu, K. Davey, T. Ling, S. Qiao, Rational design of spinel cobalt vanadate oxide Co_2VO_4 for superior electrocatalysis, Adv. Mater. 32 (2020) 1907168.

[21] S. Deng, Z. Tie, F. Yue, H. Cao, M. Yao, Z. Niu, Rational design of $ZnMn_2O_4$ quantum dots in a carbon framework for durable aqueous Zinc-ion batteries, Angew. Chem. Int. Ed. 134 (2022) e202115877.

[22] C. Wei, Z. Feng, G. G. Scherer, J. Barber, Y. Shao-Horn, Z. J. Xu, Cations in octahedral sites: a descriptor for oxygen electrocatalysis on transition-metal spinels, Adv. Mater. 29 (2017) 1606800.

[23] J. Zhang, X. Shang, H. Ren, J. Chi, H. Fu, B. Dong, C. Liu, Y. Chai, Modulation of inverse spinel Fe_3O_4 by phosphorus doping as an industrially promising electrocatalyst for hydrogen evolution, Adv. Mater. 31 (2019) 1905107.

[24] W. Xie, J. Huang, L. Huang, S. Geng, S. Song, P. Tsiakaras, Y. Wang, Novel fluorine-doped cobalt molybdate nanosheets with enriched oxygen-vacancies for improved oxygen evolution reaction activity, Appl. Catal. B Environ. 303 (2022) 120871.

[25] D. K. Bediako, Y. Surendranath, D. G. Nocera, Mechanistic studies of the oxygen evolution reaction mediated by a nickel-borate thin film electrocatalyst, J. Am. Chem. Soc. 135 (2013) 3662-3674.

[26] M. Yu, C. Weidenthaler, Y. Wang, E. Budiyanto, E. Onur Sahin, M. Chen, S. DeBeer, O. Rüdiger, H. Tüysüz, Surface boron modulation on cobalt oxide nanocrystals for electrochemical oxygen evolution reaction, Angew. Chem. Int. Ed. 61 (2022) e202211543.

[27] N. Wen, Y. Xia, H. Wang, D. Zhang, H. Wang, X. Wang, X. Jiao, D. Chen, Large-scale synthesis of spinel $Ni_xMn_{3-x}O_4$ solid solution immobilized with iridium single atoms for efficient alkaline seawater electrolysis, Adv. Sci. 9 (2022) 2200529.

[28] L. Bigiani, D. Barreca, A. Gasparotto, T. Andreu, J. Verbeeck, C. Sada, E. Modin, O.I. Lebedev, J.R. Morante, C. Maccato, Selective anodes for seawater splitting via

functionalization of manganese oxides by a plasma-assisted process, Appl. Catal. B Environ. 284 (2021) 119684.

[29] L. Wu, L. Yu, Q. Zhu, B. McElhenny, F. Zhang, C. Wu, X. Xing, J. Bao, S. Chen, Z. Ren, Boron-modified cobalt iron layered double hydroxides for high efficiency seawater oxidation, Nano Energy 83 (2021) 105838.

[30] F. Cheng, J. Shen, B. Peng, Y. Pan, Z. Tao, J. Chen, Rapid room-temperature synthesis of nanocrystalline spinels as oxygen reduction and evolution electrocatalysts, Nature Chem. 3 (2011) 79-84.

[31] M. Rinawati, Y. X. Wang, K. Y. Chen, M. H. Yeh, Designing a spontaneously deriving NiFe-LDH from bimetallic MOF-74 as an electrocatalyst for oxygen evolution reaction in alkaline solution, Chem. Eng. J 423 (2021) 130204.

[32] A. Sivakumar, S. Sahaya Jude Dhas, P. Sivaprakash, A. I. Almansour, R. Suresh Kumar, N. Arumugam, K. Perumal, S. Arumugam, S. A. Martin Britto Dhas, Raman spectroscopic and electrochemical measurements of dynamic shocked $MnFe_2O_4$ nano-crystalline materials, J. Inorg. Organomet. Polym. 32 (2022) 344-352.

[33] W. Wang, Z. Ding, X. Zhao, S. Wu, F. Li, M. Yue, J.P. Liu, Microstructure and magnetic properties of MFe_2O_4 (M = Co, Ni, and Mn) ferrite nanocrystals prepared using colloid mill and hydrothermal method, J. Appl. Phys. 117 (2015) 17A328.

[34] P. Bandyopadhyay, G. Saeed, N. H. Kim, J. H. Lee, Zinc-nickel-cobalt oxide@$NiMoO_4$ core-shell nanowire/nanosheet arrays for solid state asymmetric supercapacitors, Chem. Eng. J. 384 (2020) 123357.

[35] M. S. Matseke, H. Zheng, M. K. Mathe, E. Carleschi, B. Doyle, Influence of Co doping on physiochemical properties of $MnFe_2O_4$/C nano compounds toward oxygen reduction reaction, J. Alloys Compd. 888 (2021) 161581.

[36] J. Masa, P. Weide, D. Peeters, I. Sinev, W. Xia, Z. Sun, C. Somsen, M. Muhler, W.

Schuhmann, Amorphous cobalt boride (Co_2B) as a highly efficient nonprecious catalyst for electrochemical water splitting: oxygen and hydrogen evolution, Adv. Energy Mater. 6 (2016) 1502313.

[37] X. Zhao, X. Li, Y. Yan, Y. Xing, S. Lu, L. Zhao, S. Zhou, Z. Peng, J. Zeng, Electrical and structural engineering of cobalt selenide nanosheets by Mn modulation for efficient oxygen evolution, Appl. Catal. B 236 (2018): 569-575.

[38] L. Han, B. Li, S. Tao, J. An, B. Fu, Y. Han, W. Li, X. Li, S. Peng, T. Yin, Graphene oxide-induced formation of a boron-doped iron oxide shell on the surface of NZVI for enhancing nitrate removal, Chemosphere 252 (2020) 126496.

[39] Q. Li, L. Lina, X. Ai, H. Chen, J. Zou, G. D. Li, X. Zou, Multiple crystal phases of intermetallic tungsten borides and phasedependent electrocatalytic property for hydrogen evolution, Chem. Commun. 56 (2020) 13983-13986.

[40] Y. Wang, D. Jia, W. Zhang, G. Jia, H. Xie, W. Ye, G. Zhu, P. Gao, A boronization-induced amorphous-crystalline interface on a Prussian blue analogue for efficient and stable seawater splitting, Chem. Commun. 58 (2022) 6132-6135.

[41] M. S. Matseke, H. Zheng, Y. Wang, The ultrasonication boosts the surface properties of $CoFe_2O_4$/C nanoparticles towards ORR in alkaline media, Appl. Surf. Sci. 516 (2020) 146105.

[42] M. Fang, D. Han, W. Xu, Y. Shen, Y. Lu, P. Cao, S. Han, W. Xu, D. Zhu, W. Liu, J.C. Ho, Surface-guided formation of amorphous mixed-metal oxyhydroxides on ultrathin MnO_2 nanosheet arrays for efficient electrocatalytic oxygen evolution, Adv. Energy Mater. 10 (2020) 2001059.

[43] Y. Li, J. Chen, P. Cai, Z. Wen, An electrochemically neutralized energy-assisted low-cost acid-alkaline electrolyzer for energy-saving electrolysis hydrogen generation, J. Mater. Chem. A 6 (2018) 4948-4954.

[44] S. Sun, T. Zhai, C. Liang, S.V. Savilov, H. Xia, Boosted crystalline/amorphous $Fe_2O_{3-\delta}$ core/shell heterostructure for flexible solid-state pseudocapacitors in large scale, Nano Energy 45 (2018) 390-397.

[45] Y. Zhou, S. Sun, J. Song, S. Xi, B. Chen, Y. Du, A. C. Fisher, F. Cheng, X. Wang, H. Zhang, Z. J. Xu, Enlarged Co-O covalency in octahedral sites leading to highly efficient spinel oxides for oxygen evolution reaction, Adv. Mater. 30 (2018) 1802912.

[46] J. S. Kim, B. Kim, H. Kim, K. Kang, Recent progress on multimetal oxide catalysts for the oxygen evolution reaction, Adv. Energy Mater. 8 (2018) 1702774.

[47] C. Yang, N. Gao, X. Wang, J. Lu, L. Cao, Y. Li, H. P. Liang, Stable and efficient seawater splitting on a porous phosphate-intercalated NiFe (oxy) hydroxide@$NiMoO_4$ core-shell micropillar electrode, Energy Mater. 1 (2021) 100015.

[48] H. Zhang, S. Geng, M. Ouyang, H. Yadegari, F. Xie, D. J. Riley, A self-reconstructed bifunctional electrocatalyst of pseudo-amorphous nickel carbide@ iron oxide network for seawater splitting, Adv. Sci. (2022) 2200146.

[49] L. Li, G. Zhang, B. Wang, S. Yang, Constructing the Fe/Cr double (oxy) hydroxides on Fe_3O_4 for boosting the electrochemical oxygen evolution in alkaline seawater and domestic sewage, Appl. Catal. B 302 (2022) 120847.

[50] N. Kitiphatpiboon, M. Chen, C. Feng, Y. Zhou, C. Liu, Z. Feng, Q. Zhao, A. Abudula, G. Guan, Modification of spinel $MnCo_2O_4$ nanowire with NiFe-layered double hydroxide nanoflakes for stable seawater oxidation, J. Colloid Interface Sc. 632 (2023) 54-64.

[51] K. Jiang, W. Liu, W. Lai, M. Wang, Q. Li, Z. Wang, J. Yuan, Y. Deng, J. Bao, H. Ji, NiFe layered double hydroxide/FeOOH heterostructure nanosheets as an efficient and durable bifunctional electrocatalyst for overall seawater splitting, Inorg. Chem. 60 (2021) 17371-17378.

[52] X. Wang, X. Han, R. Du, C. Xing, X. Qi, Z. Liang, P. Guardia, J. Arbiol, A. Cabot, J. Li, Cobalt molybdenum nitride-based nanosheets for seawater splitting, ACS Appl. Mater. Interfaces 14 (2022) 41924-41933.

[53] H. Chen, S. Zhang, Q. Liu, P. Yu, J. Luo, G. Hu, X. Liu, $CoSe_2$ nanocrystals embedded into carbon framework as efficient bifunctional catalyst for alkaline seawater splitting, Inorg. Chem. Commun. 146 (2022) 110170.

[54] T. Yang, H. Lv, Q. Quan, X. Li, H. Lu, X. Cui, G. Liu, L. Jiang, Electronic structure modulation of MoO_2 via Er-doping for efficient overall water/seawater splitting and Mg/seawater batteries, Appl. Sur. Sci. (2023) 156360.

[55] L. Yu, Q. Zhu, S. Song, B. McElhenny, D. Wang, C. Wu, Z. Qin, J. Bao, Y. Yu, S. Chen, Z. Ren, Non-noble metal-nitride based electrocatalysts for high-performance alkaline seawater electrolysis, Nat. Commun. 10 (2019) 1-10.

[56] L. Wu, L. Yu, F. Zhang, B. McElhenny, D. Luo, A. Karim, S. Chen, Z. Ren, Heterogeneous bimetallic phosphide Ni_2P-Fe_2P as an efficient bifunctional catalyst for water/seawater splitting, Adv. Funct. Mater. 31 (2021) 2006484.

CHAPTER 5 Conclusions and Prospects

5.1 Conclusions

Water splitting is deemed as an effective approach for production of hydrogen due to its unlimited reactant availability, outstanding manufacturing safety and high product purity. To realize the practical applications, it is crucial to design the cost-effective electrocatalysts with high-activity and ultra-stability. For the seawater splitting, the major challenge is the energy-efficiency loss during competitive reaction between OER and ClER, as well as the high-cost and time-consuming electrocatalysts with complicated process. Thus, three different strategies have been proposed in this dissertation study, including epitaxial growing of another phase to expose more active sites, developing interfaces between amorphous and crystalline species to create more defects and introducing the heteroatoms B into spinel structure to adjust the electron structure configuration, to improve the intrinsic activity and stability. The main results are summarized as follows:

(1) A facile method was developed for the preparation of nanowire-like Ni_3S_2@NiS-250/NF electrocatalysts with a heterojunction structure on the NF substrate. It is found that the calcination temperature, in the solid-state phase transformation strategy, could affect the degree of epitaxial growing of NiS layer on the surface of the Ni_3S_2 nanowire, creating Ni_3S_2/NiS interface with abundant active unsaturated S sites to increase the conductivity and to expose more active sites. Moreover, it is found that the strong charge transfer at the Ni_3S_2/NiS heterojunction interface could modulate the d band center so that the Ni-H bond is reasonably optimized, thereby boosting the HER performance. The obtained Ni_3S_2@NiS-250/NF electrode exhibited outstanding HER performance, achieving a low overpotentials of 129 mV to deliver the standard current

density of 10 mA cm^{-2} with a small Tafel slope (75.5 mV dec^{-1}) in 1 M KOH media, as well as long-term stability. This study is expected to provide a method to develop lower-cost electrocatalysts with higher HER performance via morphology and phase transition.

(2) 2D ultrathin Zn-VO_x-Co nanosheets were successfully coated on CFP substrate by a facile electrodeposition method for the first time. The obtained Zn-VO_x-Co electrocatalysts had unique heterostructure combined with the amorphous Co metal phase and crystalline Zn-Co alloy phase. DFT calculations revealed that the dual-doping of Zn and VO_x could optimize the d-band center, significantly balance the adsorption and desorption of hydrogen species. As a result, the optimum catalyst demonstrated a superior HER performance with an overpotential as low as 46 mV to deliver the standard current density of 10 mA cm^{-2} with a small Tafel slope of 75 mV dec^{-1} and long-term electrochemical stability over 36 h in 1 M KOH solution. While, it also exhibited excellent HER performance in the neutral electrolyte solution. This study provides a facile approach to synthesize electrocatalysts working in a wide pH range with high catalytic activity and stability, which could be applied in the water electrolysis industry.

(3) A novel electrocatalyst for seawater electrolysis composed of nanocrystalline boron doped $MnFe_2O_4$ spinel with amorphous MFOC was successfully synthesized at room temperature using a reduction-crystallization method. Its hierarchical nanosheet@ nanowire structure and hydrophilic feature make the B-$MnFe_2O_4$@MFOC possess the favorable synergistic effects for seawater splitting. More importantly, boron-doped $MnFe_2O_4$ could induce the formation of oxygen vacancies and significantly promote the charge transfer between O and Fe_{Oh}. As a result, the optimum B-$MnFe_2O_4$@MFOC exhibited a superior OER activity with an overpotential as low as

298 mV cm^{-2} at 100 mA cm^{-2} and a long-stability over 7 days in freshwater-based electrolyte. Meanwhile, it also showed an excellent OER performance and high corrosion-resistance in the alkaline natural seawater. This work provides a facile method to prepare electrocatalysts suitable for different electrolytes with high stability in the seawater splitting industry.

5.2 Prospects

Although great efforts have been devoted for the achievement of the electrocatalysts for water and seawater splitting application, the efficiency of most reported catalysts remains insufficient. To improve the performance and stability of electrocatalysts for use in natural seawater, several strategies should be further considered in the future:

(i) Compared with powder-type catalysts, self-supported 3D hierarchical nanoarchitecture electrocatalysts should be further explored for seawater splitting. In particular, when the insoluble solids in the natural seawater attach on the catalyst surface, the degradation resulting from reduced active sites may occur. How to improve the stability of electrodes by avoiding the attachments of depositions of insoluble solids Ca $(OH)_2$ and Mg $(OH)_2$ should be considered. For example, development of electrocatalysts which can work in neutral or low pH electrolytes without the generation of chloride could be a good way.

(ii) Morphologies with a high surface area nanostructure and porous structure favor active site exposure and electrolyte infiltration. In particular, the heterostructure could afford a protective layer on the surface, which could block Cl^- ions near the catalysts, thus improving the stability. Moreover, creating a hydrophilic surface among gas-liquid-solid interfaces could increase the mass transport and gas release ability.

(iii) Doping heteroatoms is also an effective way to tune the conductivity, covalency, and intermediate adsorption energy. In particular, introducing vacancies into the lattices

of the electrocatalyst could expose more active sites and regulate the electronic structure. (iv) The generation of multicomponent heterostructures of electrocatalysts could boost catalytic activity by enhancing the interfacial interactions with the synergetic effect. (v) Finally, the formation of an anion-repelling layer is another effective strategy to repel Cl^- ions to avoid seawater corrosion.

Personal details

Name: CHEN MENG

Nationality: CHINA

Date of birth: 1 October,1995

E-mail: h20ds252@hirosaki-u.ac.jp

Educations

Oct. 2020 - Sep. 2023	D.Eng. (Safety Science and Technology), Hirosaki University, Japan
Sep. 2017 - Jun. 2020	M.Sc. (Chemical Engineering), Guangdong University of Technology, China
Sep. 2013 - Jun. 2017	B.Sc. (Chemical Engineering and Technology), Nanjing University of Science and Technology, China

Scholarship and Awards

1) Chinese Government (China Scholarship Council: CSC) Scholarship, Doctoral course, Hirosaki University, Japan (2020-2023).
2) Outstanding Graduates in Hirosaki University (2023)

List of Publications and Presentations

Publications

1. **Meng Chen**, Nutthaphak Kitiphatpiboon, Changrui Feng, Qiang Zhao, Abuliti Abudula, Yufei Ma, Kai Yan, Guoqing Guan, "Tuning Octahedron Sites in $MnFe_2O_4$ Spinel by Boron Doping for Highly Efficient Seawater Splitting". *Applied Catalysis B: Environmental*, **2023**, 122577.

2. **Meng Chen**, Nutthaphak Kitiphatpiboon, Changrui Feng, Abuliti Abudula, Yufei Ma, Guoqing Guan, "Recent Progress in Transition-Metal-Oxide-based Electrocatalysts for the Oxygen Evolution Reaction in Natural Seawater Splitting: A Critical Review". *eScience*, **2023**, 100111.

3. **Meng Chen**, Qing Su, Nutthaphak Kitiphatpiboon, Juan Zhang, Changrui Feng, Shasha Li, Qiang Zhao, Abuliti Abudula, Yufei Ma, Guoqing Guan, "Heterojunction Engineering of Ni_3S_2/NiS Nanowire for Electrochemical Hydrogen Evolution". *Fuel*, **2023**, *331*, 125794.

4. **Meng Chen**, Jianbin Liu, Nutthaphak Kitiphatpiboon, Xiumin Li, Junli Wang, Xiaogang Hao, Abuliti Abudula, Yufei Ma, Guoqing Guan, "Zn-VO_x-Co Nanosheets with Amorphous/crystalline Heterostructure for Highly Efficient Hydrogen Evolution Reaction". *Chemical Engineering Journal*, **2022**, *432*, 134329.

5. Xiumin Li, Qianyu Hu, **Meng Chen**, Xiaogang Hao, Yufei Ma, Jie Liu, Keyong Tang, Abuliti Abudula, Hongyan Wang, Guoqing Guan, "Charge Induced Crystal Distortion and Morphology Remodeling: Formation of Mn-CoP Nanowire @ Mn-CoOOH Nanosheet Electrocatalyst with Rich Edge Dislocation Defects". *Applied Catalysis B: Environmental*, **2021**, *292*, 120172.

6. Nutthaphak Kitiphatpiboon, **Meng Chen**, Changrui Feng, Yifan Zhou, Changlin Liu, Zhongbao Feng, Qiang Zhao, Abuliti Abudula, Guoqing Guan, "Modification of Spinel $MnCo_2O_4$ Nanowire with NiFe-Layered Double Hydroxide Nanoflakes for Stable Seawater Oxidation". *Journal of Colloid and Interface Science*, **2023**, *632*, 54.

7. Nutthaphak Kitiphatpiboon, **Meng Chen**, Xiumin Li, Changlin Liu, Shasha Li, Junli Wang, Shang Peng, Abuliti Abudula, Guoqing Guan, "Heterointerface Engineering of Ni_3S_2@NiCo-LDH Core-shell Structure for Efficient Oxygen Evolution Reaction under Intermittent Conditions". *Electrochimica Acta*, **2022**, *435*, 141438.

8. Nutthaphak Kitiphatpiboon, Suchada Sirisomboonchai, **Meng Chen**, Shasha Li, Jiwei Wang, Xixogang Hao, Abuliti Abudula, Xiumin Li, Guoqing Guan, "Facile Fabrication of O Vacancy Rich $CuVO_x$ Nanobelt@NiO Nanosheet Array for Hydrogen Evolution Reaction". *Electrochimica Acta*, **2022**, *405*, 139623.

9. Yanyan Yang, Zhongliang Yu, Xiaowei An, Xiaohui Duan, **Meng Chen**, Juan Zhang, Xiaogang Hao, Abuliti Abudula, Guoqing Guan, "$Ti_3C_2T_x$ Nanosheets with Uniformly Anchored Ru Nanoparticles for Efficient Acidic and Basic Hydrogen Evolution Reaction". *International Journal of Hydrogen Energy*, **2023**, *48*, 9163.

10. Suchada Sirisomboonchai, Nutthaphak Kitiphatpiboon, **Meng Chen**, Shasha Li, Suwadee Kongparakul, Chanatip Samart, Lei Zhang, Abuliti Abudula, Xiumin Li, Guoqing Guan, "Multi-hierarchical Porous Mn Doped CoP Catalyst on Nickel Phosphide Foam for Hydrogen Evolution Reaction". *ACS Applied Energy Material*, **2022**, *5*, 149.

11. Hideya Tsuchikado, **Meng Chen**, Guoqing Guan, Toshiyuki Abe, “Efficient Photoanode Characteristics of Cadmium Sulfide Films Multi-Deposited Through a Chemical Bath Deposition Process”. *Journal of Applied Electrochemistry*, **2023**, 1-10.

Presentations

1. **M. Chen**, N. Kitiphatpiboon, C. Feng, S. Kongparakul, C. Samart, K. Kusakabe, A. Abudula, G. Guan, “Ni3S2/NiS nanowire with heterojunction for electrochemical hydrogen evolution,” International Symposium on Chemical Engineering (ISChE) 2022, Fukuoka, Japan, Dec. 2-4, 2022. (Oral)

2. **M. Chen**, N. Kitiphatpiboon, A. Abudula, G. Guan, “Heterojunction engineering of Ni_3S_2/NiS nanowires for electrochemical hydrogen evolution,” Joint Meeting of the Tohoku Area Chemistry Societies of 2022, Morioka, Japan, Sep. 17-18, 2022. (Poster)
3. **M. Chen**, N. Kitiphatpiboon, A. Abudula, G. Guan, “Boron-doping MOF-derived hierarchical manganese iron spinel for highly efficient seawater oxidation,” *12th International Conference on Environmental Catalysis (ICEC 2022)*, Osaka, Japan, Jul. 30-Aug. 2, **2022**. *(Poster)*
4. **M. Chen**, N. Kitiphatpiboon, A. Abudula, G. Guan, “Amorphous/crystalline heterostructure zinc-vanadium oxide-cobalt nanosheets for efficient electrocatalytic hydrogen evolution,” *The Society of Chemical Engineers (SCEJ) 87th Annual Meeting*, Hyogo, Japan, Mar. 16-18, **2022**. *(Poster)*
5. **M. Chen**, N. Kitiphatpiboon, A. Abudula, G. Guan, " Efficient utilization of Zn modified vanadium oxide cluster doped Co 2D ultra-thin metal nanosheets for hydrogen evolution reaction in alkaline solution," *the Japan Institute of Energy (JIE) 30th Annual Meeting*, Toyama, Japan, Aug. 4-5, **2021**. *(Poster)*

List of Patents

1. **陳萌**, 官国清, ナッタパック・ギティパットピブーン, 関和治, 阿布里提, “酸素発生電極、水の電気分解方法及び酸素発生電極の製造方法” 出願番号:特願 2022-062000, 出願日:2022 年4月1日.

2. **陳萌**, 官国清, ナッタパック・ギティパットピブーン, 関和治, 阿布里提, “電極触媒及びその製造方法” 出願番号:特願 2021-093897, 出願日:2021 年 6 月 3 日.

3. 馮長瑞, 官国清, **陳萌**, ナッタパック・ギティパットピブーン, 関和治, 阿布里提, “水分解用触媒及びその製造方法、水分解用電極、並びに水の電気分解方法”, 特願 2022-198094, 2022 年 12 月 13 日出願.

4. 馮長瑞、官国清、**陳萌**、周奕帆、関和治、阿布里提、“水電解の酸素発生電極用触媒及びその製造方法並びに水の電気分解方法”、特願 2023-050075、2023 年 3 月 27 日出願。

5. 周奕帆、官国清、**陳萌**、馮長瑞、関和治、阿布里提、“水電解の水素発生電極用触媒、水電解の酸素発生電極用触媒及び水電解用触媒の製造方法並びに水の電気分解方法”、特願 2023-033554、2023 年 3 月 6 日出願.

6. ナッタパック・ギティパットピブーン、官国清、**陳萌**、関和治、阿布里提、“酸素発生電極及びその製造方法、並びに酸素発生電極及び水の電気分解方法”、日本特許、出願番号:特願 2022-022392、出願日:2022 年 2 月 16 日

7. ナッタパック ギティパットピブーン、官国清、**陳萌**、関和治、阿布里提、“電極触媒、酸素発生電極及び水の電気分解方法”、日本特許、出願番号:特願 2021-25200、出願日:2021 年 7 月 30 日.

8. ナッタパック ギティパットピブーン、官国清、**陳萌**、関和治、阿布里提、“新規酸素発生電極”、日本特許、出願番号:特願 2021-123675、出願日:2021 年 7 月 28 日.